Exploring the Influence of Bulk Condensation and Fog Transport on Containment Atmosphere using CFD

Zur Erlangung des akademischen Grades eines
DOKTORS DER INGENIEURWISSENSCHAFTEN (Dr.-Ing.)

von der KIT-Fakultät für Maschinenbau des
Karlsruher Instituts für Technologie (KIT)

genehmigte
DISSERTATION

von

M. Tech. Allen George

Tag der mündlichen Prüfung:	13.02.2025
Hauptreferent:	Prof. Dr.-Ing. Xu Cheng
Korreferent:	Univ.-Prof. Dr.-Ing. habil. Markus Klein

Declaration

Ich versichere wahrheitsgemäß, die Arbeit selbstständig angefertigt, alle benutzten Hilfsmittel vollständig und genau angegeben und alles kenntlich gemacht zu haben, was aus Arbeiten anderer unverändert oder mit Abänderungen entnommen wurde.

Karlsruhe, June 2, 2025

. . . . . .

(**Allen George**)

Acknowledgements

Reflecting on the past four years of my PhD journey, I am filled with gratitude for the invaluable experiences that have shaped my academic and personal growth. This journey has not only deepened my knowledge but has also opened my eyes to new perspectives and possibilities. I would like to take this opportunity to express my heartfelt appreciation to everyone who has supported me along the way, as your encouragement and guidance have been invaluable in helping me reach this milestone.

I am deeply grateful for the opportunity to pursue my doctoral studies, made possible through the generous support of the German Academic Exchange Service (DAAD) for funding my doctoral position through "Research Grants - Doctoral Programmes in Germany." I would also like to extend my gratitude to the Jülich Supercomputing Centre (JSC) for providing the computational resources necessary for running my simulations. Additionally, I am thankful to Becker Technologies GmbH for providing valuable data on the THAI experiments, which were crucial in validating the models developed during this thesis.

I extend my heartfelt thanks to my supervisors, Prof. Xu Cheng and Dr. Stephan. Prof. Xu's belief in me and his support throughout this journey have been incredibly encouraging. I owe a special debt of gratitude to Dr. Stephan, whose unwavering support, motivation, and innovative ideas have been the cornerstone of my work. His mentorship has been truly transformative, and I am profoundly thankful for his dedication.

My time at Forschungszentrum Jülich (FZJ) has been incredibly enriching. I am grateful to Ernie and Michi for their support. I would also like to express my appreciation to Astrid for her invaluable IT support, which greatly facilitated my research work. To my colleagues at FZJ - Guo, Charlie, Liam, Rui, Eva, Shannon, Gary, Khaled, Vijay, and Manohar - thank you for the friendship and great conversations. The lunches at Seecasino, the BBQs at the experimental hall, and fun-filled evenings at Domkeller have created memories I will cherish forever.

Although my time at the Institute for Applied Thermofluidics (IATF) at KIT University was limited, I am thankful for the warm welcome and collaboration I received. My sincere appreciation goes to Nikolai, Ludwig, Fabian, Jun, and Xihan for their cooperation during my visits and online meetings. Your contributions, despite the distance, have been significant and are highly valued.

Finally, I owe an immeasurable debt of gratitude to my family. To my wife, Susan, your constant motivation and support have been my pillar of strength. Your dedication and commitment have been a constant source of inspiration, and I am grateful for your encouragement to complete this journey. I am thankful that we chose to embark on our PhD journeys together, keeping us connected and driven even when miles apart. To my parents, Lissy and George, thank you for always believing in me and for your unwavering support throughout this journey. Your encouragement has fueled my determination and has been a driving force behind my success. I am truly blessed to have you as my parents, and this achievement is a testament to your love and sacrifices. To my sister Anisha, brother-in-law Shibu, and my in-laws, your unwavering encouragement and love have been my foundation. This achievement is as much yours as it is mine.

Abstract

During a severe accident in nuclear power plants, the thermo-fluid dynamic processes inside the containment are governed by the interplay of several interacting physics like turbulence, multi-component gas transport, buoyancy, wall condensation, conjugate and radiation heat transfer. Previous CFD works facilitated the formulation of models capable of simulating these phenomena and their interactions. However, the impact of bulk condensation, fog transport and re-evaporation, and condensate film formation and accumulation is less explored, and the assessment of the required modeling detail is lacking. Bulk condensation leads to the formation of fog droplets, releasing latent heat and elevating local temperatures. These fog droplets are then transported by convection, inertia, and gravity to locations where they re-evaporate, causing localized cooling. These phenomena create temperature gradients large enough to influence the buoyancy forces, gas flow velocities, gas composition, and mixing. Also, the formation and transport of condensate film and its accumulation can influence the conditions inside a containment. The purpose of this thesis is to explore the influence of bulk condensation, fog transport, and evolution as well as the formation, transport, and accumulation of condensate and conclude on an efficient and reliable approach.

In this work, a single-phase and two-phase CFD methodology are developed and implemented into OpenFOAM-based *containmentFOAM* package to model the aforementioned phenomena. The modeling of bulk condensation employs the "return to saturation at constant time scale" approach, and the droplet drift velocity is modeled using the Manninen and Stokes formulations. The droplet evolution by condensation, evaporation, and coalescence and the differential transport of droplets based on their diameters are simulated using a population balance model utilizing the method of classes. The two-phase approach integrates the mixture, film, and VOF methods into a unified multi-method solver, dynamically selecting the appropriate method based on local fluid conditions. The individual sub-models and solver approaches are systematically verified and validated using theoretical data, as well as through separate-effect small-scale and integral-effect technical-scale experiments. The integral-effect validation studies conducted on THAI TH2 and HM2 experiments revealed moderate but physically more consistent representation in TH2, while in HM2, the bulk condensation had a significant impact, with temperature gradients critically affecting gas mixing and composition. The settling of fog droplets and their re-evaporation is crucially influenced by droplet size, and the PBM approach effectively modeled this phenomenon in TH2 and HM2. The two-phase approach exhibited a substantially higher computational effort requirement than the single-phase approach, without yielding notable improvements in results to justify this increased computational cost. Nevertheless, the two-phase approach was able to simulate the intended phenomena like condensate film formation, transport, and accumulations in the containment sump region. The two-phase approach is concluded to be more suitable for smaller containments, such as SMRs with water accumulation, than for larger containment structures. Finally, the scalability of the single-phase model was successfully demonstrated by simulating the International Standard Problem (ISP-37) VANAM M3 experiment on a large-scale Batelle Model Containment (BMC) test facility.

Kurzfassung

In einem schweren Unfall in Kernkraftwerken werden die thermofluiddynamischen Prozesse innerhalb des Sicherheitsbehälters durch mehrere wechselwirkende Mechanismen wie Turbulenz, Mehrkom-ponenten-Gasgemische, Auftrieb, Wandkondensation, konjugierter Wärmeübertragung und Str-ahlungswärmetransport bestimmt. Vorangegangene CFD-Studien führten zur Entwicklung und von Modellen, die diese Phänomene und ihre Wechselwirkungen simulieren können. Die Auswirkungen der Volumenkondensation und des Nebeltransports und -wiederverdampfung, Kondensatfilme, und Kondensatansammlung sind jedoch weniger erforscht, und es fehlt eine Bewertung der erforderlichen Modellierungsdetails. Volumenkondensation führt zur Bildung von Nebeltröpfchen, wobei die latente Wärme die lokale Gastemperatur erhöht. Die Tröpfchen werden zu Orten transportiert, an denen sie wieder verdampfen können, was zu einer lokalen Abkühlung führt. Die erzeugten Temperaturgradienten sind groß genug, um die Auftriebskräfte und somit die Strömungs und die Gasvermischung zu beeinflussen. Ziel dieser Arbeit es, die Auswirkungen der Volumenkondensation, des Nebeltransport und -wiederverdampfung, sowie den Transport und die Ansammlung von Kondensat zu untersuchen und ein numerisch effizientes und belastbares Modell zu identifizieren.

In dieser Arbeit wird ein ein- und zwei-phasige CFD-Modell entwickelt und in das auf OpenFOAM basierende Paket *containmentFOAM* implementiert, um zuvorgenannte Phänomene zu abzubilden. Die Volumenkondensationsrate wird mit dem Ansatz „Rückkehr zum Sättigungzustand innerhalb einer konstanter Zeitskala“ modelliert und die Tröpfchendriftgeschwindigkeit nach Manninen und Stokes beschrieben. Die Tröpfchenentwicklung durch Kondensation, Verdunstung und Koaleszenz sowie ihr größenabhängiger Transport werden mittels eines Populationsbilanzmodells auf Basis der Methode der Klassen simuliert. Das zwei-phasige Modell integriert den Mischungs-, Film- und VOF-Ansatz in einen vereinheitlichten Löser, der dynamisch die geeignete Methode anhand der lokalen Bedingungen auswählt. Die einzelnen Teilmodelle werden systematisch anhand theoretischer Daten, sowie auf Basis kleinskaliger Einzeleffektversuche und der anwendungesorientierten Integralversuche THAI TH2 und HM2 verifiziert und validiert. Es zeigt sich dass der Einfluss der Volumenkondensation in TH2 moderat war, aber eine konsistentere Abbildung der Phenomenologie ermöglichte, während in HM2 die Volumenkondensation einen signifikanten Einfluss auf Temperaturgradienten hatte und so die Gasmischung und -zusammensetzung entscheidend beeinflusste. Das Absetzen von Nebeltröpfchen und ihre Wiederverdunstung wird entscheidend von der Tröpfchengröße beeinflusst. Der Populationsbilanzansatz modelliert dieses Phänomen in TH2 und HM2 effektiv. Der zwei-phasige Ansatz erforderte einen erheblich höheren Rechenaufwand ohne, im Vergleich zum einphasigen Ansatz, eine nennenswerte Verbesserung der Ergebnisse zu liefern, die diesen rechtfertigen können. Dennoch konnte er die relevanten Phänom- ene wie Kondensatfilmbildung, -transport und -ansammlungen im Sumpfbereich simulieren. Er eignet sich somit eher für kleinere Sicherheitsbehälter mit Wasseransammlungen, als für hier betrachtete große trockene Sicherheitsbehälter. Abschließend wurde die Skalierbarkeit des ein-phasigen Berechnungsmodells anhand des VANAM M3-Experiments des ISP-37 im großskaligen Batelle Model Containment erfolgreich nachgewiesen.

Contents

Nomenclature

List of Symbols

Symbol	Description	Unit
ρ_g	Density of the gas phase	kg/m^3
ρ_l	Density of the liquid phase	kg/m^3
ρ_m	Mixture density	kg/m^3
ρ_f	Liquid film density	kg/m^3
t	Time	s
$\vec{U}_g$	Velocity of the gas phase	m/s
$\vec{U}_m$	Mixture velocity	m/s
$\vec{U}_f$	Mean velocity of the film	m/s
S_{mg}	Mass source term in gas phase	$kg/m^3 s$
S_{ml}	Mass source term in liquid phase	$kg/m^3 s$
$\vec{S}_{Ug}$	Momentum source in gas phase	N/m^3
S_{jg}	Specie mass source term in gas phase	$kg/m^3 s$
S_{hg}	Energy source term in gas phase	W/m^3
$S_{\rho\delta}$	Film mass source term	$kg/m^3 s$
$S_{\rho\delta U}$	Film momentum source term	N/m^3
$S_{\rho\delta h}$	Film energy source term	W/m^3
S_{kg}	Turbulent kinetic energy source term in gas phase	kg/ms^2
$S_{\omega g}$	Turbulent eddy frequency source term in gas phase	$kg/m^3 s$
Y_j	Mass fraction of specie j	-
D_{jk}	Binary diffusivity of specie pair $j-k$	m^2/s
$D_{j,m}$	Molecular diffusivity of j^{th} specie in the gas mixture	m^2/s
$D_{t,g}$	Turbulent diffusivity of gas phase	m^2/s
D_B	Brownian diffusivity se	m^2/s
D_{Mp}	Diffusion coefficient of the dispersed phase	m^2/s
X_j	Molar fraction of the j^{th} specie	-
p	Pressure	Pa
τ	Viscous stress tensor	N/m^2
$\vec{g}$	Gravity vector	m/s^2
ν_g	Kinematic gas mixture viscosity	m^2/s
$\nu_{t,g}$	Turbulent eddy viscosity	m^2/s
δ	Kronecker delta	-
K_g	Specific kinetic energy of gas phase	J/kg
k	Turbulent kinetic energy	m^2/s^2
ω	Turbulent eddy frequency	$1/s$
δ_f	Film thickness	m
h_f	Mean film enthalpy	J/kg

Symbol	Description	Unit
α_l	Liquid phase volume fraction	-
α_g	Gas phase volume fraction	-
ψ_l	Gas phase compressibility	$1/Pa$
ψ_g	Liquid phase compressibility	$1/Pa$
T_{sat}	Saturation temperature	K
T	Temperature	K
p_{H_2O}	Partial pressure of steam specie in gas	Pa
X_{H_2O}	Molar fraction of steam specie	-
$\dot{Q}'''$	Energy per unit volume per unit time	W/m^3
T_c	Critical temperature of steam	K
h_{lg}	Latent heat of vaporization of steam	J/kg
Δt	Time-step size	s
$\dot{m}_{bulk}$	Bulk phase change rate per unit volume	kg/m^3s
S^+_{ml}	Bulk condensation rate per unit volume	kg/m^3s
S^-_{ml}	Bulk evaporation rate per unit volume	kg/m^3s
$S_{mf,transfer}$	Film mass source term	kg/m^3s
$\dot{m}_{cond,lim}$	Bulk condensation rate limit	kg/m^3s
$\dot{m}_{evap,lim}$	Bulk evaporation rate limit	kg/m^3s
$C_{p,g}$	Specific heat capacity of gas phase	J/kgK
C_{p,H_2O}	Specific heat capacity of steam	J/kgK
Sc_t	Turbulent Schmidt number	-
k_B	Boltzmann constant	J/K
d_l	Diameter of the dispersed droplets	m
μ_g	Gas phase mixture dynamic viscosity	kg/ms
C_c	Cunningham correction factor	-
λ	Mean free path	m
$\vec{u}_d$	Drift velocity of fog droplet	m/s
C_d	Drag coefficient	-
Re	Reynolds number	-
τ_l	Droplet relaxation time	s
d_i	Representative diameter of i^{uth} size group	m
α_{li}	Volume fraction of i^{uth} size group	-
$\vec{u}_{di}$	Drift velocity of i^{uth} size group	m/s
$\vec{U}_r$	Relative velocity between liquid and gas phase	m/s
τ_{dm}	Diffusion stress tensor	N/m^2
Ω	Phase indicator function	-

Abbreviations

Abbreviation	Long form
ALWR	Advanced Light Water Reactor
BMC	Battelle Model Containment
CFD	Computational Fluid Dynamics
CHT	Conjugate Heat Transfer
CSF	Continuum Surface Force
DM	Discrete Method
DQMOM	Direct Quadrature Method of Moments
GCI	Grid convergence index
HVAC	Heating Ventilation and Air Conditioning
LOCA	Loss of coolant accident
LP	Lumped Parameter
MOM	Method of Moments
NCGs	Non-condensable gases
NPP	Nuclear Power Plant
NSRDS	National Standard Reference Data System
PARs	Passive Auto-catalytic Recombiners
PBM	Population Balance Model
PWR	Pressurized Water Reactor
QMOM	Quadrature Method of Moments
RCS	Reactor cooling system
RPV	Reactor pressure vessel
SST	Shear-Stress Transport
THAI	Thermal Hydraulics, Aerosols, Iodine
URANS	Unsteady Reynolds Averaged Navier-Stokes
VOF	Volume of Fluid

1. Introduction

1.1. Scientific Motivation

In a nuclear power plants (NPPs), the containment structure is the final safeguard that prevents the escape of hazardous radioactive materials into the environment in the event of a severe accident. In water-cooled reactors, during severe accidents like loss of coolant accident (LOCA), a leak in the primary circuit will release large volumes of steam into the containment. This sudden release of steam at high temperature and pressure can cause a rapid rise of containment pressure and temperature. If all emergency cooling systems fail, the steam reacts with the hot zirconium fuel cladding and produces hydrogen [IAEA, 2011]. The accumulation of hydrogen, combined with the rising pressure and temperature, can pose a significant safety risk to the reactor and challenge the structural integrity of the containment.

Condensation significantly contributes to containment safety by mitigating the swift rise in pressure and temperature inside the containment [de la Rosa et al., 2009]. When the steam encounters the cooler containment structures (walls) or mixes with the colder containment gases, it condenses, resulting in the reduction of overall containment pressure. It also affects the temperature distribution due to the associated heat transfer, depending on the mechanism of condensation. Condensation takes place primarily through two mechanisms in a containment: wall condensation and bulk condensation. The wall condensation occurs when the steam makes contact with the cold walls or structures of the containment. This process results in the development of either a liquid film or droplets on the surface, which efficiently transfers the latent heat to the walls. Bulk condensation takes place when the steam gets mixed with the cooler containment atmosphere and forms fog droplets. In this scenario, the latent heat is released into the containment volume, which results in the increase in local temperature. The presence of non-condensable gases like air and hydrogen makes the condensation processes more complicated, especially wall condensation, as they can hinder the steam from reaching the wall by forming a barrier layer [de la Rosa et al., 2009]. The condensation of steam can also result in a local increase in hydrogen concentration, creating conditions favorable for hydrogen combustion. The accurate modeling of bulk and wall condensation rates is essential to analyze its impact on the containment atmosphere and overall safety of the reactor during severe accidents. Conventional condensation modeling approaches use system codes or lumped-parameter codes, like COCOSYS [Allelein et al., 2008a], to predict the spatial average conditions in a containment. These system codes are well-established, have undergone extensive validation, and are computationally efficient. They usually use simplified geometry of the containment and coarse nodalization, because of which they lack spatial resolution and cannot capture local variations. This can limit the prediction capability while analyzing complex containment geometries with several internal components and processes that are sensitive to local variations.

With the advancements in scientific computing capabilities, computational fluid dynamics (CFD) modeling has become a potential alternative for analyzing complicated thermal-hydraulic processes in a reactor containment. It offers the advantage of capturing high-resolution three-dimensi-

onal containment physics, which allows more accurate predictions of local flow and thermal conditions. This can enhance the safety assessments of reactors by improving computation of local condensation rates, gas and temperature distributions, and identifying potential regions of high hydrogen accumulation. Presently, there are several commercial CFD codes [Xiao et al., 2016, Kudriakov et al., 2008] that are well-equipped for simulating containment thermal hydraulics and validated against technical scale experiments. However, the restricted availability of their source codes prevents implementation and validation of new models and further development. To overcome these limitations, a dedicated CFD package named *containmentFOAM*, built on the open-source software OpenFOAM, is being developed in Forschungszentrum Jülich [Kelm et al., 2021] for reactor safety assessments. It is designed to model phenomena specific to reactor containment and is presently a single-phase solver that can simulate multi-component gas mixing, buoyancy-driven turbulent flows, gas radiation, conjugate heat transfer, and interaction with safety systems such as passive auto-catalytic recombiners (PARs). Additionally, it is incorporated with a wall condensation model that employs the "diffusion layer" approach [Vijaya Kumar et al., 2021] in which the condensate formed is removed through the wall boundaries.

The effect of bulk condensation is one of the least explored topics in containment thermal hydraulics. This is primarily due to its marginal impact on the water-steam mass balance compared to wall condensation. The local increase in temperature because of latent heat release during bulk condensation can significantly affect the local buoyancy forces, thereby modifying the flow dynamics and gas distribution within the containment. Moreover, it can also influence the wall condensation by altering the saturation conditions and reducing the amount of steam available for wall condensation. Therefore, the interaction between bulk and wall condensation phenomena and the containment atmosphere is critical for the safety of the reactor. The fog droplets generated during bulk condensation can get transported to different regions within the containment and re-evaporate when it is exposed to hotter containment conditions. This results in the addition of steam back to the containment, causing a rise in pressure and a cooling effect on the local gas mixture. The motion of droplets in a gas phase is highly dependent on their size, especially under the effect of gravity. The larger droplets are more likely to diverge from the main gas flow and get transported to a lower region, where they can re-evaporate or get deposited in the sump regions more readily than the smaller ones. To capture these effects, a population balance model (PBM) should be employed for fog transport. Like the droplets, the film can also get transported to hotter containment regions, re-evaporate, and add to the steam content. The condensate (water) generated during wall and bulk condensation can also accumulate in the sump regions in different compartments of the containment. During prolonged periods of steam release and condensation, the accumulated condensate can occupy a sizable volume of the containment, thereby limiting the space available for gases and affecting the overall pressure. The two-phase approach employing the two-fluid method can be computationally demanding for containment simulations, and it would be cost-effective to explore simpler two-phase approaches like Volume of Fluid (VOF), film, and mixture methods.

1.2. Objectives

The objectives of this thesis are twofold:

1. The first objective is to implement a bulk condensation model for steam and develop a fog transport passive scalar equation. The bulk condensation rate calculation will also account for evaporation, which will allow the transported fog to evaporate if the conditions are met. The fog mass generated is treated as passive scalar in a Eulerian framework and is transported by mechanisms including gas flow convection, turbulent and Brownian diffusion, and drift resulting from gravity, inertia, and drag. The evolution of fog droplet sizes by condensational growth, evaporational shrink, and coalescence is implemented by using a Population Balance Model (PBM) within the passive scalar approach. This helps in improving the fog distribution prediction, as the drift velocity is largely dependent on droplet size.

These models are implemented as an extension to the current *containmentFOAM* solver and interact with other models of the solver.

2. The second objective involves adapting the single-phase *containmentFOAM* solver to a simple two-phase solver using the mixture-film-VOF approach. This approach is particularly aimed at addressing the limitations of the single-phase approach by including the influence of condensate in reactor containments. The passive scalar approach in single-phase requires the removal of fog droplets deposited on wall boundaries to prevent numerical issues. The conservation of condensate mass generated during bulk and wall condensation within the computational domain and its accumulation in the sump regions is possible only by utilizing a two-phase approach. The two-phase mixture-film-VOF model is developed using the best features of mixture, volume of fluid (VOF) and film approaches. This helps in modeling the water (condensate) phase on multiple scales, ranging from dispersed fog droplets to wall films and even continuous phase accumulations. The bulk and wall condensation model implementations are modified for this two-phase approach.

The single- and two-phase models are initially validated using separate effect studies and then used to investigate multi-phenomena interaction on technical scale containment experiments. Finally, a comparative assessment between both models is done in terms of computational effort and accuracy to justify the required modeling effort and to identify limitations.

1.3. Structure of the Thesis

This section introduces the thesis outline. The subsequent chapter deals with the present state of the art and gives a comprehensive overview of condensation phenomena in reactor containments and experiments related to that. It also addresses the different existing modeling approaches for modeling both wall and bulk condensation and their interaction with the other containment phenomena. This chapter concludes by identifying and discussing the gaps in the existing literature to justify the relevance of the present research work. Chapter 3 explains the CFD models employed in this work and how they are implemented into the existing *containmentFOAM* solver. The extension of the current single-phase solver with bulk condensation, fog transport, and PBM models is discussed first. This is followed by detailing the development and integration of a two-phase approach for improving the solver capabilities. Chapter 4 presents the systematic verification and validation of the above models and does a comparative assessment between single and two-phase approaches. It utilizes both analytical solutions and experimental data from small-scale and technical-scale experiments to demonstrate the capability of the code. Chapter 5 highlights the practical use of the code by analyzing a large-scale containment - the VANAM M3 experiment. Chapter 6 summarizes and concludes the major findings and contributions of this work. The last chapter 7 discusses the potential future extensions and possible improvements to the current research work.

2. State of the art

This chapter offers a detailed explanation of the essential concepts and previous studies that are necessary for an in-depth understanding of this research work. It comprises five main parts: the first part provides a general summary of severe accidents, condensation phenomena, and their effects on nuclear reactor containments. The second part discusses various separate effect and integral effect experiments conducted for understanding effects on condensation on the containment atmosphere. The third part gives a brief introduction to various containment thermal hydraulics modeling strategies, from lumped parameter to computational fluid dynamics codes. The fourth part addresses the different CFD approaches, including single-phase and two-phase approaches that can be used for modeling different phenomena inside the containment like gas distribution, fog transport, thin-condensate films, condensate accumulation, population balance modeling of fog droplets, and wall and bulk condensation modeling. The final part summarizes the gaps in the available literature and outlines how this research work aims to address them.

2.1. Severe accidents and condensation in reactor containments

A severe accident is defined as an accident that leads to serious core damage that is beyond the design basis of the nuclear reactor [IAEA, 2022]. In water-cooled reactors, this could be initiated by Loss of Coolant Accident (LOCA), which exposes the reactor core resulting from a rapid depressurization of the reactor cooling systems (RCS). As the pressure drops and the reactor core heats up, super-heated steam is generated in the RPV, which reacts with the zirconium alloy in the fuel cladding, producing hydrogen [IAEA, 2011]. As a result, LOCA results in the discharge of significant quantities of steam and hydrogen into the containment atmosphere. This is followed by a rapid increase in pressure and temperature within the containment, challenging the safety and integrity of the reactor containment. Since containment is the final safeguard against the spread of radioactive material, it is necessary to analyze the events leading to it and optimize design for accident mitigation. Hydrogen, being a light gas compared to other gases in the containment, gets accumulated in the top regions of the containments and its distribution can be affected by the geometry of reactor compartments [Bentaib et al., 2015]. The convection loops inside the containment due to hot gases and condensation can enhance gas mixing and prevent stratification of hydrogen, depending upon the strength of the convection loops. It is crucial to prevent pockets of high hydrogen concentrations due to their combustible nature. The reactors are back-fitted with passive safety systems such as passive autocatalytic recombiners (PARs) to convert hydrogen into water vapor [Arnould et al., 2001]. Containment spray systems complement hydrogen management strategies by promoting gas mixing, lowering containment pressure and temperature, and scrubbing airborne fission products [IAEA, 2011]. The severe accident phenomenology in a typical pressurized water reactor (PWR) is illustrated in Figure 2.1.

Condensation of steam serves as a passive safety system for depressurizing the containment building and removing heat. Wall condensation is the primary mechanism of condensation, which results in the formation of droplets that grow into films on containment structures when steam

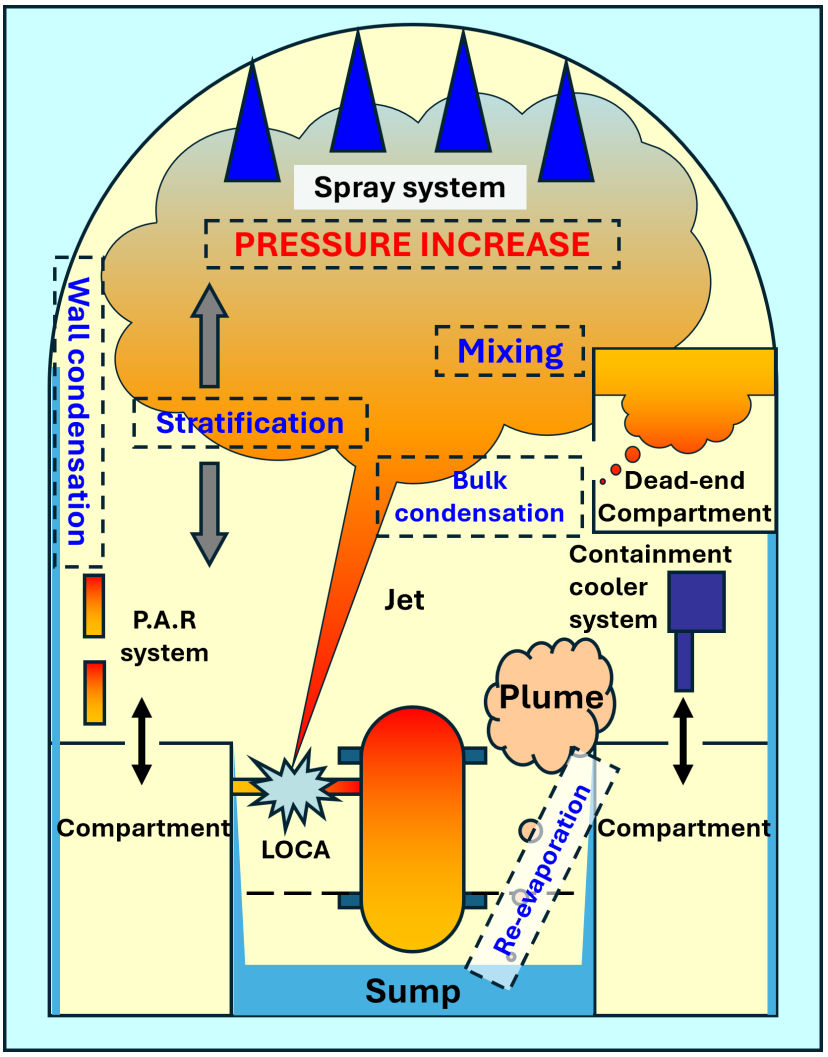

Figure 2.1.: Phenomenology in a PWR containment during a postulated accident (adapted from Paladino et al., 2012).

comes in contact with cooler surfaces. The existence of non-condensable gases (like air and hydrogen) inhibits wall condensation by forming a barrier layer through which steam must diffuse to reach the cooler wall [de la Rosa et al., 2009]. The condensate film flows down towards the sump due to gravity, making the walls available for further condensation. The wall condensation releases latent heat to the building structures, which is effective in transferring heat. However, this process also raises the wall temperature, which in turn reduces the condensation rate. The continuous wall condensation plays a crucial role in extracting the steam mass that is being steadily discharged during LOCA, which is decisive in maintaining the containment pressure. Nevertheless, this leads to higher hydrogen concentrations near the wall, posing a potential combustion risk [Bentaib et al., 2015]. The secondary mechanism of condensation in containments is bulk (or volume) condensation, which occurs in the form of fog (or mist) droplets, which are generated when the steam interacts with cooler gases. Although the proportion of bulk condensation is generally less (< 7%) [NEA, 2009] relative to wall condensation in a typical containment accident scenario, it can influence the containment conditions in several ways. The latent heat from bulk condensation is released into the gas mixture around the fog droplets, which increases the local temperature. Consequently, gas density in the region of bulk condensation decreases and affects the local buoyancy forces. This is particularly important as the containment flows are largely driven by buoyancy effects arising from the density differences due to temperature gradients and gas compositions [Kelm et al., 2016]. The bulk condensation enhances or inhibits the gas mixing inside the containment,

depending on the distribution of the gases. The higher temperature and increasing concentration of hydrogen in the bulk condensation region can also create conditions favorable for hydrogen ignition. In addition to this, the bulk condensation can affect the wall condensation by decreasing the amount of steam available for wall condensation and by altering the saturation conditions. The fog droplets generated can interact with the gas flow depending on their size and get transported to other regions under the influence of gas flow convection, gravity, diffusion, inertia, and drag. The droplet can also get deposited on walls or join the condensate film and flow towards the sump region. When the water film or fog droplets encounter hotter containment conditions, they can re-evaporate and add to the steam content. This also leads to local evaporative cooling on the structures or in the bulk, as the heat of evaporation is absorbed from the surroundings [W. Ambrosini & Oriolo, 2002]. In summary, steam condensation is vital to the safety of the reactor by influencing containment conditions, like gas distribution, pressure, and temperature. While often considered negligible, bulk condensation can interact with the other containment phenomena and completely alter the containment environment. Therefore, it is essential to investigate and model its effects, both experimentally and numerically, for design optimization and to develop strategies for accident mitigation.

2.2. Experimental studies on condensation effects in containment

There have been several experimental studies in the past few decades, and some are still ongoing, on the effect of steam condensation under the influence of non-condensable gases (NCGs) during LOCA in nuclear reactors. They are used for understanding containment condensation-related phenomena, developing correlations, and providing validation data for thermal-hydraulic codes. The experimental facilities range from small-scale separate effects to technical-scale integral effect studies. The condensation separate-effect experiments are primarily designed to isolate and measure direct effects of wall condensation by quantitatively analyzing condensation rate and wall heat flux. The impact of bulk condensation cannot be evaluated directly and can only be assessed using indirect parameters like local temperature changes. At present, there is no experimental facility that can isolate and examine the effect of bulk condensation only. Instead, these effects typically appear as by-products in these separate effect studies and must be interpreted based on that. Therefore, we must rely on analytical data like the Mollier diagram [Mollier, 1929] for verifying bulk condensation models.

The COPAIN facility [Bazin & Castelli, 1999] at CEA, France, and the CONAN facility [Ambrosini et al., 2014] at the University of Pisa, Italy, are among the first separate effect experiments for studying wall condensation under the influence of NCGs. Both consist of a channel test section of 2 m length that is vertically placed. They differ in two aspects: cross-section (COPAIN: 0.6 m x 0.5 m, CONAN: 0.34 m x 0.34 m) and convection regimes investigated. While the CONAN facility considered only forced convection measurements, the COPAIN explored convection regimes ranging from forced to natural. A recent separate effect wall condensation experimental setup is the SETCOM [Kelm et al., 2019] facility at Forschungszentrum Jülich, Germany. This facility features a test section with a square cross-section of 0.44 m x 0.44 m and 6 m length, which is longer compared to earlier experiments. A key characteristic of SETCOM is that the facility can be inclined from vertical to horizontal orientations. This enables comprehensive analysis of buoyancy effects on mixed convection flows and provides extensive condensation data, which is applicable for containment structure walls oriented at different angles. The schematic and a photograph of SETCOM facility are shown in Figure 2.2. In all the aforementioned experiments, the bottom wall of the channel is actively cooled to facilitate wall condensation, and all other walls are insulated. The injected gas consists of steam and air (with helium included in COPAIN) which captures the effect of NCGs on wall condensation. The heat flux and near-wall temperature profiles on the condensing wall are measured for validating system and CFD codes to develop wall condensation models and improve their prediction accuracy. Although the effect of bulk condensation is minimal for these experiments, it can occur close to the cooled wall and moderately influence the

local temperature and wall condensation rates. Hence, these experiments serve as valuable benchmarks for validating numerical condensation models and analyzing the dominant effect of wall condensation and the weak effect of bulk condensation.

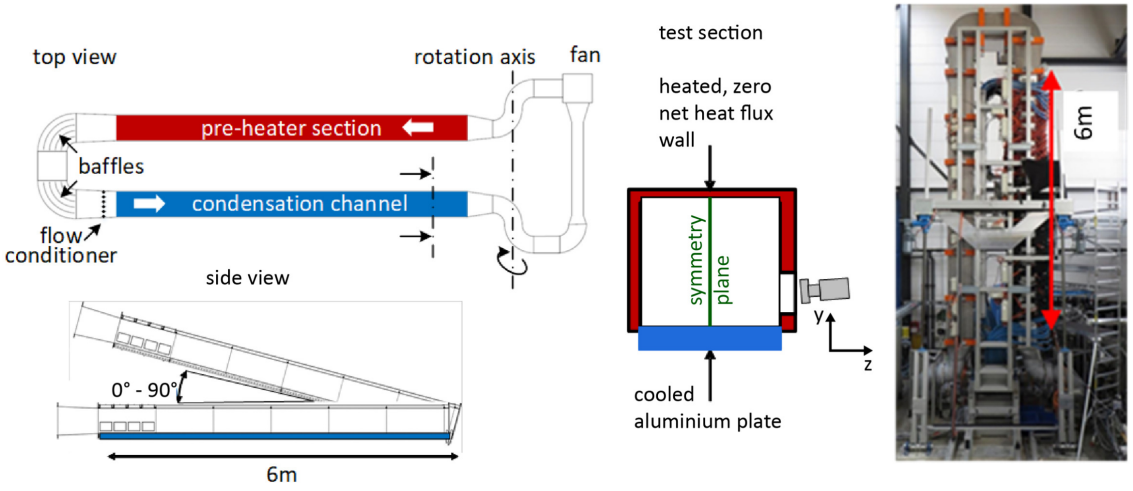

Figure 2.2.: Schematic of the SETCOM facility (left), a photograph of the facility in vertical position (right) [Kelm et al., 2019].

The technical-scale integral experiments are designed for understanding multi-phenomena interactions within nuclear reactor containments under accident conditions. The phenomena under consideration include condensation, natural circulation, gas stratification, turbulence, buoyancy, aerosol behavior, and even the effect of spray systems. Some of the experiments investigating condensation interaction with other phenomena are TOSQAN, MISTRA, THAI, PANDA, and VANAM facilities. These facilities vary in volume, geometry, internal components, compartments, and types of phenomena investigated. TOSQAN (IRSN, France) and MISTRA (CEA, France) feature simple geometries consisting of cylindrical enclosures with cooling and heating circuits close to the external walls, which create condensing and non-condensing walls [Allelein et al., 2008b, NEA, 2007]. These studies are centered on understanding how condensation, stratification, turbulence, and buoyancy interact within the system. The major difference between them is in size, where TOSQAN has a volume of 7 m^3 while MISTRA has a volume of 100 m^3. This is beneficial in understanding the scale-up effects in the containment flow phenomena to examine the applicability of models and codes developed based on small-scale facilities on actual reactor containments. The THAI experiment (Becker Technologies, Germany) has a more complex geometry and multi-compartmentalization with an internal volume of 60 m^3 [Allelein et al., 2008b, NEA, 2007]. This facility (Figure 2.3) is used in exploring more complex interactions like fog formation, wall condensate distribution, development of natural convection, and transient response to heat-conducting walls, in addition to the processes assessed in earlier experiments. The PANDA test facility (PSI, Switzerland) incorporates a modular system of six cylindrical pressure vessels and four water pools with condensers [Paladino & Dreier, 2012]. This facility is dedicated to examining the behavior of containment systems for various Advanced Light Water Reactor (ALWR) configurations, and the vessels and pools represent different compartments of the reactors. It involves investigating additional interactions, like the effect of plume and jet on stratification, spray systems, and recombiners. The six vessels, totaling about 460 m^3, can be run independently, paired, or simultaneously to analyze different containment phenomena. For example, the PANDA Test 9 and Test 9bis [Paladino et al., 2010] utilized only two vessels, which were interconnected through a 1 m diameter pipe. The VANAM facility (BMC, Germany) resembles a PWR containment with a free volume of 626 m^3 (Figure 2.4), consisting of several compartments that are interconnected by vent openings [Kanzleiter, 1993, Firnhaber et al., 1996]. The VANAM-M3 test was conducted to study how hygroscopic aerosol particles are transported and deposited, how condensation oc-

curs on these aerosols, and how these factors impact atmospheric stratification and mixing within a multi-compartment containment geometries.

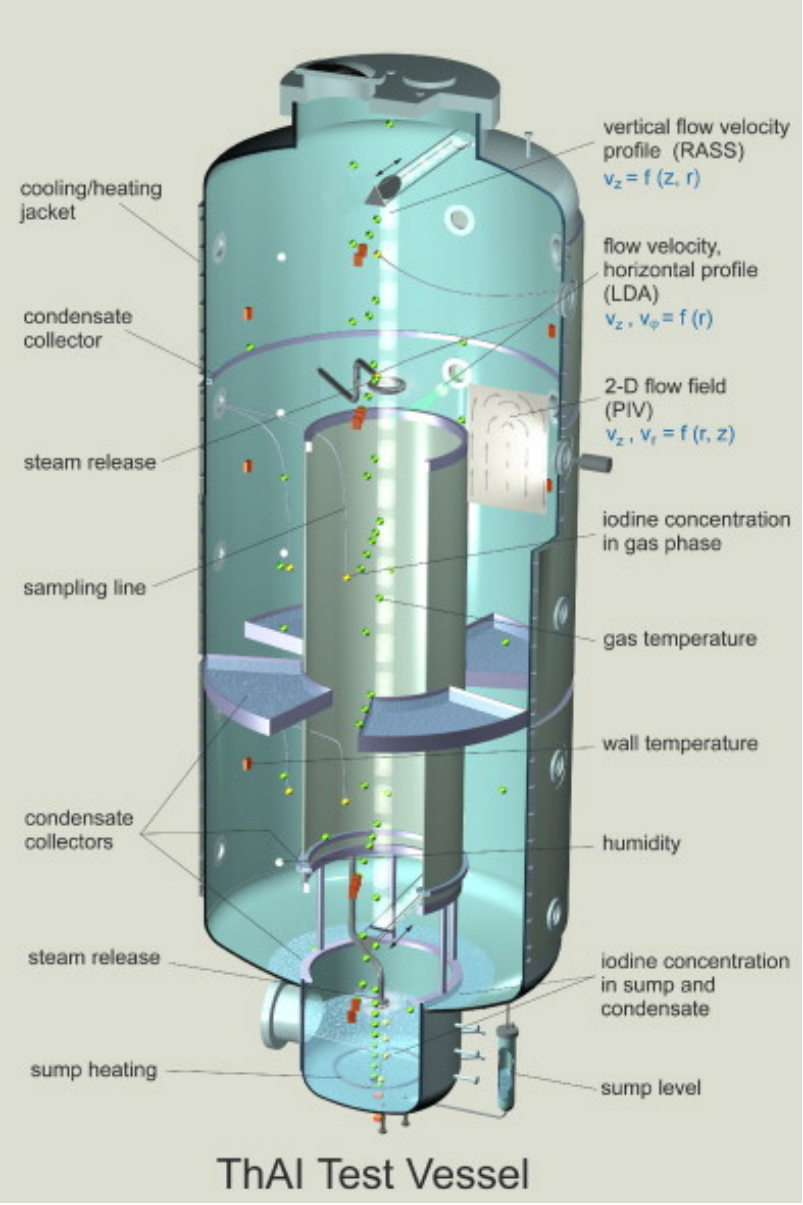

Figure 2.3.: ThAI test vessel and instrumentation [Allelein et al., 2008a].

To sum up, the integral test facilities involved a series of experiments comprising several gases (air, steam, hydrogen, helium, and nitrogen), injection temperature and locations, aerosol injection, wall temperatures, and internal pressure to generate substantial data for detailed analysis and understanding of all the major phenomena happening inside a reactor containment during a postulated accident scenario like LOCA. All of them involved wall and bulk condensation phenomena and their interaction with other processes, which is beneficial for the validation of lumped parameter (LP) and CFD codes analyzing full containment thermal hydraulic phenomena. This research work will use the SETCOM and THAI experiments for validating the CFD solver developed, and the validation process will be discussed in Chapter 4. The VANAM-M3 experiment will be used as an application case to demonstrate the capabilities of the solver in simulating large-scale containments and will be explained in Chapter 5.

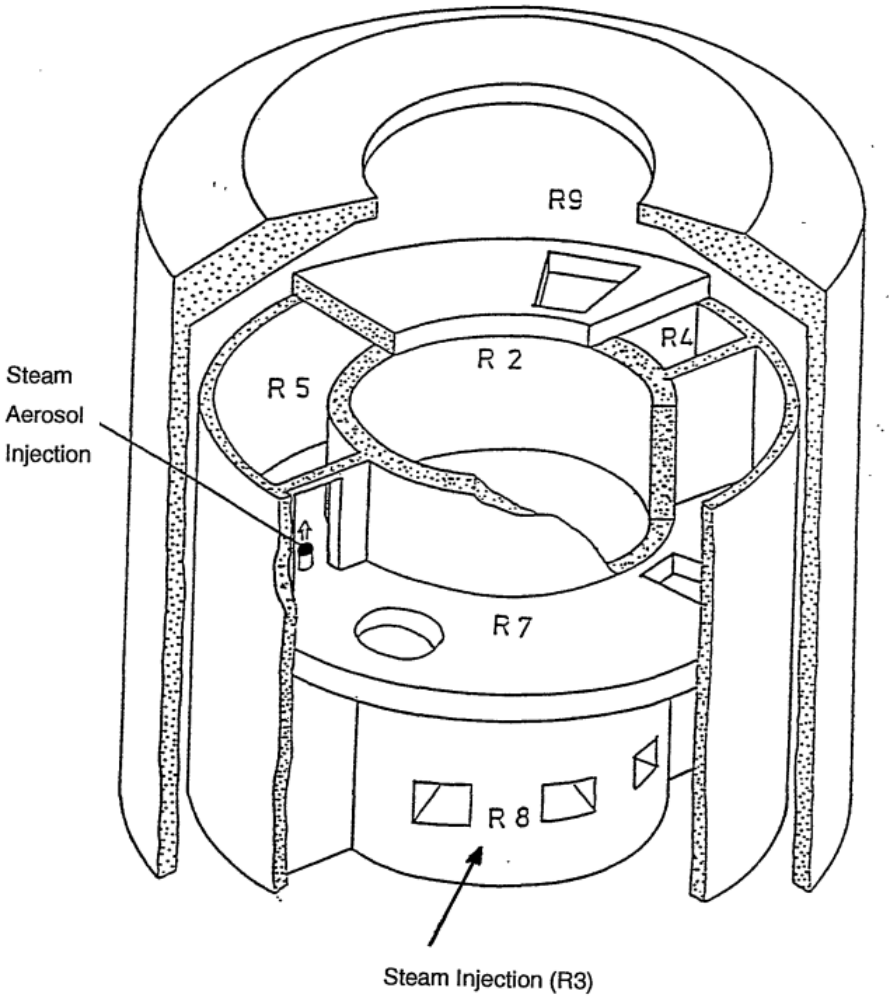

Figure 2.4.: Schematic view of the BMC VANAM test facility [Firnhaber et al., 1996].

2.3. Containment thermal hydraulics modeling strategies

The thermal hydraulic modeling strategies for containment range from lumped parameter (LP) codes to more advanced computational fluid dynamics (CFD) approaches. The LP codes are computationally efficient and use a coarse nodalization consisting of several interconnected control volumes, each representing a section of the physical containment. They are well validated and can predict the overall containment behavior without requiring large computational resources. Hence, they are particularly useful for quick assessments and are commonly used for reactor condition simulations. Codes like COCOSYS (GRS, Germany) and ASTEC (IRSN, France) are examples of LP codes for predicting containment thermal hydraulics [Bosland et al., 2012]. Both these codes are equipped with condensation models and can incorporate its effects on the thermal hydraulic phenomena inside the containment [Broxtermann & Allelein, 2013, Zambaux & Laborde, 2023]. However, the LP codes lack spatial resolution and hence may fail to capture localized phenomena, which is critical for complex containment geometries consisting of several compartments and components. The CFD approach offers higher spatial and temporal resolution, hence being suitable for in-depth analysis. It can capture the local variations in temperature, velocity, and species concentrations more accurately by using fine three-dimensional meshes and solving the full Navier-Stokes equation of fluid flow. There are several general-purpose CFD codes like ANSYS Fluent, ANSYS CFX, OpenFOAM and STAR-CCM+ that are suitable for containment analysis with some adaptations. Additionally, there are some specialized CFD codes like GASFLOW [Hughes et al., 2000], NEPTUNE [Guelfi et al., 2007] and *containmentFOAM* [Kelm et al.,

2021], which are specifically developed for containment applications. Then, there are hybrid codes like GOTHIC [Harvill et al., 2022], which encompasses both LP and CFD approaches to make use of the best features of each to simulate containment phenomena. All these CFD codes are also integrated with condensation models to capture their effects on the containment atmosphere. The ISP-47 [NEA, 2007] recommends utilizing both LP and CFD codes for analyzing hydrogen safety issues in containment.

2.4. CFD Modeling approaches

The containment flow regime during LOCA can vary from single-phase to multiphase flow, depending on the internal conditions and stage of the accident. These different approaches were individually investigated to identify the optimal combination for development and implementation in the research work.

2.4.1. Single-phase multi-component gas flow modeling

During the initial stages of LOCA, only air, steam, and hydrogen gases are present in the containment, so a single-phase analysis is appropriate. This can be modeled by most commercial general-purpose and reactor-specific CFD codes. *containmentFOAM* is capable of simulating this phenomenon and uses unsteady Reynolds-averaged Navier-Stokes (URANS) equations to describe the mixing of multiple gas components and pressurization processes within the containment. The *containmentFOAM* compressible flow governing equations [Kelm et al., 2021] are:

Mass continuity equation:

$$\frac{\partial \rho_g}{\partial t} + \nabla \cdot (\rho_g \vec{U}_g) = S_{mg} \tag{2.1}$$

where ρ_g is the density of the multi-component gas mixture and $\vec{U}_g$ is its velocity. The S_{mg} term accounts for any mass source (or sink) terms resulting from phase change or leakage.

Species mass conservation equation:

The transport of each gas component within the gas mixture is represented by its mass fraction, Y_j and with the corresponding transport equation given by:

$$\frac{\partial \rho_g Y_j}{\partial t} + \nabla \cdot (\rho_g \vec{U}_g Y_j) = \nabla \cdot \left[\rho_g \left(D_{j,m} + D_t\right) \nabla Y_j\right] + S_{jg} \tag{2.2}$$

where $D_{j,m}$ represents the molecular diffusivity of j^{th} species within the gas mixture, D_t is the turbulent diffusivity computed from the turbulence model, and S_{jg} includes the effect of species mass source terms. The diffusion coefficient for each species in the mixture is determined from binary mass diffusion coefficients, applying Fick's law.

$$D_{j,m} = \frac{1 - X_j}{\sum_{k \neq j} X_k / D_{jk}} \tag{2.3}$$

where D_{jk} denotes the binary diffusion coefficient for the species pair $j - k$ and X_j represents the molar fraction of the j^{th} species.

Momentum conservation equation:

$$\frac{\partial \left(\rho_g \vec{U}_g\right)}{\partial t} + \nabla \cdot \left(\rho_g \vec{U}_g \otimes \vec{U}_g\right) = -\nabla p + \nabla \cdot \tau + \rho_g \vec{g} + \vec{S}_{Ug} \tag{2.4}$$

where p is the gas mixture pressure, $\vec{g}$ represents the gravitational acceleration, $\vec{S}_{Ug}$ denotes the momentum source (or sink term), and τ is the viscous stress tensor, which includes both laminar and turbulence effects and is given by:

$$\tau = \rho_g \left(\nu_g + \nu_{g,t}\right)\left[\nabla \vec{U}_g + \left(\nabla \vec{U}_g\right)^T - \frac{2}{3}\delta \nabla \cdot \vec{U}_g\right] \tag{2.5}$$

Here ν_g represents the kinematic gas mixture viscosity, $\nu_{g,t}$ denotes the turbulent eddy viscosity computed from the turbulence model, and δ is the Kronecker delta.

Energy conservation equation:

The energy conservation equation is expressed in terms of enthalpy of the gas mixture, h_g and is given by:

$$\frac{\partial\left(\rho_g h_g\right)}{\partial t} + \nabla \cdot \left(\rho_g \vec{U}_g h_g\right) + \frac{\partial\left(\rho_g K_g\right)}{\partial t} + \nabla \cdot \left(\rho_g \vec{U}_g K_g\right) = \rho_g \vec{U}_g \cdot \vec{g} + \frac{\partial p}{\partial t} - \nabla \cdot \vec{q''} + S_{hg} \tag{2.6}$$

where K_g represents the specific kinetic energy of the mean flow and S_{hg} accounts for the energy source term. The $\vec{q''}$ term corresponds to the enthalpy flux due to conduction and diffusion of gas species.

Turbulence modeling:

The gas mixture flow turbulence is resolved using the isotropic $k-\omega$ SST turbulence model [Menter & Esch, 2001]. Extra terms are incorporated to represent the turbulence production and dissipation resulting from buoyancy effects. The governing equations for the transport of turbulent kinetic energy (k_g) and eddy frequency (ω_g) in *containmentFOAM* [Kampili et al., 2021] are given by:

$$\frac{\partial(\rho_g k_g)}{\partial t} + \nabla \cdot (\rho_g \vec{U}_g k_g) = \nabla \cdot [(\mu_g + \sigma_k \mu_{g,t}) \nabla k_g] + P_k + P_{k,b} - \beta^* \omega_g k_g + S_{kg} \tag{2.7}$$

$$\begin{aligned}&\frac{\partial(\rho_g \omega_g)}{\partial t} + \nabla \cdot (\rho_g \vec{U}_g \omega_g) \\ &\quad = \nabla \cdot [(\mu_g + \sigma_\omega \mu_{g,t}) \nabla \omega_g] + 2(1 - F_1)\frac{\rho_g \sigma_{\omega 2}}{\omega} \nabla k \cdot \nabla \omega + \frac{\gamma}{\nu_{g,t}} P_k + P_{\omega,b} - \beta \rho_g \omega_g^2 + S_{\omega g}\end{aligned} \tag{2.8}$$

where the eddy viscosity $\mu_{g,t}$ is given by

$$\mu_{g,t} = \frac{\rho_g a_1 k_g}{\max\left(a_1 \omega_g, S F_2\right)} \tag{2.9}$$

and $\nu_{g,t}$ is the turbulent kinematic viscosity.

The P_k is the turbulence production term given by

$$P_k = \min\left(\tau \nabla \vec{U}_g, 10 \beta^* k_g \omega_g\right) \tag{2.10}$$

The term $P_{k,b}$ represents turbulence production due to buoyancy, while $P_{\omega,b}$ denotes turbulence dissipation caused by buoyancy; both terms are formulated using the Simple Gradient Diffusion Hypothesis (SGDH) approach [Chung & Devaud, 2008].

$$P_{k,b} = \frac{\mu_{g,t}}{\sigma_t} \tag{2.11}$$

$$P_{\omega,b} = \frac{\rho_g}{\mu_{g,t}} \left[(\gamma_1 + 1)(1 - C_{3\omega}) \cdot \max(P_{k,b}, 0) - P_{k,b} \right] \tag{2.12}$$

where β^*, σ_k, σ_t, β, σ_ω, $\sigma_{\omega 2}$, γ_1, $C_{3\omega}$ and a_1 are model constants, F_1 and F_2 are blending functions, and S denotes the strain invariant; all of these are defined and calculated in accordance with the standard $k - \omega$ SST turbulence model.

2.4.2. Aerosol and fog transport modeling

The overheating of the reactor core during LOCA can lead to the generation of nuclear aerosols, which are carried into the containment by the gas mixture [NEA, 2009]. The transport of aerosols in the gas mixture is a dispersed phase flow and can be modeled using the Euler-Lagrange approach or the Euler-Euler approach or even the Euler-Passive scalar approach. Additionally, during the early LOCA stages, when the saturated steam gets mixed with the cooler containment gases, bulk condensation occurs and results in the formation of fog droplets. The fog droplets exhibit characteristics analogous to aerosols, and hence, the aerosol transport modeling methods are applicable and can be adapted for effectively simulating fog transport phenomena.

Euler-Lagrange approach

The Euler-Lagrange approach [Kampili, 2024] solves a force balance equation to track the trajectory of each individual aerosol within the computational domain. It can be utilized for containment aerosols or fog droplet tracking, like the microdroplets transport model in atmospheric clouds [Sidin et al., 2009]. This approach, while numerically accurate and capturing in-depth aerosol behavior, is computationally challenging for technical scale containment applications, as the computational load rises with the aerosol particle count.

Euler-Euler approach

The Euler-Euler approach is a simplified method that represents the aerosol phase as a continuum and uses a volume fraction equation for the aerosols to simulate their distribution. This method is computationally efficient and ideally falls under the two-phase approach. Common Euler–Euler methods include the homogeneous method, where the aerosol follows the gas flow, and the mixture method [Manninen et al., 1996], which applies a drift-flux technique to model the relative velocity of the dispersed phase to the continuous phase (gas). The mixture model equations [Manninen et al., 1996], which treat aerosols as a dispersed phase with relative motion to the continuous gas phase, are given by:

Mixture continuity equation:

$$\frac{\partial \rho_m}{\partial t} + \nabla \cdot \left(\rho_m \vec{U}_m \right) = 0 \tag{2.13}$$

where $\rho_m = \alpha_p \rho_p + (1 - \alpha_p)\rho_g$ represents the mixture density and $\vec{U}_m$ denotes the mixture velocity. Here, α_p is the volume fraction of the dispersed phase with density ρ_p.

Mixture momentum equation:

$$\frac{\partial \left(\rho_m \vec{U}_m \right)}{\partial t} + \nabla \cdot \left(\rho_m \vec{U}_m \vec{U}_m \right) = -\nabla p - \nabla \cdot \left[\rho_m c_p \left(1 - c_p \right) \vec{u}_{cp} \vec{u}_{cp} \right] + \nabla \cdot \tau_{Gm} + \rho_m \vec{g} \tag{2.14}$$

Here, the second term on the right-hand side accounts for the momentum transfer due to the relative motion of aerosols with relative velocity $\vec{u}_{cp}$, c_p represents the mass fraction of the dispersed phase in the mixture and τ_{Gm} denotes the viscous stress tensor.

Dispersed phase continuity equation:

$$\frac{\partial \alpha_p}{\partial t} + \nabla \cdot \left(\alpha_p \vec{U}_m - D_{Mp} \nabla \alpha_p\right) = -\nabla \cdot \left[\alpha_p \left(1 - c_p\right) \vec{u}_{cp}\right] \tag{2.15}$$

where D_{Mp} represents the diffusion coefficient of the dispersed phase.

Relative velocity equation:

$$|\vec{u}_{cp}|\vec{u}_{cp} = \frac{4 d_p}{3 C_D} \frac{\left(\rho_p - \rho_m\right)}{\rho_g} \left[\vec{g} - \left(\vec{U}_m \cdot \nabla\right) \vec{U}_m - \frac{\partial \vec{U}_m}{\partial t}\right] \tag{2.16}$$

where d_p denotes the diameter of the aerosol particle and C_D represents the coefficient of drag.

Another Euler-Euler approach for fog transport modeling is the two-fluid method [Zhang & Laurien, 2014], which was applied for containment safety analysis. This method accounts for thermal and mechanical non-equilibrium between the continuous gas phase and the dispersed fog droplet phase, specifically in terms of temperature and velocity differences. The fog droplet size was assumed to be fixed during a simulation, and the effects of droplet size evolution by condensation, evaporation, and coalescence were neglected. The method involves two separate sets of conservation equations, one for each phase, along with addition terms for coupling both phase equations. Hence, this method is computationally more intensive compared to the mixture model, which uses mixture equations.

Euler-Passive scalar approach

The Euler-Passive scalar approach is the simplest method, which treats an aerosol as a passive scalar and solves a concentration equation for the aerosol. It uses one-way coupling such that the aerosol transport is affected by the gas flow fields while the gas dynamics are assumed to be independent of the aerosol motion. This approach, coupled with a simplified drift-flux model [Chen et al., 2006], enables modeling of gravitational settling by drift velocity, and diffusion. For every particle size, the concentration equation can be solved simultaneously to obtain individual size group concentration, as the drift velocity can vary with the particle diameter. Based on that, the equation representing particle transport dynamics in a turbulent flow field is given as:

$$\frac{\partial C_i}{\partial t} + \nabla \cdot \left[(\vec{U} + \vec{u}_{s,i}) C_i\right] = \nabla \cdot \left[(D_i + \epsilon_p) \nabla C_i\right] \tag{2.17}$$

where C_i represents the particle mass concentration of particle size group i, $\vec{U}$ denotes the velocity of the bulk gas flow, and $\vec{u}_{s,i}$ is the particle settling velocity. Here, D_i represents the Brownian diffusion coefficient, and ϵ_p is the particle eddy diffusivity.

The passive scalar approach requires special treatment at the wall boundaries to prevent accumulation and numerical issues arising from that. Therefore, it is recommended to remove the fog droplet reaching the wall using a deposition boundary condition. This is implemented as drift velocity boundary condition [Frederix et al., 2017], which uses zero gradient velocity Neumann boundary condition when the drift velocity vector is towards the wall and zero velocity Dirichlet boundary condition if the drift velocity vector is away from the wall. This is mathematically expressed as:

$$\vec{u}_{s,i}^{wall} = \max(\vec{u}_{s,i}^{cell} \cdot \vec{n}_{wall}, 0) \vec{n}_{wall} \tag{2.18}$$

where $\vec{u}_{s,i}^{wall}$ is the drift velocity at the wall, $\vec{u}_{s,i}^{cell}$ represents the drift velocity at the cell center adjacent to the wall, and $\vec{n}_{wall}$ denotes the unit vector normal to the wall.

2.4.3. Thin surface film modeling

The interaction of steam with the cooler containment surfaces during later stages of LOCA results in the formation of droplets, rivulets, and films on the walls. The formation and transport of these films can be modeled using the two-fluid method [Mimouni et al., 2011], volume of fluid (VOF) method [El Baamrani et al., 2021, Rattner & Garimella, 2014], or thin surface film method [Meredith et al., 2011b, Sosnowski et al., 2013]. The two-fluid method is the most sophisticated approach, as it can be used to independently track the movement of mass and heat within each phase by solving distinct conservation equations for both phases. However, for capturing the detailed physics of a very thin film of the liquid phase, the two-fluid method requires remarkably high spatial resolution meshes near the wall. The VOF method is the simplest two-phase approach for modeling wall film flows. It solves the mixture conservation equations to identify the gas-liquid interface and does not consider relative motion between the phases. However, it is not applicable for very thin films whose thickness is less than the first cell near the wall and hence requires very fine meshes to resolve the interface. Therefore, both two-fluid and VOF methods are insufficient to predict the flow of very thin films accurately in a coarse mesh and can perform well only on very fine meshes, which significantly increase the computational cost and time. These methods also require rigorous mesh independence studies, as their sensitivity may also be affected by the local film thickness and reduce the model's applicability to a general containment simulation.

The thin film model is advantageous in this context, as it is specifically designed for liquid films whose thickness is insignificant compared to the other dimensions of the flow domain. It operates under the assumption that transverse velocity components normal to the film surface are minimal. Hence, the governing equations can be reduced from three dimensions to two dimensions by averaging across the film thickness. This requires a separate two-dimensional mesh that resembles the wall surfaces of the containment, on which the simple two-dimensional film equations are solved. As a result, this approach allows coarser meshes in the primary flow domain, which significantly reduces the computational cost. Additionally, the thin film model allows easier and more effective integration of surface tension and related interfacial phenomena, which is crucial for thin film dynamics. The thin surface film model governing equations [Meredith et al., 2011a, Meredith et al., 2011b] are given by:

Film thickness equation:

$$\frac{\partial\left(\rho_f \delta_f\right)}{\partial t} + \nabla_s \cdot \left(\rho_f \delta \vec{U}_f\right) = S_{\rho\delta} \tag{2.19}$$

where ρ_f denotes the liquid film density, δ_f represent the film thickness, $\vec{U}_f$ is the mean velocity of the film, ∇_s is the vector differential operator tangential to the film surface, and $S_{\rho\delta}$ quantifies the source term accounting for the film growth or depletion (e.g., condensation or evaporation).

Film momentum equation:

$$\frac{\partial\left(\rho_f \delta_f \vec{U}_f\right)}{\partial t} + \nabla_s \cdot \left(\rho_f \delta_f \vec{U}_f \vec{U}_f\right) = -\delta_f \nabla_s p + S_{\rho\delta U} \tag{2.20}$$

The first term on the right-hand side represents the momentum source terms, which are pressure-based acting perpendicular to the film surface, while the second term $S_{\rho\delta U}$, incorporates the stress-based momentum source terms acting parallel to the film surface. The pressure p comprises capillary action forces, hydrostatic pressure effects, and pressure from the local gas phase. The stress term consists of the viscous shear stresses from the wall and the gas, gravity body force tangential to the surface, and the stress related to contact angle force. The film shear stress is calculated assuming a quadratic velocity distribution, which is valid for even wavy liquid films [Trela, 1994].

Film energy equation:

$$\frac{\partial\left(\rho_f \delta_f h_f\right)}{\partial t} + \nabla_s \cdot \left(\rho_f \delta_f \vec{U}_f h_f\right) = S_{\rho\delta h} \tag{2.21}$$

where h_f denotes the mean film enthalpy and $S_{\rho\delta h}$ accounts for the energy source term due to phase change and heat fluxes at the film-gas and film-solid wall interfaces.

2.4.4. Condensate accumulation modeling

The wall condensate films and fog droplets get transported towards sump regions of the containment by gravitational forces. This results in the accumulation of liquid in the containment, creating a liquid-gas interface. Over extended periods of continuous condensation, the condensate can occupy a considerable volume of the containment and reduce the space available for gas mixtures. Moreover, as the pressure and temperature inside the containment increase, re-evaporation can occur, leading to the addition of steam back to the containment gas mixture. The best two-phase approach for modeling these phenomena is the Volume of Fluid (VOF) method [Hirt & Nichols, 1981, Weller, 2006], which is widely used for simulating flows with complex free surface dynamics. This method is more effective in capturing the interface between two fluids than the two-fluid method, which does not explicitly track the interface but rather focuses on the overall behavior of each phase [Bertolotti et al., 2020]. The VOF method can maintain sharp interfaces, which is made possible with the help of interface compression techniques [Okagaki et al., 2021]. The VOF method also uses mixture conservation equations for momentum and energy, which makes it simpler than the two-fluid method with individual phase conservation equations. The VOF method formulation is different for incompressible and compressible flows. The containment atmosphere experiences significant density variation due to the multi-component nature of the gas mixture and large temperature gradients. Therefore, the compressible VOF method is the preferable approach for containment applications. The compressible VOF method governing equations [Gärtner et al., 2020, Kleiner et al., 2019] for flow without phase change can be summarized as:

Liquid phase volume fraction transport equation:

$$\frac{\partial \alpha_l}{\partial t} + \nabla \cdot (\alpha_l \vec{U}_m) = \alpha_l \alpha_g \left[\left(\frac{\psi_g}{\rho_g} - \frac{\psi_l}{\rho_l} \right) \frac{Dp}{Dt} + \left(\frac{p}{\rho_g} \frac{D\psi_g}{Dt} - \frac{p}{\rho_l} \frac{D\psi_l}{Dt} \right) \right] + \alpha_l \nabla \cdot (\vec{U}_m) \tag{2.22}$$

where α_l and α_g represent the liquid and gas volume fractions, respectively, and ρ_l and ρ_g denote the liquid and gas phase densities, respectively. $\vec{U}_m$ quantifies the mixture velocity. D/Dt represents the material derivative. The first right-hand side term accounts for the effect of compressibility in both phases. Here, $\psi_l = \partial \rho_l / \partial p$ and $\psi_g = \partial \rho_g / \partial p$ are the compressibilities of liquid and gas phases, respectively.

Mixture momentum equation:

$$\frac{\partial \left(\rho_m \vec{U}_m \right)}{\partial t} + \nabla \cdot \left(\rho_m \vec{U}_m \vec{U}_m \right) = -\nabla p + \nabla \cdot \tau + \rho_m \vec{g} + F_\sigma \tag{2.23}$$

where ρ_m represents the mixture density and τ denotes the viscous stress tensor. The last term F_σ incorporates surface tension effects computed via the Continuum Surface Force (CSF) method [Brackbill et al., 1992].

Mixture energy equation:

The energy equation employs a single mixture temperature, T_m, which is common for both liquid and vapor phases, derived by mergingthe energy equations of both phases.

$$\rho_m \frac{DT_m}{Dt} + \left(\frac{\alpha_l}{C_{pl}} + \frac{\alpha_g}{C_{pg}} \right) \left(\rho \frac{DK_m}{Dt} - \frac{\partial p}{\partial t} \right) = \left(\alpha_l \nabla \cdot (\lambda_{\text{eff},l} \nabla T_m) + \alpha_g \nabla \cdot (\lambda_{\text{eff},g} \nabla T_m) \right) \tag{2.24}$$

where C_{pl} and C_{pg} represent the specific heat capacities of the liquid and gas phase, respectively, and K_m is the kinetic energy of the mixture. $\lambda_{\text{eff},l}$ and $\lambda_{\text{eff},g}$ denote the effective thermal conductivity of liquid and gas phases, respectively. It is also possible to have separate temperature fields

for each phase to allow thermal non-equilibrium between the phases. However, this requires solving of individual phase energy equations, which are coupled through source terms [Gärtner et al., 2020]. Moreover, this approach becomes more challenging for flows with phase change, owing to the determination ofinterface temperature, where numerical stability can be achieved only at low time step sizes.

To summarize, the VOF method is the recommended approach for condensate accumulation modeling, as it can track the gas-liquid interface with reasonable accuracy. It is also possible to couple the VOF method with the thin surface film model [Kakimpa et al., 2016] to transfer the film mass to VOF when the film is thick enough for VOF and vice versa.

2.4.5. Population balance modeling

The fog droplets generated because of bulk condensation can vary in diameters due to droplet size evolution mechanisms like nucleation, condensational growth, evaporational shrink, coalescence, and break-up. The fog droplet distribution inside the containment is significantly affected by the diameter, as the droplet drift velocity is a function of the diameter. The smaller droplets tend to follow the gas mixture and remain suspended, whereas the larger droplets deviate from the gas flow predominantly due to gravity effect and get transported towards the floor region and get deposited. These transport phenomena cannot be captured by using a fixed droplet diameter and require population balance modeling to simulate them. The droplet evolution and diameter effects can also be modeled using the Lagrangian method [Sidin et al., 2009], but it is computationally intensive for a large number of droplets. The PBM method is commonly used for predicting dispersed distributions of bubbles, crystals, polymers, aerosols, and granular materials [Singh et al., 2022]. There are several PBM approaches used in CFD like Discrete Method (DM) [Becker et al., 2011], Method of Moments (MOM) [Hulburt & Katz, 1964], Quadrature Method of Moments (QMOM) [McGraw, 1997], Direct Quadrature Method of Moments (DQMOM) [Marchisio & Fox, 2005], sectional method [Park & Rogak, 2004] and stochastic Monte Carlo method [Irizarry, 2012]. Among these, the most adopted approaches for solving PBM equations are QMOM and sectional method (also known as method of classes). The QMOM represents the particle population through a set of moments (like mean size, variance) and quadrature nodes rather than the full distribution. Therefore, it does not provide a direct representation of the distribution and requires reconstruction of the moments for getting detailed distribution information. The QMOM is more computationally efficient as it solves for a finite set of moment transport equations rather than each size group transport equation. However, it requires closure models to approximate higher-order moments, which can induce errors and can affect the accuracy and stability of processes like nucleation, growth, and coalescence at a higher rate of these phenomena.

The method of classes (sectional method) employs a direct and detailed representation of the particle size distribution by discretizing the droplet sizes into sections and using a representative size for each section to determine its properties. This allows explicit tracking of the number or mass of the droplets in each section or class by solving the PBM equation for each section. This method can accurately capture and represent complex distributions without additional assumptions, hence suitable for rapid evolution processes. Therefore, it offers higher flexibility in modeling the fog droplet evolution mechanisms like nucleation, growth, and coalescence. While computationally intensive, the sectional method offers more accurate modeling of the droplet size distribution, which is critical for accurate droplet drift velocity prediction. Hence, the sectional method will be used in the current work and can be easily implemented in both single-phase and two-phase approaches. The population balance equation [Lehnigk et al., 2022] is formulated in terms of number concentration (N_i) and the transport equation is solved for each section (or class). The droplet size space is divided into groups, each defined by lower and upper volume boundaries v_i and v_{i+1}, with representative (or pivotal) size x_i.

$$\frac{\partial N_i}{\partial t} + \nabla \cdot (\vec{U} N_i) = H_i \tag{2.25}$$

Here, H_i represents the source term, which encompasses the effects of coalescence, nucleation, growth, and breakup. Since the population is concentrated at the representative size, x_i, the evolution processes leading to non-representative sizes (v) are solved by redistributing [Kumar & Ramkrishna, 1996a] it to the nearby classes $x_i \leq v \leq x_{i+1}$.

2.4.6. Condensation modeling

During LOCA, the mixing of steam with the cooler containment gases leads to bulk condensation, while the interaction of steam with the cold containment structures causes wall condensation. These condensation processes, due to the differences in their physical mechanisms, require different approaches for modeling.

2.4.6.1. Wall condensation modeling

The wall condensation in containment is strongly affected by non-condensable gases (NCGs), which can accumulate near the wall as the steam concentration decreases and form an additional barrier to condensation and heat transfer. Therefore, the pure steam wall condensation models [Kim et al., 2011, Bonneau et al., 2019, Gubarevich et al., 2020] are inadequate in containment scenarios, necessitating wall condensation models that consider the NCG effects to accurately predict the containment wall condensation rate. These wall condensation models rely on the concept of steam diffusing toward the wall to drive condensation and have been investigated and implemented in CFD codes for containment simulations. Most of these codes use a single-phase approach in which the condensate mass formed is removed from the computational domain and are known as diffusion-layer models. This can be implemented as a volume sink in the near-wall cells [Bucci et al., 2013, Dehbi et al., 2013, Vyskocil et al., 2014] or as a face-flux [Zschaeck et al., 2014, Vijaya Kumar et al., 2021] at the condensing wall. It was found that the face-flux approach performed better on coarse meshes and demonstrated better convergence behavior and mass conservation [Vijaya Kumar et al., 2021]. The underlying assumption of the diffusion-layer models is that the liquid film formed by condensation is minimal in thickness, and its role in influencing wall condensation is therefore ignored. Figure 2.5 explains the theory and assumptions behind this model. Figure 2.5 (a) addresses the wall condensation in the case of a pure steam atmosphere. In this case, the condensation rate is influenced by the thermal resistance of the condensate film (R_L) and liquid-steam interface (R_i). In the presence of NCGs, the gases add transport resistance (R_{gas}) which is illustrated in Figure 2.5 (b) and significant already for low NCG mass fractions. Figure 2.5 (c) sums up the simplified diffusion-layer wall condensation model, where the condensation resistance due to the liquid film and interface are neglected; only the gas resistance is considered. This is found to be a reasonable simplification for containment wall condensation studies [de la Rosa et al., 2009], where large amounts of NCGs are present.

The *containmentFOAM* solver uses the simplified diffusion-layer wall condensation model, and the wall condensation rate is given by:

$$\dot{m}_{wall,flux} = \frac{\rho_g D_{H_2O,m,face}}{1 - Y_{H_2O,sat,face}} \frac{Y_{H_2O,cell} - Y_{H_2O,sat,face}}{\delta_{cell-face}} \quad [\frac{kg}{m^2 s}] \tag{2.26}$$

where $D_{H_2O,m,wall}$ represents the effective diffusivity of steam in the gas mixture, which includes both molecular and turbulence effects. The wall condensation driving force is the gradient of steam mass fraction in the wall normal direction. This can be computed as the difference between the cell center steam mass fraction ($Y_{H_2O,cell}$) and the saturation mass fraction on the wall ($Y_{H_2O,sat,wall}$)

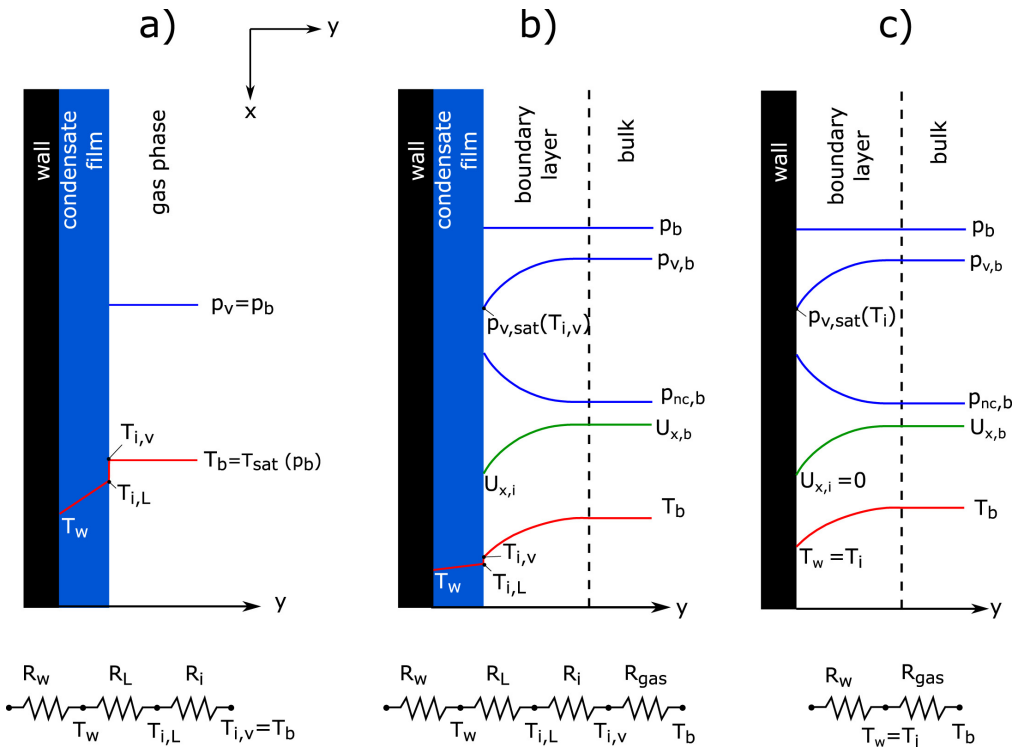

Figure 2.5.: (a) Wall film condensation when only pure steam is present, (b) Film condensation of steam in the when non-condensable gases are present, and (c) Simplified 'diffusion-layer' model for steam condensation in the presence of non-condensable gases ($T_w = T_i$) [Vijaya Kumar et al., 2021].

divided by the distance of the cell face center to the cell volume center ($\delta_{cell-face}$). The latent heat released during wall condensation is added as a heat flux to the wall.

The single-phase wall condensation approach is limited by its inability to model evaporation, as the condensate mass is not tracked. This can be important in cases where the film flows over hot containment walls, evaporates, and adds to the steam content in the containment atmosphere. Also, the simplified diffusion-layer approach becomes invalid in regions of water accumulation (horizontal wall or sump regions) where the liquid-gas interface offers significant thermal resistance that cannot be neglected. These phenomena can only be modeled using two-phase wall condensation models, which can predict the motion of the condensed liquid over the wall and include its effect on the condensate rate. NEPTUNE code [Mimouni et al., 2011] uses a two-phase approach that models the generation of droplets on the wall during condensation, their growth to film, transport over the wall under the effects of gravity, and the re-evaporation. GOTHIC [Andreani et al., 2010] employs the film theory approach to model wall condensation, which considers liquid film formation and flow on containment walls. It has the capability to model the condensation on drops, films, and pools in the presence of NCGs using a two-fluid approach. The use of the VOF approach in modeling condensation of pure substances on a wall or liquid-gas interface [Kleiner et al., 2019, Gennari et al., 2022, Welch & Wilson, 2000, Onishi et al., 2022, Höhne et al., 2017] is also interesting, as this approach could be extended to address steam wall condensation in the presence of NCGs.

2.4.6.2. Bulk condensation modeling

The bulk condensation, or homogeneous condensation, occurs when the gas mixture becomes supersaturated when steam mixes with cooler air. Two scenarios enable phase change: when vapor pressure exceeds temperature-dependent saturation pressure, or when gas temperature falls beneath the vapor pressure's saturation temperature. As a result, the excess steam condenses in the

volume as fog droplets, driving the mixture to an equilibrium state. This phenomenon commonly occurs in containment during a LOCA; however, it is usually neglected due to its marginal effect on the overall steam-condensate mass balance compared to wall condensation. Nevertheless, the latent heat release associated with bulk condensation can locally raise the gas temperature and influence the flow and even wall condensation in containments [de la Rosa et al., 2009]. Various modeling efforts using CFD have focused on understanding the effects of bulk condensation processes inside containment systems. A single-phase mass sink approach using the *return to saturation at constant time scale* method [Vyskocil et al., 2014] was implemented in ANSYS Fluent and applied to CONAN and PANDA Test 9bis experiments. The mass of steam condensed was removed from the gas mixture, and the corresponding latent heat released was transferred to the local gas mixture. However, the formation of fog and its transport, re-evaporation, and influence on the gas flow field were neglected in this approach. The condensation rate was computed from the thermal energy (Q_{v1}) required to raise the gas mixture to the saturation conditions ($T_{\text{sat}}(p_v)$) by the latent heat released during condensation at numerical time step δt. This can be summarized as:

$$Q_{v1} = c_{p,m}\rho_m \frac{T_{\text{sat}}(p_v) - T_m}{\Delta t} \quad \left[\frac{\text{W}}{\text{m}^3}\right] \quad \text{if} \quad T_m < T_{\text{sat}}(p_v) \tag{2.27}$$

where $c_{p,m}$ represents the specific heat capacity and constant pressure, T_m denotes the temperature of the gas mixture, p_v is the partial pressure of vapor, and ρ_m quantifies the density of the gas mixture. The energy Q_{v1} must be limited by the total latent heat released if the entire steam in a mesh cell condenses.

$$Q_{v2} = \rho_m Y_v \frac{h_{lg}}{\Delta t} \quad \left[\frac{\text{W}}{\text{m}^3}\right] \tag{2.28}$$

where Y_v denotes the partial pressure of vapor and h_{lg} represents the latent heat of condensation.

$$Q_v = \min(Q_{v1}, Q_{v2}) \tag{2.29}$$

Consequently, bulk condensation rate can be computed as:

$$\dot{m}_{bulk} = \frac{-Q_v}{h_{lg}} \quad < 0 \quad \left[\frac{\text{kg}}{\text{m}^3 \cdot \text{s}}\right] \tag{2.30}$$

The energy Q_v released during condensation is integrated into the energy conservation equation to drive the gas mixture to saturation temperature.

Bulk condensation can also be modeled using a two-fluid approach, considering the effect of NCGs [Zhang & Laurien, 2014] and assuming pre-existing droplets as nucleation sites or surfaces for promoting bulk condensation. This approach represents bulk condensation through mass removal and thermal energy release at the droplet surfaces, addressing gas-droplet interaction, as shown in Figure 2.6. The droplet (with diameter d) surface has a uniform temperature $\overline{T}^L$ and is in thermodynamic equilibrium. The saturated state at the droplet surface requires computing the saturation mass fraction of steam ($Y_{H_2O,sat}$) at the surface from the steam saturation partial pressure($p_{H_2O,sat}\left(\overline{T}^L\right)$). The bulk condensation driving force is the difference between the steam mass fraction in the bulk ($Y_{H_2O,bulk}$) and the steam saturation mass fraction on the droplet surface. The model employs a fixed droplet size throughout all calculations, and ignores the droplet evolution by condensation, coalescence, or breakup.

Consequently, the bulk condensation rate can be computed as:

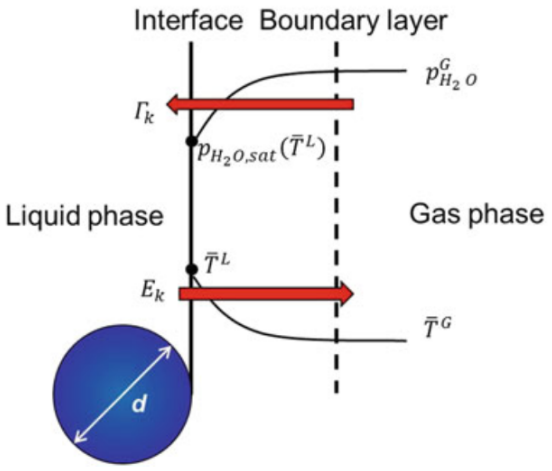

Figure 2.6.: Condensation over a droplet in the gas mixture [Zhang & Laurien, 2014].

$$\dot{m}_{bulk} = -\rho_g \beta A (Y_{H_2O,bulk} - Y_{H_2O,sat}) \tag{2.31}$$

where ρ_g represents the gas mixture density, β denotes the mass transfer coefficient, given by Ranz-Marshall correlation, and A quantifies the interfacial area density of the liquid droplets.

2.4.7. Conjugate heat transfer modeling

Containment walls typically comprise reinforced concrete with steel liners. The heat transfer between the containment fluid and the solid walls, as well as the temperature distribution on the containment solid structures, are important parameters determining the wall condensation rates and the containment gas conditions. During wall condensation, the latent heat is released into the wall, which increases its temperature. The specific heat of the wall material determines how effectively this heat is transported by conduction to the outer atmosphere. The transient variation of the structure temperature can significantly alter the internal containment fluid state. Therefore, it is necessary to model these solid phenomena coupled with the fluid phenomena, and this approach is known as conjugate heat transfer (CHT) analysis. The heat transfer in the containment structure can be solved using Fourier's law of heat conduction and is given by:

$$\rho_s c_s \frac{\partial T_s}{\partial t} = k_s \nabla^2 T_s + q_s \tag{2.32}$$

where:

- T_s is the temperature in the solid,
- ρ_s represents the density of the solid,
- c_s denotes the specific heat capacity of the solid,
- k_s quantifies the thermal conductivity of the solid,
- q_s represents any internal heat generation within the solid.

The solid region and the fluid region are coupled by using an interface temperature boundary condition so that the temperatures of the fluid and the solid match exactly at the interface. The interface temperature (T_i) by also considering the wall heat fluxes due to condensation and radiation (Figure 2.7) can be formulated as:

$$q''_{\text{condensation},i} + q''_{\text{radiation},i} + \lambda_{f,\text{eff}} \frac{T_{cell,fluid} - T_i}{\delta_{cell,fluid-i}} = \lambda_s \frac{T_i - T_{cell,solid}}{\delta_{cell,solid-i}} \tag{2.33}$$

where:

- $q''_{\text{condensation},i} = \dot{m}_{wall,flux} h_{lg}$ is the heat flux due to condensation
- $q''_{\text{radiation},i}$ is the heat flux due to radiation,
- $\lambda_{f,\text{eff}}$ represents the effective thermal conductivity of the fluid at wall comprising of both laminar and turbulence effects
- λ_s is the thermal conductivity of the solid
- $T_{cell,fluid}$ denotes the near-wall cell center temperature of the fluid
- $T_{cell,solid}$ is the near-wall cell center temperature of the solid
- $\delta_{cell,fluid-i}$ represents the distance of the near-wall fluid cell center from the interface
- $\delta_{cell,solid-i}$ is the distance of the near-wall solid cell center from the interface

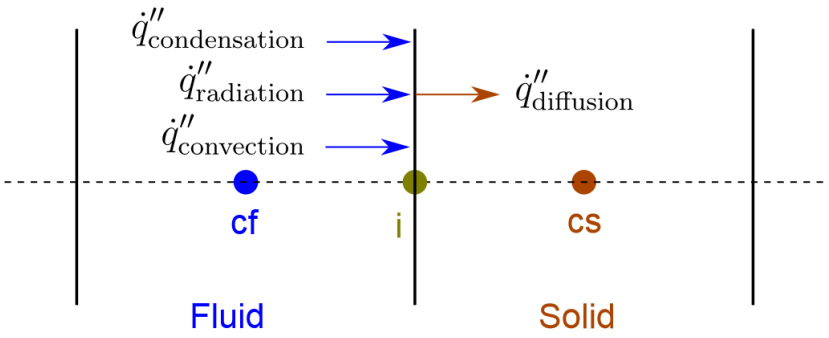

Figure 2.7.: Temperature boundary conditions at the fluid-solid interface 'i' including the wall heat flux due to convection, condensation, and radiation [Vijaya Kumar et al., 2021].

The interface temperature boundary condition is integrated into the energy equations of the solid and fluid domains. The *containmentFOAM* solver is already incorporated with the CHT model for solving the interface temperature and heat conduction equation in a solid region for single-phase flow. For two-phase flow models with thin water films over the solid structures, this CHT interface boundary condition needs special treatment to include the thermal resistance due to the film.

2.5. Motivation and objectives

The relationship between bulk condensation behavior, fog formation, and their combined impact on nuclear reactor containment integrity during accident scenarios is not yet fully understood. It is essential to explore how it interacts with wall condensation, gas distribution, and other phenomena in the containment. The fog droplet size (diameter) is an important parameter that determines its transport and distribution in the containment. The smaller droplets are carried along with the movement of the gas, while the larger droplet traverses towards the lower areas inside the containment compartments, and gets deposited. The smaller droplets will usually be located only in regions close to the steam injection zones where bulk condensation occurs, and then they grow by further condensation and coalescence while getting transported to other regions. As bulk condensation is a highly localized and rapid phenomenon, its influence can be captured only by high spatial and temporal resolution modeling approaches. The CFD method is the most suitable approach for the in-depth modeling and analysis of bulk condensation impact on containment. Although there

are several CFD codes presently available that have bulk condensation and fog transport models, they are either simple for capturing important phenomena or too complex with high computational requirements, limiting fast and feasible large-scale containment analysis. The simple single-phase model neglects fog transport and its re-evaporation. The Euler-Lagrange approach, which tracks the droplets and their evolution, is not feasible for containment applications as its computational effort significantly increases with droplet numbers. The two-phase approaches currently use two-fluid methods, which are slower due to more equations to be solved and require small time-step sizes for stability and robustness while running containment simulations. Among these two-fluid approaches, one uses it to track fog droplets by assuming constant droplet size, neglecting the size evolution of the droplet, while the other uses it to model droplet formation on walls and its growth to films by disregarding bulk condensation. It is clear that no CFD codes use a simple single-phase passive scalar approach combined with PBM for fog droplet transport and evolution. Therefore, the primary aim of this work is to implement this approach to the *containmentFOAM* solver to investigate bulk condensation effects. The *return to saturation at constant time scale* model will be used for computing bulk condensation rate, as it offers more simulation stability and speed (larger time-step size).

The single-phase passive scalar PBM approach can give detailed information about how the bulk condensation and fog interact with the bulk containment conditions, but may miss some phenomena close to walls where fog droplets join the condensate films on the wall or evaporate on contact with the wall. This is due to the limitation of the passive scalar approach that it must remove the fog getting deposited on walls to prevent numerical issues leading to high unphysical fog mass values on the wall. To conserve the fog mass within the computational domain, one must rely on two-phase approaches. However, most of the current containment two-phase codes rely on the two-fluid approach, which is computationally challenging compared to other approaches like mixture or VOF. The mixture method combined with the drift-flux approach is an efficient way to model the aforementioned phenomena, and this was not explored by any codes previously. However, the wall-condensate film effect cannot be neglected, as the fog droplets get deposited on these films. In most containment regions, the wall films are extremely thin to be captured employing the VOF approach, and the thin surface film approach is the best alternative to model the condensate film and the interaction of fog droplets with it. It offers the best balance of accuracy and computation effort for film transport on coarse meshes using CFD. During a prolonged period of wall and bulk condensation, the films and droplets can flow and accumulate in the sump region of the containment, forming a liquid-gas interface, making the film model inadequate. This can be solved using the VOF method, which is excellent in modeling and transporting interfaces. Hence, when the film gets thick enough to allow a liquid-gas interface, the VOF method can take over. The VOF model can then be added with an interface condensation model based on the diffusion layer model to promote condensation (or evaporation) on accumulated condensate. Considering all these, a novel two-phase mixture-film-VOF model developed in this work to model all the condensation (wall and bulk) related phenomena and conserve the condensate mass in a containment. Although it may sound like the model is more complex than the two-fluid approach, it is cheaper, faster, and simpler. The mixture and VOF models are combined into a single set of mixture conservation equations, using an indicator function to switch between models based on the local liquid conditions. The mixture model equations are used in cells where the liquid is in dispersed form, and VOF equations are used in cells where it is in continuous form. The hybrid mixture-VOF solver is expected to be more stable at larger time-step sizes than two-fluid, leading to faster simulations. The film model allows coarser mesh near walls, which reduces overall computational effort while providing reasonable accuracy. The implementation of the two-phase mixture-film-VOF model into the *containmentFOAM* solver, extending its capabilities to perform containment safety analysis, is the secondary objective of this research work. Concluding, a comparison of both methods is conducted to evaluate how simplification impacts computational time and result accuracy. The identified optimal approach is demonstrated on a large-scale Batelle Model Containment (BMC) using the VANAM M3 experiment.

3. Model development

The major objective of this thesis is to create a computational framework to model bulk condensation and fog transport phenomena inside a nuclear reactor containment. The method is implemented into OpenFOAM-based *containmentFOAM* [Kelm et al., 2021] CFD package, which is being developed at Forschungszentrum Jülich, Germany. The previous *containmentFOAM* works [Vijaya Kumar, 2022] developed a simplified CFD model for simulating multi-component gas flows and wall condensation using the Eulerian single-phase approach. The present work uses two approaches: a single-phase passive scalar approach and a two-phase mixture-film-VOF approach. The first approach extends *containmentFOAM*'s baseline Eulerian single-phase solver by introducing fog-phase coupling through mass source terms and a dedicated scalar transport equation for fog. The latter approach requires major restructuring of the *containmentFOAM* code, as the condensate phase affects the models and governing equations. This chapter is organized into two distinct sections. The first section discusses the single-phase passive scalar approach for modeling bulk condensation and fog transport and its implementation into the current solver. It also explores the population balance modeling of fog droplets for determining the droplet size distribution. The second section addresses the two-phase modeling approach, which combines the two-phase approaches like mixture and volume of fluid (VOF) methods with the thin surface film method. It also discusses the adaptations required in the gas governing equations, condensation, and PBM models for integrating them into the two-phase *containmentFOAM* solver.

3.1. Single-phase passive scalar approach

This approach is the simplest and computationally most efficient method for modeling bulk condensation and condensate (fog) transport in a containment. It uses a single-phase framework where the gas mixture flow is primarily solved, including source (or sink) terms due to bulk condensation. The fog generated by bulk condensation is accounted for and modeled as a passive scalar in a Eulerian framework within the computation domain, allowing for the possibility of re-evaporation. The drift of the fog droplet relative to the primary (carrier) gas path due to gravity, inertia, centrifugal force, and diffusion is also considered in the fog transport modeling. The droplet diameter was found to have a noticeable effect on the local conditions inside the containment, and to incorporate its effect in the numerical approach, a population balance model (PBM) utilizing the method of classes is included.

This section comprises five parts: first, the bulk condensation modeling and the corresponding source terms in each governing equation are discussed. The second part addresses the fog transport modeling and sub-models required for closure of the fog transport equation. The third part explains the population balance modeling of fog droplets, incorporating the processes of nucleation, coalescence, and growth (or shrinkage) of the fog droplets. The final part discusses the algorithm and solution method.

3.1.1. Bulk condensation modeling

The bulk condensation model employs the "*return to saturation at constant timescale*" [Vyskocil et al., 2014] method, which relies on achieving equilibrium at saturation temperature. This is accomplished by driving the local gas mixture to saturation temperature (T_{sat}) within a constant time frame larger than the simulation time step by condensing the surplus steam or evaporating the surplus fog. The local saturation temperature in each computational mesh cell is computed as a function of the local partial pressure of steam using the Antoine relation [Antoine, 1888, Perry et al., 2018] shown in Eqn. 3.1. In a multi-component gas mixture, the partial pressure of steam (p_{H_2O}) is calculated according to Dalton's law of partial pressures by multiplying the molar fraction of steam with the local pressure (Eqn. 3.2).

$$T_{sat} = 46.13 + \frac{3816.44}{23.196 - ln(p_{H_2O})} \quad [K] \tag{3.1}$$

$$p_{H_2O} = X_{H_2O} p \quad [Pa] \tag{3.2}$$

The quantity of energy per unit volume ($\dot{Q}'''$) needed for driving the gas mixture to saturation temperature (Eqn. 3.3) is derived based on the theory that latent heat released during condensation ($T < T_{sat}$) heats up and during evaporation ($T > T_{sat}$) cools down the gas to saturation temperature at numerical time step Δt. The volumetric mass transfer rate ($\dot{m}_{bulk}$) can be computed by dividing the energy per unit volume by the latent heat of vaporization of steam (h_{lg}) as defined in Eqn. 3.4.

$$\dot{Q}''' = \rho_g C_{p,g} \frac{T_{sat} - T}{\Delta t} \quad [W/m^3] \tag{3.3}$$

$$\dot{m}_{bulk} = -\frac{\dot{Q}'''}{h_{lg}} \quad \left[\frac{kg}{m^3 s}\right] \tag{3.4}$$

The latent heat of condensation of steam is defined as a power law function [Perry et al., 2018] of temperature ratio ($T_r = T/T_c$) which is the ratio of temperature of the gas mixture (T) to the critical temperature of steam ($T_c = 647.096\ K$)

$$h_{lg} = 3.14 \times 10^6 (1 - T_r)^{(0.612 - 0.626 T_r + 0.399 T_r^2)} \quad [J/kg] \tag{3.5}$$

However, to ensure mass-energy conservation, the mass transfer rate must be limited by the available mass of steam in case of condensation and the available mass of fog in case of evaporation within each mesh cell. The condensation and evaporation mass transfer rate limits are given by:

$$\dot{m}_{cond,lim} = -\frac{\rho_g Y_{H_2O}}{\Delta t} \quad \left[\frac{kg}{m^3 s}\right] \tag{3.6}$$

$$\dot{m}_{evap,lim} = \frac{\alpha_l \rho_l}{\Delta t} \quad \left[\frac{kg}{m^3 s}\right] \tag{3.7}$$

Finally, Eqns. 3.4, 3.6 & 3.7 are combined to obtain the mass source term (S_{mg}) for the mass conservation equation (Eqn. 2.1):

$$S_{mg} = \begin{cases} \max(\dot{m}_{bulk}, \dot{m}_{cond,lim}) & \text{if } \dot{m}_{bulk} < 0 \\ \min(\dot{m}_{bulk}, \dot{m}_{evap,lim}) & \text{if } \dot{m}_{bulk} > 0 \end{cases} \tag{3.8}$$

To avoid redundant source terms due to wall and bulk condensation in near-wall cells, the bulk condensation rate is set to zero for those cells, leaving only wall condensation effects. The volumetric source terms in the conservation equations (eqns. 2.4, 2.6, 2.2) are then computed from the mass source term (S_{mg}).

Momentum source term: $\vec{S}_{Ug} = S_{mg}\vec{U}$ (3.9)

Energy source term: $S_{hg} = S_{mg}C_{p,H_2O}T - S_{mg}h_{lg}$ (3.10)

Species mass source term: $S_{jg} = \begin{cases} S_{mg} & \text{if } j = H_2O \\ 0 & \text{if } j \neq H_2O \end{cases}$ (3.11)

Turbulent kinetic energy source term: $S_{kg} = S_{mg}k$ (3.12)

Turbulent specific dissipation rate source term: $S_{\omega g} = S_{mg}\omega$ (3.13)

3.1.2. Fog transport modeling

The fog droplets formed during bulk condensation get suspended in the gas mixture (carrier phase) in the form of droplets. Due to their distinct material characteristics compared to the gas mixture, the droplets fail to follow the carrier phase velocity field, leading to deviations from the gas flow trajectory. This motion of the fog droplets, known as drift, is significant for large-diameter droplets and is influenced by the interplay of inertia, gravitational forces, and aerodynamic drag. Additionally, the Brownian motion and gas flow turbulence can contribute to the droplet diffusion, which is especially significant for small diameter droplets. Incorporating all these interactions, the fog mass transport equation (Eqn. 3.14) is formulated in terms of fog volume fraction (α_l) using a passive scalar approach. The passive scalar approach for fog droplet transport uses a Eulerian method to track the fog mass in the computational domain. This approach relies on the assumption that the droplet-droplet interactions are negligible, which is valid for very dilute fog volume fractions (α_l) below 1% [Elghobashi, 1994]. The density of the fog (ρ_l) is considered constant (= $1000 kg/m^3$), which is reasonable for the range of pressures and temperatures in a containment.

$$\frac{\partial(\rho_l\alpha_l)}{\partial t} + \nabla\cdot\left[\rho_l\alpha_l\left(\vec{U}_g + \vec{u}_d\right)\right] = \nabla\cdot\left[\rho_l\left(D_{tg} + D_B\right)\nabla\alpha_l\right] + S_{ml} \tag{3.14}$$

The source term associated with bulk condensation in the liquid phase directly corresponds to the source term in the gas mixture mass continuity equation, but has an opposite sign ($S_{ml} = -S_{mg}$)), reflecting the transfer mass of steam removed from the gas to the fog field. The mass source term can also be split into condensation rate (S^+_{ml}) and evaporation rate (S^-_{ml}).

$$S_{ml} = S^+_{ml} + S^-_{ml} \tag{3.15}$$

The diffusion term comprises gas phase turbulent diffusivity (D_{tg}) and Brownian diffusivity (D_B). The turbulent diffusivity is defined as:

$$D_{tg} = \nu_{tg}/Sc_t \tag{3.16}$$

where ν_{tg} is the gas turbulent viscosity and Sc_t (= 0.9) denotes the turbulent Schmidt number. The Brownian diffusivity depends on droplet diameter (d_l) and is modeled using the Stokes-Einstein relation [Hinds, 1999, Frederix et al., 2017] which is applicable for diffusion of spherical bodies like droplets.

$$D_B = \frac{k_B C_c T}{3\pi\mu_g d_l} \tag{3.17}$$

where k_B represents the Boltzmann constant, μ_g denotes the gas mixture dynamic viscosity, and C_c is the Cunningham correction factor given by:

$$C_c = 1 + \frac{\lambda}{d_l}\left[2.34 + 1.05exp\left(-0.39\frac{d_l}{\lambda}\right)\right] \tag{3.18}$$

where λ represents the mean free path of the gas mixture.

The convective term constitutes the gas flow velocity term, which is determined by solving the gas mixture momentum equation (Eqn. 2.4) and a drift velocity term that requires further modeling. The fog drift velocity is computed from the droplet total velocity ($\vec{U}_l$) which is obtained by solving a force balance partial differential equation [Manninen et al., 1996, Frederix et al., 2017] for a droplet given by

$$\frac{\partial \vec{U}_l}{\partial t} + \left(\vec{U}_l \cdot \nabla\right)\vec{U}_l = -\frac{C_d}{\tau_l}\left(\vec{U}_l - \vec{U}_g\right) + \left(\frac{\rho_l - \rho_g}{\rho_l}\right)\vec{g} \tag{3.19}$$

The term on the left-hand side represents the influence of inertial forces acting on the droplet. On the right-hand side, the first term corresponds to the drag, and the second term accounts for the gravitational force. The remaining variables in Eqn. 3.19 are defined as

$$\text{Droplet total velocity: } \vec{U}_l = \vec{u}_d + \vec{U}_g \tag{3.20}$$

$$\text{Droplet relaxation time: } \tau_l = \frac{\rho_l d_l^2}{18\mu_g} \tag{3.21}$$

The drag coefficient (C_d) is determined using the Schiller-Naumann relation

$$C_d = 1 + 0.15Re^{0.687} \tag{3.22}$$

where droplet Reynolds number, $Re = |\vec{u}_d| d_l \rho_g / \mu_g$.

Using Eqn. 3.20, Eqn. 3.19 is rewritten to solve for the droplet's drift velocity $\vec{u}_d$ which offers numerical advantage as the value of gas flow velocity $\vec{U}_g$ is already available.

$$\frac{\partial \vec{u}_d}{\partial t} + \left[\left(\vec{u}_d + \vec{U}_g\right)\cdot\nabla\right]\vec{u}_d + \frac{C_d}{\tau_l}\vec{u}_d = -\frac{\partial \vec{U}_g}{\partial t} - \left[\left(\vec{u}_d + \vec{U}_g\right)\cdot\nabla\right]\vec{U}_g + \left(\frac{\rho_l - \rho_g}{\rho_l}\right)\vec{g} \tag{3.23}$$

Eqn. 3.23 is the Stokes formulation and requires iterative solvers to compute $\vec{u}_d$ and may be computationally expensive for containment scale simulations. To reduce the computational effort, a simplified Manninen formulation [Manninen et al., 1996] is proposed to compute the droplet's total velocity under the assumption that droplet acceleration matches the local instantaneous gas mixture acceleration (Eqn. 3.24).

$$\frac{\partial \vec{U}_l}{\partial t} + \left(\vec{U}_l \cdot \nabla\right) \vec{U}_l \approx \frac{\partial \vec{U}_g}{\partial t} \tag{3.24}$$

As a result, the Manninen formulation transforms Eqn. 3.23 to

$$\vec{u}_d = \left(\frac{\rho_l - \rho_g}{\rho_l}\right) \frac{\tau_l}{C_d} \vec{g} - \frac{\tau_l}{C_d} \frac{\partial \vec{U}_g}{\partial t} \tag{3.25}$$

This work incorporates the Stokes and Manninen approaches to modeling drift velocity, with a comparative assessment of their performance presented in section 4.3.

The equations governing Brownian diffusivity and drift velocity demonstrate that both parameters are strongly dependent on droplet diameter, which critically influences fog transport dynamics. At this stage, it is assumed that the droplet diameter is held constant throughout each simulation, and a diameter dependency study is performed to investigate its impact on containment scale simulations.

3.1.2.1. Drift velocity boundary condition

The passive scalar treatment of fog volume fraction can lead to the accumulation of fog mass near wall boundaries of the computational domain and become numerically unstable if the α_l is not within acceptable values. To prevent this accumulation, the fog mass that gets deposited on the walls needs to be continuously removed from the domain through the walls. As drift velocity is the major factor driving the droplets towards the walls, it is desirable to use the wall normal component of $\vec{u}_d$ to calculate fog mass flux through wall boundaries for removing fog mass from the computational domain. Hence, a special deposition velocity boundary condition is used for drift velocity on the wall boundaries, which is computed using the Eqn. 2.18.

3.1.3. Population Balance Modeling

The influence of droplet diameter on drift velocity and Brownian diffusivity underlines its crucial role in the distribution of fog inside the containment. Hence, a mono-disperse droplet approach is insufficient, and a poly-disperse approach is necessary as the local droplet diameter variation directly affects the droplet transport in the computational domain. The droplet diameter evolution is influenced by nucleation, condensational growth, evaporational shrink, and coalescence. The droplet breakup phenomenon is neglected in this work, as the maximum fog droplet diameter in a typical containment scenario is too small to trigger breakup. A population balance model utilizing the method of classes [Lehnigk et al., 2022] is implemented in which the droplets are distributed into n discrete size groups based on their volume, which approximates the size distribution function. Each size group is denoted with a single representative volume x_i as illustrated in Figure 3.1.

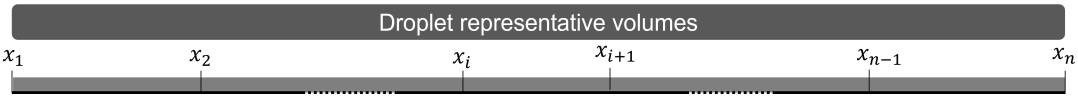

Figure 3.1.: The PBM fixed grid showing the representative droplet volumes.

The droplets are considered to have spherical shape, and therefore, the representative group volume is computed from the representative group diameter (d_i) using the equation $x_i = \pi d_i^3/6$. The volume fraction of each size group within a cell is defined using the field α_{li} for which the transport equation of each group is solved. The relationship between the size group volume fraction and the total fog volume fraction is expressed as:

$$\sum_{i=1}^{n} \alpha_{li} = \alpha_l \tag{3.26}$$

Consequently, the size group mass transport equation is formulated based on Eqn. 3.14 as follows:

$$\frac{\partial (\rho_l \alpha_{li})}{\partial t} + \nabla \cdot \left[\rho_l \alpha_{li} \left(\vec{U}_g + \vec{u}_{di}\right)\right] = \nabla \cdot \left[\rho_l \left(D_{tg} + D_{Bi}\right) \nabla \alpha_{li}\right] + S_{mi} \tag{3.27}$$

The group drift velocity ($\vec{u}_{di}$) and Brownian diffusivity (D_{Bi}) are functions of the group representative diameter and can be computed using Eqns. 3.23 and 3.17 respectively. The group mass source term (S_{mi}) combines the effects of nucleation (Nu_i), condensational growth (G_i^+), evaporational shrink (G_i^-) and coalescence into and from present group i (C_i^+ & C_i^-):

$$S_{mi} = Nu_i + G_i^+ + G_i^- + C_i^+ + C_i^- \tag{3.28}$$

The size group source term (S_{mi}) is obtained via the fixed pivot technique by [Kumar & Ramkrishna, 1996a] which assumes that all droplets within a group are concentrated at the representative volumes. The technique utilizes the mean value theorem to redistribute droplets in non-representative volumes generated during coalescence, growth, and shrink events. In this work, this method is applied to maintain conservation of the overall number and mass of droplets.

The size groups are generated based on the representative diameters given by the user in ascending order. So, for n size groups, the diameter should be specified such that $d_1 < d_2 < ..... < d_{n-1} < d_n$ and the group representative volumes (x_i) and group representative surface area (a_i) are computed from d_i.

3.1.3.1. Nucleation

The nucleation process refers to the generation of fog droplets due to bulk condensation in the lowest size group with the representative volume of x_1. The underlying assumption is that the nucleation diameter is no greater than the diameter of the smallest size group. This assumption does not affect the droplet transport if the drift velocity of the lowest group is negligible. The numerical treatment of nucleation involves the following considerations:

- If no droplets are present in a particular cell, then the entire mass of fog created during bulk condensation is added to the nucleation size group. i.e., the nucleation rate is identical to the bulk condensation rate (S_{ml}^+).
- If the cell already has droplets belonging to any size group, only a fraction (r_{nuc}) of the bulk condensation rate contributes to nucleation, and the remaining is added to the condensational growth term (G_i^+). The typical value for r_{nuc} chosen in this work is 0.1, which means that 10% of bulk condensation results in nucleation and the rest leads to droplet growth.

$$Nu_i = \begin{cases} S_{ml}^+ & \text{if } \alpha_l = 0 \text{ and } i = 1 \\ r_{nuc} S_{ml}^+ & \text{if } \alpha_l \neq 0 \text{ and } i = 1 \\ 0 & \text{if } i \neq 1 \end{cases} \tag{3.29}$$

3.1.3.2. Condensational growth and evaporational shrinkage

Condensational growth refers to the increase in fog droplet diameter due to condensation on its surface, and evaporational shrink is the decrease in droplet diameter because of evaporation from its surface. The condensation rate ($\dot{m}_i^+$) and evaporation rate ($\dot{m}_i^-$) for each size group is computed as a weighted function of bulk condensation rate (S_{ml}). The weight function (w_i) applied here is the fraction of surface area of droplets in each size group to the overall droplet surface area. In condensation scenarios, the weight function also considers the effect of the nucleation fraction r_{nuc}. This can be summarized as:

$$\dot{m}_i^+ = w_i S_{ml}^+ \tag{3.30}$$

$$\dot{m}_i^- = w_i S_{ml}^- \tag{3.31}$$

where

$$w_i = \begin{cases} \frac{\alpha_{li} a_i / x_i}{\sum_{i=1}^{n} \alpha_{li} a_i / x_i} (1 - r_{nuc}) & \text{if } S_{ml}^+ > 0 \\ \\ \frac{\alpha_{li} a_i / x_i}{\sum_{i=1}^{n} \alpha_{li} a_i / x_i} & \text{if } S_{ml}^- < 0 \end{cases} \tag{3.32}$$

The change in droplet diameter creates droplets with diameters different from group representative diameters and is redistributed to the nearby groups using the mean value theorem with special considerations for the boundary groups. Hence, the net growth rate in a group is influenced by the condensation rate in the current group as well as the previous group, which can be described as:

$$G_i^+ = \begin{cases} -\dot{m}_i^+ \alpha_{li} \frac{x_i}{x_{i+1} - x_i} & \text{if } i = 1 \\ \\ -\dot{m}_i^+ \alpha_{li} \frac{x_i}{x_{i+1} - x_i} + \dot{m}_{i-1}^+ \alpha_{li-1} \frac{x_i}{x_i - x_{i-1}} & \text{if } 1 < i < n \\ \\ \dot{m}_i^+ \alpha_{li} + \dot{m}_{i-1}^+ \alpha_{li-1} \frac{x_i}{x_i - x_{i-1}} & \text{if } i = n \end{cases} \tag{3.33}$$

Similarly, the net shrink rate in a given group is affected by the evaporation rate in the current group and the following group, which can be formulated as:

$$G_i^- = \begin{cases} -\dot{m}_i^- \alpha_{li} + \dot{m}_{i+1}^- \alpha_{li+1} \frac{x_i}{x_i - x_{i+1}} & \text{if } i = 1 \\ \\ -\dot{m}_i^- \alpha_{li} \frac{x_i}{x_{i-1} - x_i} + \dot{m}_{i+1}^- \alpha_{li+1} \frac{x_i}{x_i - x_{i+1}} & \text{if } 1 < i < n \\ \\ -\dot{m}_i^- \alpha_{li} \frac{x_i}{x_{i-1} - x_i} & \text{if } i = n \end{cases} \tag{3.34}$$

3.1.3.3. Coalescence

Coalescence refers to the aggregation of fog droplets belonging to the same or different size group resulting in the formation of a bigger droplet. This also uses the fixed pivot technique to redistribute the bigger droplet to nearby representative groups to conserve both mass and number of droplets. For a particular group, coalescence can result in the addition of mass in that group only by aggregation of droplets with diameters less than or equal to the given group diameter. Based on this theory, the coalescence source term for a size group can be formulated as:

$$C_i^+ = \rho_l \sum_{j=1}^{i} \sum_{k=j}^{i} C_{jk}(1 - \frac{1}{2}\delta_{jk}) N_{ijk} x_i \frac{\alpha_{lj}}{x_j} \frac{\alpha_{lk}}{x_k} \tag{3.35}$$

Here, C_{jk} is the pair-wise coalescence rate, and the Kronecker's delta δ_{jk} is used to disallow the repetition of coalescence events within the same size group. N_{ijk} is the coalescence matrix that determines the factor of mass to be added to the i^{th} size group, which is generated during aggregation of droplets belonging to groups j and k. This can be defined as:

$$N_{ijk} = \begin{cases} \frac{(x_j + x_k) - x_{i-1}}{x_i - x_{i-1}} & \text{if } x_{i-1} < x_j + x_k < x_i \\ \frac{x_{i+1} - (x_j + x_k)}{x_{i+1} - x_i} & \text{if } x_i < x_j + x_k < x_{i+1} \\ 0 & \text{else} \end{cases} \tag{3.36}$$

The loss of mass from a particular group due to coalescence occurs when a droplet belonging to the current group aggregates with droplets of the same or a different group. This yields the coalescence sink term, which can be described as:

$$C_i^- = -\rho_l \sum_{j=1}^{n} C_{ij} x_i \frac{\alpha_{lj}}{x_j} \frac{\alpha_{li}}{x_i} \tag{3.37}$$

Finally, the pair-wise coalescence rate is modeled using the turbulent aggregation kernel [ANSYS, Inc., 2013] which is the dominant coalescence mechanism in turbulent flows. This model uses the Saffman & Turner, 1956 aggregation method for droplets in the viscous subrange and the Abrahamson, 1975 aggregation method for droplets in the inertial subrange. The viscous subrange is characterized by droplets with diameter less than Kolmogorov microscale (η) where droplet collisions are governed by the shear forces within local eddies. The droplets bigger than Kolmogorov microscale lie in the inertial subrange in which the droplet collisions are influenced by velocity variation in the turbulent flow field. The Kolmogorov microscale is the size of the smallest eddy and is calculated from the kinematic viscosity (ν_g) and turbulent energy dissipation rate (ϵ_g) of the gas mixture:

$$\eta = \left(\frac{\nu_g^3}{\epsilon_g} \right)^{\frac{1}{4}} \tag{3.38}$$

Consequently, the coalescence rate is defined as:

$$C_{ij} = \begin{cases} \zeta_T \sqrt{\frac{8\pi}{15}} \dot{\gamma} \frac{(x_i + x_j)^3}{8} & \text{if } \frac{d_i + d_j}{2} < \eta \\ \zeta_T 2^{3/2} \sqrt{\pi} \frac{(x_i + x_j)^2}{4} \sqrt{\left(\left| \vec{U}_g + \vec{u}_{di} \right|^2 + \left| \vec{U}_g + \vec{u}_{dj} \right|^2 \right)} & \text{if } \frac{d_i + d_j}{2} \geq \eta \end{cases} \tag{3.39}$$

where ζ_T represents the factor that takes into account the capture efficiency coefficient of turbulent collision:

$$\zeta_T = \begin{cases} 0.732 \left(\frac{5}{N_T} \right)^{0.242} & \text{if } N_T \geq 5 \\ 0.732 & \text{if } N_T < 5 \end{cases} \tag{3.40}$$

Here N_T denotes the proportion between the viscous force and the Van der Waals force, described as:

$$N_T = \frac{6\pi\mu_g \left(x_i + x_j\right)^3 \dot{\lambda}}{8H} \tag{3.41}$$

where H represents the Hawmaker constant ($H = 3.7e - 20$ J for water) and $\dot{\lambda}$ quantifies the deformation rate,

$$\dot{\lambda} = \left(\frac{4\epsilon_g}{15\pi\nu_g}\right)^{1/2} \tag{3.42}$$

The turbulent shear rate ($\dot{\gamma}$) is given by:

$$\dot{\gamma} = \frac{\epsilon_g^{1/2}}{\nu_g} \tag{3.43}$$

3.1.4. Solution algorithm

Figure 3.2 explains the iterative numerical algorithm of the single-phase passive scalar solver and how bulk condensation, drift velocity, and fog transport (or PBM) models interact with the basic *containmentFOAM* algorithm. The coupling of the fluid region solver with the solid region solver using conjugate heat transfer (CHT) is also illustrated. The algorithm begins by incrementing time by the specified time-step size. Initially, the fluid region is solved, starting with updating the bulk condensation mass source term, followed by wall condensation mass flux. Then, the continuity species mass fraction and energy equations are solved in order. Subsequently, the gas density is updated by accounting for the change in mass fraction and temperature. Next, the momentum equation is solved to compute the velocity and pressure. The gas mixture density is updated again to include the effect of pressure change. Afterward, turbulent kinetic energy and eddy frequency are computed by solving the turbulence equations. Subsequently, the droplet drift velocity is computed, which is followed by calculating the nucleation, growth, shrink, and coalescence source or sink terms. The fog transport or PBM equations are then solved to obtain fog volume fractions. If a solid region is present, then the CHT model is activated, and the solid heat diffusion equation is solved. Then, the residuals of all equations are examined to determine convergence. If convergence is not achieved, the aforementioned operations are iterated until the solution converges. Once convergence is attained, the solver advances to the subsequent time step and repeats the entire process.

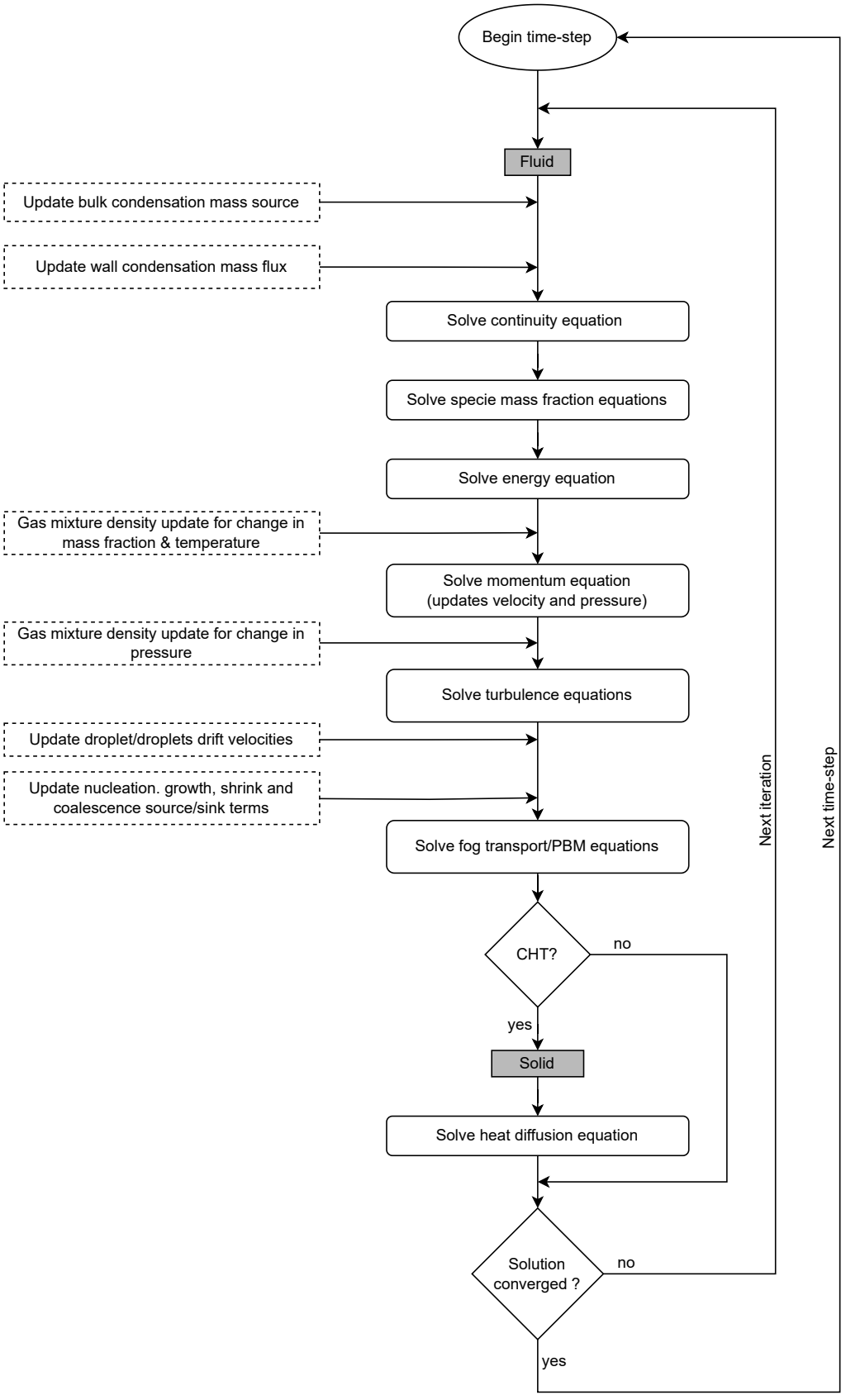

Figure 3.2.: Flowchart illustrating the solution algorithm of the single-phase passive scalar solver with the inclusion of bulk condensation model, fog transport equation and population balance model.

3.2. Two-phase mixture-film-VOF approach

This approach treats the dispersed fog droplets in volume, liquid film on walls, and accumulated liquid forming a continuous liquid-gas interface as a separate phase from the gas mixture. The gas mixture comprising NCGs like air, hydrogen, and helium and condensable steam gas that exchanges mass with the liquid phase is the primary phase. The dispersed fog droplets are generated in the volume due to bulk condensation. The simplest method of modeling the transport of dispersed droplets within the gas mixture in a two-phase framework is the mixture approach. It allows the phases to be interpenetrating, with relative velocities for fog droplets with respect to the liquid-gas mixture flow. The formation of a liquid film on the vessel walls is due to the deposition of droplets from the bulk onto the walls and wall condensation. A surface film approach is adopted to simulate the behavior of the thin liquid film, which assumes a two-dimensional flow along the surface of walls by neglecting flow perpendicular to the wall. The liquid films in the vessel sump regions can get thicker than the near-wall cell, leading to liquid accumulation and filling several mesh cells, resulting in the formation of a liquid-gas interface that is beyond the applicability of the thin surface film approach. This is modeled using the volume of fluid (VOF) approach, which is applicable for transport of immiscible phases and has the capability of capturing the phase interfaces. In this work, the mixture and VOF approaches can be combined as a single set of governing equations by using an indicator function to activate terms that are specific to each approach. The surface film approach uses a different set of equations that are solved on a separate mesh region, which is a surface mesh extruded from the wall. The mixture-VOF and surface film models interact with each other through mass, momentum, and energy transfer terms.

This section is structured into five subsections: first, the two-phase mixture-VOF modeling is discussed. The second part explains the surface film approach and its interaction with the mixture-VOF approach. The third part addresses the changes required for the wall condensation and bulk condensation models in the two-phase approach. The extension of the wall condensation model to facilitate interface condensation is also discussed in this part. The fourth part describes the integration of PBM into the mixture approach. Finally, the solver algorithm for the two-phase approach is discussed.

3.2.1. Mixture-VOF modeling

The two-phase mixture-VOF model uses a hybrid approach in which the model equations are switched between mixture and VOF methods. This is performed with the help of an indicator function Ω which is defined as:

$$\Omega = \begin{cases} 0 & \text{for cells with dispersed droplets or no liquid - mixture approach} \\ 1 & \text{for cells containing phase interface or filled with liquid - VOF approach} \end{cases} \tag{3.44}$$

The distribution of the indicator function for a generic computational domain containing fog droplets and accumulated liquid is shown in Figure 3.3. In the governing equations, the terms specific to the VOF approach are multiplied by Ω, whereas for the mixture approach, they are multiplied by $(1 - \Omega)$.

The two-phase approach primarily requires a transport equation for the phase volume fraction to track the droplets and interface. This is accomplished by combining the mass conservation equations of each phase and the net mass equation. The total momentum and energy conservation equations are then solved. Since the gas phase is a multi-component mixture, species transport equations are also needed to be solved for obtaining the individual species mass fraction. The detailed explanation of the governing equations for the mixture-VOF approach is addressed in the upcoming sections.

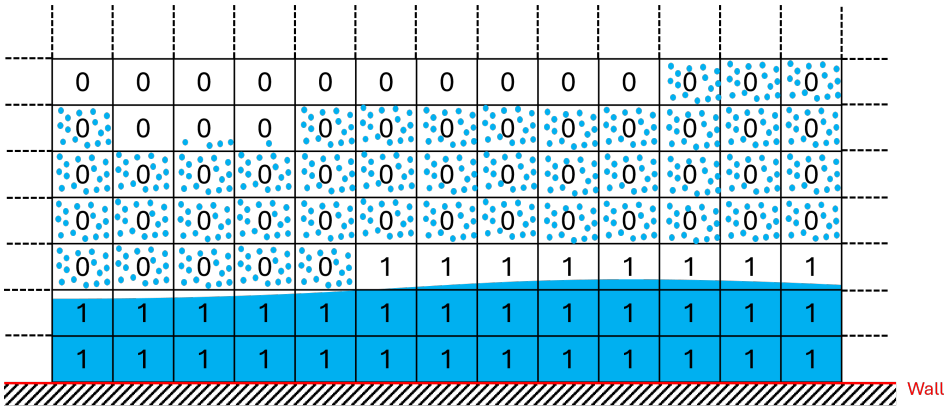

Figure 3.3.: The distribution of the indicator function value on computational mesh containing dispersed fog droplets and continuous liquid with gas-liquid interface.

3.2.1.1. Phase mass conservation equations

The mass conservation equations for the liquid and gas phases are defined in terms of the phase volume fractions with additional terms to account for phase change (condensation and evaporation) as well as mass transfer from the surface film model.

$$\frac{\partial\left(\alpha_l\rho_l\right)}{\partial t}+\nabla\cdot\left(\alpha_l\rho_l\vec{U}_l\right)-\nabla\cdot\left(\rho_l\Gamma_l\nabla\alpha_l\right)=S_{ml}+S_{mf,transfer} \tag{3.45}$$

$$\frac{\partial\left(\alpha_g\rho_g\right)}{\partial t}+\nabla\cdot\left(\alpha_g\rho_g\vec{U}_g\right)-\nabla\cdot\left(\rho_g\Gamma_g\nabla\alpha_g\right)=S_{mg}+S_{mf} \tag{3.46}$$

Here, α_g and α_l represent the phase volume fractions of gas and liquid phases, respectively. The densities ρ_g and ρ_l are functions of pressure and temperature, whose effects are significant for the gas mixture phase due to ideal gas assumption and marginal for the liquid phase due to extremely low compressibility. The gas and liquid phase velocities are represented using $\vec{U}_g$ and $\vec{U}_l$ respectively. The mass source terms S_{mg} and S_{ml} incorporate the mass exchanges between steam and water within the fluid region due to condensation (or evaporation) such that $S_{mg}=-S_{ml}$. The mass source S_{mf} accounts for the mass exchange between steam in the fluid region and water in the film region resulting from condensation or evaporation. The mass transfer of liquid phase between the surface film region and the fluid region arising from the model switching between film and VOF approaches is included by $S_{mf,transfer}$. The third term on the left-hand side includes the diffusive transport of the dispersed fog droplets, and is enabled only for the mixture approach. This is achieved by defining the phase diffusion coefficients Γ_g and Γ_l as functions of the indicator function, such that they are zero when $\Omega=1$. For overall mass conservation during the diffusion process, it is necessary that the following relation is satisfied.

$$\rho_g\Gamma_g=\rho_l\Gamma_l\implies\Gamma_g=\frac{\rho_l}{\rho_g}\Gamma_l \tag{3.47}$$

The diffusion of dispersed fog droplets is due to gas phase turbulence and Brownian motion, and uses the diffusion coefficients from Eqns. 3.16 and 3.17. Accordingly,

$$\Gamma_l=(1-\Omega)(D_{tg}+D_B) \tag{3.48}$$

Eqns. 3.45 and 3.46 are added to obtain the total mass conservation equation for the mixture-VOF approach:

$$\frac{\partial \rho_m}{\partial t} + \nabla \cdot \left(\rho_m \vec{U}_m\right) = S_{mf,transfer} \tag{3.49}$$

Mixture density : $\rho_m = \alpha_l \rho_l + \alpha_g \rho_g$ (3.50)

Mixture velocity : $\vec{U}_m = \frac{\alpha_l \rho_l \vec{U}_l + \alpha_g \rho_g \vec{U}_g}{\rho_m}$ (3.51)

The relative velocity $\vec{U}_r$ between the liquid and gas phases is given by

$$\vec{U}_r = \vec{U}_l - \vec{U}_g \tag{3.52}$$

The difference between the mixture and VOF approach lies in the modeling of the relative velocity. In the VOF approach, the phases are immiscible, and cells are occupied by liquid, gas, or an interface. Hence, the relative velocity is zero at all cells except at the interface. At the interface, the relative velocity is modeled as an artificial compression velocity ($\vec{U}_c$) which is a function of α_l to keep the interface sharp.

$$\vec{U}_{r,VOF} = \begin{cases} 0 & \text{if} \quad \alpha_l = 0 \text{ or } 1 \implies \vec{U}_l = \vec{U}_g = \vec{U}_m \\ \vec{U}_c = f(\alpha_l) & \text{if} \quad 0 < \alpha_l < 1 \end{cases} \tag{3.53}$$

However, in the mixture approach, the phases are interpenetrating, and there is a relative motion between the liquid and gas phases in cells where the liquid phase is in the form of dispersed fog droplets.

$$\vec{U}_{r,mixture} = \begin{cases} 0 & \text{if} \quad \alpha_l = 0 \text{ or } 1 \implies \vec{U}_l = \vec{U}_g = \vec{U}_m \\ f(\vec{U}_m, C_d, \vec{g}) & \text{if} \quad 0 < \alpha_l < 1 \end{cases} \tag{3.54}$$

The switching between mixture and VOF approaches for the relative velocity model is accomplished with the help of the following expression:

$$\vec{U}_r = \Omega \vec{U}_{r,VOF} + (1 - \Omega)\vec{U}_{r,mixture} \tag{3.55}$$

For simplifying the phase volume fraction equations, let us define the relative velocity of liquid phase relative to the center of the mixture mass as drift-diffusion velocity of liquid phase ($\vec{U}_{ml}$):

$$\vec{U}_{ml} = \vec{U}_l - \vec{U}_m = \frac{\alpha_g \rho_g}{\rho_m} \vec{U}_r \tag{3.56}$$

Similarly, the drift-diffusion velocity of the gas phase ($\vec{U}_{mg}$) can be expressed as:

$$\vec{U}_{mg} = \vec{U}_g - \vec{U}_m = -\frac{\alpha_l \rho_l}{\rho_m} \vec{U}_r \tag{3.57}$$

Based on Eqns. 3.56 and 3.57, the phase mass conservation equations (Eqns. 3.45 and 3.46) can be rewritten in terms of mixture and phase drift-diffusion velocities as:

$$\frac{\partial(\alpha_l\rho_l)}{\partial t} + \nabla\cdot\left(\alpha_l\rho_l\vec{U}_m\right) + \nabla\cdot\left(\alpha_l\rho_l\vec{U}_{ml}\right) - \nabla\cdot(\rho_l\Gamma_l\nabla\alpha_l) = S_{ml} + S_{mf,transfer} \tag{3.58}$$

$$\frac{\partial\left(\alpha_g\rho_g\right)}{\partial t} + \nabla\cdot\left(\alpha_g\rho_g\vec{U}_m\right) + \nabla\cdot\left(\alpha_g\rho_g\vec{U}_{mg}\right) - \nabla\cdot\left(\rho_g\Gamma_g\nabla\alpha_g\right) = S_{mg} + S_{mf} \tag{3.59}$$

Summing Eqns. 3.58 and 3.59 will give back the total mass conservation equation (Eqn. 3.49) as $\alpha_l\rho_l\vec{U}_{ml} + \alpha_g\rho_g\vec{U}_{mg} = 0$.

The tracking of the dispersed droplet fraction or the interface requires solving for liquid volume fraction (α_l), whose derivation is explained in Appendix. A. The final transport equation of the liquid phase volume fraction for a hybrid mixture-VOF approach is given by

$$\begin{aligned}
&\frac{\partial\alpha_l}{\partial t} + \nabla\cdot\left(\alpha_l\vec{U}_m\right) + \nabla\cdot\left(\alpha_l\vec{U}_{ml}\right) - \nabla\cdot(\Gamma_l\nabla\alpha_l) \\
&\quad= \alpha_l\nabla\cdot\vec{U}_m - \alpha_l\left[\nabla\cdot\left(\alpha_l\left(\frac{\rho_l}{\rho_g}-1\right)\vec{U}_{ml} - \Gamma_l\left(\frac{\rho_l}{\rho_g}-1\right)\nabla\alpha_l\right)\right] + \alpha_l\alpha_g\left[\frac{1}{\rho_g}\frac{D\rho_g}{Dt} - \frac{1}{\rho_l}\frac{D\rho_l}{Dt}\right] \\
&\qquad + S_{ml}\left[\frac{1}{\rho_l} - \alpha_l\left(\frac{1}{\rho_l}-\frac{1}{\rho_g}\right)\right] - \alpha_l\frac{S_{mf}}{\rho_g} + S_{mf,transfer}\left[\frac{1}{\rho_l} - \alpha_l\frac{1}{\rho_l}\right]
\end{aligned} \tag{3.60}$$

The gas phase volume fraction is then computed using the constraint:

$$\alpha_l + \alpha_g = 1 \tag{3.61}$$

3.2.1.2. Relative velocity modeling

Mixture Approach

The relative velocity in the mixture approach is obtained from the force balance equation of the droplet (Eqn. 3.20) as in the single-phase approach (Sec.3.1.2). However, for the two-phase approach, the Stokes formulation (Eqn. 3.23) needs to be expressed in terms of mixture velocity ($\vec{U}_m$) and liquid phase drift-diffusion velocity ($\vec{U}_{ml}$) because $\vec{U}_g$ is unknown. Therefore, using the relation for $\vec{U}_l$ (Eqn. 3.56), Eqn. 3.23 can be rewritten as:

$$\begin{aligned}
&\frac{\partial\vec{U}_{ml}}{\partial t} + \left[\left(\vec{U}_{ml}+\vec{U}_m\right)\cdot\nabla\right]\vec{U}_{ml} + \frac{C_d}{\tau_l}\frac{\rho_m}{\alpha_g\rho_g}\vec{U}_{ml} \\
&\qquad = -\frac{\partial\vec{U}_m}{\partial t} - \left[\left(\vec{U}_{ml}+\vec{U}_m\right)\cdot\nabla\right]\vec{U}_m + \left(\frac{\rho_l-\rho_g}{\rho_l}\right)\vec{g}
\end{aligned} \tag{3.62}$$

The above equation is solved to obtain $\vec{U}_{ml}$, from which the relative velocity is computed as

$$\vec{U}_{r,mixture} = \frac{\rho_m}{\alpha_g\rho_g}\vec{U}_{ml} \tag{3.63}$$

The Manninen formulation simplifies calculations by assuming local equilibrium, where a droplet's acceleration matches the surrounding mixture's acceleration.

$$\frac{\partial \vec{U}_l}{\partial t} + \left(\vec{U}_l \cdot \nabla\right) \vec{U}_l \approx \frac{\partial \vec{U}_m}{\partial t} \tag{3.64}$$

This gives Manninen formulation for relative velocity

$$\vec{U}_{r,mixture} = \left(\frac{\rho_l - \rho_g}{\rho_l}\right) \frac{\tau_l}{C_d} \vec{g} - \frac{\tau_l}{C_d} \frac{\partial \vec{U}_m}{\partial t} \tag{3.65}$$

VOF Approach

The relative velocity in the VOF approach aims to keep the interface sharp by employing an artificial compression velocity ($\vec{U}_c$) at the interface cells. The compression velocity acts perpendicular to the interface and is computed based on [Weller, 2006]

$$\vec{U}_{r,VOF} = \vec{U}_c = \min\left[C_\alpha |\vec{U}_m|,\ \max\left(|\vec{U}_m|\right)\right] \frac{\nabla \alpha_l}{|\nabla \alpha_l|} \tag{3.66}$$

Here, C_α is the compression coefficient that adjusts the compressive effect at the interface, where $C_\alpha = 0$ means no compression and $C_\alpha = 1$ means conservative compression. The compression velocity is also bounded to the maximum flow field velocity ($\max(|\vec{U}_m|)$) to prevent unphysical compression velocities. The interface normal vector ($\nabla\alpha_l/|\nabla\alpha_l|$) ensures that the compression velocity acts perpendicular to the interface.

3.2.1.3. Mixture momentum conservation equation

The conservation of momentum in the mixture-VOF framework is established by integrating the momentum equations for both phases, and is given by:

$$\frac{\partial \left(\rho_m \vec{U}_m\right)}{\partial t} + \nabla \cdot \left(\rho_m \vec{U}_m \otimes \vec{U}_m\right) = -\nabla p_m + \nabla \cdot \tau + \nabla \cdot \tau_{dm} + F_\sigma + \rho_m \vec{g} + \vec{S}_{U_m} \tag{3.67}$$

Here τ defines the viscous stress tensor given by

$$\tau = (\mu_m + \mu_{m,t}) \left[\nabla \vec{U}_m + \left(\nabla \vec{U}_m\right)^T - \frac{2}{3}\delta \nabla \vec{U}_m\right] \tag{3.68}$$

where μ_m and $\mu_{m,t}$ are the molecular and turbulent viscosities of the mixture, respectively and is computed as the phase volume fraction weighted average of the individual viscosities of the phases. i.e., $\mu_m = \alpha_l \mu_l + \alpha_g \mu_g$ and $\mu_{m,t} = \alpha_l \mu_{l,t} + \alpha_g \mu_{g,t}$.

In the mixture approach, the relative motion of droplets in the gas introduces momentum diffusion, which is implemented employing diffusion stress tensor, τ_{dm}. This term should be active only in the dispersed droplet region, and multiplication by $(1 - \Omega)$ ensures it.

$$\tau_{dm} = (1 - \Omega)\left(\alpha_l \rho_l \vec{U}_{ml} \otimes \vec{U}_{ml} + \alpha_g \rho_g \vec{U}_{mg} \otimes \vec{U}_{mg}\right) \tag{3.69}$$

In the VOF approach, the surface tension plays a significant role and is accounted for in the momentum equation through the inclusion of the term F_σ. This is implemented using the continuum surface force (CSF) model [Brackbill et al., 1992] which transforms the surface force to a volumetric source term that acts only at the interface cells. To prevent the model from adding artificial forces in the dispersed droplet region, the surface tension force is made active only in the VOF region by multiplying the term with Ω.

$$F_\sigma = \Omega\ \sigma\kappa\nabla\alpha_l \tag{3.70}$$

where σ represents the surface tension coefficient and κ denotes the curvature of the surface given by:

$$\kappa = \nabla \cdot \left(\frac{\nabla\alpha_l}{|\nabla\alpha_l|} \right) \tag{3.71}$$

The momentum source term $\vec{S}_{U_m}$ accounts for the momentum transfer from two events, namely,

- Mass exchange between steam in the fluid region and water in the film region, resulting from condensation or evaporation.
- Mass transfer of the liquid phase between the film region and the fluid region, rising from the model switching between film and VOF approaches.

$$\vec{S}_{U_m} = S^+_{mf,transfer}\vec{U}_f + S^-_{mf,transfer}\vec{U}_m + S^+_{mf}\vec{U}_f + S^-_{mf}\vec{U}_m \tag{3.72}$$

where $\vec{U}_f$ represents the velocity of the film, $S^+_{mf,transfer}$ quantifies the mass of liquid added to the liquid phase in the fluid region from the liquid film, and $S^-_{mf,transfer}$ denotes the mass of liquid lost from the liquid phase in the fluid region to the liquid film. The mass of liquid film that evaporates and joins the gas phase of the fluid region as steam is denoted by S^+_{mf} and the mass of steam that condenses from the fluid region to the film region is denoted by S^-_{mf}.

3.2.1.4. Gas phase species mass conservation equations

The gas phase constitutes a multi-component system with N different species, and its mass conservation equation is expressed via individual species mass fractions (Y_j). For containment applications, this typically involves a mixture of condensable species (such as H_2O) and non-condensable species like H_2, N_2 and O_2. The transport equation of a general species takes the following form:

$$\frac{\partial\left(\alpha_g\rho_g Y_j\right)}{\partial t} + \nabla\cdot\left(\alpha_g\rho_g\vec{U}_g Y_j\right) = \nabla\cdot\left[\alpha_g\rho_g\left(D_{jm} + D_{tg}\right)\nabla Y_j\right] + S_{Y_{jg}} \tag{3.73}$$

where D_{jm} represents the molecular diffusivity of the j^{th} species with respect to the mixture and is calculated according to Fick's law of diffusion (Eqn. 2.3). The term D_{tg} encompasses the effects of turbulent diffusion in the gas phase flow and is determined using Eqn. 3.16. The $S_{Y_{jg}}$ accounts for the source (or sink) term due to condensation (or evaporation) within the fluid region (S_{mg}) and between the fluid and film regions (S_{mf}). This is applicable only for condensable H_2O species and is zero for all other species.

$$S_{Y_{jg}} = \begin{cases} S_{mg} + S_{mf} & \text{if } j = H_2O \\ 0 & \text{if } j \neq H_2O \end{cases} \tag{3.74}$$

For N species systems, $N-1$ species mass conservation equations are solved. The N^{th} species mass fraction is derived from the unity constraint (Eqn. 3.75). The N^{th} species is preferred to be the one with the largest mass fraction (usually air or N_2) to reduce numerical error.

$$\sum_j^N Y_j = 1 \tag{3.75}$$

3.2.1.5. Mixture energy conservation equation

The total mixture energy conservation equation for the mixture-VOF approach is derived by summing the energy equations of the individual phases. It is assumed that thermal equilibrium holds between the liquid and gas phases in both dispersed and phase-interface regions. This results in a continuous temperature field, $T_l = T_g = T_m$, eliminating separate thermal variables for both phases. The total enthalpy transport equations of liquid and gas phases are expressed using the mixture temperature (T_m) as follows:

$$\frac{\partial\left(\alpha_l\rho_l C_{pl}T_m\right)}{\partial t} + \nabla\cdot\left(\alpha_l\rho_l\vec{U}_l C_{pl}T_m\right) + \frac{\partial\left(\alpha_l\rho_l K_l\right)}{\partial t} + \nabla\cdot\left(\alpha_l\rho_l\vec{U}_l K_l\right) = \nabla\cdot\left(\alpha_l\lambda_{eff,l}\nabla T_m\right) + \alpha_l\rho_l\vec{U}_l\cdot\vec{g} + \alpha_l\frac{\partial p}{\partial t} + S_{Tl} \quad (3.76)$$

$$\frac{\partial\left(\alpha_g\rho_g C_{pg}T_m\right)}{\partial t} + \nabla\cdot\left(\alpha_g\rho_g\vec{U}_g C_{pg}T_m\right) + \frac{\partial\left(\alpha_g\rho_g K_g\right)}{\partial t} + \nabla\cdot\left(\alpha_g\rho_g\vec{U}_g K_g\right) = \nabla\cdot\left(\alpha_g\lambda_{eff,g}\nabla T_m\right) + \alpha_g\rho_g\vec{U}_g\cdot\vec{g} + \alpha_g\frac{\partial p}{\partial t} + \sum_j^N \nabla\cdot\left[\alpha_g\rho_g C_{pg,j}T_m\left(D_{jm}+D_t\right)\nabla Y_j\right] + S_{Tg} \quad (3.77)$$

where C_{pl} and C_{pg} represents the specific heat capacities at constant pressure of liquid and gas phases, respectively. Here K_l ($= \frac{1}{2}|\vec{U}_l|^2$) represents the specific kinetic energy of the liquid phase, while K_g ($= \frac{1}{2}|\vec{U}_g|^2$) corresponds to the specific kinetic energy of the gas phase. The effective thermal conductivities, which account for both molecular and turbulent contributions in each phase, are denoted by $\lambda_{eff,l}$ and $\lambda_{eff,g}$. The fourth term on the RHS of Eqn.3.77 is present only in the gas phase energy equation and represents the enthalpy transport resulting from species diffusion. The terms S_{Tl} and S_{Tg} account for the energy source terms in liquid and gas phases, respectively, arising from phase change processes and mass transfer between the surface film and liquid phase.

$$S_{Tl} = S_{ml}C_{pl}T_m + \alpha_l S_{ml}h_{lg} + S^+_{ml}K_g + S^-_{ml}K_l + S^+_{mf,transfer}\left(C_{pf}T_f + K_f\right) + S^-_{mf,transfer}\left(C_{pl}T_m + K_l\right) \quad (3.78)$$

$$S_{Tg} = S_{mg}C_{pg,H_2O}T_m + \alpha_g S_{mg}h_{gl} + S^+_{mg}K_l + S^-_{mg}K_g + S^+_{mf}\left(C_{pg,H_2O}T_f + K_f\right) + S^-_{mf}\left((C_{pg,H_2O}T_m + K_g\right) \quad (3.79)$$

where h_{lg} denotes the latent heat of condensation (Eqn. 3.5), while h_{gl} represents the latent heat of evaporation such that $h_{gl} = -h_{lg}$. The specific heat at constant pressure for film is indicated by C_{pf} and, for steam species in gas phase, it is represented by C_{pg,H_2O}. The specific kinetic energy of the film is denoted by K_f. The latent heat term due to S_{mf} is considered in the film region, as it is released or absorbed from the film or the solid wall adjacent to it during phase change.

Adding the phase energy equations 3.76 and 3.77 gives the two-phase mixture energy equation, which is solved to obtain T_m directly.

$$\frac{\partial\left[\left(\alpha_l\rho_l C_{pl}+\alpha_g\rho_g C_{pg}\right)T_m\right]}{\partial t}+\nabla\cdot\left[\left(\alpha_l\rho_l\vec{U}_l C_{pl}+\alpha_g\rho_g\vec{U}_g C_{pg}\right)T_m\right]+\frac{\partial\left[\alpha_l\rho_l K_l+\alpha_g\rho_g K_g\right]}{\partial t}$$
$$+\nabla\cdot\left[\alpha_l\rho_l\vec{U}_l K_l+\alpha_g\rho_g\vec{U}_g K_g\right]$$
$$=\nabla\cdot\left(\lambda_{eff,m}\nabla T_m\right)+\rho_m\vec{U}_m\cdot\vec{g}+\frac{\partial p}{\partial t}+\sum_j^N\nabla\cdot\left[\alpha_g\rho_g C_{pg,j}T_m\left(D_{jm}+D_t\right)\nabla Y_j\right]+S_{Tm} \quad (3.80)$$

Here, $\lambda_{eff,m}$ represents the effective mixture thermal conductivity, and S_{Tm} quantifies the total energy source term, which can be simplified as

$$S_{Tm}=S_{ml}\left(C_{pl}-C_{pg,H_2O}\right)T_m+S_{ml}h_{lg}+S^+_{mf,transfer}\left(C_{pf}T_f+K_f\right)$$
$$+S^-_{mf,transfer}\left(C_{pl}T_m+K_l\right)+S^+_{mf}\left(C_{pg,H_2O}T_f+K_f\right)+S^-_{mf}\left((C_{pg,H_2O}T_m+K_g\right) \quad (3.81)$$

3.2.1.6. Turbulence modeling

The effect of turbulence is considered only for the gas phase, utilizing the $k-\omega$ SST model [Menter & Esch, 2001]. The turbulence parameters like the eddy viscosity ν_{tg}, turbulent diffusivity D_{tg} and turbulent thermal conductivity λ_{tg} interact with the mixture momentum, gas species, and energy conservation equations. Phase change processes like condensation and evaporation result in inter-phase mass transfer, introducing volumetric source terms in the governing equations of turbulent kinetic energy as $S_{mg}k_g$ and eddy frequency as $S_{mg}\omega_g$. The liquid phase is treated as laminar; hence, the turbulence-related terms for the liquid phase, such as μ_{tl} and λ_{tl} are zero. For containment applications explored in this work, this is a valid assumption because the liquid phase flow velocities are extremely low, and the liquid tends to accumulate in sump zones of the containment compartments.

3.2.2. Surface thin film approach

The VOF approach fails to model the flow of thin films whose thickness is less than the first cell thickness. To address this issue, one solution is to use fine meshes in the near-wall region. However, this refinement increases the computational cost of the overall simulation. An alternative and more feasible solution is to use the surface thin film approach to model the formation and transport of thin liquid films on wall surfaces. It involves solving a two-dimensional conservation equation for a separate single-layer mesh region generated by extruding the wall boundary mesh. The film mesh region is realistically a thin region inside the near-wall cells of the fluid mesh region. When the film gets thick enough to fill the first near-wall cell, the film mass is transferred from the film region to the fluid region, which then solves the liquid transport using VOF approach. The governing equations and sub-models for the surface film approach are addressed in the following sections:

3.2.2.1. Film mass conservation equation

The mass conservation for film is defined in terms of film volume fraction (α_f), which is the volume of the mesh element occupied by the film. The α_f conserves the film mass irrespective of the element size and works better for curved boundary surfaces [OpenFOAM, 2023], in contrast to the traditional method of solving for the film thickness (δ_f).

$$\frac{\partial\left(\alpha_f \rho_f\right)}{\partial t} + \nabla \cdot \left(\alpha_f \rho_f \vec{U}_f\right) = -S_{mf} - S_{mf,transfer} \tag{3.82}$$

Here, ρ_f represents the liquid film density, and $\vec{U}_f$ denotes the mean film velocity, which is parallel to the wall. Also, S_{mf} quantifies the mass source term from wall condensation (or evaporation), and $S_{mf,transfer}$ represents the transfer term accounting for the mass exchange between the liquid phase in the fluid and film regions. The film thickness is then determined by utilizing the film volume fraction, cell volume (V_{cell}) and cell wall face area ($A_{face,w}$).

$$\delta_f = \frac{\alpha_f V_{cell}}{A_{face,w}} \tag{3.83}$$

An important parameter in the film approach is coverage factor (η_f), which quantifies whether the wall surface is covered by film or not and is given by:

$$\eta_f = \begin{cases} 1 & \text{if } \delta_f \geq \delta_{f,crit} \\ 0 & \text{else} \end{cases} \tag{3.84}$$

where $\delta_{f,crit}$ is the critical film thickness and varies from 0.3 mm for vertical walls to 9 mm for horizontal walls [Hartley & Murgatroyd, 1964]. A coverage factor of 1 in a cell indicates that the corresponding wall face is fully covered with film. Conversely, a coverage factor of 0 signifies that the wall face contains droplets, or rivulets, or no liquid at all. This factor is used to determine velocity and temperature boundary conditions between the gas-film interface. For instance, if $\eta_f = 1$, heat transfer at the interface takes place between the film and gas, and for $\eta_f = 0$, it occurs between the gas and the solid wall.

3.2.2.2. Film momentum conservation equation

The thin film approach neglects any flow perpendicular to the film surface and assumes that the flow is parallel to the wall. Consequently, the film momentum equation is given as:

$$\frac{\partial\left(\alpha_f \rho_f \vec{U}_f\right)}{\partial t} + \nabla \cdot \left(\alpha_f \rho_f \vec{U}_f \otimes \vec{U}_f\right) = -\alpha_f \nabla p_f + \alpha_f \rho_f \vec{g}_t + \vec{\tau}_f + \vec{S}_{U_f} \tag{3.85}$$

where p_f accounts for the forces acting normal to the film surface. This includes the effects of fluid pressure (p_m), gravitational force component normal to the film surface ($p_{gravity}$), surface tension ($p_{\sigma f}$), and pressure component due to condensation or evaporation ($p_{cond/evap}$), also known as vapor recoil effect.

$$p_f = p_m + p_{gravity} + p_{\sigma f} + p_{cond/evap} \tag{3.86}$$

The gravity, surface tension and vapor recoil effect pressures can be computed using Eqns. 3.87, 3.88 and 3.89, where $\vec{n}$ is the unit vector normal to the film surface.

$$p_{gravity} = -\rho_f \delta_f \left(\vec{n} \cdot \vec{g}\right) \tag{3.87}$$

$$p_{\sigma f} = -\sigma_f \nabla \cdot \left(\nabla \delta_f\right) \tag{3.88}$$

$$p_{cond/evap} = \frac{S_{mf}^2}{2\rho_g} \tag{3.89}$$

The gravitational body force that acts parallel to the film surface is addressed by the $\alpha_f \rho_f \vec{g}_t$ term, where $\vec{g}_t$ represents the gravity component tangential to the wall. The solid wall and the gas flow exert shear stress on the film, and this force is integrated into the film momentum equation using the $\vec{\tau}_f$ term.

$$\vec{\tau}_f = \vec{\tau}_w + \vec{\tau}_g \tag{3.90}$$

Any shear stress acting normal to the film surface is neglected owing to the thin nature of the film. The film velocity profile in the wall-normal direction is assumed to take a parabolic profile (Eqn. 3.91), based on which the shear force applied by wall ($\vec{\tau}_w$) and gas flow ($\vec{\tau}_g$) is calculated.

$$\vec{U}_f(z) = \frac{3\vec{U}_f}{\delta_f}\left(z - \frac{z^2}{2\delta_f}\right) \tag{3.91}$$

where z represents the film surface-normal coordinate. Consequently, the volumetric momentum source term due to wall shear stress is given by:

$$\vec{\tau}_w = -\mu_f \frac{3\vec{U}_f}{\delta_f} \frac{A_{face,w}}{V_{cell}} \tag{3.92}$$

where μ_f represents the dynamic viscosity of the film.

The shear stress exerted by the gas flow employs a simple coefficient-based model that gives the volumetric momentum source as:

$$\vec{\tau}_g = C_s\left(\vec{U}_m - \vec{U}_f\right) \tag{3.93}$$

where C_s is the shear stress coefficient given by:

$$C_s = C_f \rho_g |\vec{U}_m - \vec{U}_f| \frac{A_{face,w}}{V_{cell}} \tag{3.94}$$

where C_f is the film surface roughness coefficient ,whose value is equal to 0.005 for the simulations in this research work.

The last term ($\vec{S}_{U_f}$) on the RHS of Eqn. 3.85 addresses the momentum source term arising from phase change, as well as mass exchange between film and the liquid phase.

$$\vec{S}_{U_f} = -S_{mf}^{+}\vec{U}_f - S_{mf}^{-}\vec{U}_m - S_{mf,transfer}^{+}\vec{U}_f - S_{mf,transfer}^{-}\vec{U}_m \tag{3.95}$$

where S_{mf}^{+} is the mass lost from the film due to evaporation and S_{mf}^{-} is the mass generated in the film due to condensation.

3.2.2.3. Film energy conservation equation

The energy transport equation of the film is defined in terms of mean enthalpy (h_f) and from which the mean film temperature (T_f) is calculated.

$$\frac{\partial\left(\alpha_f \rho_f h_f\right)}{\partial t} + \nabla \cdot \left(\alpha_f \rho_f \vec{U}_f h_f\right) + \nabla \cdot \left(\alpha_f \rho_f \vec{U}_f K_f\right) = \nabla \cdot \left(\alpha_f \lambda_f \nabla T_f\right) + q_f + S_{h_f} \tag{3.96}$$

where $\nabla \cdot \left(\alpha_f \lambda_f \nabla T_f\right)$ considers the effect of diffusive transport of enthalpy in the wall tangential direction. In the present study, this term is disregarded attributing to the film's thin characteristics, which results in convective transport dominating the heat transfer process. Here, λ_f represents the thermal conductivity of liquid film.

The term q_f accounts for the volumetric energy source terms arising from the heat transfer between the film and gas and, between the film and wall and is given by:

$$q_f = \left[\frac{\lambda_f\left(T_{fs} - T_f\right)}{\delta_f/2} + \frac{\lambda_f\left(T_{fw} - T_f\right)}{\delta_f/2}\right]\eta_f \frac{A_{face,w}}{V_{cell}} \tag{3.97}$$

where T_{fs} and T_{fw} define the film surface and film wall temperatures, respectively, computed from the temperature boundary conditions. The multiplication by the coverage factor ensures that the film exchanges energy with the gas or wall interface only if it has sufficient thickness. This is also necessary for the stability of the film temperature field in the numerical solver.

The last term, S_{h_f}, term addresses the energy source term arising from phase change (including latent heat) and also mass exchange between the film and liquid phase.

$$\begin{aligned} S_{h_f} = &-S^{+}_{mf,transfer}\left(C_{pf}T_f + K_f\right) - S^{-}_{mf,transfer}\left(C_{pl}T_m + K_l\right) \\ &- S^{+}_{mf}\left(C_{pf}T_f + K_f\right) - S^{-}_{mf}\left(C_{pl}T_m + K_g\right) - \eta_f S_{mf} h_{lg} \end{aligned} \tag{3.98}$$

The last term on the RHS considers the effect of latent heat release or absorption during condensation to or evaporation from the film. The multiplication with coverage factor allows latent heat transfer only to film and prevents it for droplets or rivulet regime. For the non-film regime, the latent heat is directly transferred to the solid wall.

3.2.2.4. Film-liquid phase mass transfer model

A dedicated transfer model is formulated to determine the mass of liquid exchanged between the film region and the mixture-VOF (fluid) region, denoted by $S_{mf,transfer}$. Figure 3.4 shows the inter-region mass transfer in which the liquid is exchanged between the film elements and the adjacent near-wall cells of the fluid. The basic principle behind this model is that when the wall film is thick enough for a VOF treatment in the near-wall cells of the fluid region, film mass with its associated momentum and energy is transferred as liquid phase. Similarly, when the liquid phase volume fraction in the near-wall cell of the fluid region is small enough to be considered as a film, the liquid mass is transferred to the film region.

This can be summarized as:

- Liquid mass is transferred from film to fluid when one of these conditions is satisfied:

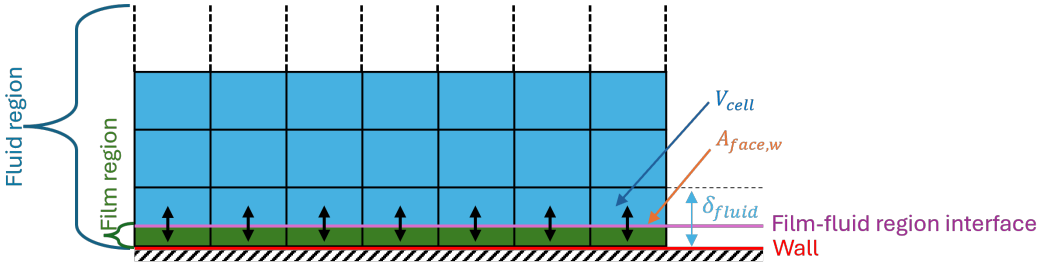

Figure 3.4.: The inter-region mass transfer between the film and fluid region across the interface.

  - Film thickness (δ_f) is greater than $f_{\delta,VOF}$ times the near wall cell thickness of the fluid (δ_{fluid})
  - Liquid phase volume fraction (α_l) in the near wall cell of the fluid region is greater than the limiting volume fraction for VOF interface, denoted by $\alpha_{VOF,lim}$
- Liquid mass is transferred from fluid to film when both these conditions are satisfied:
  - Film thickness (δ_f) is less than $f_{\delta,film}$ times the near wall cell thickness of the fluid (δ_{fluid})
  - Additionally, liquid phase volume fraction (α_l) in the near wall cell of the fluid region is less than the limiting volume fraction for film, denoted by $\alpha_{film,lim}$

This can be expressed mathematically as:

$$S_{mf,transfer} = \begin{cases} \frac{r_{tr}}{\Delta t}\delta_f \rho_f \frac{A_{face,w}}{V_{cell}} & \text{if } \delta_f > f_{\delta,VOF}\delta_{fluid} \text{ or } \alpha_l > \alpha_{VOF,lim} \\ -\frac{r_{tr}}{\Delta t}\alpha_l \rho_l \frac{1}{V_{cell}} & \text{if } \delta_f < f_{\delta,film}\delta_{fluid} \text{ and } \alpha_l < \alpha_{film,lim} \end{cases} \tag{3.99}$$

The transfer rate coefficient (r_{tr}) determines the fraction of current liquid mass that is transferred across the region interface during simulation time step size Δt. The typical values of the model parameters for containment applications used in the present work are shown in Table 3.1.

Table 3.1.: The film-liquid mass transfer model parameter values.

Parameter	r_{tr}	$f_{\delta,VOF}$	$f_{\delta,film}$	$\alpha_{VOF,lim}$	$\alpha_{film,lim}$
Value	0.05	1.0	0.7	0.9	0.6

3.2.3. Condensation modeling

The condensation processes in the two-phase approach constitute the combined effects of bulk, wall, and interface condensation. Figure 3.5 demonstrates the condensation model selection based on the local cell conditions and can be explained as:

(a) When there is no gas-liquid interface in the fluid region, the wall condensation model becomes active in the near-wall cells. The resulting mass source term (S_{mf}) is introduced to the film region. In all other cells within the fluid region, the bulk condensation model is active, and its mass source term is denoted as $S_{mg,bulk}$.

(b) When the near-wall cells in the fluid region contain sufficient liquid to form an interface, the interface condensation model becomes active in those cells. The resulting mass source term ($S_{mg,interface}$) is added to the fluid region liquid phase. In this scenario, the wall condensation model remains inactive. For all other bulk cells, the bulk condensation model remains active.

(c) When the liquid in the fluid region fills several layers of cells above the wall, forming an interface, the interface condensation becomes active in those interface cells. For all other cells above the interface cells, the bulk condensation model remains active. Like scenario (b), the wall condensation model is inactive in this case. The boiling phenomena in the near-wall cells are not in the scope of this work and are disregarded.

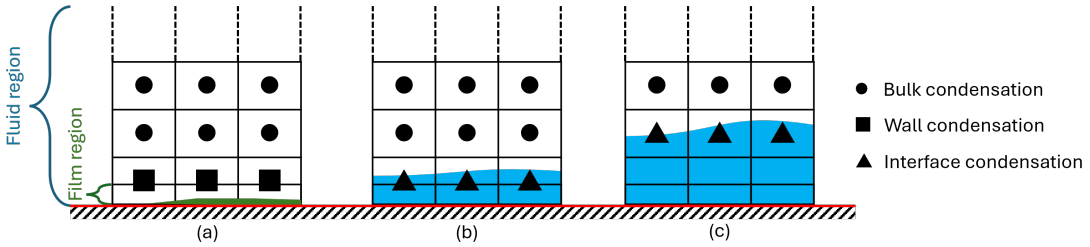

Figure 3.5.: The mode of condensation in the computational domain based on the local mesh cell conditions. (a) Film region is empty or partially filled. (b) Near-wall cells of fluid region has gas-liquid interface. Film mass is entirely transferred to fluid region. (c) The liquid phase is filling one or more cell layers of the fluid region.

The bulk and wall condensation models of the single-phase approach are adapted for the two-phase approach. The interface condensation modeling is an extension of the wall condensation model. The specifics of these modeling approaches can be found in the subsequent sections.

3.2.3.1. Bulk condensation modeling

The two-phase bulk condensation model uses the principle of driving local mixtures to saturation temperature, as discussed in Sec.3.1.1. Unlike the single-phase scenario, where the local gas mixture is brought to saturation, in the two-phase approach, the liquid-gas mixture is brought to saturation. Hence, the energy required (Q) for heating or cooling the mixture to saturation temperature (Eqn. 3.3), changes to:

$$Q = \rho_m C_{pm} \frac{T_{sat} - T_m}{\Delta t} \quad [W/m^3] \tag{3.100}$$

where C_{pm} represents the specific heat capacity of the two-phase mixture computed as:

$$C_{pm} = \frac{\alpha_l \rho_l C_{pl} + \alpha_g \rho_g C_{pg}}{\rho_m} \tag{3.101}$$

Consequently, the bulk condensation mass transfer rate ($\dot{m}_{bulk}$) is calculated using Eqn. 3.4. The latent heat of condensation (h_{lg}) is computed using Eqn. 3.5 where $T_r = T_m/T_c$. The evaporate rate limit ($\dot{m}_{evap,lim}$) remains the same (Eqn. 3.7) as in the single-phase approach. However, the condensation mass transfer rate limit ($\dot{m}_{cond,lim}$) needs to be redefined for the two-phase approach as:

$$\dot{m}_{cond,lim} = -\frac{\alpha_g \rho_g Y_{H_2O}}{\Delta t} \quad \left[\frac{kg}{m^3 s}\right] \tag{3.102}$$

Finally, the mass source term resulting from bulk condensation ($S_{mg,bulk}$) for the two-phase approach can be summarized as:

$$S_{mg,bulk} = \begin{cases} \max(\dot{m}_{bulk}, \dot{m}_{cond,lim}) & \text{if } \dot{m}_{bulk} < 0 \\ \min(\dot{m}_{bulk}, \dot{m}_{evap,lim}) & \text{if } \dot{m}_{bulk} > 0 \end{cases} \tag{3.103}$$

3.2.3.2. Wall condensation modeling

The wall condensation model computes the mass transfer rate between steam in the fluid region and liquid in the film region. In contrast to the single-phase approach, where the wall condensation mass flux serves as an out-flux boundary condition, the two-phase approach treats it as a volumetric source term denoted by S_{mf}. This can be mathematically expressed as:

$$S_{mf} = -\frac{\rho_g D_{H_2O,m,wall}}{1 - Y_{H_2O,sat,wall}} \left(\frac{Y_{H_2O,cell} - Y_{H_2O,sat,wall}}{\delta_{cell-face}} \right) \frac{A_{face,wall}}{V_{cell}} \tag{3.104}$$

where $D_{H_2O,m,wall}$ represents the effective diffusivity of steam in the gas mixture, which includes both molecular and turbulence effects. The wall condensation driving force is the gradient of steam mass fraction in the wall normal direction. This can be computed as the difference between the cell center steam mass fraction ($Y_{H_2O,cell}$) and the saturation mass fraction on the wall ($Y_{H_2O,sat,wall}$) divided by the distance of the cell face center to the cell volume center ($\delta_{cell-face}$). To convert the condensation mass flux to volumetric source term, it is multiplied with wall face area ($A_{face,wall}$) and then divided by the cell volume (V_{cell}).

3.2.3.3. Interface condensation modeling

The interface condensation formulation is an extension of the wall condensation model, which utilizes cell center values instead of the face values. The driving force is calculated as a gradient of the corrected steam mass fraction ($Y^*_{H_2O}$) in the direction of the interface ($\vec{n}_{interface}$). Moreover, the conversion to volumetric source term is facilitated by multiplying with interfacial area density ($A_{interface,V}$). Therefore, the interfacial condensation mass source term can be defined as:

$$S_{mg,interface} = \frac{\rho_g D_{H_2O,m}}{1 - Y_{H_2O,sat}} \left(\nabla Y^*_{H_2O} \cdot \vec{n}_{interface} \right) A_{interface,V} \tag{3.105}$$

Here, $D_{H_2O,m}$ denotes the effective diffusivity of steam in the gas mixture and $Y_{H_2O,sat}$ represents the saturation mass fraction of steam determined from the local temperature and partial pressure. The corrected steam mass fraction is computed assuming that the liquid region and interface are in saturation condition and can be defined mathematically as:

$$Y^*_{H_2O} = \alpha_l Y_{H_2O,sat} + \alpha_g Y_{H_2O} \tag{3.106}$$

The interface normal vector can be computed from the liquid volume fraction as:

$$\vec{n}_{interface} = \frac{\nabla \alpha_l}{|\nabla \alpha_l|} \tag{3.107}$$

The interfacial area density, which is the area of the interface per unit volume, is given by:

$$A_{interface,V} = |\nabla \alpha_l| \tag{3.108}$$

3.2.4. Population Balance Modeling

The two-phase population balance model uses formulations similar to the single-phase PBM discussed in Sec.3.1.3. However, the PBM in two-phase is applicable only to the liquid phase. which is in dispersed form. This means that the PBM interacts with the mixture approach and does influence the VOF approach. The dispersed phase volume fraction ($\alpha_{l,disp}$) in the computational domain is computed as:

$$\alpha_{l,disp} = (1 - \Omega)\,\alpha_l \tag{3.109}$$

The numerical solver initially solves the phase volume fraction equation (Eqn. 3.60) following which the dispersed phase fraction is solved using the above relation. Therefore, if we adopt the single-phase approach of solving the individual size group volume fraction (α_{li}) first and then sum it up to obtain the net dispersed volume fraction, there may be inconsistencies with the $\alpha_{l,disp}$ calculated from Eqn. 3.109. This discrepancy is particularly likely in the near-wall and interface cells, where the dispersed droplets join the film or the continuous liquid interface. The solution to this is to solve the population balance equation after computing ($\alpha_{l,disp}$) and using a different transport field, which is the volume fraction of each size group in the total dispersed liquid volume fraction, denoted by ϵ_{li} and is defined as:

$$\epsilon_{li} = \frac{\alpha_{li}}{\alpha_{l,disp}} \tag{3.110}$$

Additionally,

$$\sum_{i}^{n} \epsilon_{li} = 1 \tag{3.111}$$

Consequently, the size group transport equation in the two-phase approach is reformulated based on Eqns. 3.27 and 3.60 to:

$$\frac{\partial\left(\epsilon_{li}\alpha_{l,disp}\right)}{\partial t} + \nabla\cdot\left(\epsilon_{li}\alpha_{l,disp}\vec{U}_m\right) + \nabla\cdot\left(\epsilon_{li}\alpha_{l,disp}\vec{U}_{mli}\right) - \nabla\cdot\left[\Gamma_{li}\nabla\left(\epsilon_{li}\alpha_{l,disp}\right)\right] = S_{\epsilon i} + S_{\epsilon i,corr} + S_{\alpha i} \tag{3.112}$$

where, $\vec{U}_{mli}$ and Γ_{li} are the individual size group drift-diffusion velocity and diffusion coefficient, respectively. The source term $S_{\epsilon i}$ accounts for the volume source/sink in the respective group due to nucleation, condensational growth, evaporational shrink, and coalescence. The distinction between two-phase and single-phase approaches in the computation of these sub-models is examined below.

$$S_{\epsilon i} = Nu_i + G_i^+ + G_i^- + C_i^+ + C_i^- \tag{3.113}$$

The second term on the RHS $S_{\epsilon i,corr}$ addresses the correction term resulting from the drift and diffusion of the droplets, which considers the effects of the second term on the right-hand side of Eqn. 3.60.

$$S_{\epsilon i,corr} = -\epsilon_{li}\alpha_{l,disp}\left[\nabla\cdot\left(\epsilon_{li}\alpha_{l,disp}\left(\frac{\rho_l}{\rho_g} - 1\right)\vec{U}_{mli} - \Gamma_{li}\left(\frac{\rho_l}{\rho_g} - 1\right)\nabla\epsilon_{li}\alpha_{l,disp}\right)\right] \tag{3.114}$$

The third term on the right-hand side, $S_{\alpha i}$ constitutes the effect of the first and third terms on the right-hand side of Eqn. 3.60.

$$S_{\alpha i} = \epsilon_{li}\alpha_{l,disp}\nabla\cdot\vec{U}_m + \epsilon_{li}\alpha_{l,disp}\alpha_g\left[\frac{1}{\rho_g}\frac{D\rho_g}{Dt} - \frac{1}{\rho_l}\frac{D\rho_l}{Dt}\right] \tag{3.115}$$

The last two terms of Eqn. 3.60 do not influence the PBM transport equation. These terms are not relevant for the dispersed phase, which employs a mixture approach. The summation of the size group transport equation over all groups should give back the original liquid phase volume fraction equation (Eqn. 3.60). To ensure this, the corresponding terms of both equations are compared, and then effective terms are computed from the summation of size group equations to be used in the total liquid volume fraction equation. For example, the effective drift-diffusion velocity $\vec{U}_{ml}$ is computed as:

$$\sum_{i}^{n} \epsilon_{li}\alpha_{l,disp}\vec{U}_{mli} = \alpha_{l,disp}\vec{U}_{ml} \quad \Longrightarrow \quad \vec{U}_{ml} = \sum_{i}^{n} \epsilon_{li}\vec{U}_{mli} \tag{3.116}$$

Similarly, the effective diffusion term becomes,

$$\sum_{i}^{n} \Gamma_{li}\nabla\left(\epsilon_{li}\alpha_{l,disp}\right) = \Gamma_{l}\nabla\alpha_{l,disp} \tag{3.117}$$

The $S_{\epsilon i,corr}$ and $S_{\alpha i}$ are calculated similarly. To summarize, we first use the effective terms obtained from the summation of size group equations to solve the total liquid phase volume fraction equation. Then, we solve the individual group transport equations to obtain ϵ_{li}.

The single-phase size group equation has the units of mass, whereas the two-phase approach uses volume fraction units. Consequently, the source terms related to nucleation, condensation (or evaporation), and coalescence need to be reformulated for the two-phase population balance model. The volumetric source term attributing to phase change that is required for computing the size group nucleation and condensation rates can be defined as:

$$S_{\alpha l} = S_{ml}\left[\frac{1}{\rho_l} - \alpha_{l,disp}\left(\frac{1}{\rho_l} - \frac{1}{\rho_g}\right)\right] \tag{3.118}$$

Hence, the nucleation rate becomes

$$Nu_i = \begin{cases} S^{+}_{\alpha l} & \text{if } \alpha_{l,disp} = 0 \text{ and } i = 1 \\ r_{nuc}S^{+}_{\alpha l} & \text{if } \alpha_{l,disp} \neq 0 \text{ and } i = 1 \\ 0 & \text{if } i \neq 1 \end{cases} \tag{3.119}$$

For condensational growth and evaporation shrink model, the condensation rate ($\dot{m}_i^{+}$) and evaporation rate ($\dot{m}_i^{-}$) are redefined as:

$$\dot{m}_i^{+} = w_i S^{+}_{\alpha l} \tag{3.120}$$

$$\dot{m}_i^{-} = w_i S^{-}_{\alpha l} \tag{3.121}$$

Here, the weight factor (w_i) is evaluated using the Eqn. 3.32. Eventually, the size group growth rate (G_i^{+}) can be computed from Eqn. 3.33 and shrink rate (G_i^{-}) can be calculated using Eqn. 3.34. The coalescence source (C_i^{+}) and sink (C_i^{-}) terms utilize the same formulations as in Eqns. 3.35 and 3.37 respectively, but with the exclusion of ρ_l.

3.2.5. Solution algorithm

Figure 3.6 explains the iterative algorithm of the two-phase solver and how different sub-models interact with the mixture-VOF and film approaches. The coupling of the fluid region and film region solver with the solid region solver using conjugate heat transfer (CHT) is also illustrated. The algorithm begins by incrementing time by the specified time-step size. Initially, the fluid region is solved, starting with updating the bulk and wall condensation mass sources. Then, the dispersed phase drift velocities are updated, which is used to solve the phase volume fraction equation. Subsequently, the dispersed phase volume fraction is determined, and the droplet evolution rates like nucleation, growth, shrinkage, and coalescence rates are calculated. This is followed by solving the dispersed-phase PBM equations to obtain the individual size group volume fraction. Next, the gas phase species mass fraction equation is solved. Following this, it proceeds to solve the fluid mixture energy equation. The gas mixture and liquid densities are then updated based on the changes in species mass fraction and temperature. Subsequently, the fluid mixture momentum equation is solved to update the velocity and pressure. The gas mixture and liquid densities are updated again by accounting for changes in pressure. Next, the fluid gas phase turbulence equations are solved to obtain the gas phase turbulent kinetic energy and eddy frequency. Thereafter, the film region equations are solved, starting with the film mass fraction equation, followed by film energy and momentum equations. If a solid region is present, then the CHT model is activated, and the solid heat diffusion equation is solved. Then, the residuals of all equations are examined to determine convergence. If convergence is not achieved, the aforementioned operations are iterated until the solution converges. Once convergence is attained, the solver advances to the subsequent time step and repeats the entire process.

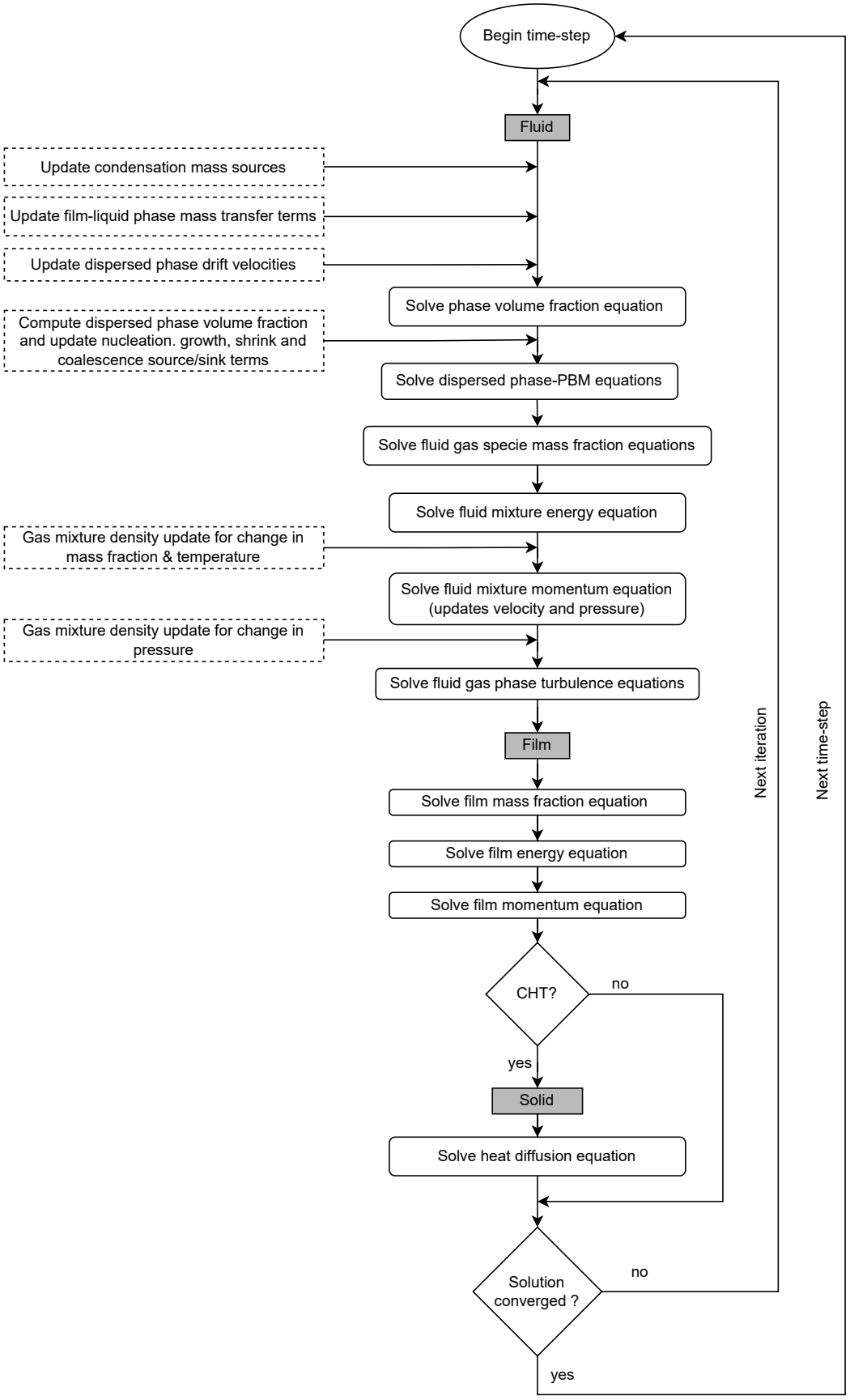

Figure 3.6.: Flowchart illustrating the solution algorithm of the two-phase mixture-film-VOF solver.

4. Model Verification and Validation

This chapter describes various verification and validation studies performed to ensure the applicability of the numerical models established in preceding chapter. It involves comparing the numerical results against analytical models and experimental data using separate effect and integral effect experiments. The first section addresses the strategy adopted to verify or validate each sub-model by focusing on the modeled physical phenomena. It also explains the baseline CFD settings for all the single-phase and two-phase solver simulations presented in this thesis. The subsequent sections discuss a series of verification and validation studies, starting with separate effect tests followed by integral effect tests to demonstrate the accuracy and validity of the models.

4.1. Verification and Validation strategy

The physical processes within a nuclear reactor containment in the course of a severe accident following, e.g., a loss of coolant accident (LOCA), is a multi-phenomena interaction problem. This involves various phenomena like multi-component gas transport, buoyancy-driven flow, turbulence, bulk condensation, wall condensation in the presence of non-condensable gases (NCGs), gas radiation, conjugate heat transfer with reactor structures and internal components, and nuclear aerosol transport. Additionally, during long transient and continuous steam condensation, the condensate can accumulate inside the containment, occupy considerable space, and interact with the other phenomena. To ensure the applicability of the developed CFD models, it is essential to verify and validate them against appropriate analytical and experimental data obtained from both small-scale and large-scale test facilities, focusing on both single-phenomenon and multi-phenomenon interactions. Hence, a series of simulations were carefully selected, ranging from single phenomenon to multi-phenomena cases, which are summarized in the validation matrix (Table 4.1)

The existing *containmentFOAM* models like multi-component gas diffusion and transport, turbulence, buoyancy-driven flow, wall condensation, and conjugate heat transfer have been validated in previous works [Vijaya Kumar, 2022, Kampili, 2024]. As the primary objective of this thesis is modeling bulk condensation and fog transport, the validation studies will focus mainly on those phenomena and how their interaction with other physics can affect the prediction of local conditions inside the containment. Also, the results are analyzed using both single and two-phase solvers to compare the effectiveness, feasibility, and accuracy of the solvers in simulating complex containment scenarios. Due to a lack of experiments involving only bulk condensation, the bulk condensation model is verified by comparing the simulation against the Mollier diagram [Mollier, 1929]. For this purpose, a two-dimensional mixing nozzle case is employed to compare the amount of fog formed and the change in temperature due to condensation. The same case is then redesigned to verify the bulk evaporation model by modifying the inlet flow conditions of the nozzle. The fog droplet transport model and its inertia sub-model are then validated against the bent pipe deposition experiment [Pui et al., 1987] in which the inertial deposition efficiency of droplets on the pipe walls is compared with the simulations. Then, the gravitational settling part

of the drift velocity model is validated using a ventilation chamber experiment [Chen et al., 2006] where the gravitational settling of particles is simulated, and the particle distribution is compared with the experimental data. The effectiveness of the Stokes and Manninen drift velocity models is compared in terms of accuracy and computational effort to choose the right model for large-scale application. The preliminary simulations use the mono-dispersed droplets approach, which is then followed by poly-dispersed droplets approach to confirm the replication of results using population balance model (PBM) framework. The verification of the coalescence and growth models in PBM is performed using analytical data by comparing the droplet number density evolution over time. Then the surface film model is validated by simulating the flow of film over an inclined plate and its thickening in a countercurrent flow. The film-to-liquid phase mass transfer is verified using a hypothetical vessel in which the film flows along the wall towards a sump region and starts accumulating, forming a gas-liquid interface.

Table 4.1.: Verification and validation matrix: Overview of analytical and experimental tests and associated physical phenomena.

Phenomenon \ Test case	Mollier mixing nozzle	Bent pipe deposition	Ventilation chamber	Analytical studies - coalescence & growth	Falling film	Water accumulation	SETCOM	THAI-TH2	THAI-HM2
Bulk condensation	×						×	×	×
Bulk evaporation	×							×	×
Drift flux model - inertia		×						×	×
Drift flux model - gravity			×					×	×
Poly-dispersed droplets transport		×						×	×
Poly-dispersed droplets evolution				×				×	×
Surface film flow					×		×	×	×
Film-liquid phase mass transfer						×		×	
Wall condensation							×	×	×
Multi-component gas	×						×	×	×
Light-heavy gas mixture									×
Buoyancy								×	×
Turbulence			×				×	×	×
Gas mixing & layer erosion									×
Stratification layer formation								×	
Condensate accumulation								×	

The next step of validation involves the investigation of the influence of bulk condensation on wall condensation dominant experiments like SETCOM [Kelm et al., 2019]. These simulations aim to understand how fog formation in the vicinity of condensing surfaces can interact with the wall condensation process and to quantify its effect. The two-phase simulations compare the condensate film thickness on the walls with differently refined meshes. Following validation with small-scale experiments, the model's validity is then assessed on a technical-scale THAI facility with multi-phenomena interaction. Two THAI experiments with conditions favorable for bulk and wall condensation are chosen for this purpose. The first one is the THAI-TH2 experiment, which

involves a two-component gas mixture (steam and air), and the steam injection happens in the upper section of the vessel, leading to the formation of a stratified layer of steam. The second one is the THAI-HM2 experiment that includes a three-component gas mixture comprising light gas hydrogen and heavy gases, nitrogen, and steam. In this case, steam is introduced from the vessel's lower section to break the hydrogen cloud at the upper section. Here the steam plume, driven by buoyancy, turbulence, and condensation, leads to the mixing and erosion of the hydrogen layer. These validation studies compare the transient vessel pressure and local temperatures with and without bulk condensation and fog transport to demonstrate its influence.

4.1.1. Baseline CFD model

The baseline models, properties, solver settings, and discretization schemes for the single-phase and two-phase solvers are discussed here.

Single-phase solver

The turbulence model uses the standard $k-\omega$ SST model with supplementary turbulence production and dissipation terms attributed to buoyancy, which is determined utilizing the Simple Gradient Diffusion Hypothesis (SGDH) model [Chung & Devaud, 2008]. The gas mixture properties are computed using Wilke's model [Wilke, 1950] from individual species temperature-dependent properties. The binary gas diffusion coefficients are computed using the Fuller model [Fuller et al., 1966] from which the species-specific effective diffusivities in gas mixtures are computed. The passive scalar approach for fog droplets requires only the water density, whose value is fixed at 1000 kg/m^3 irrespective of temperature and pressure, and the definition of droplet diameters. For the simulations with poly-dispersed droplets, the PBM approach requires specification of the number of size groups and their representative diameter. For most of the simulations in this thesis, eight size groups with diameters in geometric progression starting from 1 μm to 128 μm are considered. The spatial discretization of the convective transport term in the conservation equations uses second-order schemes except for turbulence quantities, which use first-order upwind schemes for better stability. The coupled equations are solved using the PIMPLE algorithm (Figure 3.2) with repeated PIMPLE iterations within each time step until all residuals satisfy the convergence threshold less than 10^{-4}. For non-orthogonal meshes, the pressure-velocity coupling equation solver uses additional non-orthogonal corrector iteration to reduce discretization errors introduced by mesh non-orthogonality. Temporal discretization uses the Crank-Nicolson scheme, which is a blend of the fully implicit scheme (backward Euler) and the explicit scheme (forward Euler) to provide better accuracy and stability. The single-phase simulations in this thesis use a blending factor of 0.9, which gives 90% weight for implicit scheme and 10% weight for explicit scheme.

Two-phase solver

The turbulence modeling is restricted to the gas phase, employing the same formulation as in the single-phase, while laminar flow assumptions are made for both the water phase and the liquid film surface film model. All the gas properties are computed as single-phase, and water phase properties are defined using NSRDS (National Standard Reference Data System) functions. The properties of the phase mixture are determined by averaging based on phase volume fractions, as discussed in.3.2.1. The PBM utilizes the same size groups as in the single-phase solver. The spatial discretization of the convection term in the fluid region uses the same schemes as in the single-phase solver. For the film region, the discretization in space employs first-order upwind schemes for all equations. The series of equations is solved using the PIMPLE algorithm outlined in Figure 3.6 with convergence criteria the same as the single-phase. The time discretization uses the explicit Euler scheme, which is simple, effectively faster per time step in the present two-phase runs and reduces computational overhead for large simulations.

4.2. Mollier mixing nozzle

The verification of bulk condensation model using Mollier diagram theory with single-phase and two-phase approaches is discussed in this section. It begins with an overview of the Mollier diagram and how to utilize it for this verification study. Two cases, one for condensation and another for evaporation, are chosen, and the boundary conditions and the data for verification are extracted from the diagram. Subsequently, the computational geometry and mesh are introduced, along with the simulation parameters. This is followed by grid and time-step sensitivity analyses to determine the optimum mesh and quantify the dependency of results on time-step size. Finally, the condensation and evaporation simulations are conducted, and the results are compared with the theoretical data for model verification.

4.2.1. Mollier diagram theory

The Mollier diagram [Mollier, 1929] graphically illustrates the relationships among key thermodynamic variables for steam or humid air, including enthalpy, entropy, and temperature. This diagram is generally used for evaluating the conditions of humid air and steam to simplify the analysis of energy transfer processes in heating, cooling, and humidification systems. It depicts how the enthalpy, or heat content, of air varies with its water vapor content, as shown in Figure 4.1.

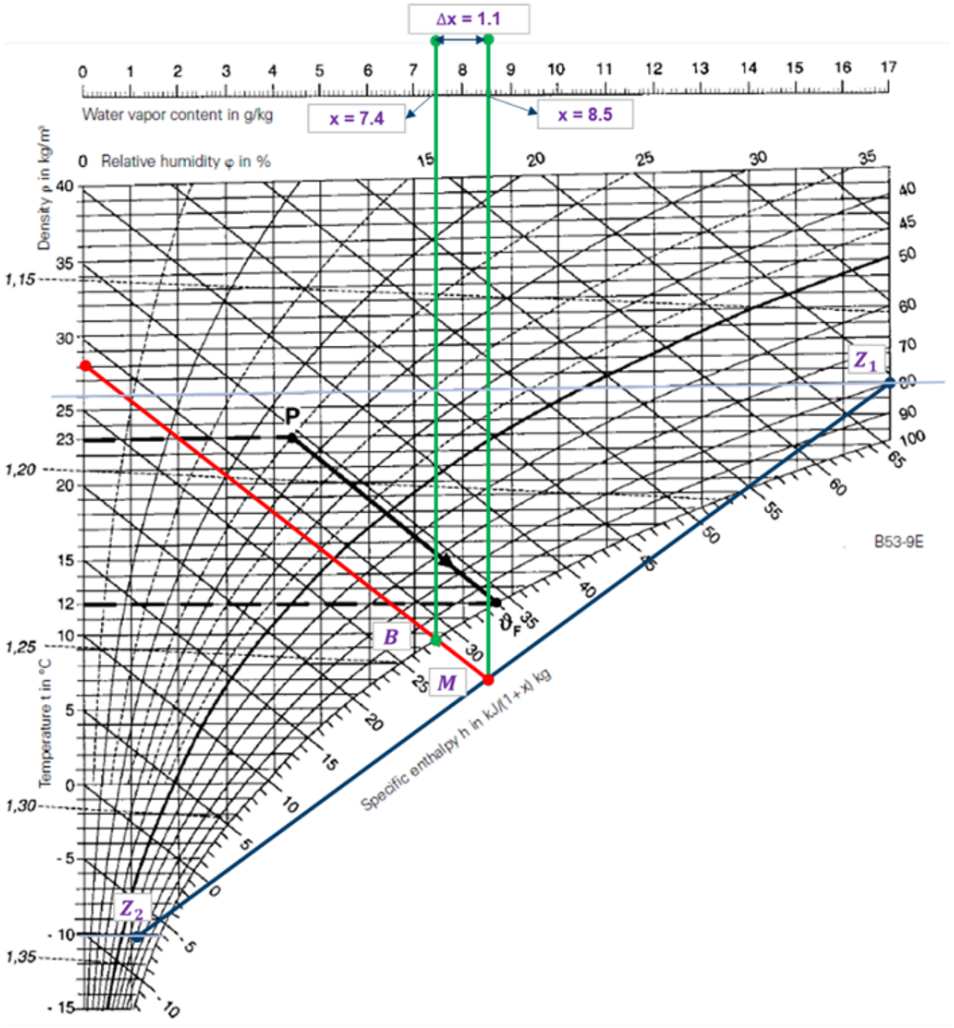

Figure 4.1.: Mollier diagram [Siemens, 2007] and illustration of property determination while mixing of air-steam mixtures at different state (Z_1 and Z_2).

Since measuring heat content directly is difficult, the diagram incorporates temperature and relative humidity, which are more straightforward to obtain experimentally. In HVAC applications, the Mollier diagram is commonly used to analyze the mixing of hot and cold air-steam mixtures to ensure the desired conditions for efficient heat transfer. When hot and cold air-steam streams are mixed, the resulting mixture temperature, vapor content, and fog mass can be determined using the diagram. This application of the Mollier diagram is used to verify the bulk condensation model and, subsequently, the bulk evaporation model.

When two airstreams with mass flow rates $\dot{m}_1$ and $\dot{m}_2$ and distinct thermodynamic states Z_1 and Z_2 mix, their combined state Z_m can be located on the Mollier diagram (Figure 4.1), through a linear interpolation inversely proportional to their flow rates. The mixing point M lies closer to the state with greater mass flux.

The mixing point's vapor content (M) is determined through

$$x_M = \frac{x_1\dot{m}_1 + x_2\dot{m}_2}{\dot{m}_1 + \dot{m}_2} \quad [g/kg] \tag{4.1}$$

where vapor content, $x = m_{steam}/m_{air}$

Similarly, the mixing point's specific enthalpy is estimated by

$$h_M = \frac{h_1\dot{m}_1 + h_2\dot{m}_2}{\dot{m}_1 + \dot{m}_2} \quad [kJ/kg] \tag{4.2}$$

The values of h_M and x_M determine the position of the mixing point on the Mollier diagram, from which other state properties can be obtained. If the mixing point falls below the saturation curve (100 % relative humidity), the air is supersaturated and contains more water vapor than it can hold at that temperature, so the excess condenses into fine droplets, forming fog or mist. If there is more fog than the air can hold at its saturation temperature, some of the fog evaporates back into vapor. The air state then moves along mist isotherms to the saturation point B, where the final temperature and vapor content are measured, and the difference in vapor content between initial and final states gives the amount of fog formed. To verify the bulk condensation model, a hot and cold air-steam mixture is combined so that the mixing point is below the saturation line. Similarly, the fog evaporation model can be verified by mixing a hot air-steam mixture with a cold air-steam-fog mixture that initially contains fog. Table 4.2 shows the initial and final conditions for both condensation and evaporation, as determined from the Mollier diagram. The estimation of the mixing point and its related properties using the Mollier diagram for the condensation case is illustrated in Figure 4.1.

Table 4.2.: Properties of initial states Z_1 and Z_2 and final state B for condensation and evaporation scenarios estimated from Mollier diagram analysis

	Condensation			Evaporation		
	State Z_1	State Z_2	State B	State Z_1	State Z_2	State B
Temperature $[^oC]$	26	-10	9.5	26	9.5	17
Vapor content $[g/kg]$	17	1.1	7.4	17	7.4	12.2
Fog content $[g/kg]$	0.0	0.0	1.1	0.0	1.1	0.4
Relative humidity [%]	80	70	100	80	100	100
Density $[kg/m^3]$	1.18	1.34	1.24	1.18	1.26	1.21

4.2.2. Simulation setup

The mixing process is analyzed utilizing CFD using a nozzle geometry [Zhang & Laurien, 2014] with two inlets and an outlet, with mixing length (= 5 m) long enough to ensure complete mixing of the gas mixtures, as shown in Figure 4.2. As the major objective of the simulation is to achieve full mixing and measure the mixture properties at the outlet, a two-dimensional grid is employed to make the simulation more efficient and less resource-intensive. The boundary conditions for inlet 1 and inlet 2 are set to match the states Z_1 and Z_2 respectively based on Table 4.2. The inlet flow velocities at both inlets are assigned a magnitude of 1 m/s and normal to the inlet boundary. All the wall boundaries are treated as adiabatic to prevent any heat loss through walls. Turbulence is modeled to enhance mixing, and effects of gravity, Brownian diffusion, and drift velocity are neglected to focus on the main physics of interest. Also, the fog droplets are treated as mono-dispersed droplets of diameter 1 μm, a choice that does not impact the simulation results as drift and Brownian motions are disregarded. For both cases, the simulations are executed until steady state is established-requiring 20 seconds for condensation and 25 seconds for evaporation. Moreover, the simulations using the two-phase approach do not incorporate the surface-film model, as the condensation on walls is not considered.

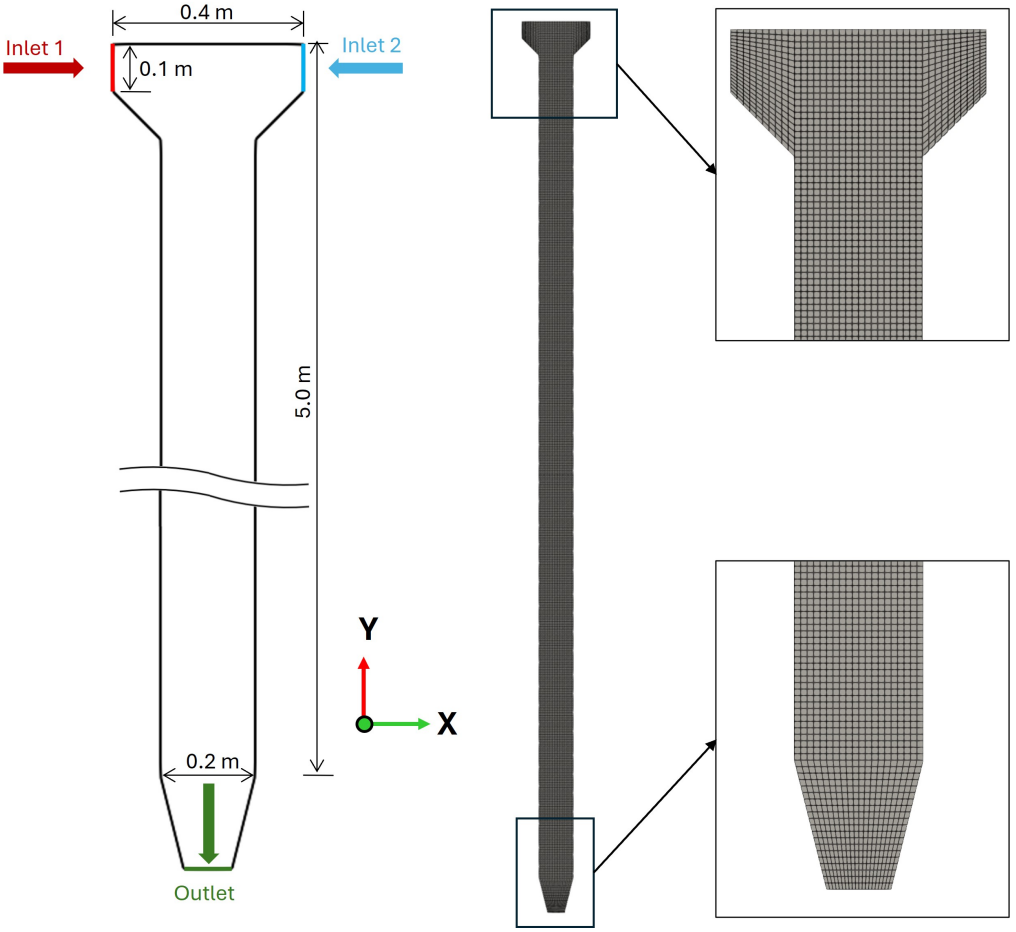

Figure 4.2.: Left: Mixing nozzle geometry with dimensions. Right: 2D computational mesh of the nozzle.

4.2.3. Grid sensitivity study

Initially, a grid sensitivity analysis is performed on the condensation test case to identify the optimum mesh. The simulations use a constant time step of $\Delta t = 10^{-3} s$ to ensure the Courant number

is less than 1. The integral condensation rate is used to assess the effect of the mesh refinement on the model predictions based on the standard Grid convergence index (GCI) method [ASME, 2008], which are summarized in Table 4.3. For the single-phase solver, the relative difference in the net condensation rate decreased from 0.41 % for the coarse mesh to 0.22 % for the medium mesh. Similarly, for the two-phase solver, the relative difference reduced from 0.52 % to 0.22 %. This clearly indicates that the effect of mesh refinement on the results is minimal. Richardson extrapolation yielded an apparent order of convergence of approximately 0.86, with a Grid Convergence Index (GCI) between the fine and medium meshes of about 0.35 % for the single-phase solver, confirming mesh independence. Consequently, the medium-refined mesh shown in Figure 4.2 is chosen for the entire verification study. The discrepancy in condensation rate between the single-phase and two-phase simulations is also minor, at under 1 %.

Table 4.3.: Grid independency study of the Mollier mixing nozzle condensation case using single-phase and two-phase solvers by comparing the integral condensation rate $[kg/s]$.

	No. of elements	Single-phase		Two-phase	
		Net rate $[kg/s]$	Relative difference [%]	Net rate $[kg/s]$	Relative difference [%]
Coarse mesh	2700	5.5584×10^{-6}	0.41	5.5262×10^{-6}	0.52
Medium mesh	10800	5.5812×10^{-6}	0.22	5.5550×10^{-6}	0.22
Fine mesh	43200	5.5938×10^{-6}	-	5.5675×10^{-6}	-

4.2.4. Time-step sensitivity study

Following the grid sensitivity analysis, a time-step sensitivity study is conducted to confirm that the results do not depend on the selected time-step size. This is particularly important for the bulk condensation model, as the time-step size is a parameter for computing the condensation rate. The condensation case with medium refined mesh is selected for the study, and the integral condensation rate parameter is used to assess the sensitivity. Three time-step sizes are considered: $\Delta t = 2 \times 10^{-3}$, 1×10^{-3} and 5×10^{-4} seconds. The time-step sizes larger than 2×10^{-3} seconds are excluded because of instabilities and convergence issues arising from Courant numbers exceeding 1. The summary of the time-step sensitivity findings is provided in Table 4.4. It is clear that the deviations in the net condensation rate are marginal (< 0.05 %) with successive decrements in time-step size for both single-phase and two-phase approaches. Consequently, it can be concluded that the bulk condensation rate remains unaffected by the time-step size. Based on these findings, a time-step size of $\Delta t = 2 \times 10^{-3}$ is selected for the bulk condensation and evaporation verification studies, as it achieves a suitable trade-off between accuracy and computational efficiency.

4.2.5. Verification results

The verification study is finally performed, which comprises a total of four simulations: condensation case with the single-phase approach, condensation case with the two-phase approach, evaporation case with the single-phase approach and evaporation case with the two-phase approach. The boundary conditions and theoretical data for comparison with the simulation for all simulations are taken from Table 4.2. The converged steady-state simulation results demonstrating the spatial distribution of the condensation rate, temperature, vapor content, and fog content are shown in Figures. 4.3 - 4.6.

Table 4.4.: Time step sensitivity study of the Mollier mixing nozzle condensation case using single-phase and two-phase solvers by comparing the integral condensation rate $[kg/s]$.

Time step size	Single-phase		Two-phase	
	Net rate $[kg/s]$	Relative difference $[\%]$	Net rate $[kg/s]$	Relative difference $[\%]$
2×10^{-3}	5.5794×10^{-6}	0.03	5.5551×10^{-6}	0.002
1×10^{-3}	5.5812×10^{-6}	0.04	5.5550×10^{-6}	0.002
5×10^{-4}	5.5837×10^{-6}	-	5.5549×10^{-6}	-

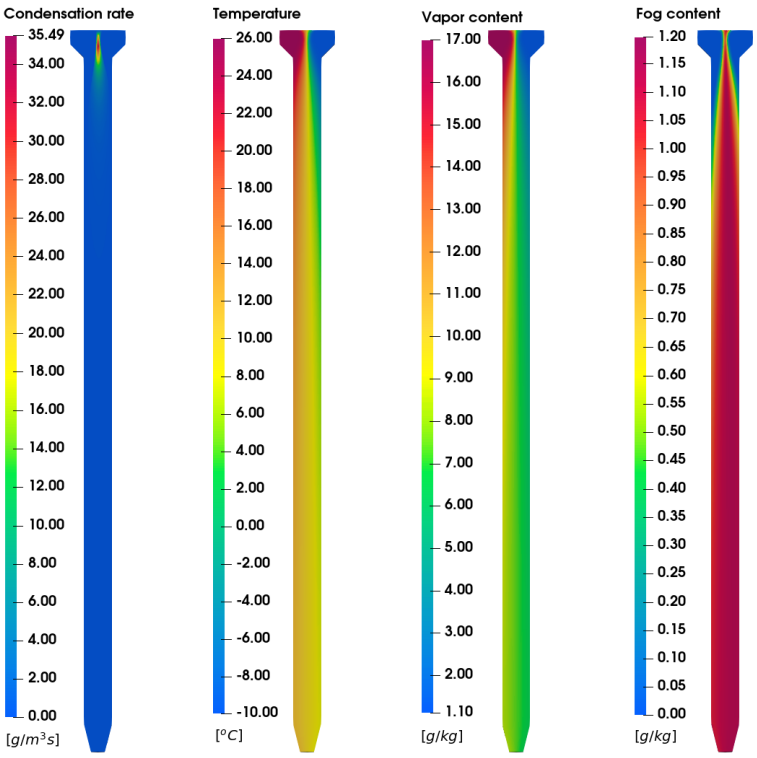

Figure 4.3.: Condensation rate, temperature, vapor content and fog content distributions in the mixing nozzle after steady state for single-phase condensation case.

The simulation results reveal that the majority of condensation and evaporation processes take place in the upper section of the nozzle, and the gases uniformly mixed at the nozzle exit. Moreover, there is little to no condensation or evaporation occurring at the nozzle's lower end, and any fog generated is carried away with the outflow. In both condensation and evaporation scenarios, the balance between these phase-change mechanisms maintains the mixture at saturation conditions. For instance, in the condensation case, a small amount of evaporation also occurs, but at a relatively lower rate. Similarly, for the evaporation case, there is some condensation present at small rates. However, to display the dominant process in the respective cases, the condensation and evaporation rate distribution (Figures. 4.3 - 4.6) scales are clipped. It is also notable that the field distributions are almost the same, with only minor differences between single-phase and two-phase approaches for the corresponding phase change simulations. The observed minor differences are due to the inherent variations in the modeling strategies employed. For verification, the area-averaged outlet properties like temperature, vapor content, and fog content from the sim-

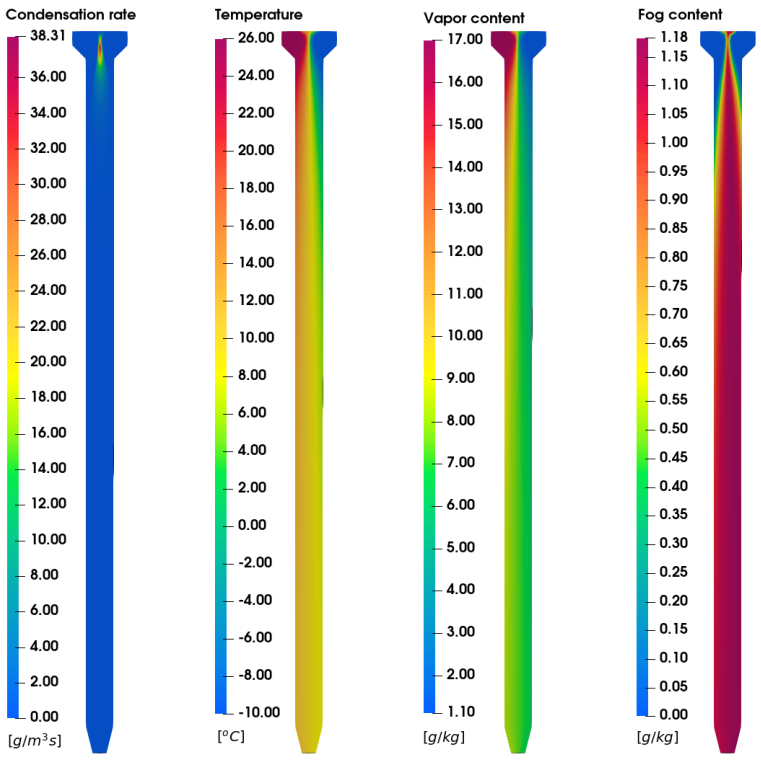

Figure 4.4.: Condensation rate, temperature, vapor content and fog content distributions in the mixing nozzle after steady state for two-phase condensation case.

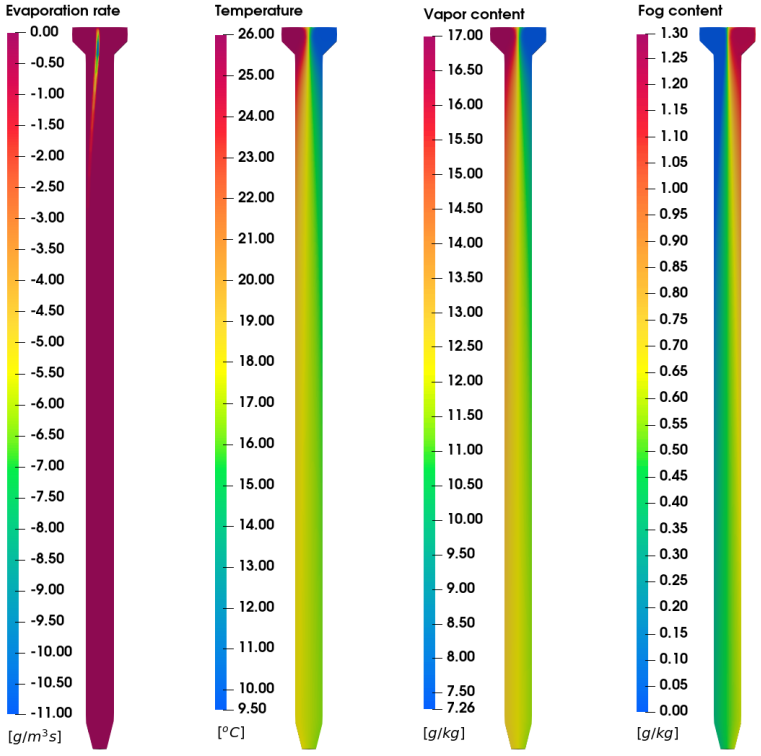

Figure 4.5.: Evaporation rate, temperature, vapor content and fog content distributions in the mixing nozzle after steady state for single-phase evaporation case.

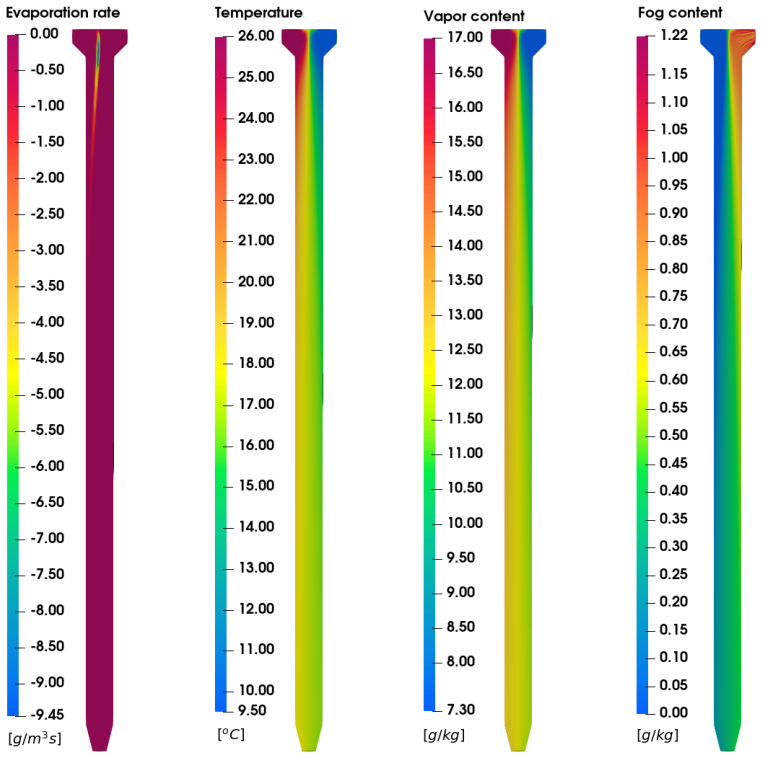

Figure 4.6.: Evaporation rate, temperature, vapor content and fog content distributions in the mixing nozzle after steady state for two-phase evaporation case.

Table 4.5.: Comparison of Mollier diagram theory data with simulation results for condensation and evaporation cases using single-phase and two-phase approaches.

		Condensation			Evaporation		
		Mollier	Simulation	Error [%]	Mollier	Simulation	Error [%]
Single-phase	Temperature $[^oC]$	9.5	9.64	1.44	17	17.18	1.54
	Vapor content $[g/kg]$	7.4	7.32	1.06	12.2	12.1	0.01
	Fog content $[g/kg]$	1.1	1.12	2.19	0.4	0.41	2.06
Two-phase	Temperature $[^oC]$	9.5	9.59	0.95	17	17.26	1.06
	Vapor content $[g/kg]$	7.4	7.32	1.07	12.2	12.22	0.37
	Fog content $[g/kg]$	1.1	1.15	4.12	0.4	0.42	5.06

ulations are compared against the corresponding properties from the Mollier diagram at final state B. Table 4.5 summarizes the findings, revealing that the bulk condensation model maintains accuracy within 6 % and aligns well with theoretical predictions for both single-phase and two-phase approaches. Furthermore, the computational cost assessment showed that, in this scenario, the two-phase method requires about 12 % more resources than the single-phase approach.

4.2.6. Discussion

In this section, the bulk condensation model verification against the Mollier diagram was performed employing both single-phase and two-phase approaches. Firstly, a grid sensitivity study was conducted, which helped in identifying the optimum mesh with 10800 elements and also confirmed that the deviation in the results with further mesh refinements was less than 0.3 %. In the next step, a time-step size sensitivity study was carried out to understand its effect on the results, especially due to the inclusion of time-step size in the bulk condensation rate calculation model. The findings showed that varying the time-step size had a minimal effect on the results (< 0.1 %) and as long as the Courant numbers are less than 1, the simulations are stable and converge rapidly. Consequently, a time-step size of 2×10^{-3} was chosen for the further Mollier mixing nozzle verification study. The condensation case was used for both sensitivity studies, with the integral condensation rate serving as the key parameter. Finally, the model was verified by comparing simulation results-specifically outlet temperature, vapor content, and fog content-for both condensation and evaporation scenarios with theoretical predictions. This study verified that the single-phase and two-phase bulk condensation model implemented in *containmentFOAM* closely matches the theoretical predictions by the Mollier diagram, indicating its suitability for further studies.

4.3. Bent pipe deposition

This section discusses the validation of the drift velocity model for the transport of fog droplets (or particles), with a primary emphasis on the inertial effects. It starts with an overview of the bent pipe particle deposition experiment and an analytical study and a computational investigation into it. Next, the computational geometry and mesh are introduced, followed by a grid sensitivity analysis. Finally, the simulations are performed using both the Manninen and Stokes drift velocity models, incorporating single-phase and two-phase approaches, and the results are compared with previous data.

4.3.1. Inertial deposition of particles in a bent pipe

The particles in a gas flowing through a 90^o bent pipe get deposited on the walls due to inertia. One of the first analytical investigations into this phenomena was conducted by Cheng & Wang, 1981 for a fully developed laminar flow. They presented numerical equations for calculating the behavior of particles in the flow through a 90° bend in a pipe of circular cross-section. Later, Pui et al., 1987 performed a detailed experimental study on the particle deposition in bent pipe for both laminar and turbulent flows using mono-disperse aerosols. Numerical studies have also been conducted to model the aerosol flow and deposition in bent pipes. Pilou et al., 2011 numerically studied this problem in an Euler–Euler framework with one-way coupling between the aerosol and the primary flow. More recently, Frederix et al., 2017 used the CFD approach to predict the aerosol deposition using an internally mixed Eulerian aerosol model. Following these works, the bent pipe deposition problem is utilized to validate the drift velocity model and its inertial effect by comparing the deposition efficiency as a function of Stokes number against experimental, analytical, and simulation data. The deposition efficiency (η_d) is defined as the percentage of rate of aerosol deposition on walls relative to the rate of aerosols injected into the pipe. Mathematically, this can be expressed as:

$$\eta_d = \frac{\dot{m}_{deposit}}{\dot{m}_{inlet}} \tag{4.3}$$

where $\dot{m}_{deposit}$ is the aerosol mass deposition rate and $\dot{m}_{inlet}$ is the aerosol mass inflow rate.

The Stokes number(St) is defined as the ratio of the aerosol inertial timescale over the flow convective timescale and is expressed as:

$$St = \frac{\rho_a d_a^2 C_c U_g}{18 \mu_g R_b} \tag{4.4}$$

where ρ_a is the material density of the aerosol, d_a represents the aerosol particle diameter, C_c denotes the Cunningham slip correction factor, U_g quantifies the inlet gas flow velocity, μ_g represents the kinematic viscosity of the gas, and R_b is the radius of curvature of the bend.

From the large experimental database [Pui et al., 1987], one case with flow Reynolds number = 1000, representing a laminar flow, is chosen for the validation study, and its details are specified in Table 4.6. The deposition efficiency was esitmated for 11 distinct droplet sizes ranging from 4 μm to 15 μm and this same size spectrum will be used for the simulations.

Table 4.6.: Gas and aerosol properties, and bent pipe dimensions of the selected experimental data for the validation simulations.

Gas temperature T	273 K
Gas density ρ_g	1.18 kg/m^3
Gas dynamic viscosity μ_g	1.85×10^{-5} Ns/m^2
Droplet diameters d_a	4−15 μm
Droplet material density ρ_a	895 kg/m^3
Pipe diameter D	3.95×10^{-3} m
Pipe bend radius of curvature R_b	22.515×10^{-3} m
Gas mean inlet velocity U_g	3.86 m/s
Cunningham slip correction factor C_c	1.028

4.3.2. Simulation setup

The simulation of the deposition of aerosols due to inertia in a 90^o bend of circular cross-section is performed on a three-dimensional computational domain by adopting the geometry shown in Figure 4.7. The geometry features a pipe of diameter D and consists of two linear sections: horizontal inlet of length D and vertical outlet of length 2D, and a bend of radius R_b. The linear sections are essential for the simulations to affirm that the flow behavior in the bend is not affected by the inlet and outlet boundary conditions. Based on the geometry and dimensions specified in Table 4.6, a 3D structured mesh is generated as depicted in Figure 4.7. The boundary conditions and gas and aerosol properties for the simulations are also taken from Table 4.6. The inlet aerosol injection volume fraction is set at $\alpha_l = 10^{-10}$ to minimize any disturbances in the gas flow caused by the aerosols and to guarantee the validity of the one-way coupling model. The drift velocity deposition boundary condition discussed in Sec.3.1.2.1 is applied on all walls, which removes only the aerosols that are deposited on the walls. This boundary condition is particularly advantageous as it directly gives the deposition rate, which can then be used to compute deposition efficiency. Additionally, the pipe walls are treated as adiabatic, and the no-slip boundary condition is applied to primary gas flow velocity on these walls. The primary flow is treated as laminar as in the experiments, and effects of gravity and Brownian diffusion are included to match the experimental conditions. The simulations are conducted using both the Manninen and Stokes drift velocity models, incorporating single-phase and two-phase approaches. Additionally, the simulations utilize a mono-disperse approach for each aerosol diameter, resulting in a total of 11 simulations corresponding to the different diameters. The simulations are also carried out using the Population Balance Model (PBM) approach, which integrates all the 11 simulations into a single simulation. This is done to assess whether the PBM approach can effectively replicate the results obtained from the mono-disperse simulations. The simulations are run until a steady state is achieved,

which occurs after 0.2 seconds for all cases. The time-step size used for all simulations is equal to 2×10^{-5} seconds, keeping the Courant numbers below 1, giving stability to the simulations. Moreover, the simulations using the two-phase approach do not employ the surface-film model, as there is no flow of aerosols (or droplets) along the walls. Since the aerosols are removed through the walls, the mixture-VOF model is sufficient to capture the required phenomenon.

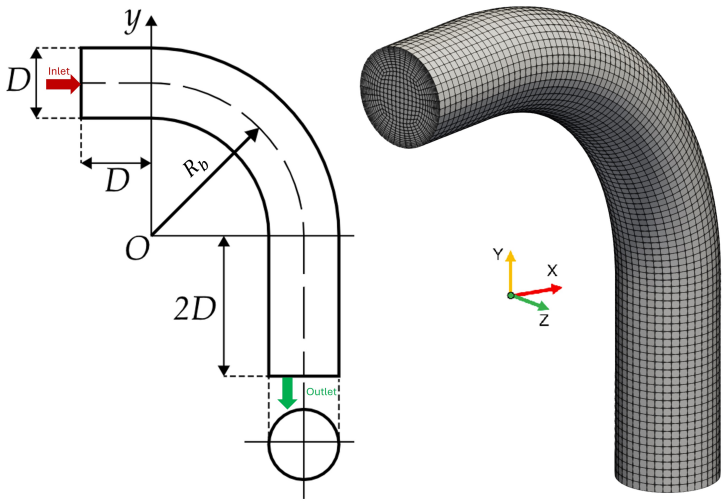

Figure 4.7.: Left: Geometry of the bent pipe [Frederix et al., 2017]. Right: 3D computational mesh of the bent pipe

4.3.3. Grid sensitivity study

The effect of mesh refinement on the results is investigated initially to determine the optimum mesh. For this purpose, a simulation with mono-dispersed aerosols of diameter 8.28 μm, Stokes number 0.37, and Manninen drift velocity model is run on differently refined meshes, and the deposition efficiency parameter is used for comparison. The grid sensitivity analysis is conducted using both single-phase and two-phase approaches, and the findings are summarized in Table 4.7. For the single-phase solver, the relative difference in deposition efficiency decreased from 0.46 % for the coarse mesh to 0.26 % for the medium mesh. Similarly, for the two-phase solver, the relative difference reduced from 2.32 % to 0.69 % with mesh refinement. This clearly indicates that the effect of mesh on the results is minor. Richardson extrapolation was applied, yielding an apparent order of convergence of approximately 1.96 with a GCI between the fine and medium meshes of about 0.41 % for the single-phase solver, confirming mesh independence. Hence, the medium mesh (Figure 4.7) is the optimum mesh for all cases and is chosen for further validation study.

4.3.4. Validation results

The validation simulations consist of mainly four cases: Manninen model with single-phase method, Stokes model with single-phase method, Manninen model with two-phase method, and Stokes model with two-phase method. Each of these cases involves 11 simulations, corresponding to each aerosol diameter, when using a mono-dispersed approach. However, the PBM approach enables us to reduce these 11 simulations to a single case by treating each diameter aerosol as a size group in the population. The PBM approach for the bent pipe deposition simulation disregards the effects of aerosol evolution by coalescence, growth, or phase change. The comparison of the deposition efficiency using the mono-disperse approach for some aerosol diameters and the PBM approach revealed that the PBM approach was able to replicate the mono-disperse results. This comparison is also performed for the different drift velocity models as well as the phase approaches. Therefore, the results discussed here are obtained using the PBM approach. The fluid in

Table 4.7.: Grid independency study of the bent pipe deposition case using single-phase and two-phase solvers by comparing the deposition efficiency based on Manninen drift velocity model for aerosol diameter = 8.28 μm equivalent to $St = 0.37$.

	No. of elements	Single-phase		Two-phase	
		Deposition efficiency [%]	Relative difference [%]	Deposition efficiency [%]	Relative difference [%]
Coarse mesh	28800	34.65	0.46	33.91	2.32
Medium mesh	56260	34.81	0.26	34.70	0.69
Fine mesh	101400	34.90	-	34.94	-

the pipe gets accelerated due to a change in direction while flowing through the bend region. The aerosols, by virtue of their inertia, cannot follow the fluid flow path and deviate, leading to their deposition on the walls. The aerosol inertia is proportional to its diameter; hence, larger droplets easily get deposited while smaller droplets tend to follow the flow path and exit through the outlet. This is confirmed by the aerosol deposition concentration contour for different Stokes numbers in Figure 4.8.

It is evident that the aerosol concentration on the pipe walls due to deposition increases with Stokes number, indicating that larger aerosol diameters lead to increased deposition. Furthermore, for lower Stokes numbers, the deposition occurs predominantly towards the end of the bend, where the flow acceleration is highest. However, as the Stokes number increases, the deposition zone starts moving towards the start of the bend, where the flow acceleration is lower. This means that the high-inertia fog droplets can deviate from the primary flow path even when subjected to small accelerations caused by changes in direction, and the drift velocity model can capture this phenomenon. Moreover, it can be observed that the Stokes model predicts higher deposition rates compared to the Manninen model. This finding is consistent for all Stokes numbers and in both single-phase and two-phase approaches. When comparing single-phase and two-phase approaches using the Stokes drift velocity model, the predicted deposition rates show marginal variation across all Stokes numbers. However, the Manninen model shows a notable difference between the two approaches, where the two-phase approach predicts lower deposition rates than the single-phase approach, and this difference becomes more evident as the Stokes number increases. The quantitative comparison between different models and approaches with the experimental, analytical, and numerical data is shown in Figure 4.9.

The Stokes drift model demonstrates >95% accuracy in predicting deposition efficiency across the full Stokes number range for both single-phase and two-phase approaches. There is only a negligible difference in the efficiency predictions between both phase methods. However, the Manninen model shows a notable difference in deposition efficiency between the single-phase and two-phase approaches, with deviations (< 1 %) beginning at the mid-range Stokes numbers and increasing up to around 15 % at high Stokes numbers. This reveals that the Manninen model is slightly sensitive to the phase approach at high Stokes numbers. The comparison with the validation data indicates that the Manninen model with the single-phase approach offers good accuracy (> 95 %) at both low and high Stokes numbers, but it tends to underestimate deposition efficiency by 20-30 % at medium Stokes number range. In contrast, the Manninen model with the two-phase approach offers good accuracy (> 95 %) at low Stokes numbers but under-predicts the deposition efficiency by 20 - 30 % at medium to high Stokes numbers. The analysis of computational costs revealed that the two-phase approach is only 16 % more computationally intensive than the single-phase approach for the whole simulation. However, when comparing the Stokes and Manninen models, the Stokes model is around 3 times more expensive than the Manninen model for both phase approaches for

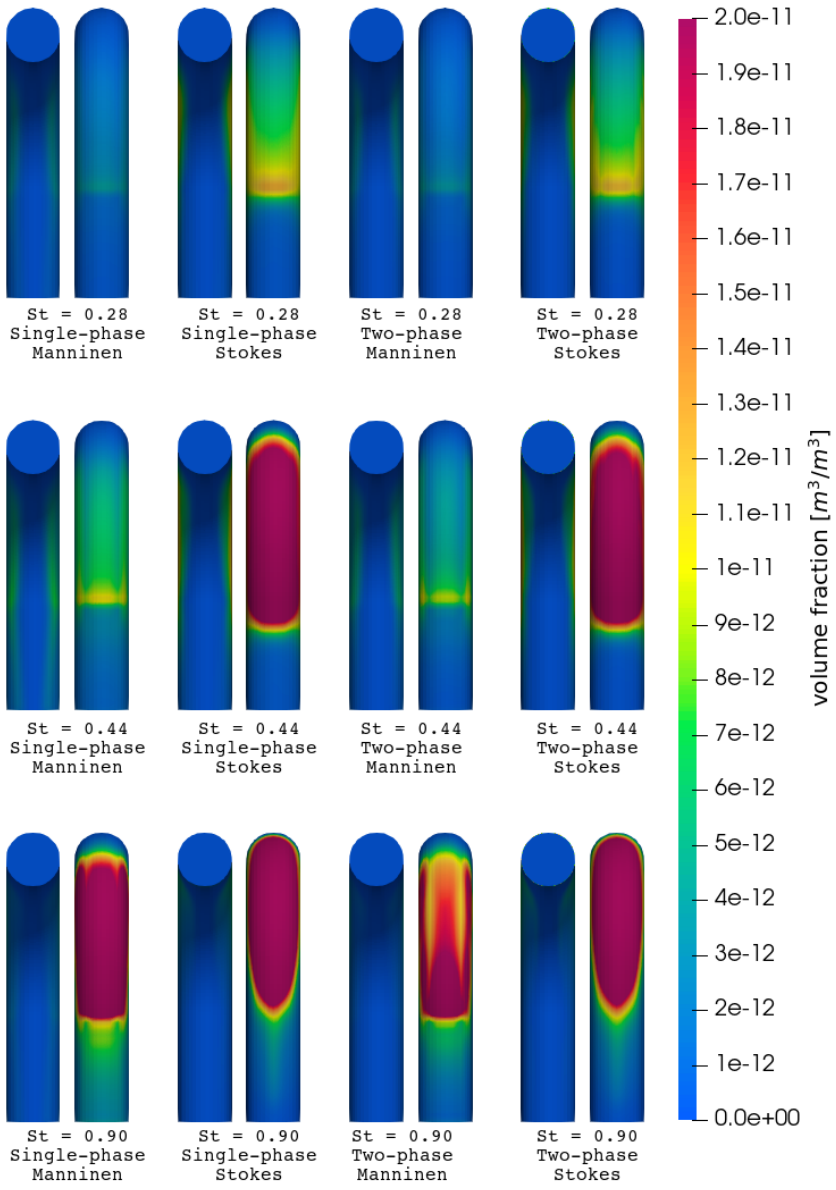

Figure 4.8.: Aerosol distribution on the pipe walls due to deposition for three different Stokes numbers and using different drift velocity models and phase approaches.

the whole simulation. This additional computational power requirement for the Stokes model is huge and cannot justify the additional accuracy it offers. Therefore, for large-scale simulations, it may be more practical to use the Manninen model to reduce computational overhead.

4.3.5. Discussion

This section validated the inertia effect component of both Manninen and Stokes drift velocity models using a bent pipe deposition simulation, employing both single-phase and two-phase approaches. A grid sensitivity study was initially performed to quantify the influence of the mesh refinement on the results, leading to the selection of an optimum mesh with around 56,000 elements for the validation study. The simulations indicated that both models were able to predict the deposition efficiency with reasonable accuracy, with the Stokes model performing better than the Manninen model at all Stokes number ranges. Also, it was found that the Manninen model is sensitive to the phase approach used. However, the comparison of computational costs revealed

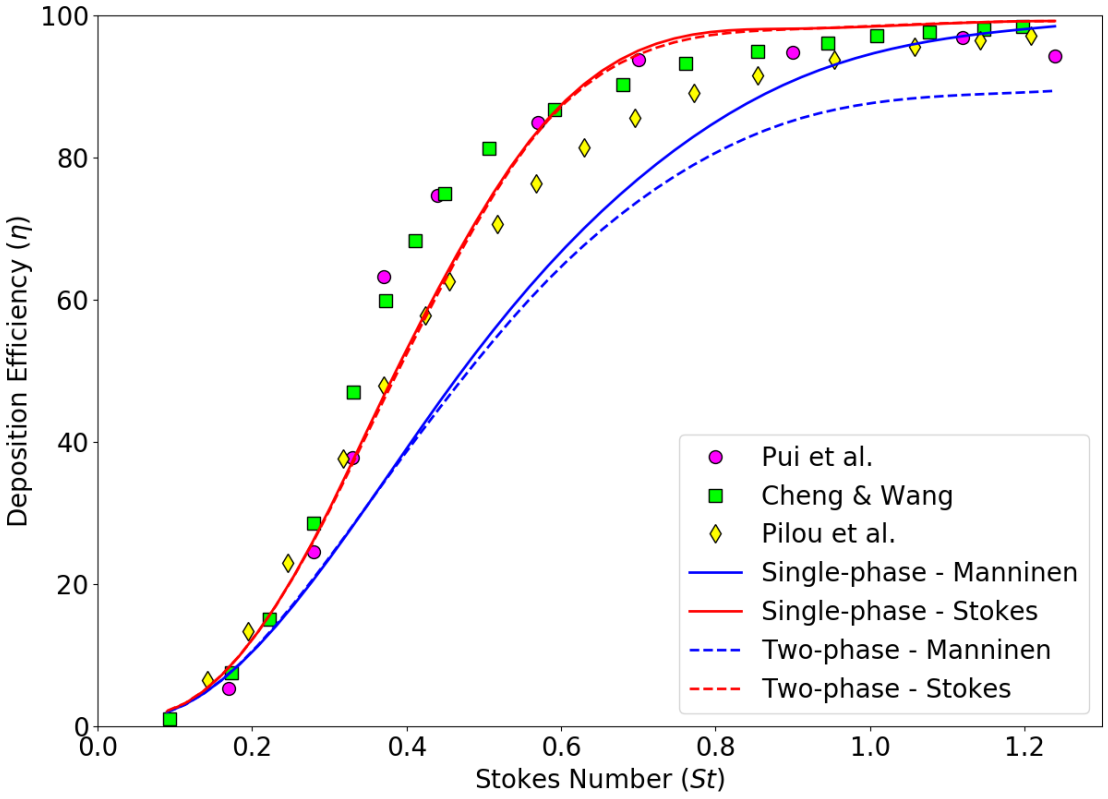

Figure 4.9.: Inertial deposition efficiency vs. Stokes number: Experimental [Pui et al., 1987], analytical [Cheng & Wang, 1981], and numerical [Pilou et al., 2011] benchmarks vs. current simulations using single-phase and two-phase approaches with Manninen and Stokes drift velocity models

that the Stokes model is 3 times more expensive than the Manninen model and cannot justify the additional accuracy it provides. Hence, the Manninen model seems to be the best applicable option for technical-scale containment simulations.

4.4. Ventilation chamber

In this section, the validation of the gravitational effect in the drift velocity model is performed by using a ventilation chamber experiment to compare the spatial particle distribution at different inlet velocities. It begins with an overview of the experiment and discusses the parameters of the experiment. This is followed by explaining the computational setup to simulate the experiment. Finally, simulations are conducted using both the Manninen and Stokes drift velocity models, incorporating single-phase and two-phase approaches, and the results are validated against experimental data to assess their accuracy.

4.4.1. Gravitational settling of particles in a ventilation chamber

The ventilation chamber experiment [Chen et al., 2006] was designed to investigate how particles settle and deposit under gravity, as well as to develop and validate models for simulating particle distribution in a ventilated room. The configuration of the experiment is presented in Figure 4.10. It features a rectangular chamber of 0.8 m × 0.4 m × 0.4 m, and is equipped with inlet and outlet ports each measuring 0.04 m × 0.04 m. The inlet is located on the left face with its center at coordinates (0, 0.2, 0.36) and the outlet on the right face with its center at coordinates (0.8, 0.2, 0.04). The experiment utilized hollow glass spheres coated with silver, with an average size of 10 μm, a nominal diameter spanning 2 to 20 μm, and a material density of 1400 kg/m^3. These particles

were introduced at the inlet, and the concentration of the 10 μm particles was measured along the z-axis at 3 different locations (x = 0.2 m, 0.4 m and 0.6 m) on the center plane, as illustrated in Figure 4.10. The measurements were taken for two distinct inlet velocities of 0.225 m/s and 0.45 m/s. For this validation study, the particle normalized concentration at transient time, t = 1800 s, is used for comparison. The normalized concentration is determined from the ratio of the local particle volume fraction to the inlet volume fraction.

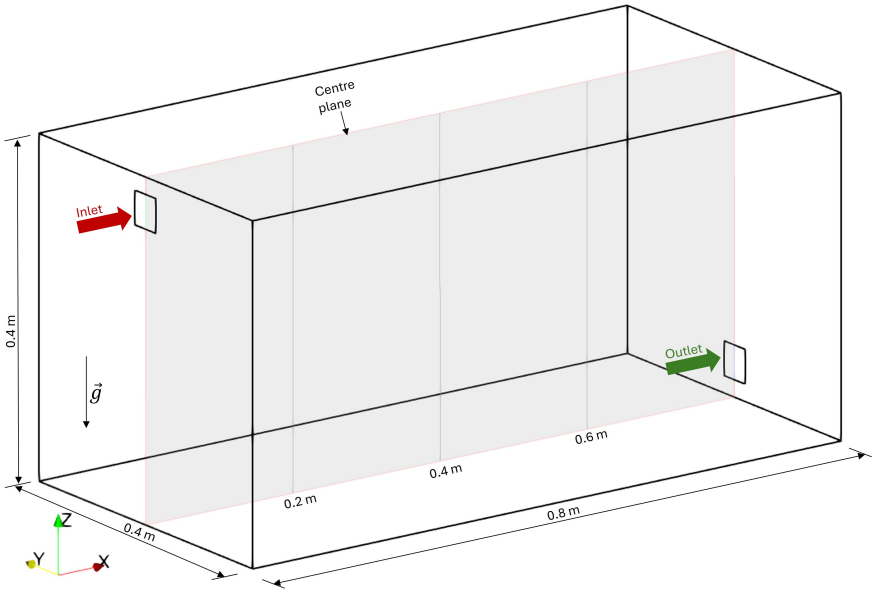

Figure 4.10.: Schematic of the ventilation chamber experiment.

4.4.2. Simulation setup

The simulation of the particle settling and deposition in the ventilation chamber under gravity is conducted by adopting a three-dimensional computational domain of the geometry displayed in Figure 4.10. Due to the simplicity of geometry, the computation mesh consisting of a single block of structured mesh with uniformly sized elements is generated. Initially, a grid sensitivity study is performed with three sets of grids, coarse ($40 \times 20 \times 20$) , medium ($80 \times 40 \times 40$) and fine($160 \times 80 \times 80$). The sensitivity studies revealed negligible discrepancies in integral deposition rate (< 1 %) between the medium and fine mesh, justifying the use of the medium grid for further validation. The simulations are conducted using both inlet velocities (0.225 m/s and 0.45 m/s), including both Manninen and Stokes drift velocity models and employing both single-phase and two-phase approaches. The walls are treated to be adiabatic and are applied with the drift velocity deposition boundary condition (Sec.3.1.2.1) to facilitate particle deposition. The inlet aerosol injection volume fraction is set at $\alpha_l = 10^{-12}$ to minimize the particle influence on the primary flow, consistent with the experiment. The flow is treated as turbulent using the $k-\omega$ SST model. Since the focus is solely on the distribution of 10 μm particles, a mono-disperse simulation method is employed. A time-step size of 1×10^{-2} is selected for all simulations to maintain Courant numbers below 1. In this study also, the surface film approach is not incorporated in the two-phase approach, as the mixture-VOF model is sufficient to model the required phenomenon.

4.4.3. Validation results

The main validation study includes a total of eight simulations, resulting from the combination of two inlet velocities, two drift velocity models, and two phase approaches. The particle normalized concentration profiles at 1800 s are evaluated against experimental data and displayed in Figure 4.11. It is evident that the model predicts normalized particle concentrations with over

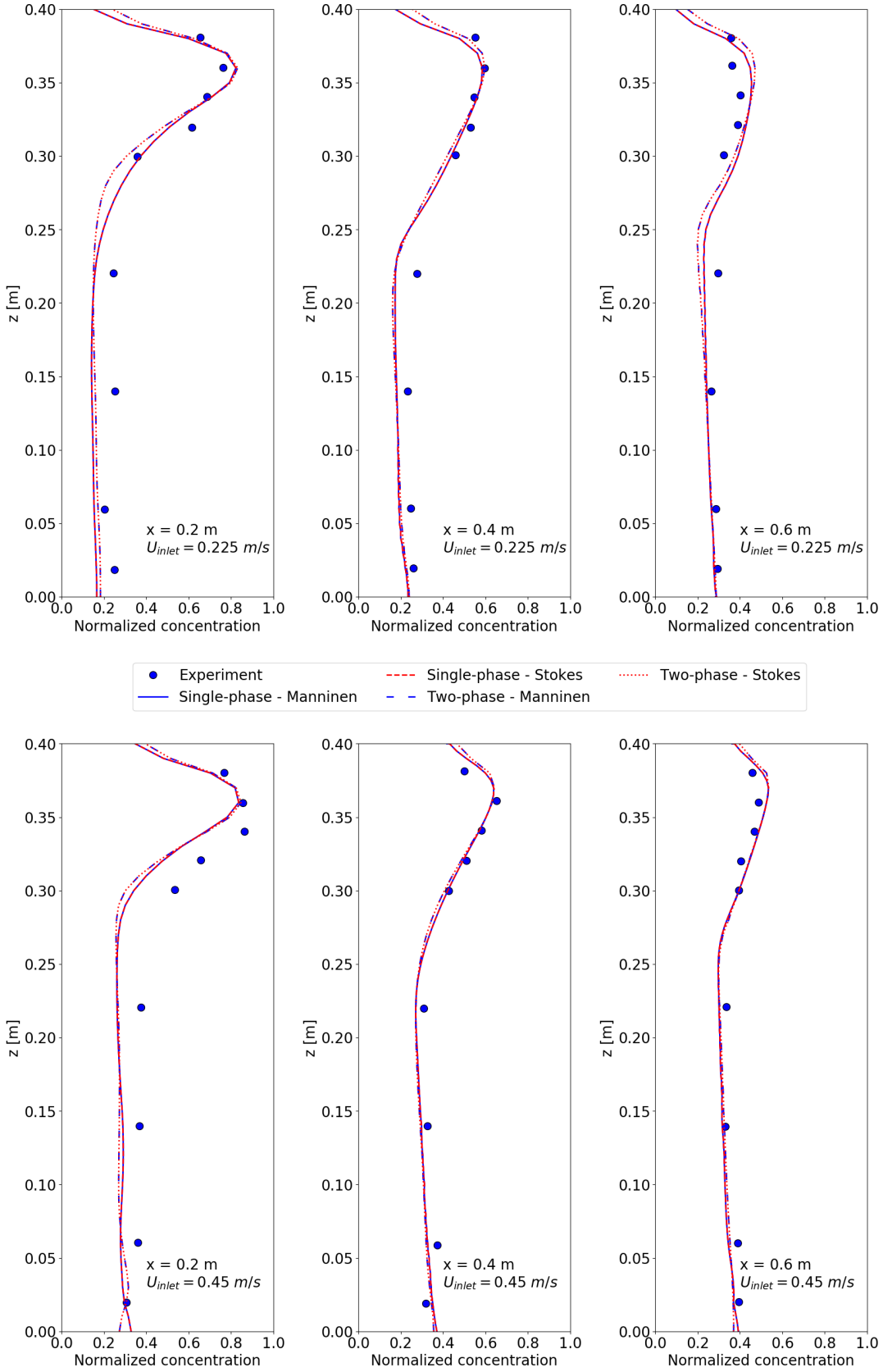

Figure 4.11.: Comparison of experimental and predicted normalized concentrations of 10 μm particles at three distinct locations at t = 1800 s for two different inlet velocities, two drift velocity models and two phase approaches.

90 % accuracy across all measured positions and inlet velocities. The maximum deviations with experimental results appear near the inlet region (x = 0.2 m), attributable to the simplification of the inlet for simulation. In the experiment, the inlet consists of a long square channel that allows flow to be developed before reaching the chamber, which is not considered in the simulations. The Manninen and Stokes model exhibits nearly identical profiles for both single-phase and two-phase approaches, indicating that the simple and computationally efficient Manninen model is enough to capture the gravitational transport of the particles. There is only a marginal difference (< 1 %) between the single-phase and two-phase approaches, which can be attributed to the differences in the modeling methods.

To illustrate the influence of gravity on particle settling more effectively, two additional simulations are conducted at both inlet velocities using the two-phase approach by excluding the gravitational effect in the Manninen drift velocity model. The comparison of normalized particle concentration distribution at the center plane from these simulations with the gravity included model is shown in Figure 4.12.

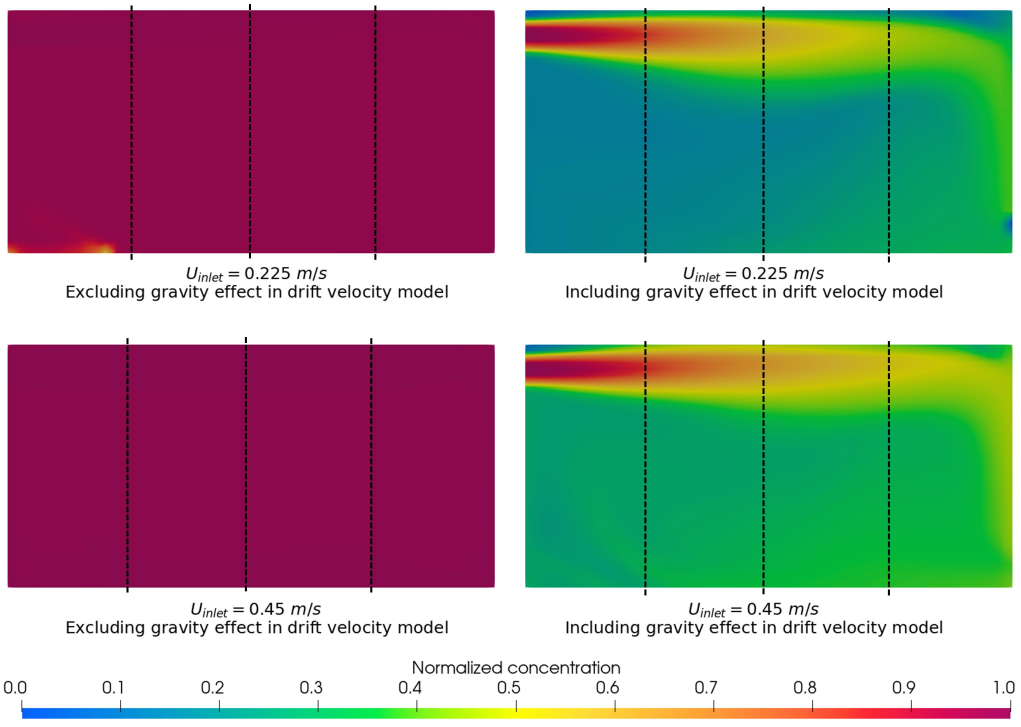

Figure 4.12.: Comparison of normalized concentrations of 10 μm particles at the center plane for two different inlet velocities at t = 1800 s, excluding and including gravity effect, using Manninen drift velocity model and two-phase approach.

It demonstrates the significant impact of gravity on the particle distribution. The exclusion of gravity results in a nearly uniform concentration for both low and high inlet velocities. However, when the gravitational effect is included, particles are deflected from the main flow, descend to the bottom of the chamber, and deposit. This effect is more pronounced at lower inlet velocities, as the weaker primary flow exerts less resistance to gravitational settling. At higher inlet velocities, the gas velocities in the chamber are higher and can dominate over the gravitational drift velocity and result in better mixing. The inertia part in the drift velocity model was active in these simulations. However, its impact is minimal because of the low flow velocities, which lead to reduced accelerations when the flow direction changes. The inertial forces in this case are insufficient to cause the particles to deviate from the primary flow and deposit.

4.4.4. Discussion

In this section, the validation of the gravitational component of both Manninen and Stokes drift velocity models was performed using a ventilation chamber particle settling simulation, employing both single-phase and two-phase approaches. The simulations demonstrated that the drift velocity models were able to predict particle transport and distribution under the effect of gravity with good accuracy. Moreover, it was found that the Manninen and Stokes models produced nearly identical results, suggesting that the computationally efficient Manninen model is the best option for large-scale containment simulations. Additionally, the deviations between the single-phase and two-phase approaches were marginal.

4.5. PBM analytical verification studies

This section features the verification of the Population Balance Model (PBM) droplet evolution models like coalescence and growth against analytical data. It starts by discussing the analytical study on cloud droplet coalescence and the correlations to determine the number density distribution variation with time t. Then, the simulation setup to verify the models is explained and finally, the simulation data is compared with the analytical solution.

4.5.1. Analytical studies of droplet coalescence and growth

Scott, 1968 performed an analytical study on cloud droplet coalescence to calculate the droplet size distribution at any time, given an initial distribution. He explored three different coalescence kernels to compute the coalescence rate between groups i and j:

- Constant kernel: $C_{ij} = c$ - Constant probability.
- Sum kernel: $C_{ij} = b(x_i + x_j)$ - Proportional to the sum of the droplet volumes.
- Product kernel: $C_{ij} = ax_ix_j$ - Proportional to the product of the droplet volumes.

Analytical relations on how the number density distribution will evolve over time were provided for all three kernels. The number density function (n_v) is defined as the number of droplets per unit volume having representative volume (x_i) and can be computed as:

$$n_v = \frac{\alpha_{li}}{x_i(x_{i+1} - x_i)} \tag{4.5}$$

where α_{li} represents the volume fraction of droplet size group within a cell.

The initial density function (at t = 0) for all cases is given by:

$$n(x_i, 0) = \frac{N_0}{x_0}\left(\frac{x_i}{x_0}\right)e^{-\frac{x_i}{x_0}} \tag{4.6}$$

The constant values used in the above equations for this verification study are listed in Table 4.8.

Table 4.8.: Parameters for the analytical coalescence kernels and initial distribution functions.

Parameter	c $[m^3/s]$	b $[s^{-1}]$	a $[\ m^{-3}s^{-1}]$	N_0 $[m^{-3}]$	x_0 $[m^3]$
Value	1.0	1.0	1.0	2.5	0.01

For the growth model verification, a constant growth kernel ($G^+ = 1\ kgm^3/s$) was utilized, whose density distribution can be directly calculated without any special analytical function. This simplification arises because the constant growth rate merely results in a uniform shift of the initial density function along the size axis, proportional to the growth rate. This straightforward behavior enables easy comparison between analytical data and simulation results.

4.5.2. Simulation setup

The computational domain for this verification study requires only a single element (1 m × 1 m × 1 m) as we are interested only in the droplet evolution by the coalescence kernels discussed above. The parameters affecting the coalescence rate are only the representative volumes of the corresponding groups. The effects of turbulent flow and thermodynamic properties are not a part of this model, and hence, the simulations are performed in stagnant laminar flow. Symmetry boundary conditions are applied to all fields and boundaries. The time-step size for all simulations is set at 0.2 s, based on time sensitivity studies. For the coalescence verification simulations, 71 droplet size groups in logarithmic series ranging from 2.65×10^{-2} m to 4.83 m are used. For the growth model verification simulations, 28 droplet size groups in arithmetic series ranging from 1 m to 3.058 m are utilized. The simulations are performed employing both single-phase and two-phase approaches.

4.5.3. Verification results

The two-phase and single-phase results are challenging to distinguish for this verification study, as the flow is stagnant and the PBM implementation is comparable in both approaches. Hence, the simulation results shown here are based on the single-phase approach. The simulated number density distributions of the coalescence cases at different times compared with the analytical solution are illustrated in Figures. 4.13 - 4.15.

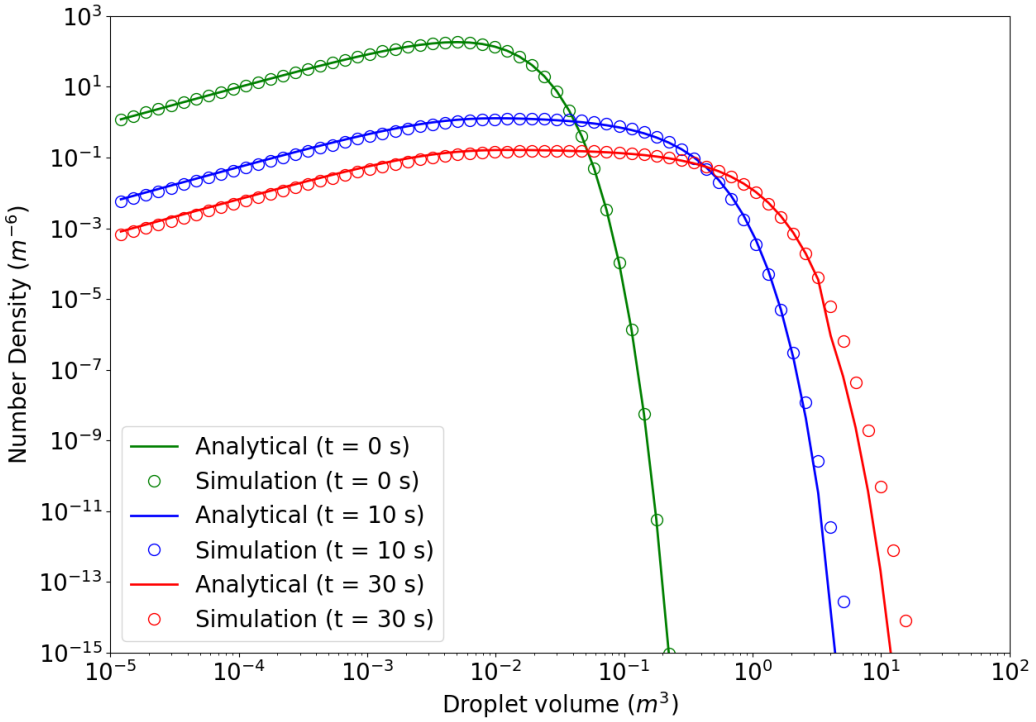

Figure 4.13.: Comparison of analytical and simulation number density for different droplet sizes at different times with constant coalescence model.

It can be observed that the model reproduced the distribution pattern very well, with excellent (> 99 %) accuracy for the high number density droplets and with reasonable accuracy (> 90 %) for the low number density droplets. The deviations for the low-concentration droplets also tend to increase with time for all cases. This deviation for the low-density droplets could be due to the numerical errors arising from computations using small numbers. It can also be observed that there is a gradual decrease in the number density of low-volume droplets and an increase in the number

density of high-volume droplets. These findings imply that smaller droplets are coming together and evolving into larger droplets.

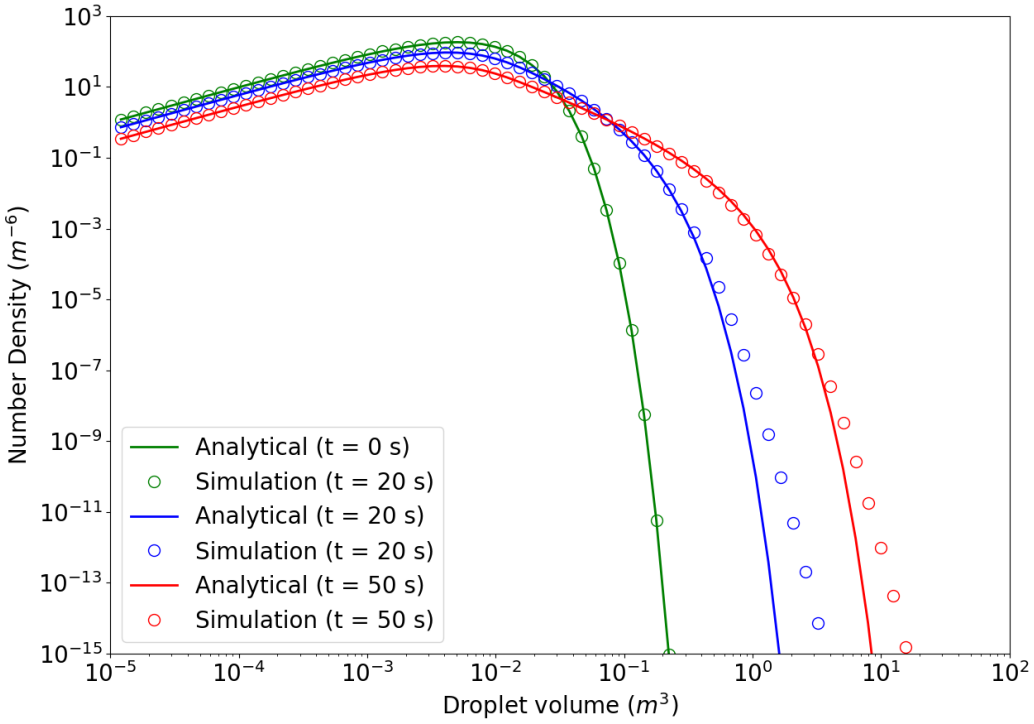

Figure 4.14.: Comparison of analytical and simulation number density for different droplet sizes at different times with sum coalescence model.

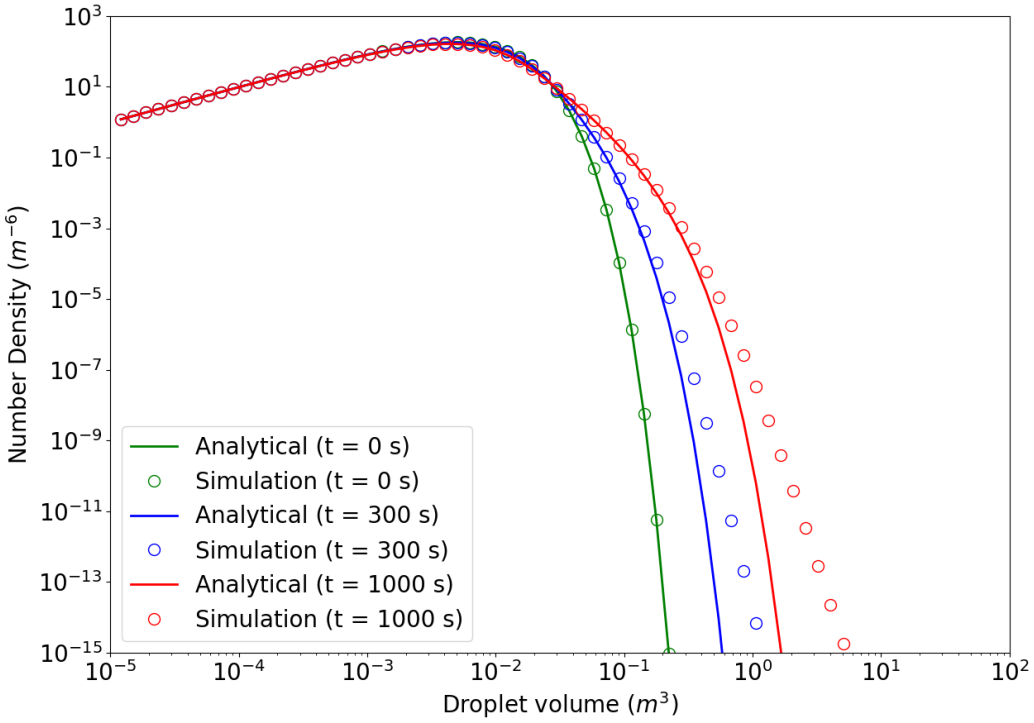

Figure 4.15.: Comparison of analytical and simulation number density for different droplet sizes at different times with product coalescence model.

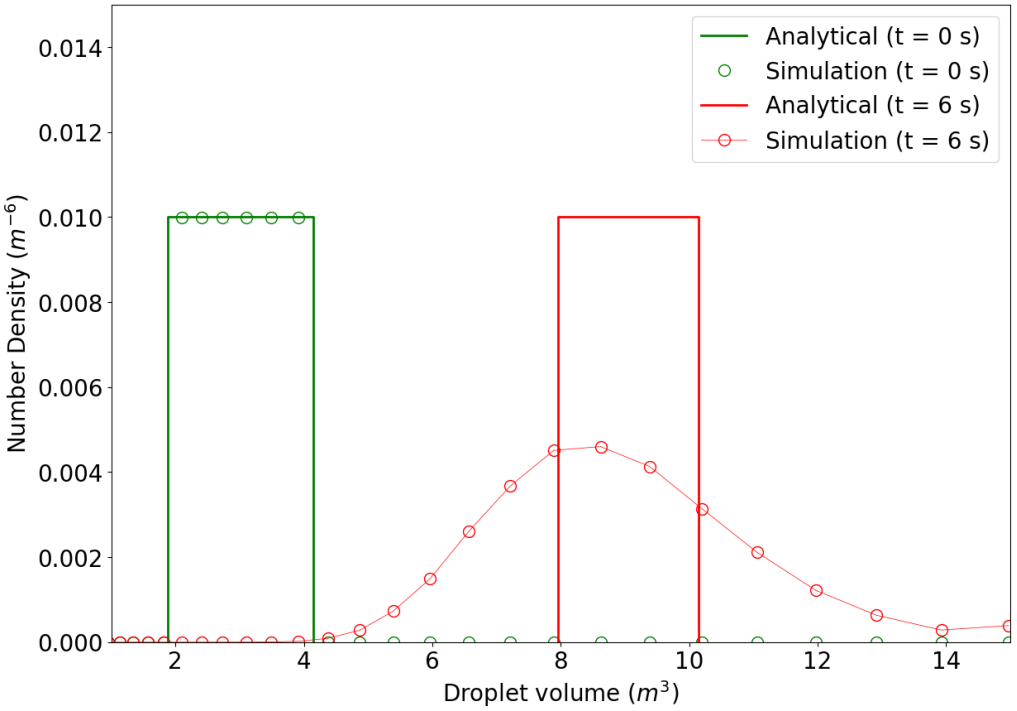

Figure 4.16.: Comparison of analytical and simulation number density for different droplet sizes at different times with constant growth model.

In the case of constant growth simulation (Figure 4.16), the model was unable to accurately reproduce the distribution. This is due to the inherent flaw in the sectional PBM approach where fixed representative droplet sizes are used. The exact nature of the droplet growth can only be predicted by using a moving pivot technique [Kumar & Ramkrishna, 1996b], whose implementation is complex and beyond the scope of this thesis. Nevertheless, the model is able to conserve the number of droplets and predict the peak density location in droplet volume.

4.5.4. Discussion

This section presented the analytical verification of the coalescence and growth droplet evolution models. Although the modeled evolution rates used for this study do not represent realistic conditions, it demonstrated that the numerical implementation of the model in the PBM framework is effective in predicting the corresponding phenomena. Moreover, the results were identical for both single-phase and two-phase approaches, confirming their consistent implementation, although not illustrated explicitly. The coalescence simulations showed good model accuracy, while the growth simulations exhibited higher but acceptable error, which can be attributed to the method of classes fixed-pivot approach. Both coalescence and growth models indicated a reduction in the number density of low-volume droplets and an increase in the number density of high-volume droplets. This implies that the PBM droplet evolution implementation is effective and can be used for predicting the fog droplet coalescence by collisions and condensation growth (evaporation shrink).

4.6. Falling film

This section presents the validation of the surface film model through a comparison of the mean film thickness for a thin water film flowing down an inclined plate with and without counter-current flow. It begins with an overview of the experimental setup, detailing the measured quantities and parameters of the experiment. Following this, the computational domain is defined, and mesh parameters and boundary conditions are discussed. Lastly, the simulated film thickness is evaluated against experimental measurements to assess the surface film model's performance.

4.6.1. Thin water film flow down an inclined plate

The behavior of a thin water film flowing down a flat inclined plate, both in the presence and absence of counter-current airflow, was studied experimentally by Roy & Jain, 1959. The configuration of the test section channel is presented in Figure 4.17. The channel is 381 mm long, 190 m wide, and 15.9 mm thick. The water film (red color) flows in the positive x-direction, and the counter-current airflows in the negative x-direction. The test section can be inclined at three different angles of 40^o, 50^o and 61^o degrees to the horizontal so that the film flows downwards. For this validation study, only the 40^o inclination angle is considered because this experimental data was readily available, and the list of film and airflow rates is summarized in the Table 4.9. The measured quantity is the mean film thickness for different film and airflow rates. The experiments were performed for five different film flow rates with four different counter-current air flows for each film flow, leading to a total of 20 data points. The experiments used distilled water at room temperature of 23 ^oC and thermophysical properties are calculated at this temperature.

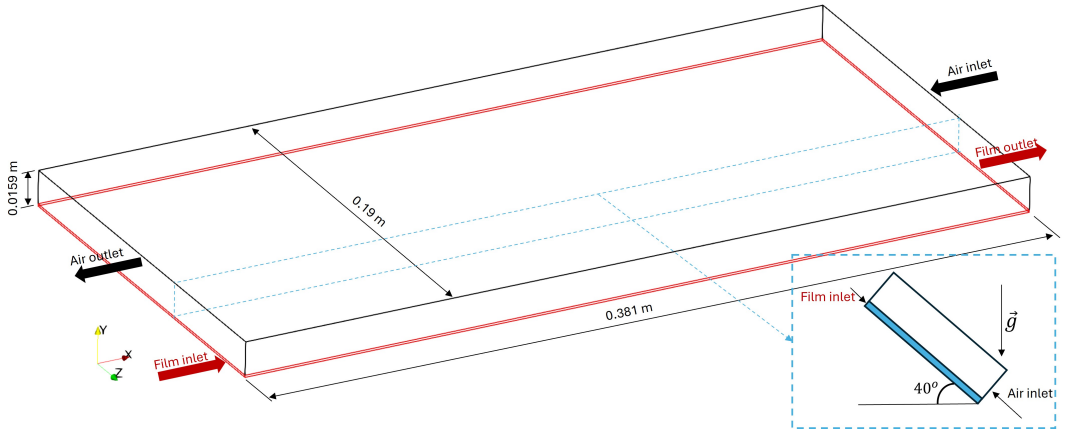

Figure 4.17.: Schematic of the test section of the falling film experiment with counter-current air flow.

Table 4.9.: Film and air volumetric flow rates and their corresponding Reynolds numbers.

No.	Film flow rate $[m^3/s]$	Film Reynolds number (Re_L)	Air flow rate $[m^3/s]$	Air Reynolds number (Re_G)
1	3.78×10^{-5}	218	0	0
2	5.05×10^{-5}	290	6.29×10^{-3}	2165
3	6.31×10^{-5}	363	8.65×10^{-3}	2975
4	7.25×10^{-5}	417	9.85×10^{-3}	3470
5	8.2×10^{-5}	472	-	-

4.6.2. Simulation setup

The simulation of the falling film behavior down the inclined plate with and without the influence of the counter airflow is performed by adopting a multi-region three-dimensional computational domain from the geometry in Figure 4.17. The primary region is the airflow domain, having dimensions of the test section channel, with an inlet on the right side and an outlet on the left side. The secondary region is the surface film region having the same length and width as the primary region but small thickness in the z-direction. For the film region, the inlet is on the left side and the outlet is on the right side. For the simulations, a thickness of 1mm is used, and this choice

does not have any impact on the results because of the two-dimensional nature of the surface film model. The simulations are initially performed for the base case ($Re_L = 218$ and $Re_G = 0$) with two different grids: coarse ($50 \times 10 \times 20$) and fine ($100 \times 20 \times 40$). The mean film thickness deviations were less than 5 % between both meshes, and hence, the coarse mesh is used for further studies. The gravity vector is defined by computing the x and y components for the inclination of 40^o. All boundaries other than inlets and outlets are treated as walls, and adiabatic temperature and no slip velocity boundary conditions are specified on these walls. The simulations are performed using the two-phase approach only, as the surface film model is incorporated only into this approach. The primary region is free of any droplets as the main flow is in the film region; hence, the drift velocity model is also neglected. The inlet film thickness is taken from the experiment with no airflow, and the corresponding inlet velocity is calculated using Nusselt theory [Nusselt, 1916]. A fixed time step size of $\Delta t = 10^{-2}$ is used for all simulations to ensure stability. The airflow is treated as turbulent and is simulated employing the $k - \omega$ SST model.

4.6.3. Validation results

The validation study comprised a total of 20 simulations, arising from the combination of five film and four gas flow Reynolds numbers. The simulations are run until steady-state, which occurs after 5 seconds for all cases. The comparison of simulated film thickness distribution over the plate surface for all simulations after attaining steady-state is presented in Figure 4.18.

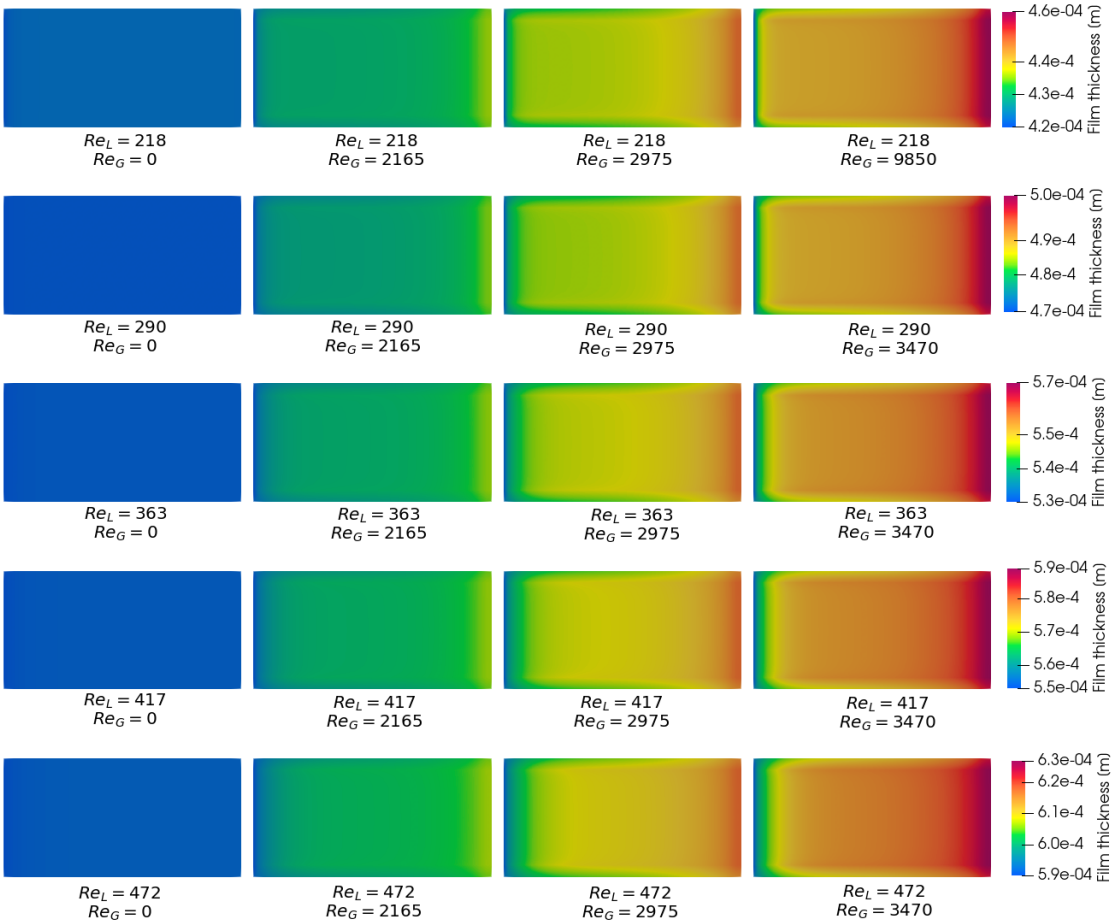

Figure 4.18.: The film thickness distribution over the plate surface for different film and gas flow Reynolds numbers with plate inclination = 40^o (film inlet-left, air inlet-right) in steady-state.

It can be observed that film flow along the surface is smooth and nearly uniform without the counter-airflow for all film Reynolds numbers. The increased counter-current airflow leads to the

thickening of the film layer and results in non-uniform film thickness on the plate surface. For the largest airflow rate (Re_G = 9850), the maximum film thickness is around 0.04 mm greater than that of the base flow (Re_G = 0). This trend is consistent for all film flow Reynolds numbers. The mean film thickness from all simulations is evaluated and compared with the experimental data [Roy & Jain, 1959] in Figure 4.19.

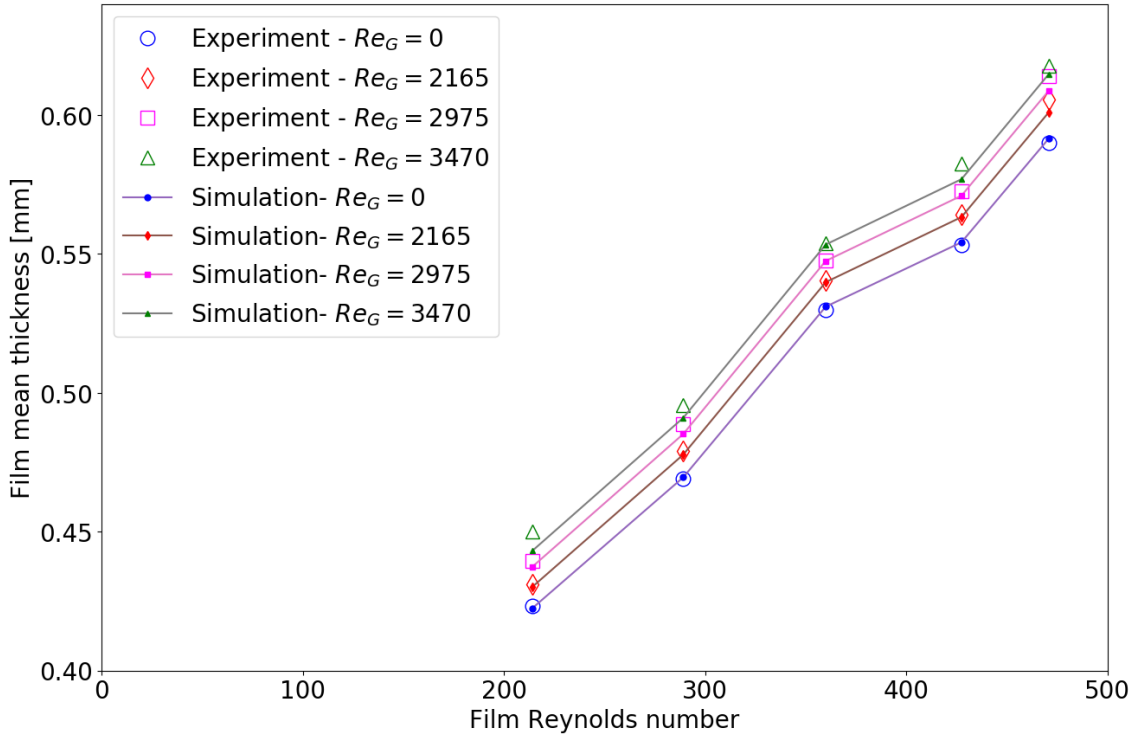

Figure 4.19.: Comparison of the mean film thickness between experiment and simulations for all film and gas flow Reynolds numbers with plate inclination = 40^o.

The simulations demonstrate excellent accuracy (> 90%) with respect to the measured values, and the model was able to predict the relative thickening of the film resulting from the counter-current airflow. This validation study is an excellent illustration of the modeling interaction between the film region flow and the mixture-VOF region flow, leading to the thickening of the film caused by shear force exerted by the counter airflow.

4.6.4. Discussion

This section discussed the validation of the surface film model by simulating a thin film flow behavior over a flat plate with and without counter-current airflow. The results indicated that the model effectively captured the relative thickening of the film with the increase in the airflow rates. Furthermore, comparing the mean film thickness experimental measurements revealed that the two-phase surface film model coupled with the mixture-VOF model accurately predicted the thickness values. Therefore, the film model is a good addition to the two-phase framework and can be utilized to predict the thin film flow over containment structures and surfaces.

4.7. Water accumulation

The verification of the film-to-liquid phase mass transfer model is performed in this section by performing a simulation in which a thin film flows along the vertical walls of a closed cubical vessel. The idea is introduced first, and then the computational domain and simulation parameters are presented. Subsequently, the conversion of film to VOF is investigated to see whether the mass of film injected is conserved and forms a gas-liquid interface.

4.7.1. Introduction and simulation setup

During loss of coolant accidents in reactors, the steam condenses on the structures by wall condensation and results in the formation of a film, which grows and flows towards the sump region. This results in the accumulation of the condensate in the compartment sump, which cannot be modeled using a single-phase approach. The two-phase approach presented in this work should be able to capture this film to gas-liquid interface formation. This is investigated using a hypothetical closed cubical vessel of size 0.45 m × 0.45 m × 0.45 m, which is presented in Figure 4.20.

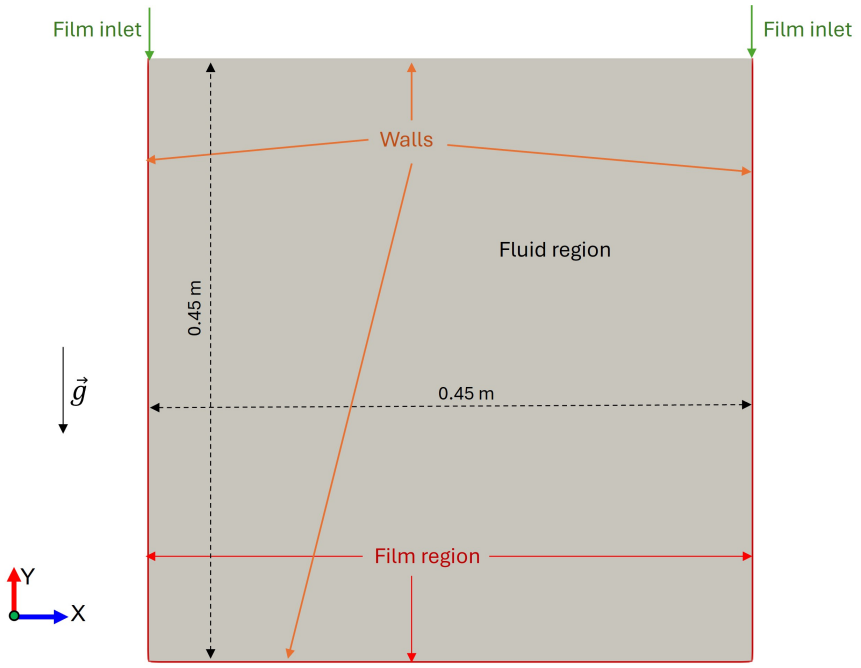

Figure 4.20.: Schematic of the hypothetical test vessel with film falling along the walls.

The computational setup is reduced to a two-dimensional domain consisting of two regions: the fluid region and the film region. The film region is added only on three walls of the fluid domain: two vertical and one bottom. The film is injected through two inlets at a velocity of 1 m/s and a film thickness of 0.1 mm. A mesh sensitivity study is initially performed with two grids: coarse (45 × 45) and fine (90 × 90). The discrepancy in the water-liquid interface position between the two meshes was less than 5 %, so the coarse mesh is selected for further analysis. The simulations are conducted with the two-phase approach employing the mixture-VOF-film method. The drift velocity model is neglected in this study as there are no dispersed droplets in the fluid region and the primary focus is on the film. A time step-size of 10^{-2} seconds is used, and the gas flow is assumed to be laminar.

4.7.2. Results

The simulation is performed for a transient time of 500 seconds, which is sufficient to demonstrate the conversion of film to gas-liquid interface in the VOF framework. Figure 4.21 demonstrates the gradual formation of a gas-liquid interface in the simulations. During the initial stages, the film has to reach the bottom wall to get converted to VOF liquid. As time progresses, the liquid starts filling up the vessel, and the interface moves upwards. At this stage, the film on the vertical walls close to the interface starts to join the liquid phase, and the film no longer flows to the bottom of the vessel. The location of mass transfer keeps moving upwards as the vessel starts filling up, as indicated in the Figure 4.21. To perform a quantitative analysis, the mass of film injected during

its entire transient is compared with the water mass in the VOF domain. The net film mass injected into the domain during 500 seconds can be calculated as:

$$\begin{aligned} m_{film} &= \delta_{film,in} w \rho_{film} \Delta t \\ &= 10^{-4} \times 0.45 \times 994.5 \times 500 \\ &= 44.75\,\text{kg} \end{aligned} \tag{4.7}$$

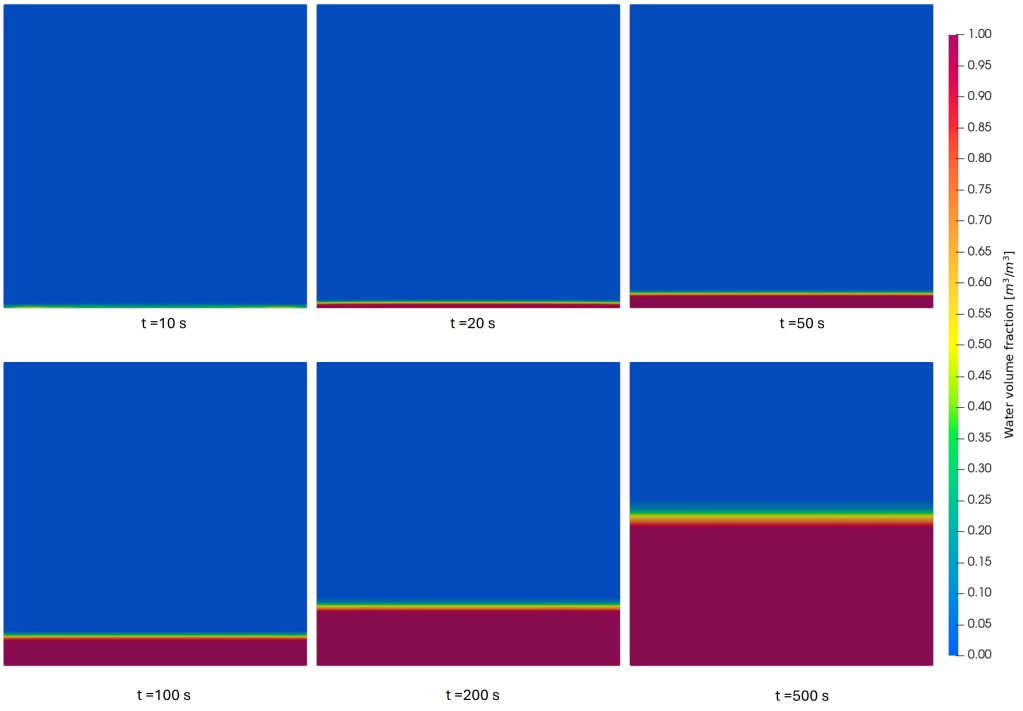

Figure 4.21.: The accumulation of water in the sump of a vessel by conversion of film to VOF liquid-phase.

The simulation results at the 500-seconds revealed a net accumulated liquid mass of 44.64 kg and a film mass of 0.11 kg, which is still wetting the vertical walls. The sum of these values closely (99.7 %) matches the injected mass, demonstrating that the film-liquid phase mass transfer model is mass conservative and can be effectively used.

4.7.3. Discussion

This section demonstrated the verification of the film-liquid phase mass transfer model by performing a simulation with film flow along the wall of a closed vessel, which gets converted to VOF liquid phase. This conversion occurs at the bottom, where the film is thick enough to form a gas-liquid interface. The model demonstrated the ability to simulate these phenomena and ensured mass was conserved. These findings suggest that the model is well-suited for two-phase containment simulations, particularly in scenarios where wall condensate films accumulate within containment compartments.

4.8. SETCOM

This section focuses on the validation of the wall condensation model using the SETCOM experiment and investigates the influence of bulk condensation on the wall condensation. It begins by

outlining the experimental conditions and parameters chosen for the validation simulations. Next, the computation domain, simulation setup, and mesh details are presented. Finally, the simulations are conducted using both single-phase and two-phase approaches, and a comparative analysis is performed by disregarding and considering bulk condensation to understand its impact.

4.8.1. The SETCOM experiment

The SETCOM (Separate Effects Tests for Condensation Modeling) facility at Forschungszentrum Jülich is utilized to generate benchmark data for the validation of condensation modeling approaches. The test section (Figure 2.2) features a 6 m long channel having a cross-section of 0.44 m × 0.44 m with the bottom wall cooled to induce wall condensation, while the other three walls are insulated to prevent any heat loss. The entire facility can be oriented at different angles between horizontal and vertical to assess different flow regimes. In an earlier work [Vijaya Kumar et al., 2021], the SETCOM experiment was employed to benchmark containmentFOAM's the single-phase wall condensation model, which utilized wall-based mass sinks for condensate removal while neglecting fog formation near condensing surfaces. Vijaya Kumar et al., 2021 conducted wall condensation simulations with varying mesh densities, comparing a fine grid ($y^+ \approx 1$) against a coarse grid ($y^+ \approx 75$). Their findings indicated that while the fine mesh calculations consistently matched experimental results throughout the domain, the coarse mesh approximations showed notable inaccuracies in the initial flow development zone ($x < 1m$). From the comprehensive SETCOM database of 81 experiments ranging from low to high condensation rates, a number of experiments with vertical steam-air mixture flow were selected to examine the influence of fog formation and phase approach. For the sake of brevity, only a single characteristic experiment with a high condensation rate is discussed. The boundary conditions of the selected experiment, in which the facility is vertical, are summarized in Table: 4.10. The distribution of total wall heat flux along the plate surface is used as the primary metric for evaluating the agreement between experimental and simulation results.

Table 4.10.: Parameters of the specific SETCOM experiment for validation simulation.

Parameter	Inlet velocity $[m/s]$	Inlet temperature $[^oC]$	Inlet steam volume fraction $[\%]$	Coolant temperature $[^oC]$
Value	4.2	80	30	10

4.8.2. Simulation Setup

The SETCOM simulations are performed on a simplified two-dimensional multi-region computational domain as shown in Figure 4.22.

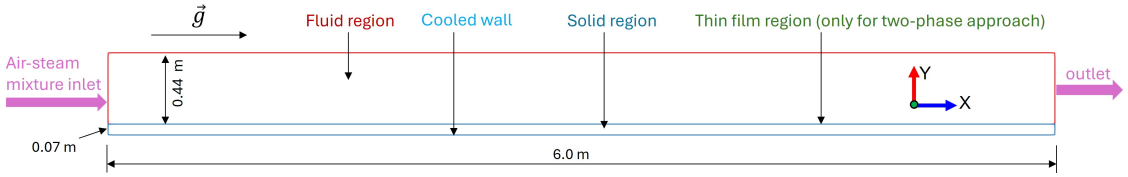

Figure 4.22.: Schematic of the SETCOM test channel: multi-region 2D computational domain

In the fluid region, the air-steam mixture flow occurs. The solid region represents the condensing wall, on which the heat conduction equation is solved to determine the spatial distribution of temperature resulting from the bottom wall cooling. The temperature coupling of the interface between the regions is modeled using the conjugate heat transfer (CHT) boundary condition explained in Sec.2.4.7. The single-phase simulations do not involve water film formation and transport at the

interface due to the mass sink approach utilized by the wall condensation model. However, the two-phase simulation leads to the generation of the film by wall condensation and deposition of fog droplets. Hence, it is essential for the two-phase approach to employ the surface film model to predict the condensate flow along the wall. This requires an additional thin film region in the computational domain, which is added at the fluid-solid interface. The coupling of temperature between the film-solid and film-fluid interfaces is done using the CHT boundary condition by adding the effect of the coverage factor also into it. To investigate the effect of grid refinement, especially near the condensing wall, the simulations are performed on four different meshes with y^+ of approximately 1, 25, 45, and 75. The fluid region comprises 20,000 elements, the solid region contains 3,500 elements, and the film region consists of 270 elements. The gas flow is turbulent and is modeled using the $k-\omega$ SST model, and wall functions were applied to the coarse meshes. The Manninen drift velocity model combined with the population balance approach, employing eight droplet size groups ranging from 1 μm to 128 μm is used to model fog transport and evolution. The simulations are conducted both with and without bulk condensation to isolate the influence of bulk condensation. A fixed time step size of $\Delta t = 10^{-3}$ s (CFL < 10) is used for all simulations to ensure computational stability. The simulations are run until steady-state is achieved and the total wall heat flux is compared with the experimental values.

4.8.3. Results

The validation study consisted of a total of 8 simulations, arising from 4 meshes, single-phase and two-phase approaches, and inclusion and exclusion of bulk condensation model. The comparison of the total wall heat fluxes between these simulations is illustrated in Figure 4.23. It can be observed that the models can predict the total wall heat fluxes with reasonable accuracy (> 90 %) for all cases. The simulations with $y^+ \approx 1$ demonstrated the least difference between the two-phase and single-phase approaches. This is attributed to the similar predictions of the condensation rate by both approaches, which can be interpreted from Table: 4.11.

Table 4.11.: Comparison of integral wall, bulk and total condensation rates for different y^+ meshes, with and without bulk condensation, employing single-phase and two-phase approaches.

		Wall condensation only			Wall + bulk condensation		
	Mesh Refinement	Wall $[g/s]$	Bulk $[g/s]$	Total $[g/s]$	Wall $[g/s]$	Bulk $[g/s]$	Total $[g/s]$
Single-phase	$y^+ \approx 1$	11.933	0	11.933	11.193	0.736	11.929
	$y^+ \approx 25$	11.266	0	11.266	11.070	0.142	11.242
	$y^+ \approx 45$	11.191	0	11.191	11.097	0.081	11.178
	$y^+ \approx 75$	11.356	0	11.356	11.304	0.034	11.338
Two-phase	$y^+ \approx 1$	11.512	0	11.512	11.125	0.868	11.993
	$y^+ \approx 25$	10.352	0	10.352	10.085	0.408	10.493
	$y^+ \approx 45$	10.041	0	10.041	9.815	0.377	10.192
	$y^+ \approx 75$	9.987	0	9.987	9.800	0.330	10.130

The relatively close condensation prediction is due to the good resolution of the near-wall region, providing sufficient resolution of velocity, species, and temperature gradients. The slightly lower

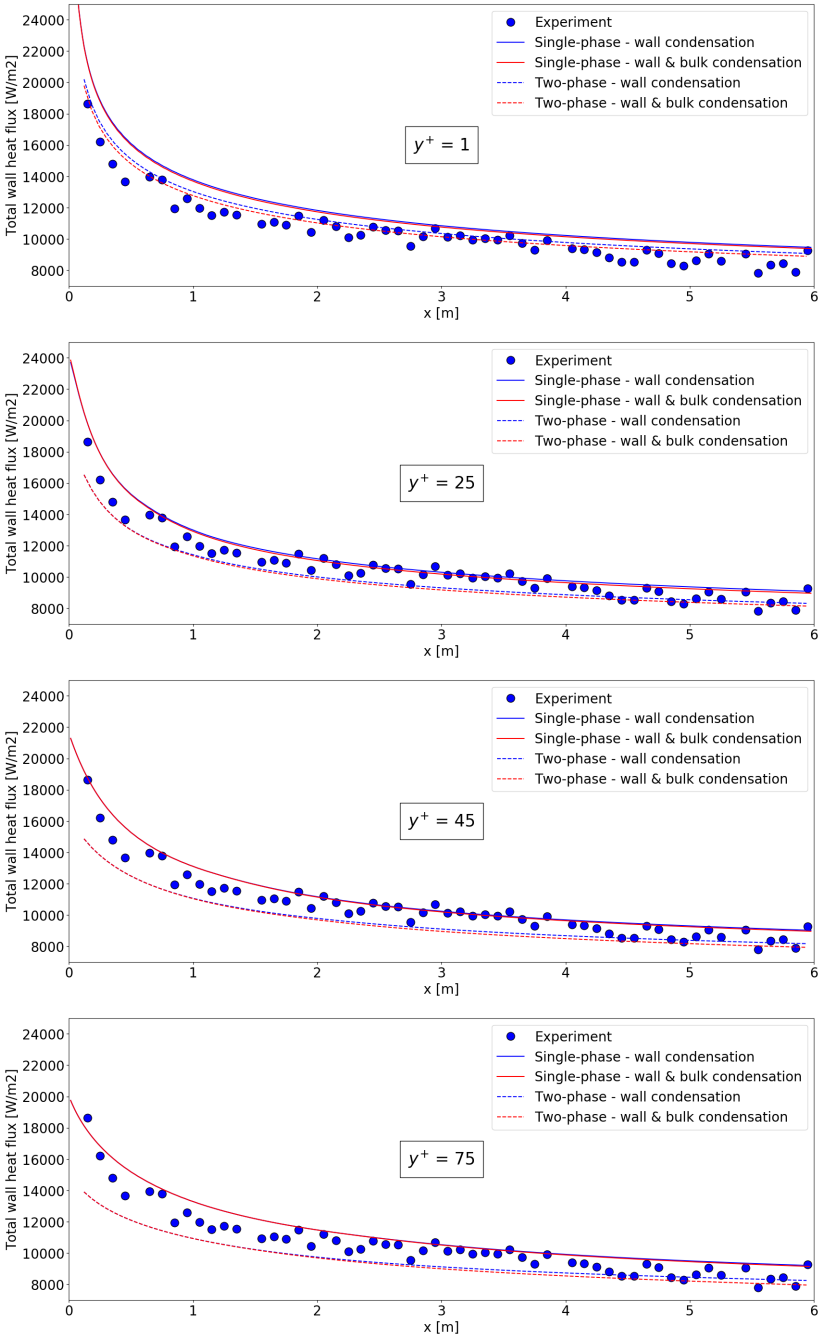

Figure 4.23.: Total wall heat flux profiles along the cooled wall for different y^+ values, comparing cases with and without bulk condensation, and using single-phase and two-phase approaches.

wall heat fluxes (5 %) while using the two-phase approach are related to two factors. Firstly, the single-phase approach considers the effect of suction velocity by using face fluxes instead of volumetric source terms. Secondly, the presence of water droplets or films increases condensation resistance. This effect increases (maximum 15 %) as the near-wall mesh becomes coarser, as illustrated in Figure 4.23. The comparison between inclusion and exclusion of bulk condensation exhibits that the bulk condensation decreased the total wall heat flux by around 2 %, consistently for all meshes. This is caused by the release of latent heat into the fluid during condensation, leading to the increase in local temperatures, affecting the saturation conditions, and thereby, wall condensation. The comparison of integral condensation rates (Table 4.11) shows that the inclusion of bulk condensation model decreases the wall condensation rate consistently for all meshes and

phase approaches. The total condensation rates show contrasting behavior between the single-phase and two-phase approaches. For simulations employing the single-phase method, introducing the bulk condensation model lowers the total condensation rate. However, the two-phase method predicted an increase in total condensation rate with the inclusion of the bulk condensation model. It can be observed that the bulk condensation rates are particularly higher with the two-phase approach. This difference is due to the presence of a water film and fog droplets in the two-phase method, which allows absorption of heat by the high heat capacity water. This leads to the relative cooling of the local fluid in the region with fog and film, prompting further bulk condensation.

The distribution of the condensate film thickness along the plate surface, obtained using the two-phase mixture-VOF-film method is shown in Figure 4.24.

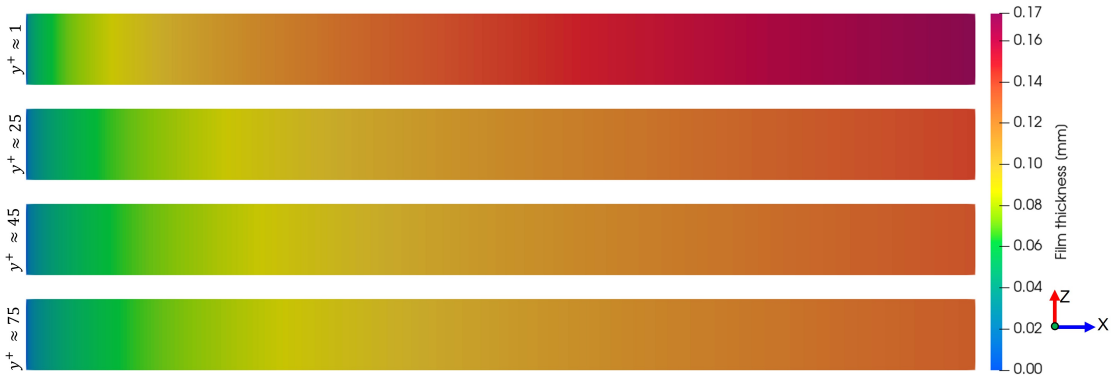

Figure 4.24.: Film thickness distribution on the condensing wall surface for different y^+ meshes for the case with both wall and bulk condensation.

The case with both wall and bulk condensation is considered, and the film thickness deviation with mesh refinement is investigated. The fine mesh revealed a maximum film thickness of around 0.17 mm, located at the exit of the channel. The coarser meshes exhibit a similar trend, with the highest film thickness of around 0.15 mm, resulting from the under-predicted condensation rates in the developing flow section of the plate. This discrepancy represents an error of around 10 %, which needs to be considered when designing meshes for practical applications. These variations in film thickness can be attributed to the differences in the condensation rate on different meshes (Table 4.11). The integral amount of film mass over the channel condensing surface with and without bulk condensation for all meshes is discussed in Table 4.12.

Table 4.12.: Integral film mass calculated from the simulations for different meshes with and without bulk condensation model, using two-phase approach.

Mesh	$y^+ \approx 1$	$y^+ \approx 25$	$y^+ \approx 45$	$y^+ \approx 75$
Integral film mass with wall condensation [g]	338.5	316.9	303.1	295.0
Integral film mass with wall & bulk condensation [g]	325.7	309.6	298.6	292.5

Although the total condensation rate with the two-phase approach is higher when bulk condensation is considered, the integral film mass is lower. This is because most of the fog droplets remain suspended in the gas and leave through the outlet without depositing on the film. This trend is also consistent for mesh refinements.

4.8.4. Discussion

The validation of the wall condensation model using the SETCOM experimental database was performed in this section. The total wall heat fluxes predicted by the model using single-phase and

two-phase approaches showed reasonable accuracy. The influence of bulk condensation was observed to be marginal; nevertheless, the model was able to capture its influence. The single-phase passive scalar approach was unable to include the effect of heat absorption by fog droplets due to its higher heat capacity. However, the two-phase method was capable of incorporating this feature, and its effects were observed. The film model could simulate the condensate film formation, its transport, and thickening. Therefore, both single-phase and two-phase bulk condensation approaches are relevant additions to the existing *containmentFOAM* single-phase wall condensation model and can be utilized for technical-scale containment analysis.

4.9. THAI TH2

This section summarizes the validation of the entire computation model using a technical-scale THAI-TH2 experiment to assess the capability of the *containmentFOAM* in predicting a multi-phenomena interaction problem. The major focus is on investigating the effect of bulk condensation on the events and conditions inside the test vessel by comparing the results with and without bulk condensation. The experiment objective and details about the vessel and its components are discussed first. This is followed by defining the computational domain, mesh, and boundary conditions. A comparative analysis is conducted in three parts: first, simulations with and without bulk condensation model using the single-phase passive scalar approach are compared to assess the implications of including bulk condensation and fog transport; second, a comparison between the single-phase and two-approaches is performed by considering simulations incorporating both wall and bulk condensation models; and third, an investigation of the influence of condensate accumulation using a further simplified geometry using the two-phase approach.

4.9.1. The TH2 experiment

The TH2 experiment [Kanzleiter, 2002] examines how stratified atmospheric layers form and disintegrate through the injection of high-temperature steam into a humid air mixture. The test vessel (Figure 2.3) features a 9.2 m tall cylindrical structure with 60 m^3 internal volume, including a main cylindrical section measuring 3.156 m in diameter. The vessel steel structure includes a 22 mm thick inner wall, a 16.5 mm thermal oil gap, followed by a 6 mm thick outer wall, all enclosed in a 120 mm of rockwool insulation. Inside the vessel, there are two key components: a hollow inner cylinder (1.4 m outer diameter, 10 mm thickness, and 4 m height), which is co-axial with the main cylinder and is positioned between 2.2 m and 6.2 m from the base of the main vessel, and four horizontal condensate trays (60° sectors) positioned between the inner cylinder and vessel wall at a 4 m height from the base of the main vessel. The coolant circuit between the vessel wall and outer wall is not operated and hence remains stagnant, and heat transfer between the coolant and the walls occurs predominantly by conduction. The vessel is initially filled with air and the steam injected at the upper part (Y = 6.7 m) via a toroidal feed pipe, having a diameter of 0.7 m and 19 horizontal holes. The vessel pressure before the steam injection is 1.042 bar, and the containment temperature ranges from 23.5 ^oC in the lower vessel region (1.6 m - 2.1 m) to 24.5 ^oC in the dome region (8.4 m - 9 m). The steam injection phase is performed at a 35 g/s mass flow rate for a duration of 2.75 hours, and this phase will be used for the validation study. The steam injection rate, transient pressure, and gas temperature at several locations are measured in the experiment.

4.9.2. Simulation Setup

Due to the quarter-symmetric nature of the TH2 vessel, the computational domain is simplified to encompass only one-fourth of the domain, as shown in Figure 4.25. The thermal inertia of the steel structures and thermal oil are significant; hence, cannot be omitted from the computational domain. Also, it is challenging to determine and apply boundary conditions at these locations. Therefore, the computational domain consists of three regions (Figure 4.25) based on their material properties: one, the fluid region where the air-steam gas mixture flow happens; two, the vessel wall,

inner cylinder, condensate tray, and outer wall region; and three, the coolant thermal oil region. Additionally, for the two-phase simulations, there is also a thin film region at the interface between the fluid and vessel.

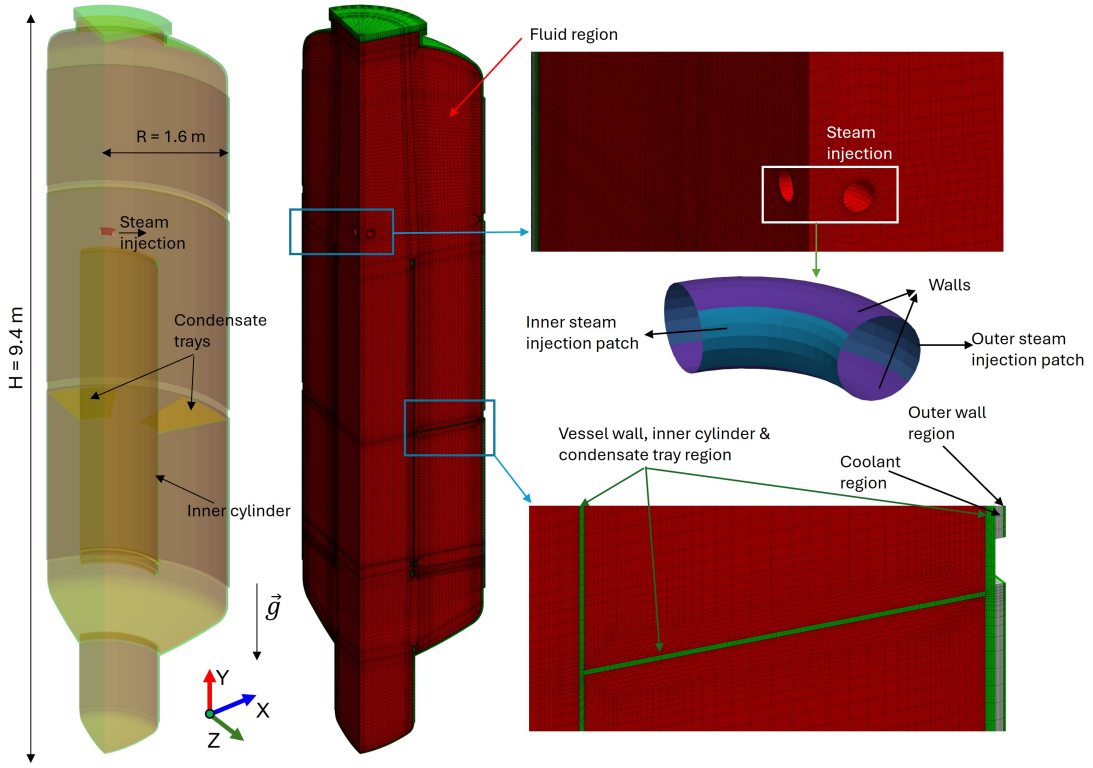

Figure 4.25.: TH2 vessel computational domain components and mesh with detailed views: fluid-vessel interface, steam injection boundary.

The coolant region is treated as a solid, as it is stagnant, with material properties of the coolant. The steam inlet is simplified by replacing the holes in the inner and outer faces of the toroidal pipe with annular sections, as shown in Figure 4.25. The structured mesh is generated using ICEM-CFD software with $y^+ \approx 1$ and consists of 0.35 million elements in the fluid region, 70,000 elements in the vessel region, 15,000 elements in the coolant region, and 11,000 elements in the film region. The computational mesh used in the simulations is derived from prior THAI vessel studies [Kelm et al., 2016, Vijaya Kumar et al., 2020], thereby eliminating the need for explicit grid independence studies. The initial conditions for all regions are extracted from the experiments, in which the air and steam mass fractions are computed assuming a relative humidity of 95 %. The region interfaces are applied with conjugate heat transfer boundary conditions for the temperature. The temperature at the outer wall boundary utilizes a heat transfer coefficient boundary condition, considering the insulation layer in the heat transfer coefficient. The fog droplet diameters for the PBM model range from 1 μm to 128 μm in 8 different size groups. The single-phase approach drift velocity uses the Manninen model with the deposition velocity boundary conditions on walls, whereas there is no slip for the two-phase approach. The air-steam mixture gas flow is turbulent and is modeled using the $k-\omega$ SST model. A fixed time step size of $\Delta t = 10^{-3}$ seconds is utilized for the single-phase approach, while the two-phase approach uses adaptive time stepping to adjust time-step size to maintain both convergence and stability in the simulations. The single-phase simulations are carried out with and without the bulk condensation model, whereas the two-phase simulations are conducted by including both wall and bulk condensation models.

4.9.3. Results

4.9.3.1. Single-phase approach results

The single-phase simulations including and excluding bulk condensation are run until 9000 s. The steam, owing to its higher temperature and lower density compared to the cold surrounding air, exhibits strong buoyancy and rises towards the dome of the vessel and forms a stratification. The bulk condensate rate, fog, and droplet Sauter mean diameter distributions at a section of the vessel at different time intervals for the wall and bulk condensation simulation are shown in Figure 4.26.

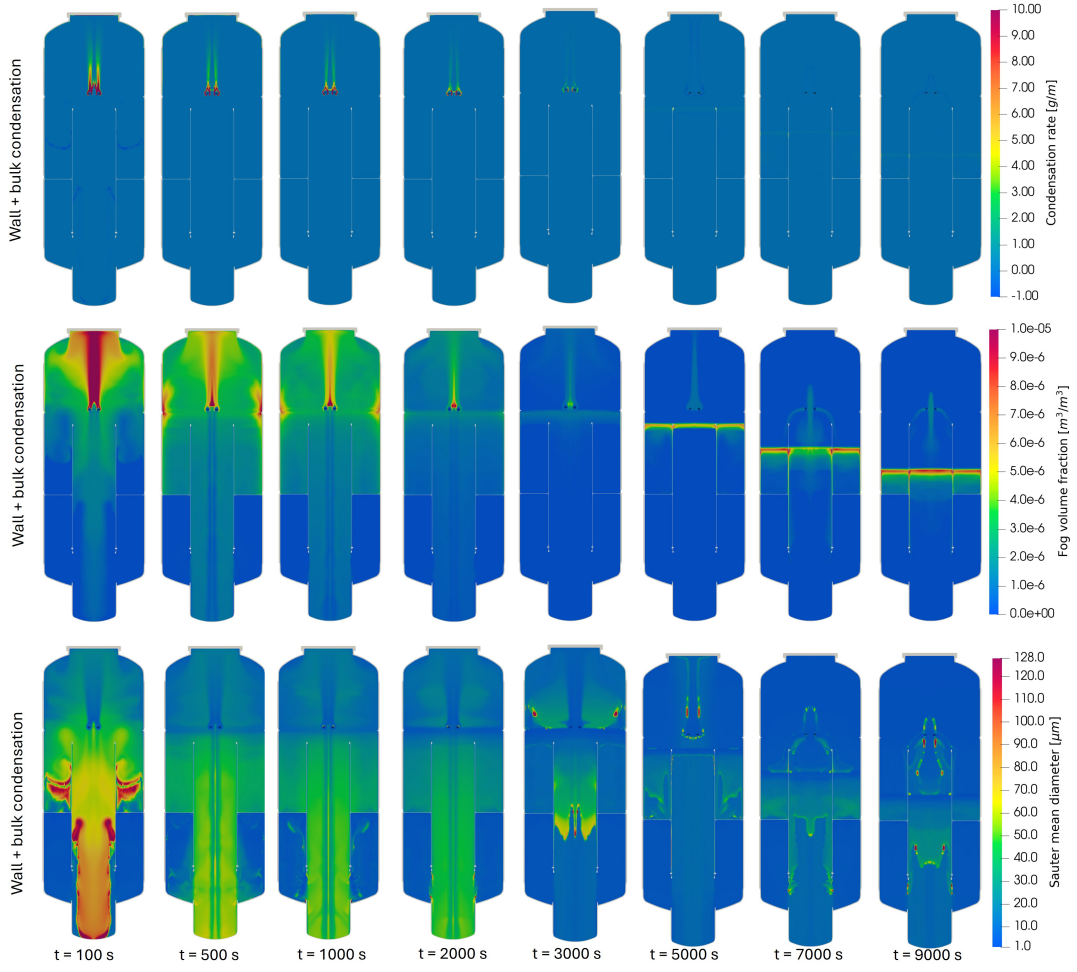

Figure 4.26.: TH2: Condensation rate (top), Fog volume fraction (middle) and Sauter mean diameter (bottom) distributions at the X-Y plane section at different transient times, with wall and bulk condensation, employing single-phase approach.

It can be observed that the bulk condensation happens predominantly in the upper section of the vessel, with maximum condensation close to the steam injection zone. The results indicate that maximum bulk condensation occurs during the initial stages (t = 100 s), leading to the formation of fog droplets of small sizes ($\approx$ 1μm) close to the steam feed pipe. These droplets easily get transported by the convection currents towards the dome region, during which they start to grow by further condensation and coalescence. When the steam current reaches the dome wall, it gets deflected in radial directions, leading to high accelerations due to change in direction. This results in their deviation as droplets from the gas flow path due to their inertia and getting deposited on the walls. Some of the droplets, while moving up, get transported away from the injection axis by convection and diffusion. The larger droplets, grown by coalescence and condensation, are carried towards the sump zone primarily under the influence of gravity and get deposited on the condensate

trays or the bottom sump structures. The fog droplets are concentrated in the upper region above the injection, as can be observed in Figure 4.26. Also, the droplets in this region are small, as they are evolving within the smaller diameter ranges. The larger droplets are concentrated in the lower region, as the drift velocity is much higher than the convection velocity for them. This is indicated in the Sauter mean diameter distribution in the figure. These droplets, while drifting towards the sump, also get evaporated in regions where the saturation temperature is higher. The evaporation locations can be observed in the condensation rate distribution where the values are negative.

As the time progresses (t = 500-2000 s), the bulk condensation rate starts decreasing, and the already present droplets either get deposited on the structure or grow and get transported towards the lower regions. This results in a decrease in fog concentration in the upper region and an increase in the lower region. The Sauter mean diameter distribution indicates that the concentration of larger droplets is decreasing due to a reduction in condensation rates and deposition. Towards the later stages (t = 3000-7000 s), the bulk condensation is nearly zero, and the remaining fog concentration and Sauter mean diameter are reduced further by deposition and drift. The fog droplets in the upper region traverse like a layer of fog, gradually moving toward the sump. The effective bulk condensation rate is nearly zero at the final stage after reaching thermal equilibrium (t = 9000 s) and the fog-rich layer drifts further downwards.

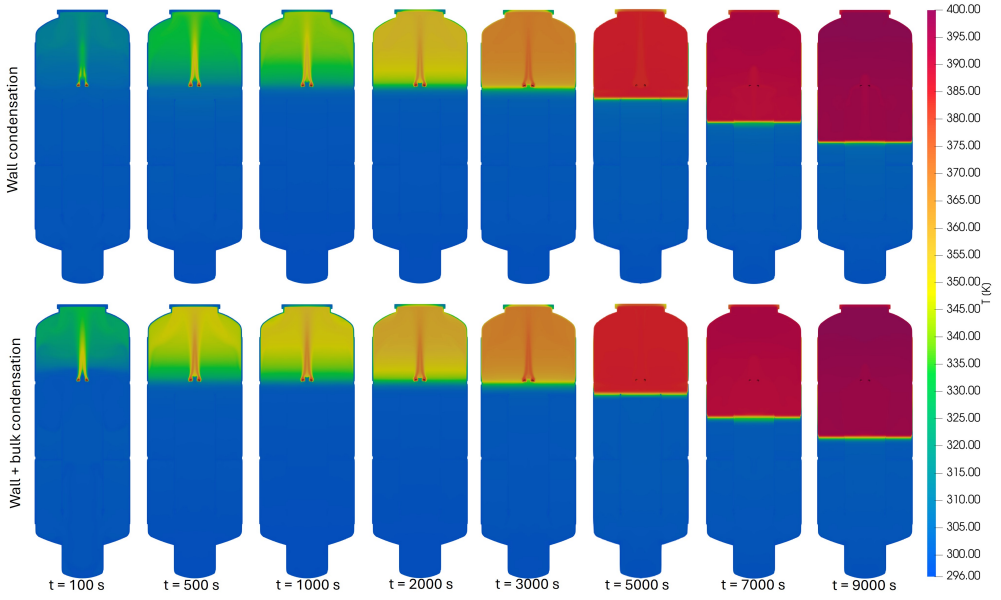

Figure 4.27.: TH2: Temperature distribution at the X-Y plane section at different transient times, with and without bulk condensation, employing single-phase approach.

The latent heat release during bulk condensation has a significant impact on the temperature distribution in the upper vessel region. This can be observed in the comparison of temperature distribution (Figure 4.27) in the vessel with and without bulk condensation model. During the initial stages (t = 100-1000 s) the temperature in the upper vessel region in simulation with bulk condensation is higher by around 10-15 K than without bulk condensation. This difference becomes less significant during the middle stages (1000-3000 s) as the bulk condensation rate decreases. The temperature distribution is almost the same in the latter to final stages, where bulk condensation and resulting latent heat release are negligible due to thermal equilibrium. The comparison at different times of the simulated vertical temperature gradient with the experiment using sensors located at a radial distance of 0.7 m is shown in Figure 4.28. At the beginning (t = 60 s) of the steam injection, the temperature at the uppermost section with the inclusion of bulk condensations shows better agreement with the experimental values. The experimental data shows that the temperatures are higher in the region starting from the injection zone to the dome, which is not captured by both

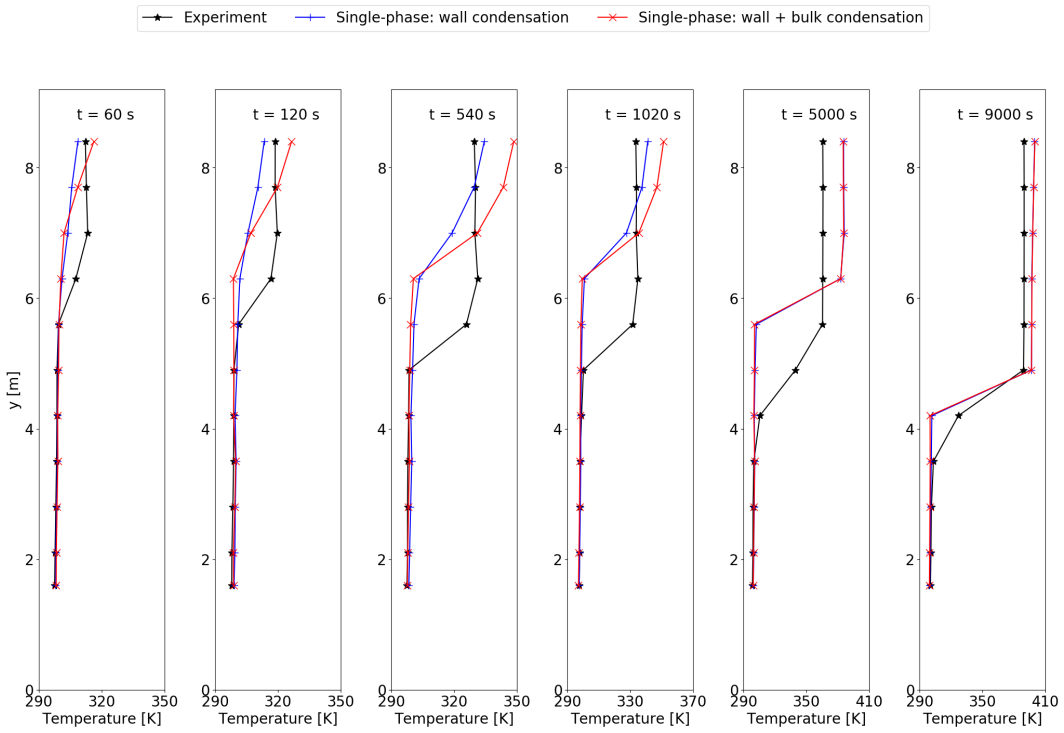

Figure 4.28.: TH2: Gas temperature distribution with and without bulk condensation along the vessel height at a radial distance of 1.1 m and 300^o angular position at different time intervals.

simulations. The bulk condensation model is expected to perform better, as only this phenomenon can explain higher temperatures. However, due to the under-prediction of the bulk condensation rate, it was unable to raise the temperature in the region close to the steam nozzle. As the times progress, the thickness of the stratified layer is under-predicted. Nevertheless, the bulk condensation model displayed its expected behavior of higher temperature, resulting from the latent heat release during condensation. At the later stages, bulk condensation becomes negligible, the temperatures of wall and bulk condensation coincide, and towards the end (t = 9000 s), the model temperature predictions are in good agreement with the experiments. This is because, at this stage, the energy transport is predominantly due to diffusion and fog settling, and the gas convection effect is marginal. The movement of the stratified layer of temperature towards the lower vessel region is also under-predicted by both models, which could be due to deviations in the outer wall boundary conditions with the experiments leading to removal of more heat than occurred in the experiment.

The comparison of the transient pressure inside the vessel (Figure 4.29) indicates that the influence of bulk condensation is negligible. This is because the vessel pressure is predominantly affected by the total steam mass converted to water. Therefore, the pressure is affected only by the net amount of condensation rate rather than the mode of condensation. The higher gas temperature has a small effect at the beginning of the transient. The transient variation of the net condensation rate with time, quantifying the contributions of each mode of condensation, is illustrated in Figure 4.30. This clearly indicates that the net condensation rate is only marginally influenced by the inclusion of the bulk condensation model. This is because the decrease in wall condensation rate is compensated by the bulk condensation rate. The bulk condensation contribution to the net condensation rate is 10 % in the beginning (t = 100 s), which reduces to 3 % during the middle stages (t = 2700 s) and becomes nearly zero towards the end (t = 7000 s). The comparison of the pressure evolution with the experiment indicates that the model predictions were excellent during the initial to mid-stages (t = 0-3000 s). In the subsequent stages, the pressure was overpredicted by the model, which is due

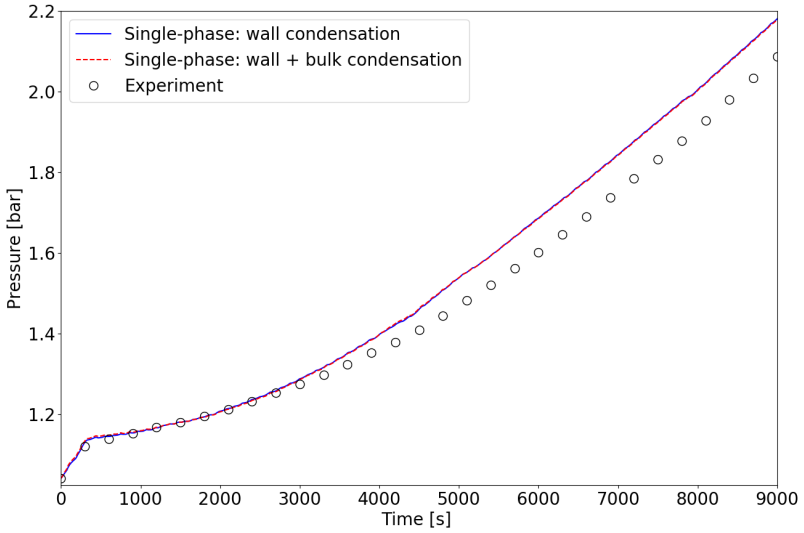

Figure 4.29.: TH2: Transient average vessel pressure variation with and without bulk condensation, employing single-phase approach.

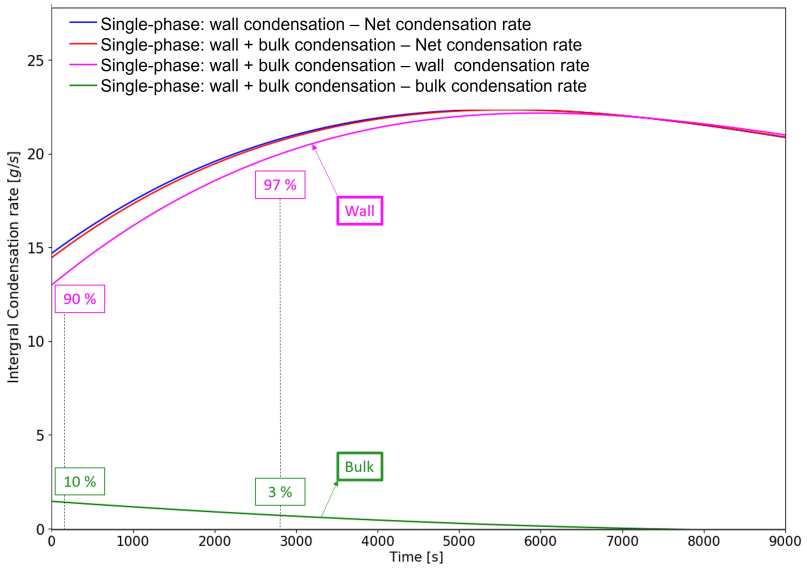

Figure 4.30.: TH2: Quantitative comparison of integral condensation rates with and without bulk condensation, including condensation mechanism-specific contributions to net condensation rate.

to the underprediction of wall condensation rate arising from the uncertainties in modeling heat losses. The downward movement of the steam stratification layer is the same as the temperature stratification layer shown in Figure 4.27. However, due to the under-prediction of this motion, the amount of steam in contact with the cooler lower vessel walls is lower. This led to the under-prediction of the wall condensation rate by both simulations. Nevertheless, the pressure prediction is within 10 % errors, which is acceptable considering the uncertainties in the boundary conditions of large-scale simulations.

4.9.3.2. Single-phase v/s two-phase approach results

The two-phase simulations are performed with both wall and bulk condensation models. However, it presents significant computational challenges for large-scale simulations. The simulations are slower compared to the single-phase approach, primarily as a consequence of the requirement of

lower time-step size for stability reasons. The presence of two phases makes the energy equation unstable at larger time-step sizes, causing temperature field oscillations and convergence difficulties. This instability arises from the condensation models overpredicting condensation rates, which leads to excessive latent heat release and temperatures exceeding saturation states. As condensed water or fog is released, it re-evaporates to achieve saturation conditions, potentially at higher than expected rates, causing further condensation. This creates a series of oscillations, which hinders the simulation convergence. To mitigate this issue, the solution employed in this work is the reduction of the time-step size, which increases the overall computational efforts. Hence, the simulation results of two-phase simulations are available only for up to 280 seconds, whose results are compared with the single-phase results.

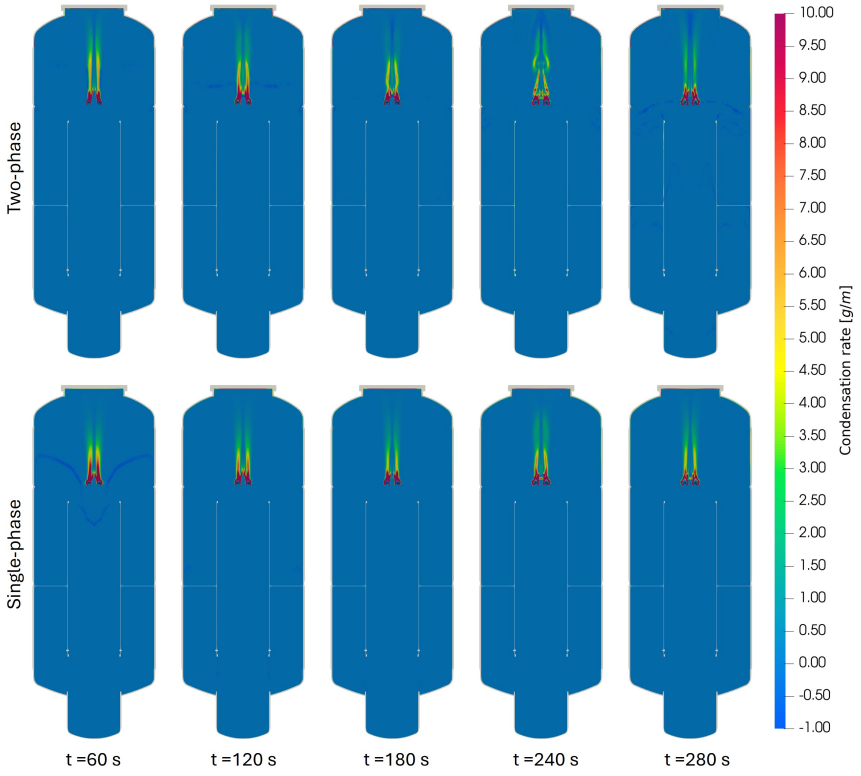

Figure 4.31.: TH2: Comparison of condensation rate distribution at the at different transient times between single-phase and two-phase approach.

The condensation rate distribution comparison at different time intervals shows that the two-phase solver predicts slightly larger and more spread condensation than the single-phase approach (Figure 4.31). This is due to the inherent differences between the modeling approach and bulk condensation rate calculation. In the two-phase approach, the latent heat released is absorbed by both the gas mixture and water (or) fog. The water, due to its higher specific heat capacity and density, absorbs a significant portion of this latent heat, which was not considered in the single-phase model. Hence, the energy required to bring the mixture to saturation is higher for the two-phase approach, as demonstrated by Eqn. 3.100. Hence, the bulk condensation rates are higher for the two-phase approach. This leads to a higher concentration of fog in the upper section of the vessel, as evidenced by Figure 4.32. Also, in the two-phase, the fog drift velocity does not use the deposition velocity boundary condition, which removes the fog mass from the domain. The continuous fog removal through the walls in single-phase creates a driving force towards the wall for fog, which is absent in the two-phase approach. The drift of fog droplets towards the condensate tray is also captured by the model illustrated in the figure. The latent heat released is absorbed more in the region with higher fog concentrations due to its higher average heat capacity. This results in higher temperatures in these regions, as demonstrated by the temperature contours in Figure 4.33.

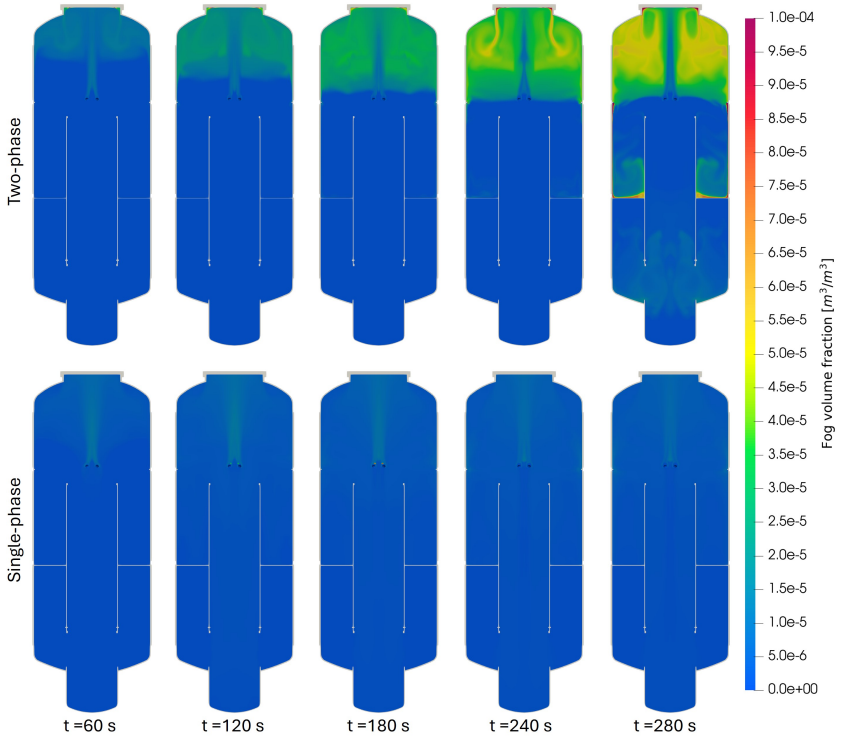

Figure 4.32.: TH2: Comparison of fog distribution at the at different transient times between single-phase and two-phase approach

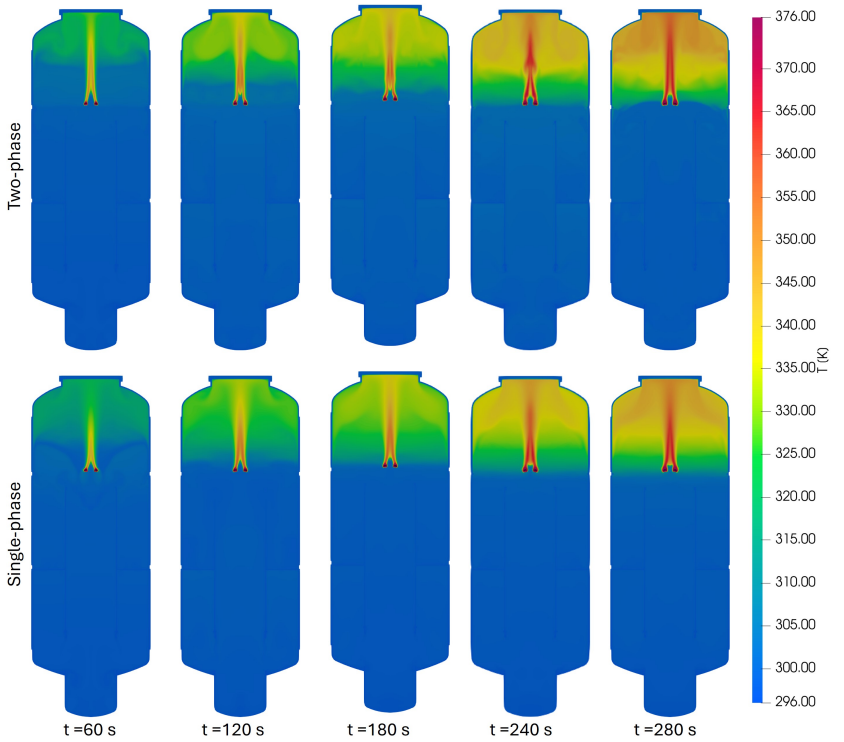

Figure 4.33.: TH2: Comparison of temperature distribution at the at different transient times between single-phase and two-phase approach.

It can be observed that the temperature fields are not spread for the single-phase, whereas they are more concentrated for the two-phase during the initial phase (t = 60-180 s). As the fog starts

settling to the lower regions, the temperature field gets more spread in the two-phase approach than in the single-phase approach, which is indicated by the temperature contour at times t = 240 -280 s. This phenomenon is quantitatively shown in Figure 4.34, where the temperature distribution along the height of the vessel is illustrated. The two-phase approach does not display any significant improvement in the temperature profile prediction. It is slightly improved in some locations and worse in others at any given time compared with the experimental data. The higher condensation rate with associated latent heat release resulted in slightly higher temperatures for the two-phase model, which is indicated by the temperature plot at a time of 240 s.

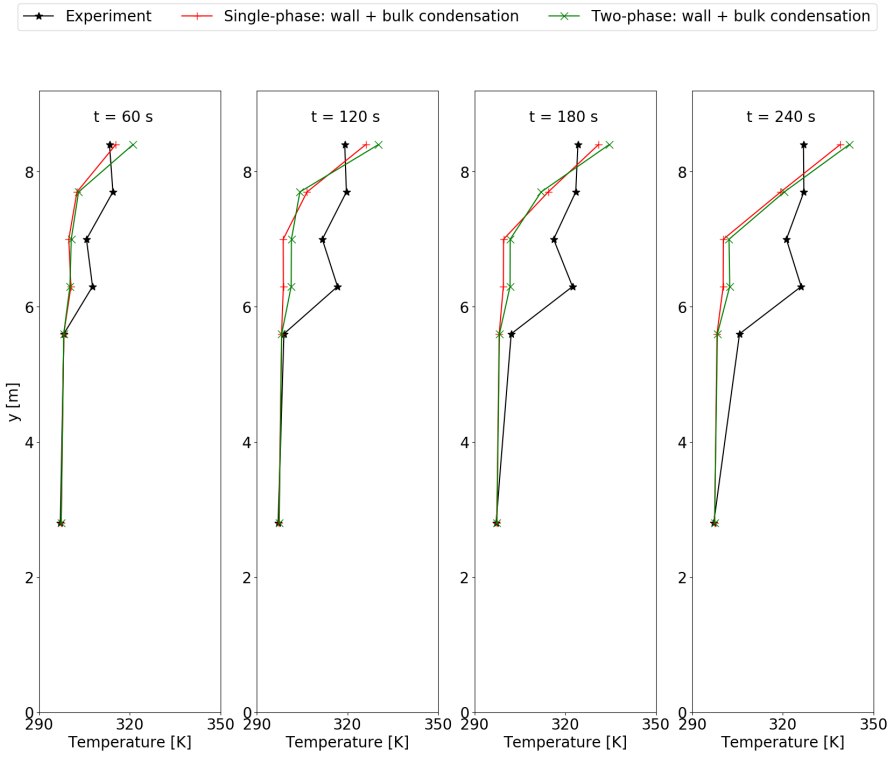

Figure 4.34.: TH2: Comparison of gas temperature distribution along the vessel height at a radial distance of 1.1 m and 300^o angular position at different time intervals between single-phase and two-phase approach.

The formation of surface wall films and their transport along the vessel wall are demonstrated in Figure 4.35. The steam on contact with the dome and the wall in the upper section results in wall condensation, generating films on those surfaces. The films on the dome wall experience high tangential force due to the steam jet injection and spreading. This drives the film away from the dome towards the side walls. The steam wall condensation on the side walls also generates film, which joins the dome film and flows along the vessel walls towards the upper condensate gutter. This flow is driven by gravity and the surface shear force exerted by the gas flow field. The films, on reaching the condensate trays, spread over it as demonstrated at a time of 280 s. The comparison of the transient vessel pressure between the single-phase, two-phase, and experiment up to t = 280 s (Figure 4.36) indicates that the two-phase approach initially predicts slightly lower pressure than the single-phase approach around 60 seconds but predicts higher pressure afterward. This is due to the combined interaction between three events: one, the higher condensation rate removes the steam mass, reducing the pressure; two, the higher latent heat release raises the temperature and subsequently pressure; and three, the fog and film mass generated, which occupies space and cause pressure increase. However, the simulated time frame of 250 s is too short to observe the influence on pressure considering the size of the vessel, the overall transient of the experiment, and uncertainties in the boundary conditions.

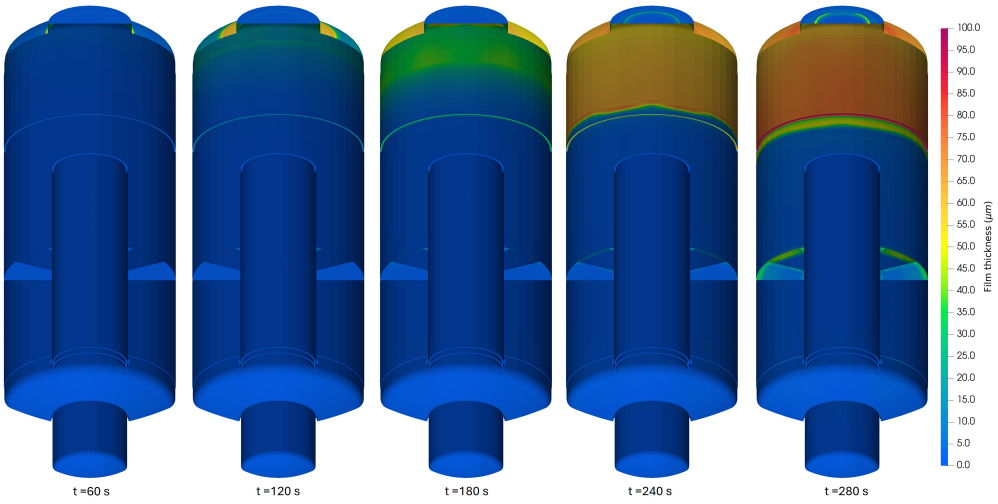

Figure 4.35.: TH2: Evolution of the film thickness along time, employing a two-phase approach.

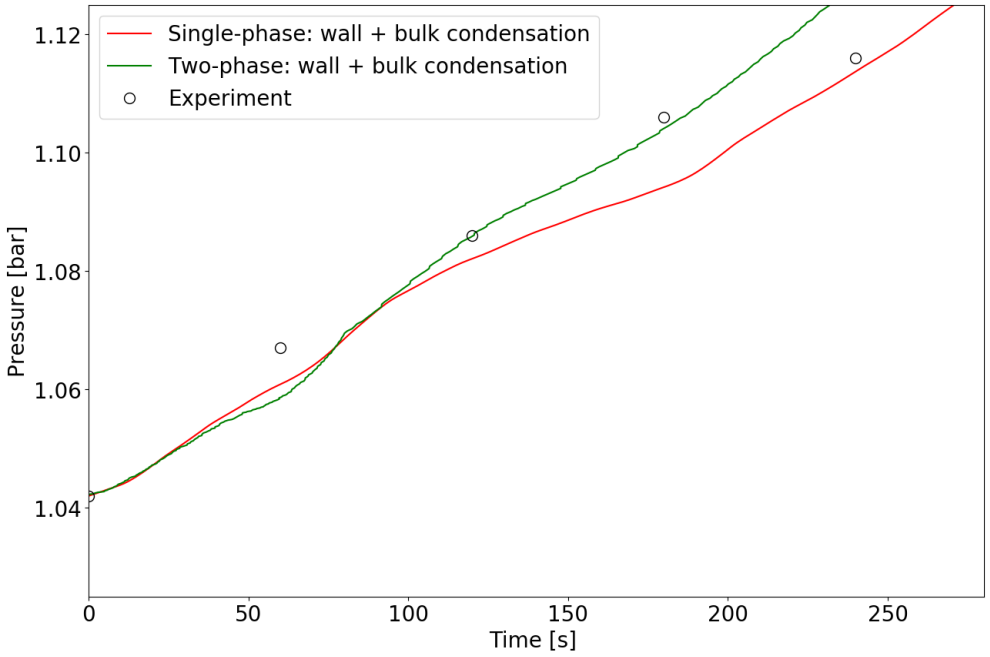

Figure 4.36.: TH2: Comparison of transient average vessel pressure variation between single-phase and two-phase approach.

4.9.3.3. Two-phase approach with simplified 2D geometry results

Arising from the significant computational requirement for the three-dimensional simulation using the two-phase approach, a simplified two-dimensional axis-symmetric mesh is selected to perform a faster two-phase simulation. This involved removing the condensate trays from the computational domain, as it will block the flow between the upper and lower annular regions. This simulation is mainly performed to investigate whether the two-phase approach can model the condensate accumulation at the sump region and investigate its influence on the vessel pressure. Figure 4.37 demonstrates the evolution of water accumulation during different time intervals of the simulations.

As condensation from both the wall and the bulk occurs, the resulting liquid slowly accumulates in the sump, eventually forming a water-gas interface there. However, the amount of water collected

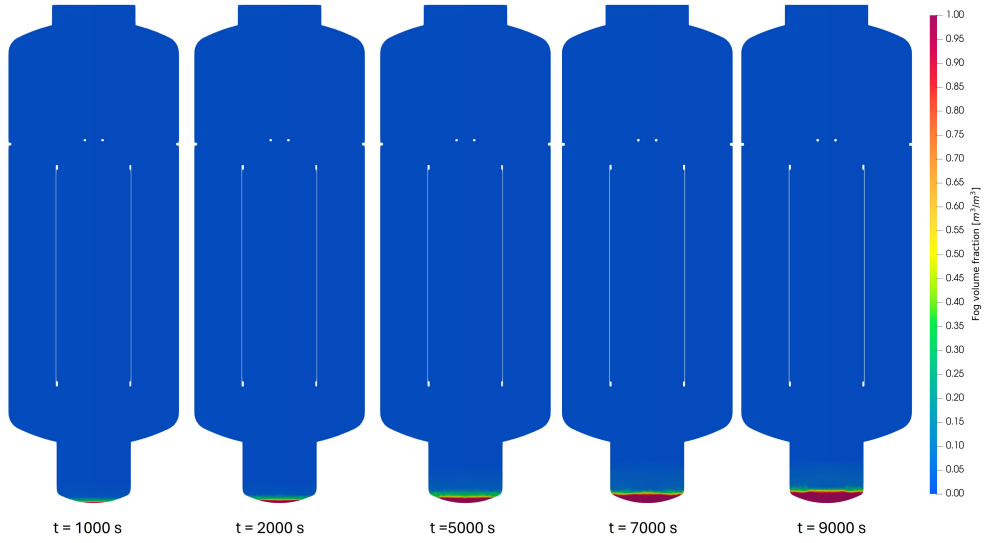

Figure 4.37.: TH2: Evolution of water accumulation at the at different time intervals using two-phase approach with simplified mesh.

in the sump is minor when compared to the total volume of the vessel. Hence, its impact on the vessel pressure is marginal compared to the single-phase approach. This transient pressure variation within the vessel is shown in Figure 4.38.

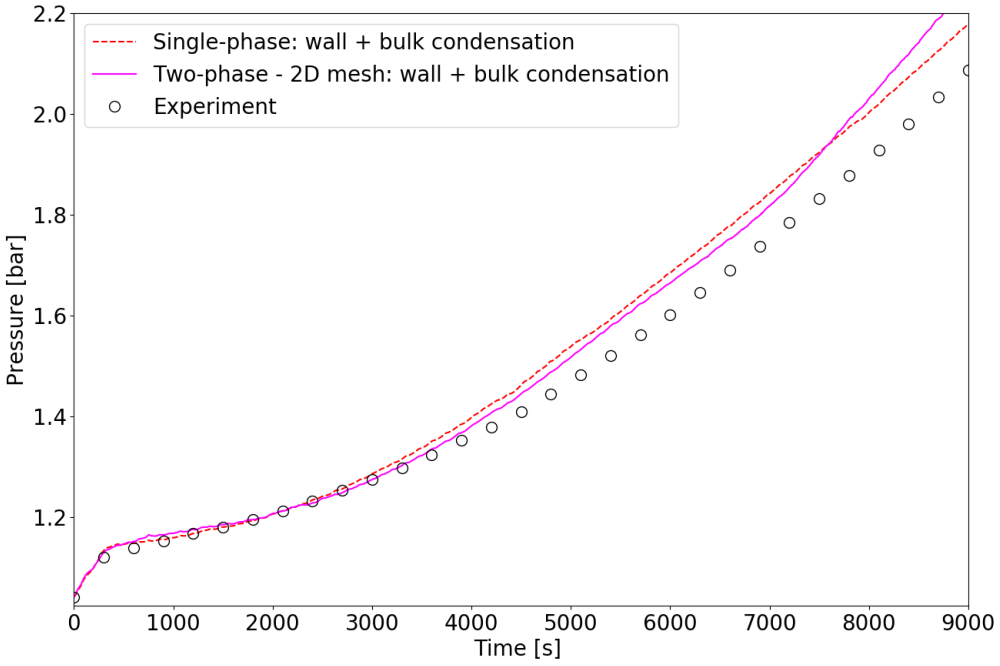

Figure 4.38.: TH2: Comparison of transient average vessel pressure variation between single-phase and two-phase approach with simplified mesh.

The slightly lower pressure with the two-phase during the first 7000 s is due to the higher condensation rates in the two-phase approach and also due to the simplified two-dimensional geometry. Towards the final stages of the simulation, the two-phase pressure rises, caused by the re-evaporation of sump condensate that raises the steam content. These results also indicate that the two-phase approach, although it captures more features, does not offer any significant improvement in the prediction of vessel conditions than the single-phase approach.

4.9.4. Discussion

The assessment of the influence of the interaction of the bulk condensation with other phenomena in the containment and also the capability of the two-phase approach is discussed using the THAI TH2 experiment simulation in this section. The comparison between the simulations with and without the bulk condensation model revealed that the bulk condensation model was able to reproduce higher temperatures in the upper vessel zone due to the latent heat release. The comparison with sensor temperatures indicated better prediction at some locations, while it was worse in some other locations. The model was capable of simulating the fog transport, droplet evolution, and differential settling of the droplets depending on their diameter. However, experimental data were unavailable to compare these model influences on the containment event prediction accuracy. The influence of bulk condensation on the pressure is marginal if the overall condensation rate (wall + bulk) remains the same. Additionally, bulk condensation accounts for at most 10 % of the total condensation rate, which is too minor to significantly affect the pressure. The two-phase approach simulations demonstrated that they require lower time-step sizes for a stable simulation, resulting in high processing times. The comparison of the available two-phase results with single-phase results indicated that the two-phase approach does not offer any additional accuracy. The condensation rates were higher with the two-phase approach, which arises from the presence of water in the bulk, which has higher specific heat capacity and density. Additionally, the fog volume fractions exceeded those in the single-phase approach, likely because the latter uses a deposition boundary condition to remove fog accumulating on the walls. The two-phase film approach was able to model the generation and transport of the film along the vessel structures. The comparison of the single-phase results with simplified two-dimensional two-phase simulations demonstrated that the two-phase approach was capable of modeling the condensate accumulation phenomena. Nevertheless, the amount of condensate collected was marginal relative to the vessel's total volume to have any notable impact on containment pressure. The influence on the vessel pressure was predominantly due to higher condensation rates with the two-phase approach and re-evaporation of the accumulated condensate. The TH2 experiment involved significant uncertainties in the definition of boundary and initial conditions as well as only sparse instrumentation, which did not further enable to evaluate specific modeling aspects.

4.10. THAI HM2

This section discusses the validation of the *containmentFOAM* multi-phenomena interaction using another technical-scale THAI hydrogen mixing experiment called HM2. The experiment's objectives and details about the vessel and its components are discussed first. This is followed by defining the computational domain, mesh, and boundary conditions. A comparative analysis is conducted in two parts: first, simulations with and without the bulk condensation model using the single-phase passive scalar approach are compared to assess the implications of including bulk condensation and fog transport; second, a comparison between the single-phase and two-approaches is performed by considering simulations incorporating both wall and bulk condensation models.

4.10.1. The HM2 experiment

The HM2 experiment [Kanzleiter et al., 2008] is dedicated to studying the distribution and mixing behavior of hydrogen stratification when steam is injected into the vessel. It represents a more straightforward and thoroughly instrumented replication of the THAI ISP-47 experiment. The vessel geometry and components are the same as in the TH2 experiment (Sec.4.9). The vessel internal components, condensate trays, and the inner cylinder are fitted. The coolant circuit is not operated, and hence, the coolant is stagnant, and heat losses as well as thermal insulation of wall and oil represent the heat sink. The vessel is initially filled with nitrogen with small amounts of oxygen and steam present. This is followed by the injection of hydrogen into the upper part (height

= 4.8 m) of the vessel for a duration of 4200 s (phase 1) to form a hydrogen cloud in the dome region. Then, there is a short period of 120 s without injection to allow the hydrogen cloud to settle down. Finally, in phase 2, this cloud is dissolved by a steam plume rising upwards from injection in the lower part of the vessel (height = 1.8 m) through a nozzle of internal diameter of 138 mm. The location and shape of the injection nozzle are the only geometric differences between the TH2 and HM2 experiments. The vessel pressure before the steam injection phase is 1.259 bar with gas temperatures ranging from 292 to 300 K. The steam injection rate is approximately 24 g/s for a duration of 2160 s and gradually decreases to zero at around 2500 s. The phenomenology observed in the experiment is that the injected steam first clears the inner cylinder while condensing on its structure and then begins to erode the hydrogen cloud in the dome due to condensation on the vessel walls; a circulation is created. The vessel pressure and temperatures increase during this period. When the steam reaches the dome region, there is a sudden decrease in the pressure due to wall condensation on the dome. The simulations aim to predict this behavior inside the vessel by using different models and phase approaches.

4.10.2. Simulation Setup

The HM2 geometry is also a quarter-symmetrical like TH2, and hence the computational domain and mesh are similar to the one shown in Figure 4.25. The only difference is in the location and shape of the injection nozzle, which is a vertical cylindrical injector for HM2. The computational domain (Figure 4.39 (a)) encompasses the vessel, coolant, and fluid regions, with the two-phase approach incorporating an additional film region.

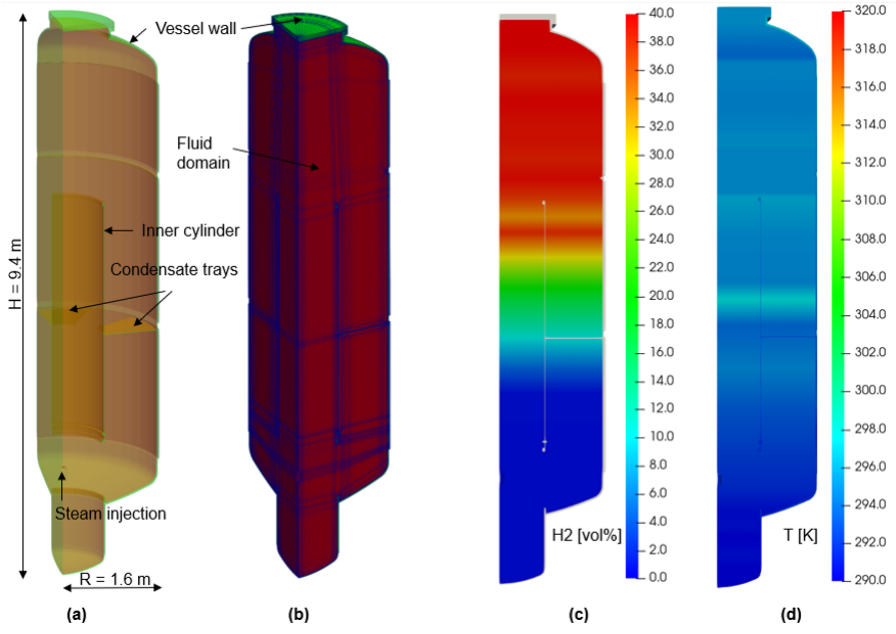

Figure 4.39.: HM2:(a) Computational domain components and dimensions. (b) Quarter-symmetric mesh with the all regions. Sectional view hydrogen (c) and temperature (d) distribution inside the vessel at simulation time t = 0 s.

The coolant region is treated as solid with material properties of the thermal oil as in TH2 simulations. The mesh (Figure 4.39 (b)) consisted of 0.4 million elements in the fluid region with $y^+ \approx 1$ on walls, 75,000 elements in the vessel region, 16,000 elements in the coolant region, and 12,000 elements in the film region. Simulations are performed only for the steam injection phase using the initial conditions. The initial conditions interpolated from the experiments for hydrogen volume fraction and temperature are shown in Figure 4.39 (c, d). The region interfaces are applied with conjugate heat transfer boundary conditions for the temperature. The temperature at the outer

wall boundary is modeled with a heat transfer coefficient boundary condition, considering the rock wool insulation layer effect. The fog droplet diameters for the PBM model range from 1 μm to 128 μm in 8 different size groups. The single-phase approach drift velocity uses Manninen model with the deposition velocity boundary condition on walls, whereas there is no slip for the two-phase approach. The air-steam mixture gas flow is turbulent and is modeled using the $k-\omega$ SST model. A fixed time step size of $\Delta t = 10^{-3}$ seconds is used for the single-phase approach, while the two-phase approach uses adaptive time stepping to adjust time-step size to allow convergence and stability of the simulations. The single-phase simulations are conducted with and without the bulk condensation model, whereas the two-phase simulations are conducted by including both wall and bulk condensation models.

4.10.3. Results

4.10.3.1. Single-phase approach results

The single-phase simulations including and excluding the bulk condensation are run until 2500 seconds, i.e., the dissolution of the hydrogen cloud. The spatial distributions of bulk condensation rate, fog volume fraction, and Sauter mean diameter at a section of the vessel at different time intervals are shown in Figure 4.40.

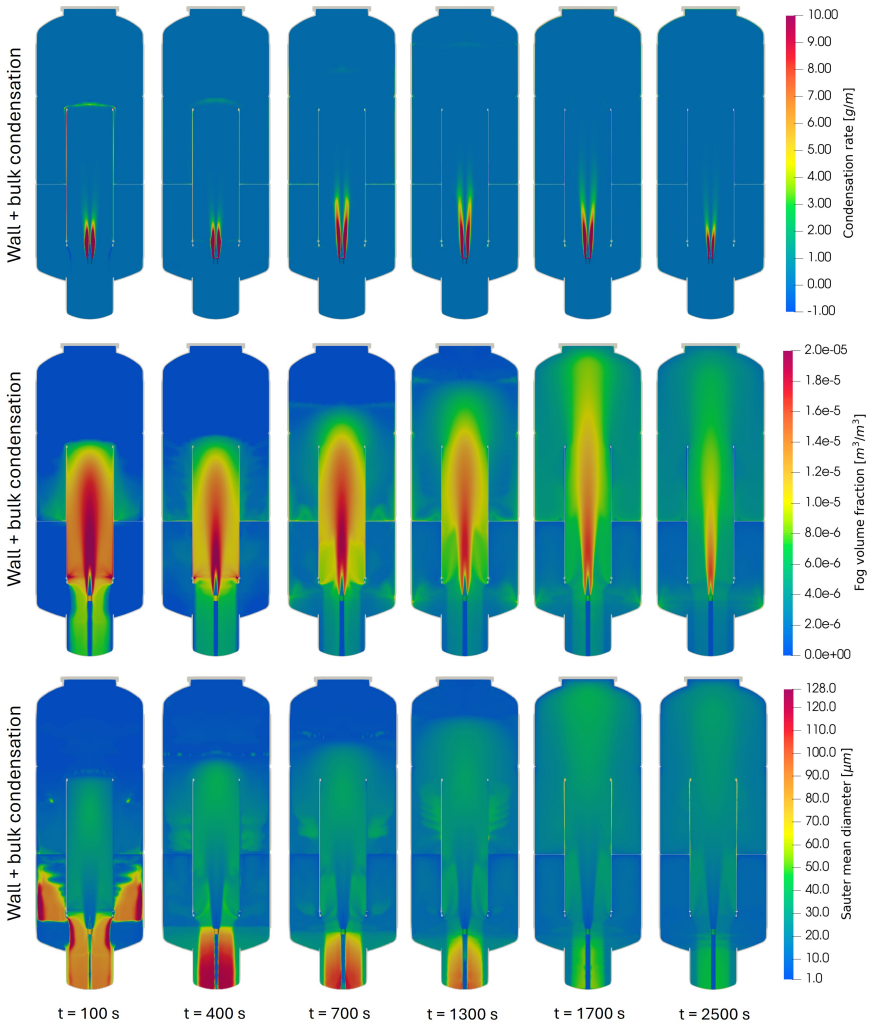

Figure 4.40.: HM2: Condensation rate (top), Fog volume fraction (middle) and Sauter mean diameter (bottom) distributions at the X-Y plane section at different transient times, with wall and bulk condensation, employing single-phase approach.

During the initial stages (t = 100-400 s), the bulk condensation primarily occurs in the inner cylinder region, with maximum condensation happening close to the injection zone. This high bulk condensation in the inner cylinder results in the formation of small diameter droplets of diameters ($\approx 1\mu m$) close to the injection nozzle. These droplets easily get transported by the convection currents towards the exit of the inner cylinder, during which they start to grow by further condensation and coalescence. Some of these droplets flow towards the walls by convection, drift, and diffusion, and get deposited on contact with the walls.

The larger droplets that clear the inner cylinder move towards the annular region and then drift towards the sump region predominately by gravity and also grow by coalescence and minor condensation during this drift. This is the reason for higher Sauter mean diameters in the lower annular region. The larger droplets in the inner cylinder region, which are radially away from the high convection region, also drift towards the sump, as indicated in the figure. There is also some minor evaporation in the lower boundary between the inner cylinder and the annular region close to the steam nozzle. During the mid-stages (t = 700-1700 s), the bulk condensation zone starts spreading away from the nozzle to the interface between the cold hydrogen layer and hot steam plume. The convection zone also starts moving upwards, pushing the fog towards the dome regions and also on to the side walls, where they get deposited. The larger droplets start settling down, and the Sauter mean diameters begin to drop in the sump region. Once the steam convection current reaches the dome (1700-2500 s), the fog concentration starts to a decrease due to further deposition and decrease in bulk condensation rate. A comparison of the steam-front movement from the inner cylinder towards the dome between the simulations with and without bulk condensation is shown in Figure 4.41.

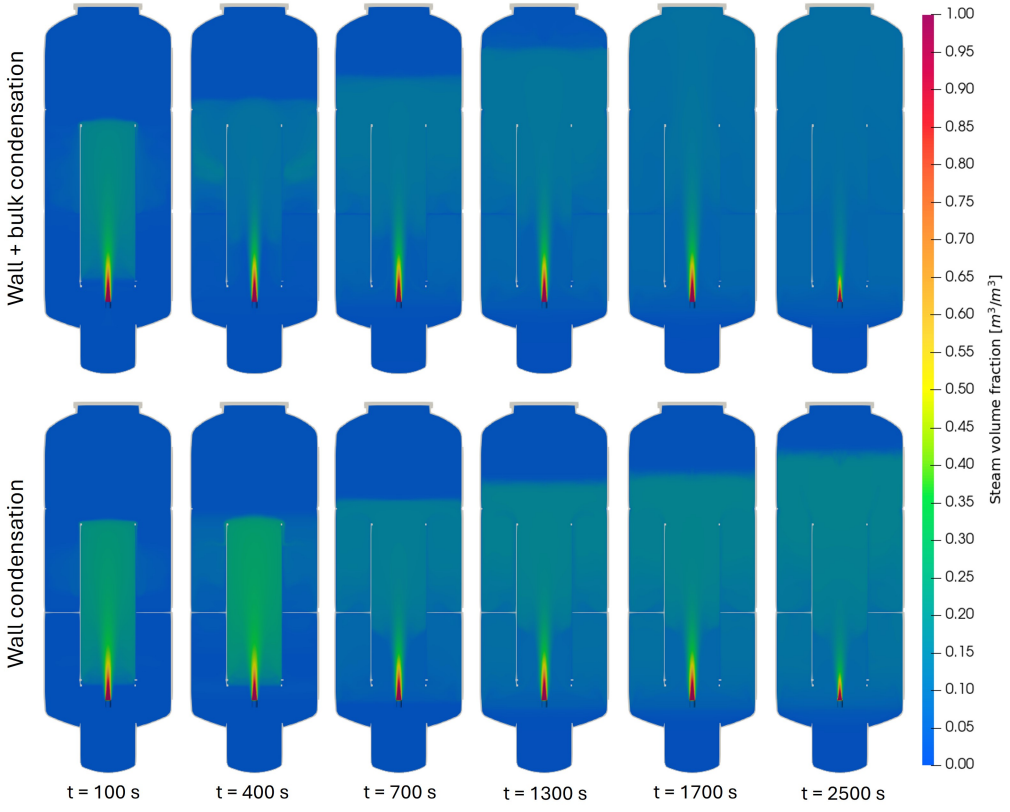

Figure 4.41.: HM2: Steam distribution at the X-Y plane section at different transient times, with and without bulk condensation, employing single-phase approach.

It can be observed that the steam motion is slower if the bulk condensation model is omitted. This reduced movement is due to the weaker convection currents for the wall condensation-only

simulation. The convection currents towards the dome are predominately driven by the buoyancy effect, with steam injection velocity playing a minor role. The latent heat released during bulk condensation results in higher temperatures in the inner vessel zone, which is consistently higher for the simulations with bulk condensation throughout the transient, as demonstrated in Figure 4.42. This leads to higher buoyancy forces in this region, generating stronger convection currents and reduced density differences between hot plume and cold hydrogen-rich clouds compared to the simulation without bulk condensation. Consequently, these enhanced currents drive the steam front at a faster rate to the dome. The concentration of steam in the inner cylinder region during the initial stages (t = 100-400 s) is slightly higher for the wall condensation only simulation. This difference is attributed to the bulk condensation model, which condenses steam in this region, in addition to the condensation walls of the inner cylinder.

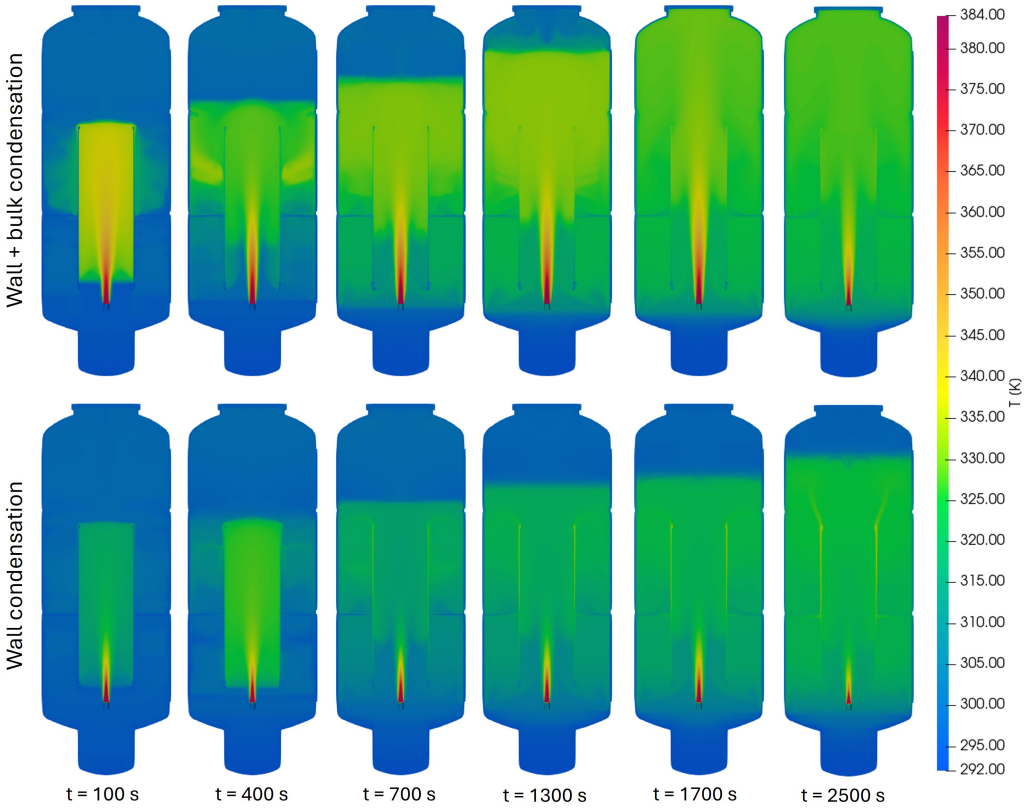

Figure 4.42.: HM2: Temperature distribution at the X-Y plane section at different transient times, with and without bulk condensation, employing single-phase approach.

The comparison of the simulation with the experiment using temperature distribution along the vessel height in the inner cylinder region at different time intervals is illustrated in Figure 4.43. It clearly indicates that the bulk condensation model inclusion was able to predict the temperatures inside the cylinder with excellent consistency with the experiment. The wall condensation-only simulation shows deviations in the range of around 15-20 K in the inner cylinder region in the initial stages (t = 100-400s). This difference decreases to the range of 5-10 K in the mid-stages (t = 700-1300 s). Even towards the end of the experiment (t = 1700-2500 s), the wall condensation-only simulation shows a small deviation (2-5 K) in the upper and lower sections. However, the simulations with bulk condensation offered better agreement with the experimental temperatures during the entire transient. This implies that the latent heat release associated with the bulk condensation has a significant impact on the temperature field in the HM2 experiment, and the model was able to predict it. This relevant difference in the gas temperature field is responsible for driving the steam front at a faster rate towards the dome by strong buoyancy effects.

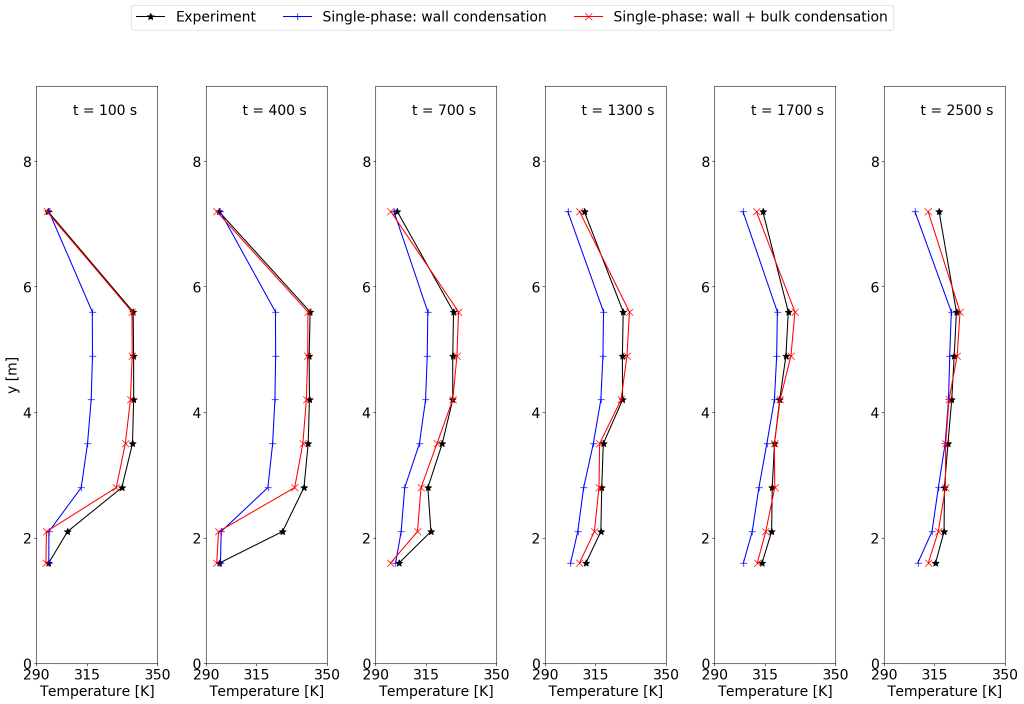

Figure 4.43.: HM2: Gas temperature distribution with and without bulk condensation along the vessel height at a radial distance of 0.35 m and 300^o angular position at different time intervals.

The dissolution of the hydrogen cloud is directly related to the progression of the steam to the dome as, demonstrated in Figure 4.44.

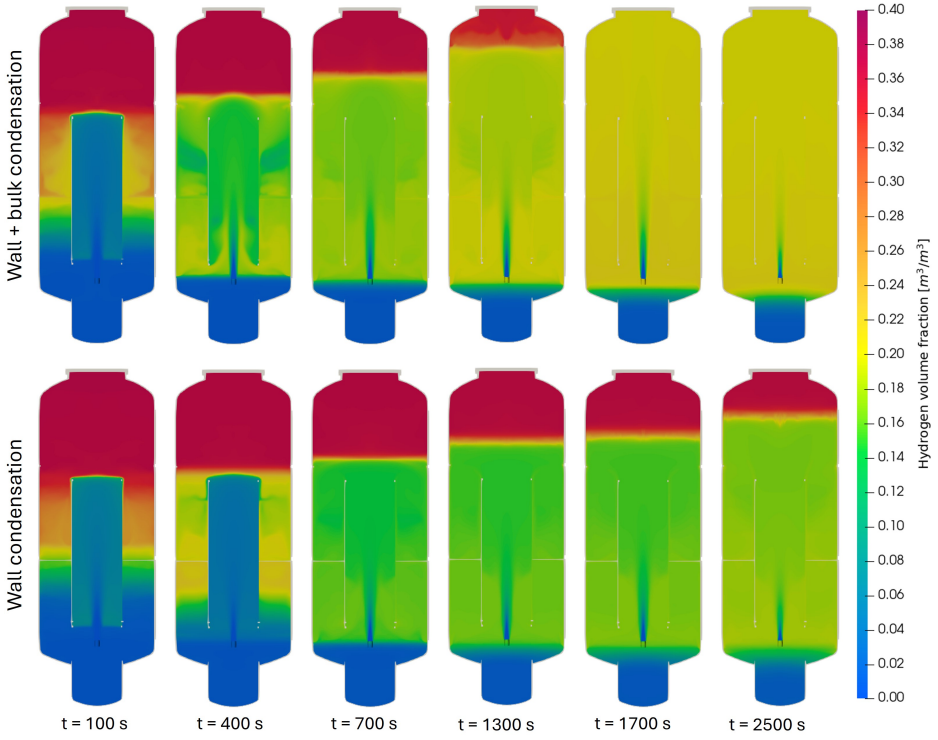

Figure 4.44.: HM2: Hydrogen distribution at the X-Y plane section at different transient times, with and without bulk condensation, employing single-phase approach.

The hydrogen layer starts dissolving as the steam reaches the upper end of the inner cylinder (t = 100 s). Consequently, some steam spreads towards the annular region and starts flowing downwards towards the sump region. This results in the formation of a weak convection loop, with downward flow in the annulus and upward flow in the inner cylinder. The convection gradually erodes the hydrogen cloud in the annular region. Mixing is more pronounced in the bulk condensation simulation due to stronger buoyancy forces. As the steam front progresses, the convection loop starts to get stronger, accelerating the dissolution of the hydrogen cloud. This process occurs consistently faster for the simulation with bulk condensation, and when the steam reaches dome, the hydrogen is fully mixed. In the simulation incorporating bulk condensation, complete hydrogen dissolution occurs at approximately 1700 seconds. In contrast, the simulation considering only wall condensation fails to achieve full hydrogen dissolution even by the end of the simulated transient (2500 s).

The comparison of the simulation hydrogen distribution with the experiment along the vessel height in the annular region at different time instances is illustrated in Figure 4.45.

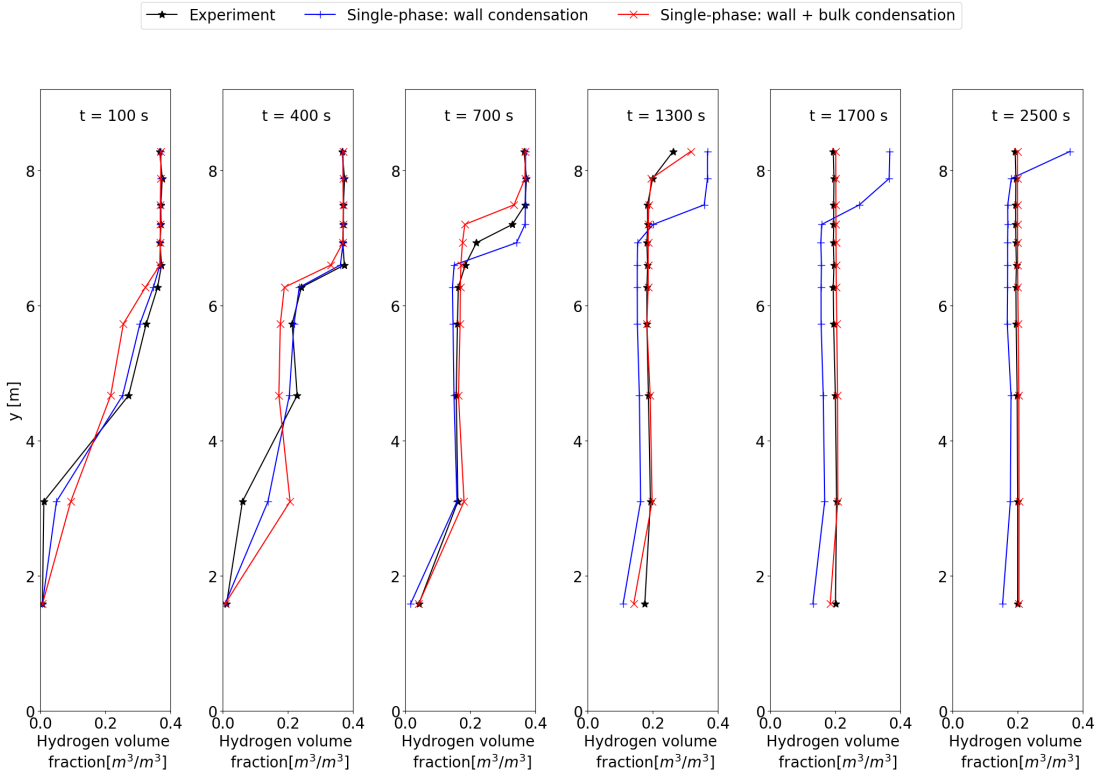

Figure 4.45.: HM2: Hydrogen distribution with and without bulk condensation along the vessel height at a radial distance of 1 m and 300^o angular position at different time intervals.

During the initial stages (t = 100-400 s), the wall condensation-only case showed slightly better prediction of the hydrogen concentration. However, this measurement is made in the annular region, which is not yet affected by the steam injection. A minor overprediction of bulk condensation rate can lead to this by starting the convection loop earlier. However, as the time progresses (t = 700-1300 s), the bulk condensation model offers better consistency as compared with the wall condensation-only simulation. In the vessel mid-section, the hydrogen concentration predicted by the bulk condensation model coincides with the experimental values, whereas the wall condensation only model exhibited an error of around 10 %. The simulations without the bulk condensation model displays a significant delay in the dissolution and have not been able to dissolve even after the end of the transient.

The transient variation of the vessel pressure (Figure 4.46) indicates better prediction compared to

the experiment during the initial stages (t = 100 s) by the inclusion of bulk condensation model. As the time progresses (t = 400-1300 s), the bulk condensation model exhibits some notable over-prediction of the pressure, whereas the wall condensation-only simulation displayed minor under-prediction. At this stage, the omission of bulk condensation model seems to predict the vessel pressure better. There is a sudden decrease in the pressure at around 1600-1700 s in the experiments, which is attributed to the rapid increase in the wall condensation rate when the steam plume reaches the cold upper dome walls. The simulation incorporating the bulk condensation model more accurately predicts the timing of this event, as evidenced by a corresponding pressure drop in the simulation results. These phenomena are also consistent with the previous observations on the steam and hydrogen distributions. The wall condensation-only simulation cannot predict the pressure drop because of the delay in the steam reaching the upper walls. The evolution of the net condensation rate with time, quantifying the contributions of each mode of condensation, is illustrated in Figure 4.47.

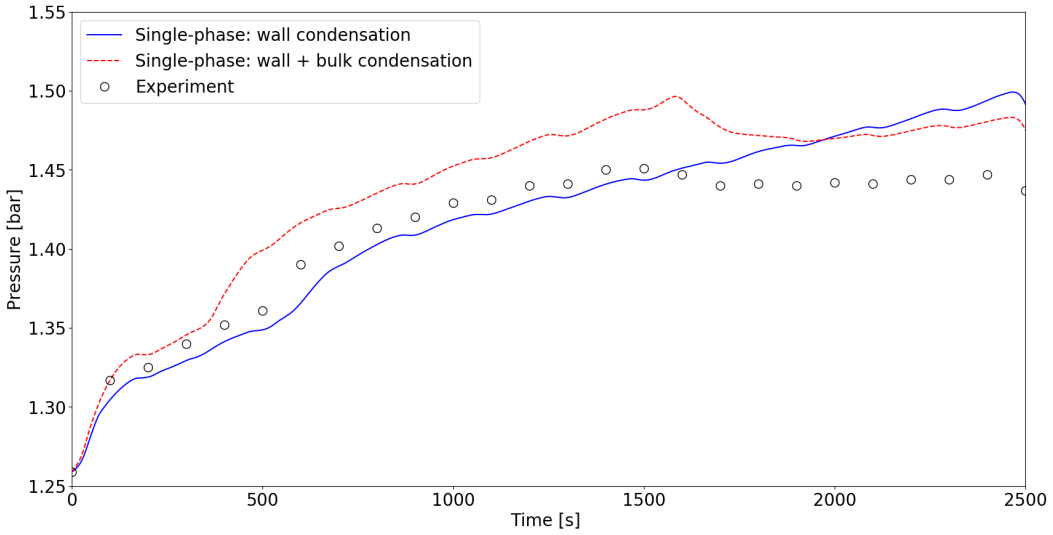

Figure 4.46.: HM2: Transient average vessel pressure variation with and without bulk condensation, employing single-phase approach.

During the initial stages, the steam plume gradually ascends through the inner cylinder and gets condensed on the inner walls. This can be seen as an increase in wall condensation rate, which is then followed by a sudden drop. This drop is due to the time required for the steam from the inner cylinder to reach the cooler vessel walls to cause further wall condensation. Then, the wall condensation remains steady until the steam reaches the cooler dome walls, which results in an abrupt increase in condensation rate that is consistent with the pressure decrease. These events occur in simulations with and without bulk condensation, but at different times. The simulation without considering bulk condensation exhibits considerable delay in representing these phenomena, while the bulk condensation simulations displayed good consistency with the experiment.

4.10.3.2. Single-phase v/s two-phase approach results

The two-phase simulations are performed with both wall and bulk condensation models. However, similar to the TH2 two-phase simulations, the HM2 also presents substantial computational challenges. The simulations must be run at lower time-step sizes for stability and convergence. Hence, the HM2 two-phase simulation is available only for up to 240 seconds, and those results are compared with the single-phase results to assess whether it can provide any considerable improvements in the physical phenomenology.

The comparison of the condensation rate distributions between both approaches (Figure 4.48) shows that the condensation zone with the two-phase approach is slightly more spread than the

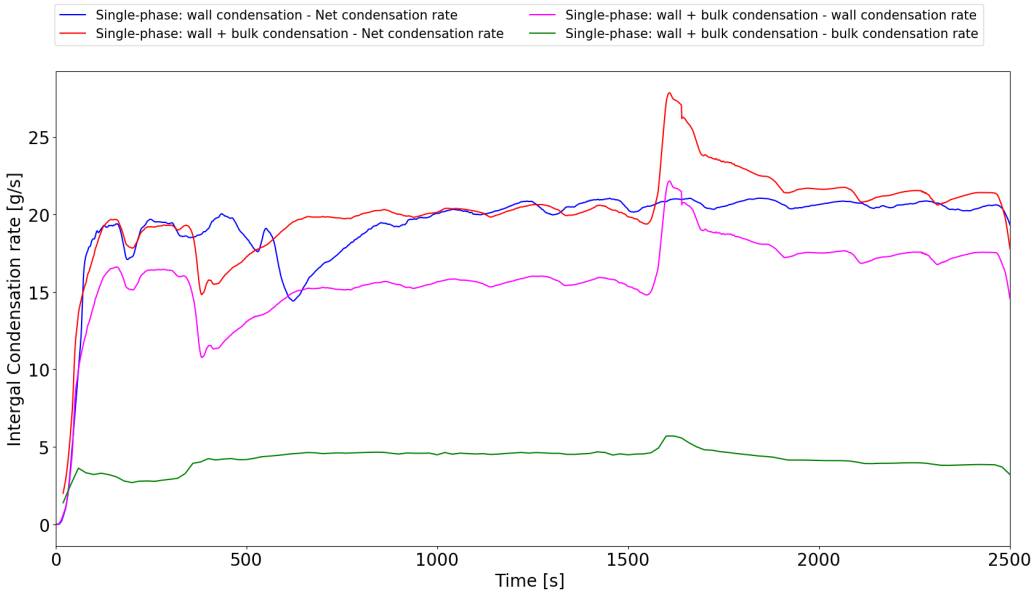

Figure 4.47.: HM2: Quantitative comparison of integral condensation rates with and without bulk condensation, including condensation mechanism-specific contributions to net condensation rate.

single-phase approach. The condensation rates are hence higher in the two-phase approach, and the reason for that is the inherent differences in the bulk condensation models of both approaches, as discussed in Sec.4.9.3.2. This results in higher fog concentration in the vessel, which can be observed in Figure 4.49. Also, due to the differences in the drift velocity boundary conditions between both phase approaches, the two-phase model keeps the water phase conserved with the computational domain. This reduced the deposition driving force towards the wall, resulting in higher fog concentrations. For the temperature field (Figure 4.50), the two-phase approach also predicts slightly higher values than the single-phase. This is related to higher condensation rates and the associated latent heat release. The quantitative comparison of the temperature (Figure 4.51) and hydrogen volume fraction fields (Figure 4.52) with the single-phase simulation and the experiments does not yield any significant improvement in the prediction accuracy by the two-phase approach. While minor local improvements were observed at certain locations during specific time intervals, the deviation from experimental data increased in other locations. The formation of surface wall films and their transport along the walls of the inner cylinder and vessel walls are demonstrated in Figure 4.53.

The continuous wall condensation and deposition of the droplets on the walls leads to the formation of films on the inner cylinder surface. These films flow down towards the sump region by gravity and the surface shear force exerted by the gas flow field. The film flow towards, combined with larger droplet depositions, results in the generation of film on the condensate trays and sump walls. The effect of the two-phase approach on the pressure is marginal in the considered short time period. The impact of condensate accumulation in the sump is not investigated due to the short duration of the experiment compared to TH2, which is insufficient to lead to any accumulation of water in the sump region.

4.10.4. Discussion

This section discussed the influence of the bulk condensation model in improving the prediction accuracy of gas mixing in a containment by simulating the THAI HM2 experiment. The comparison between the simulations including and excluding bulk condensation using the single-phase approach revealed that bulk condensation has a substantial effect on the local gas temperature distribution and mixing. The latent heat release associated with bulk condensation resulted in higher

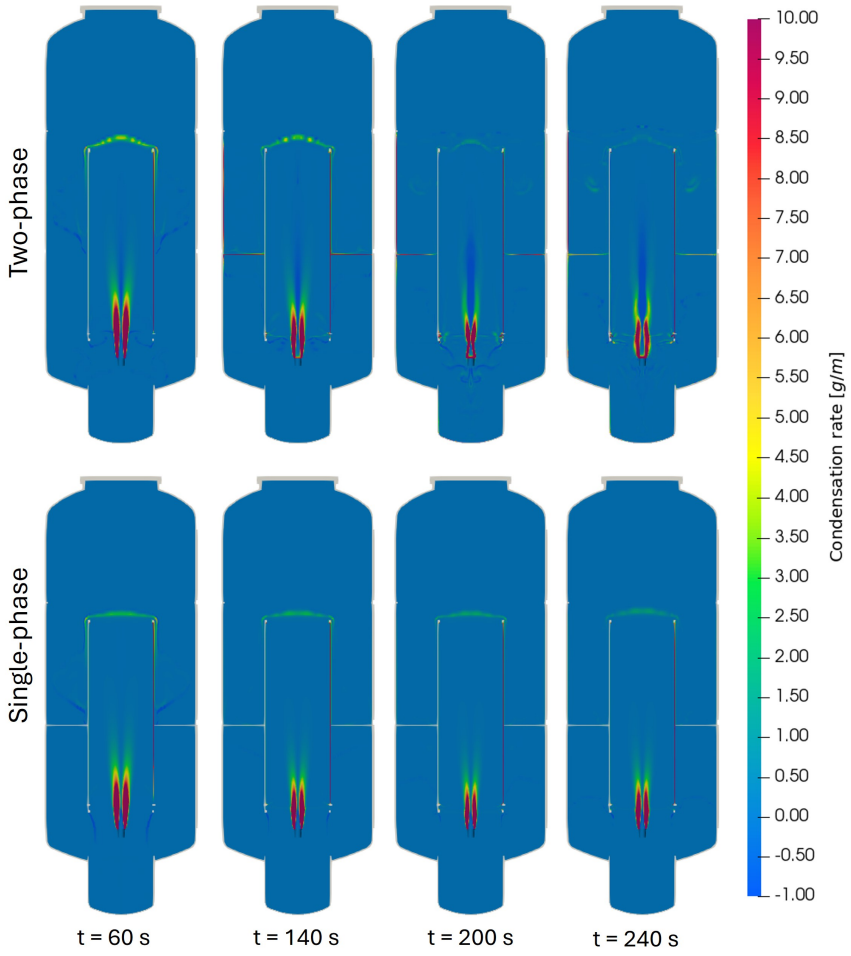

Figure 4.48.: HM2: Comparison of condensation rate distribution at the at different transient times between single-phase and two-phase approach.

temperatures and consequently higher buoyancy forces, which reduced density differences in the inner cylinder region compared with the simulation with only wall condensation. This resulted in faster dissolution of the hydrogen cloud by the injected steam, which is consistent with the experiment. The bulk condensation model significantly improved the predictions of the temperature and hydrogen concentration along the vessel height at different time intervals. The bulk condensation model also enabled better prediction of the timing of the steam plume contact with the dome wall and complete mixing of the hydrogen cloud. This validation study demonstrated that in scenarios where buoyancy effects are crucial, particularly with light gas/heavy gas mixture present, bulk condensation is a vital phenomenon that should not be omitted, which is usually important in nuclear reactor containment flows. The comparison of the available two-phase results with single-phase results indicated that the comparably costly two-phase approach does not offer any additional accuracy.

4.11. Summary

The systematic verification and validation of the computational models developed during the research work was conducted in this chapter. The Mollier mixing nozzle cases were used to verify the bulk condensation model against the Mollier diagram theory. The models are able to predict the quantity of fog, final mixture temperature, and steam content with reasonable accuracy for both condensation and evaporation simulations. The bent pipe deposition and ventilation chamber experiments validated the inertia and gravity sub-models of the drift velocity model, respectively.

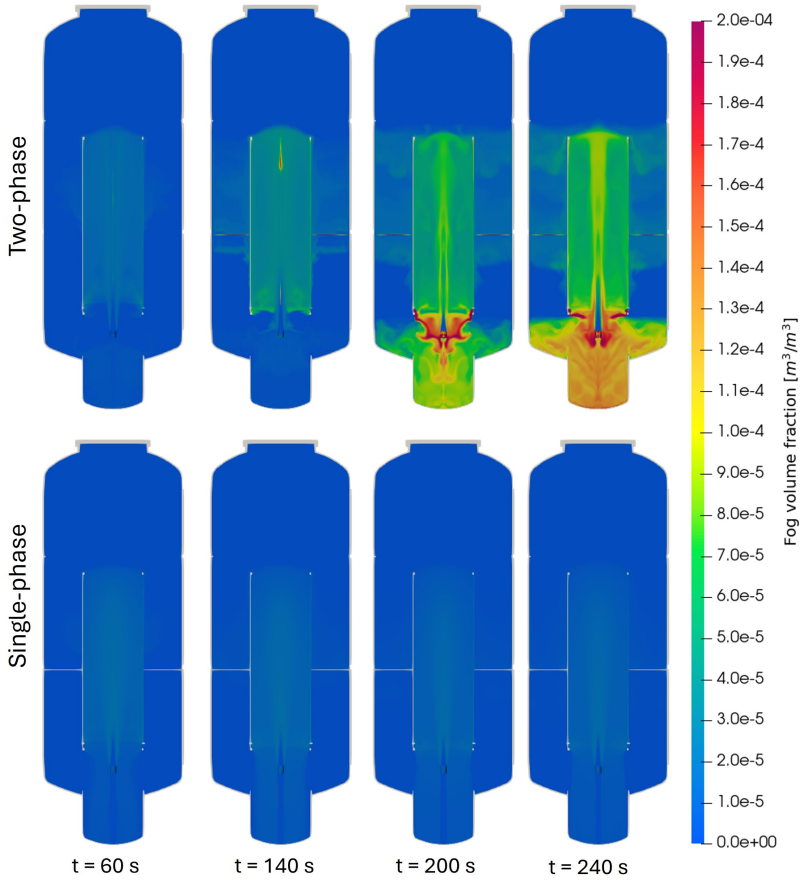

Figure 4.49.: HM2: Comparison of fog distribution at the at different transient times between single-phase and two-phase approach.

The Manninen drift velocity model offered the best trade-off between computational cost and accuracy than the Stokes model. Both single-phase and two-phase approaches yielded similar predictions across these simulations. The population balance model (PBM) was analytically verified using simple coalescence and growth simulation cases, which implied that the PBM droplet evolution model is effective. The surface film model in the two-phase approach was validated by simulating a thin film flow behavior over a flat plate, which demonstrated the capability of the model to capture the relative thickening of the film by the effect of counter-current airflow over the film. The conversion of the film mass to VOF liquid mass using the film-liquid phase mass transfer model demonstrated that the model is mass conservative and effective for the intended applications. The SETCOM simulations demonstrated that the bulk condensation has a marginal effect on the wall condensation rates. The comparison between the single-phase and two-phase approaches revealed that the two-phase approach is more sensitive to the mesh. However, this is primarily attributed to the mass sink method in the two-phase approach, against the face-flux method employed in the single-phase approach. Nevertheless, both approaches were able to predict the wall heat fluxes in the SETCOM experiment with reasonable accuracy. The two-phase approach was capable of modeling the film formation and its transport along the condensing wall. Subsequently, the models were tested on technical-scale experiments by including interactions with other sub-models. This was initially performed on the THAI TH2 experiment, which indicated the clear effect of bulk condensation on the local temperature field, fog formation and evolution, and its transport and deposition. However, there was no quantitative improvement in the temperature and pressure predictions compared to the experiment. The two-phase approach presented significant computational challenges, affecting the stability and convergence of the simulations. Even though the film formation and condensate accumulation were predicted by the model, it did not offer sig-

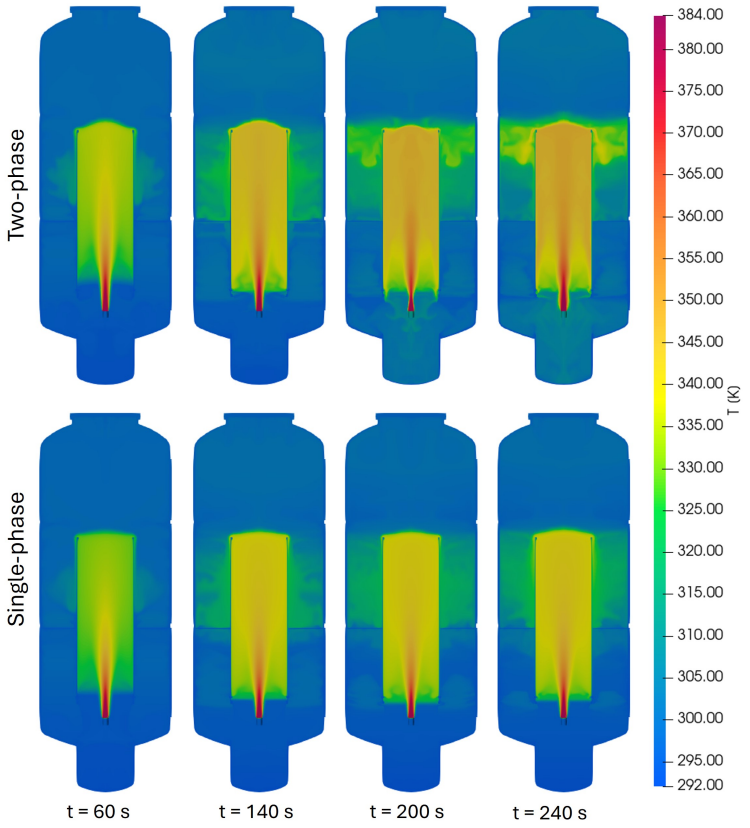

Figure 4.50.: HM2: Comparison of temperature distribution at the at different transient times between single-phase and two-phase approach.

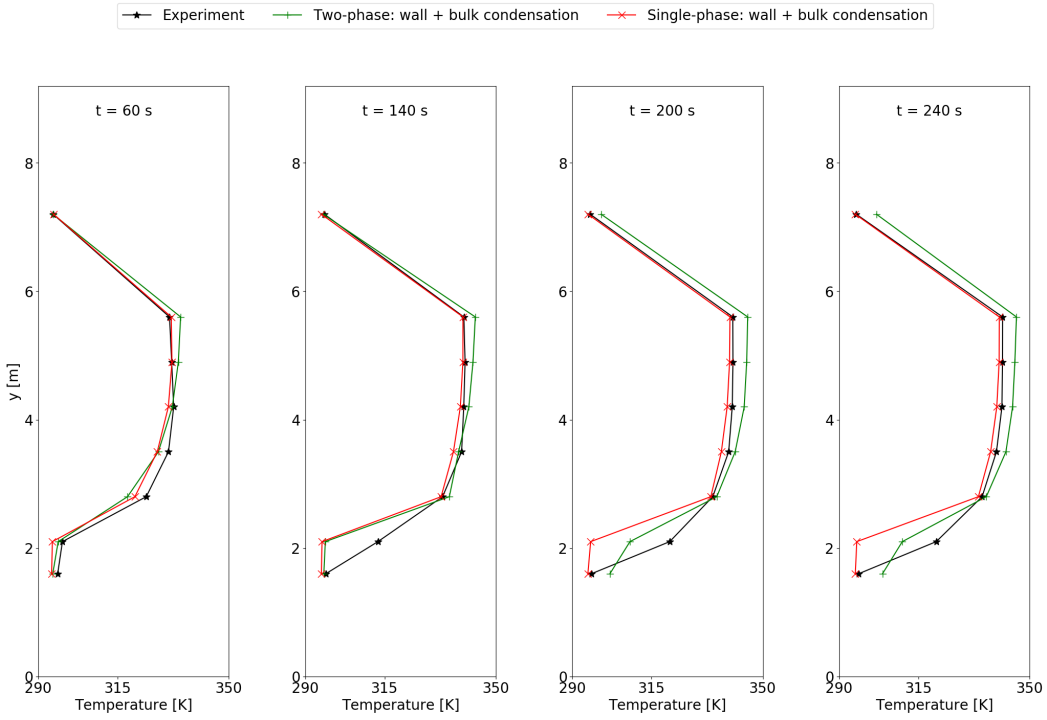

Figure 4.51.: HM2: Comparison of gas temperature distribution along the vessel height at a radial distance of 0.35 m and 300^o angular position at different time intervals between single-phase and two-phase approach.

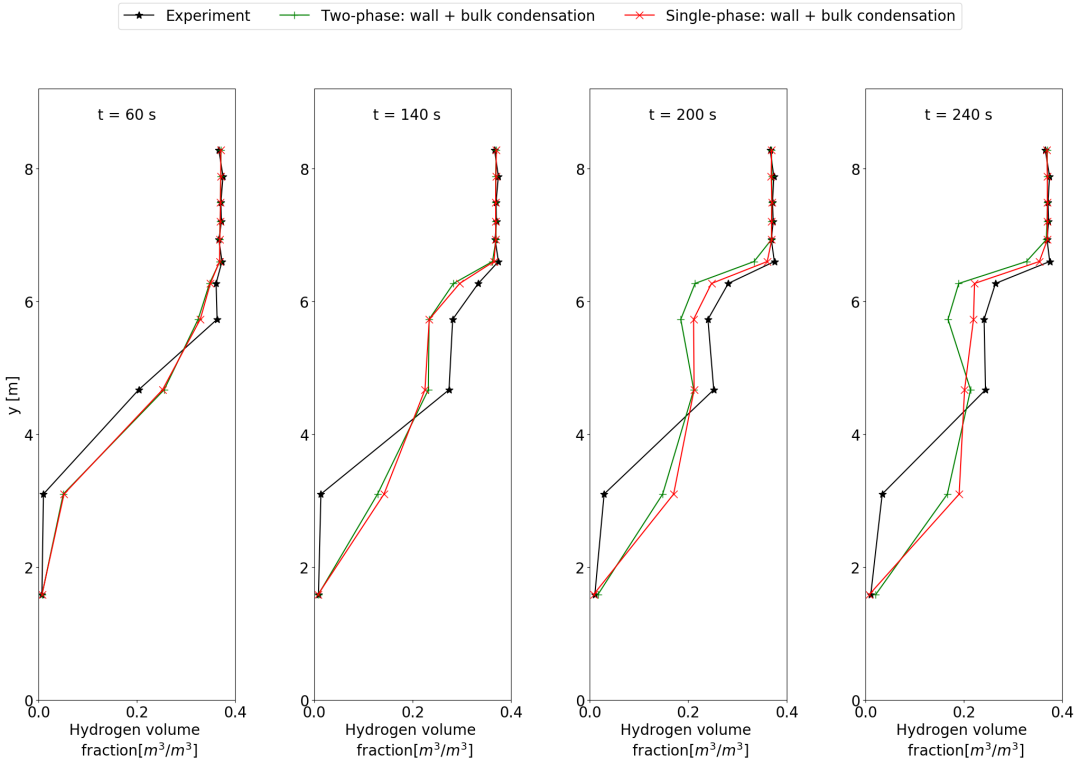

Figure 4.52.: HM2: Comparison of hydrogen volume fraction distribution along the vessel height at a radial distance of 1 m and 300^o angular position at different time intervals between single-phase and two-phase approach.

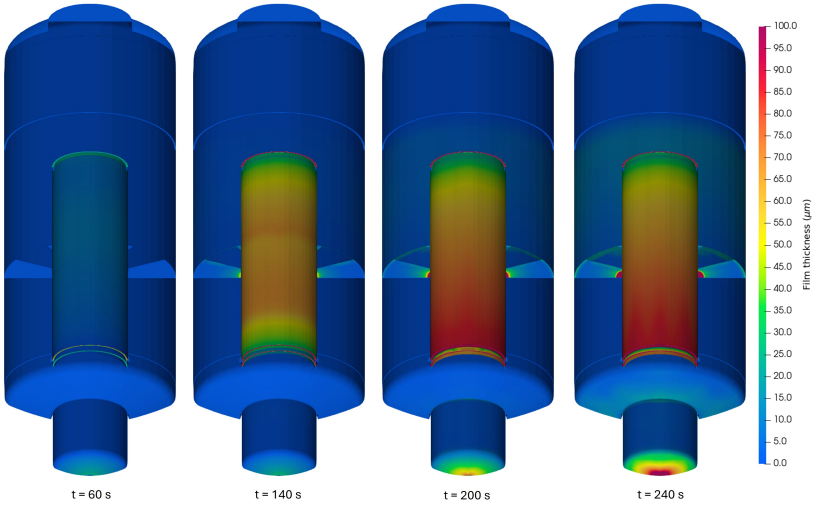

Figure 4.53.: HM2: Evolution of the film thickness along time, employing a two-phase approach.

nificant improvement in resulting pressurization and atmospheric composition. The THAI HM2 experiment was used for validation, which clearly demonstrated the effect of bulk condensation on gas mixing inside a containment. The simulations with the inclusion of the bulk condensation model were able to predict the vessel temperature and hydrogen concentration with excellent accuracy. It demonstrated the relevant impact of latent heat release and associated temperature rise, resulting in higher buoyancy forces, which were not captured by simulation with only wall condensation. The bulk condensation model enabled improved prediction of the timing of the steam plume reaching the dome, the complete mixing of the hydrogen cloud, and the trend in the pressure

transient. Again, the two-phase approach did not offer any additional improvement in the result, although it was able to capture the film generation and its transport. The HM2 simulation with the bulk condensation model revealed that bulk condensation has a substantial effect on the containment gas mixing and local temperature distribution and hence is an important phenomenon to be considered while developing CFD models for containment atmosphere mixing and H_2/CO risk mitigation. Hence, the developed single-phase bulk condensation model is a valuable addition to the *containmentFOAM* package for containment safety analysis. The settling of fog droplets and their re-evaporation is crucially influenced by droplet size, and the PBM approach can model this phenomenon effectively. While the two-phase approach demonstrates potential, it requires further refinement to improve stability, computational speed, and convergence. Also, it will be more valuable in scenarios where the volume of water or condensate constitutes a substantial portion of the overall containment space and films are of relevance (e.g., condensation of pure steam). Such a situation can be found in SMR (e.g., NuScale) and should be the focus of future development of the two-phase model.

5. Model Application

This chapter focuses on the application of the computational model developed and validated during this research work to simulate the VANAM-M3 experiment. The primary aim is to investigate the effect of bulk condensation and its interaction with other phenomena, while also demonstrating the capability of the CFD code to perform realistic large-scale containment simulations with multi-phenomenon interaction. The first section explains the International Standard Problem (ISP-37) VANAM-M3 experiment, its components, and the experimental procedure. This is followed by defining the computational domain, mesh, boundary and initial conditions, and other relevant simulation parameters. The study concludes by analyzing the differences between results with and without the bulk condensation model, and by comparing simulation results to those from experiments.

5.1. The VANAM M3 experiment

The VANAM M3 experiment was a part of the International Standard Problem No. 37 (ISP-37), which aimed at validation of the numerical codes developed for nuclear safety analysis. The experiment was conducted in the Battelle Model Containment (BMC) facility to investigate multi-compartment aerosol depletion and thermal-hydraulic behavior in a nuclear reactor containment during severe accident conditions. The containment phenomena of interest in this experiment in addition to aerosol distribution and settling were the formation of stratified atmosphere, atmospheric mixing by convection loops, the thermal energy balance, wall and bulk condensation, and structural heat transfer. To investigate the hygroscopic aerosol component and steam condensation on the aerosols, saturated and super-saturated conditions were considered.

The BMC VANAM facility (Figure 2.4) has a free volume of 626 m^3 consisting of several compartments that are interconnected to replicate a German PWR containment. The different compartments and the location of the air-steam injection in the facility are illustrated in Figure 5.1. The reactor room, central compartment, and reactor cavity are represented by R1, R2, and R3, respectively. The room R4 is a dead-end compartment with surrounding walls representing staircases. The remaining rooms R5, R6, R7, and R8 symbolize the upper and lower steam generator compartments. The room R9 constitutes the containment dome, sump, and annular region between the concrete structure and the compartments. The air-steam and aerosol injections are located in the upper steam generator room R5 through a vertical pipe, as indicated in Figure 5.1. The inner and outer walls of the facility are made of reinforced concrete. The reinforced concrete, with no steel liner, resulted in the leakage of gases to the surroundings under high pressures. This introduces significant challenges in CFD simulations as this leak rate is difficult to quantify [Vijaya Kumar, 2022].

The experimental procedure consists of several phases, each representing different stages of a hypothetical accident. The first phase (t = -57850 - 0 s) is the preconditioning of the test facility by steam injection. The steam is released into the R5 compartment to heat up the facility, and the steam release rate is controlled to maintain the containment pressure at 1.25 bar. During this

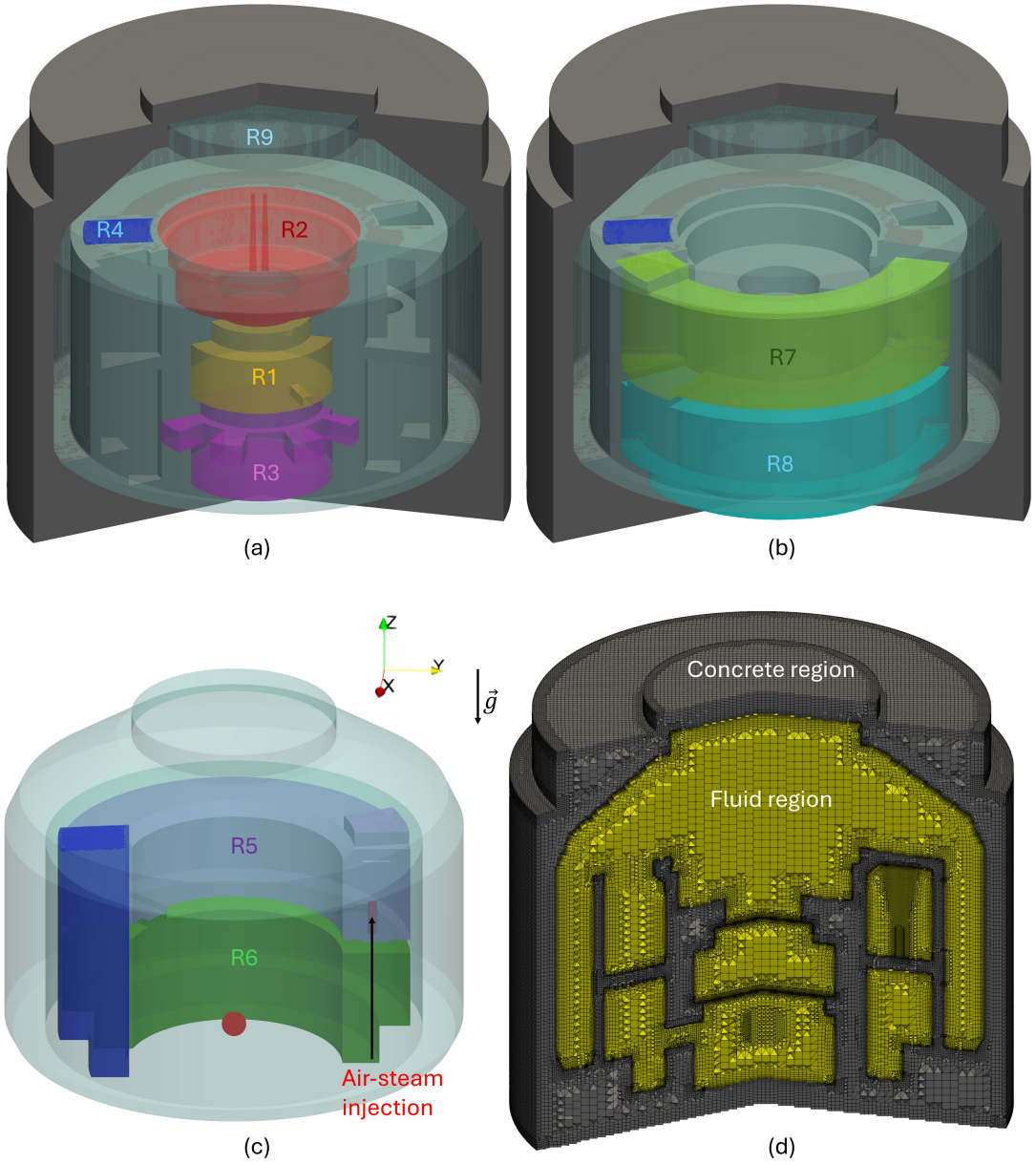

Figure 5.1.: VANAM: (a,b,c) The geometry of the Battelle Model Containment (BMC) illustrating the different compartments and location of air-steam injection. (d) Section view of the two-region mesh used for performing the simulation.

phase, the air is also drained out through R9, which allows the steam to enter the lower sections of the containment and heat up the walls. Towards the end of phase 1, the drained air is re-injected into the R9 to achieve the desired air content and pressure level. The second phase (t = 0-3700 s) constitutes the injection of the NaOH aerosol along with the hot air-steam mixture into the R5 compartment. This leads to the increase in the containment pressure from 1.25 to 2.05 bar. The third phase (t = 3700-19800 s) is the aerosol depletion stage, during which no gas is injected into the containment. The condensation of steam during this phase leads to a pressure drop to 1.25 bar in the containment. This is followed by 3 more phases, which include a second aerosol release, wet aerosol depletion, and further wet aerosol depletion, spanning a transient period from t = 19800 to 46080 seconds. However, the application analysis is conducted only for phases 2 and 3.

The experiment was equipped with instrumentation necessary to measure several key parameters. The containment pressure was measured by two strain gauge pressure transducers. Thermocou-

ples were used to monitor the temperatures of the containment atmosphere, concrete structure, and compartment sumps. The gas flow velocities across the compartments were measured by bidirectional turbine flow meters. The relative humidity of the containment atmosphere was measured by multiple capacitive humidity sensors. Steam mass flow rate was determined by using orifice obstruction meters. The aerosol concentration and particle size distribution were measured by filter stations operated at seven different locations in the containment.

5.2. Simulation setup

The VANAM application simulation is an extension of the previous work by Kelm et al., 2022 andVijaya Kumar, 2022. Due to the complicated nature of the geometry and lack of symmetry, a complete three-dimensional mesh is required to encompass the full containment. The construction of block-structured mesh using ICEM-CFD for such a geometry is not feasible. Hence, a hex-dominant unstructured mesh is generated using commercial automatic meshing software, *cfMesh+*, which is shown in Figure 5.1. It constitutes the fluid region with 2.61 million elements and the concrete solid region with 2.92 million elements [Kelm et al., 2022, Vijaya Kumar, 2022]. Two simulations are performed, one with wall condensation and the other including wall and bulk condensation, to assess the effect of bulk condensation on containment conditions and solver stability and runtime. The simulations were conducted using only the single-phase approach, as two-phase is computationally expensive for large-scale experiments. The fog transport is modeled using Manninen drift velocity method with the deposition boundary condition on the walls. The PBM approach is used with fog droplet diameter range between 1 μm and 128 μm in 8 different size groups. The droplet evolution by condensational growth, evaporational shrink, and coalescence are also included. The air-steam gas mixture flow is turbulent and is modeled using $k-\omega$ SST model [Kelm et al., 2022, Vijaya Kumar, 2022]. At the fluid-solid interface, the conjugate heat transfer boundary condition is used for the temperature field.

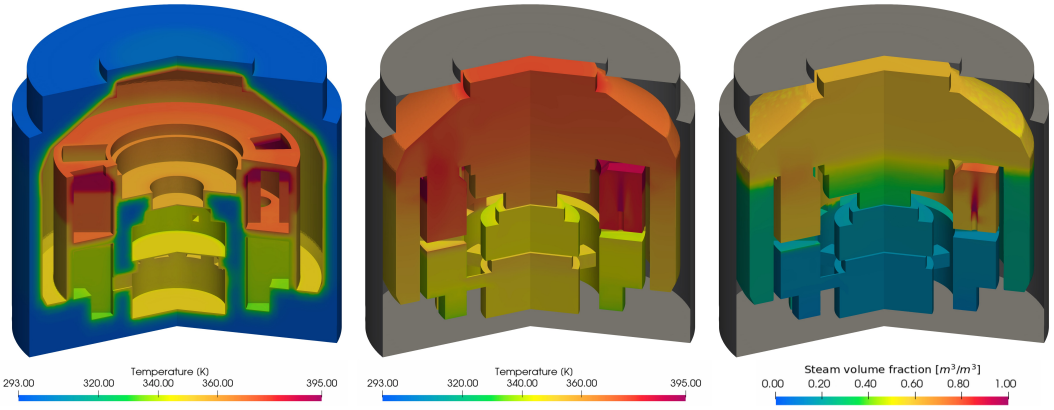

Figure 5.2.: VANAM: The structure temperature (left), fluid region temperature (middle) and steam distribution (right) approximated for the initialization of phase 2 based on experimental data.

Phase 1 of the experiment is substantially long, and it is not computationally feasible to run such long transients ($\approx$ 16 hours). Hence, the simulations that are performed span only phases 2 and 3, with a total duration of around 18000 seconds. The initial structure and fluid temperature (Figure 5.2) are estimated by interpolating the sensor values into the computational domain. Also, the initialization of steam distribution (Figure 5.2) is done by mapping the relative humidity sensor values into the fluid region. This causes significant uncertainties in the simulation conditions compared to the experiment, but still represents the most feasible approach. However, the objective of this simulation is to investigate the effect of the bulk condensation model and demonstrate its ability to run large-scale containment analysis, which remains achievable. The steam injection

during phase 1 also generates fog droplets, which can remain suspended in the containment until the end of phase 1. Regardless, this quantity and distribution of fog are unknown and hence the simulation is initialized with zero fog assuming all fog settled and thermal equilibrium is achieved. Phase 2 of the experiment involved injection of an aerosol along with an air-steam mixture. However, the aerosol transport and depletion are not in the scope of this application study. Hence, the simulation is performed with only the injection of the air-steam mixture into the R5 compartment. Another important parameter to be considered in the simulation is the leakage of the gas mixture through the concrete structures. This is modeled as a volumetric sink in the R9 compartment, with mass loss rate estimated from the transient variation of air mass measured in the experiment. The previous simulation [Vijaya Kumar, 2022] overestimated this leak rate; consequently, the current work employs 10% of reduced rate to improve the accuracy. The simulations used adaptive time-stepping during the initial stages (t = 0-200 s) due to the initial condition uncertainties, lack of thermal equilibrium, and deviation from saturation conditions. As the simulation became stable, a fixed time-step size of 10^{-3} s with Courant numbers in the range of one to five was employed to accelerate the computation process.

5.3. Results

The bulk condensation and wall condensation simulations are run for 14000 seconds. The bulk condensation simulation is analyzed first to examine the influence of bulk condensation. The bulk condensation rate, fog volume fraction, and droplet Sauter mean diameter distributions are shown in Figure 5.3. During the initial stages (t = 900-2000 s), the bulk condensation primarily occurs in the R6 and R9 compartments, which is predominantly due to the presence of cold structures. This resulted in bulk condensation in those regions, even before the phase 2 injected steam reached these locations. The associated fog formation and drift of the larger droplets towards the sump of the compartments can also be observed.

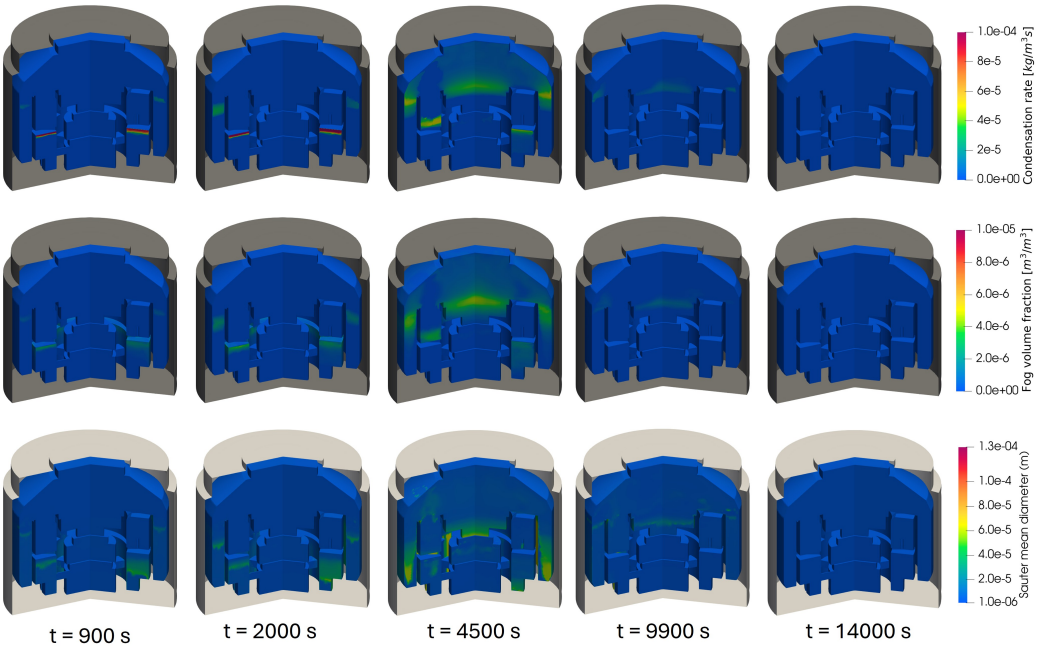

Figure 5.3.: VANAM:Condensation rate (top), Fog volume fraction (middle) and Sauter mean diameter (bottom) distributions with wall and bulk condensation at different time intervals.

After the completion of the steam injection (t = 3700 s), at the mid-stage (t = 4500 s), the steam released from the R5 compartment reaches the R9 dome and annular regions and starts condensing

in the form of fog in those locations. This can be seen as a large cloud of fog in the upper containment and annular regions. Some of the steam also reaches the other end of the R5 compartment and leads to bulk condensation and fog formation. The coalescence and growth, followed by gravity effects, force the larger droplets in the dome region to deposit on the R2 and R9 sump. This can be observed in the Sauter mean diameter distribution. As the steam concentration inside the containment decreases by condensation, the bulk condensation rate is reduced to t = 9900 s. The remaining fog gradually settles down on the compartment structures, decreasing the fog content further. Finally, towards the end of the simulation (t = 14000 s), the steam concentration has diminished to levels insufficient to trigger bulk condensation, and the residual fog has deposited on the compartment sumps.

The qualitative comparison of the transient evolution of gas temperature (Figure 5.4 and 5.5) and steam concentration (Figure 5.6) distributions between the simulations with and without bulk condensation did not indicate any notable differences. The bulk condensation rates are small compared to previous THAI simulations, resulting in insufficient latent heat release to induce large temperature changes.

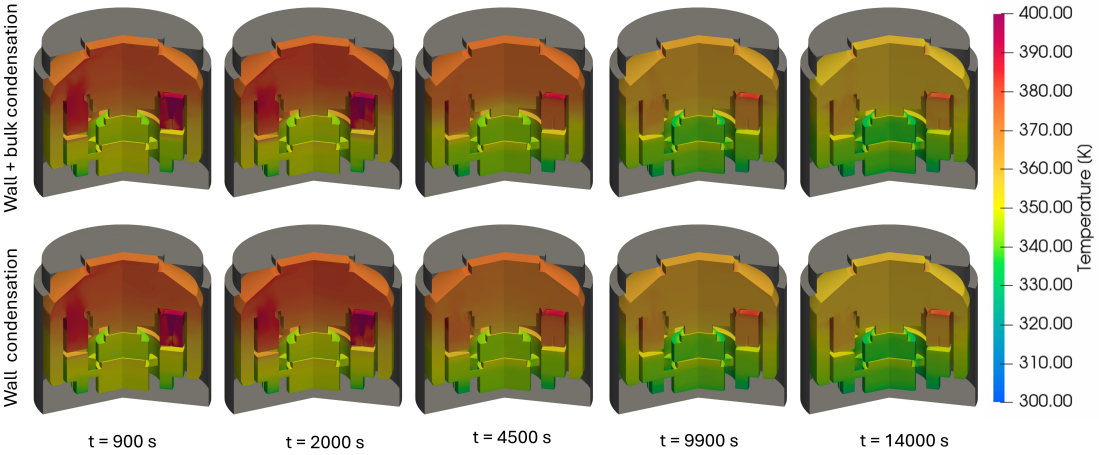

Figure 5.4.: VANAM: Comparison of transient gas temperature distribution between simulations with wall condensation and with wall and bulk condensation.

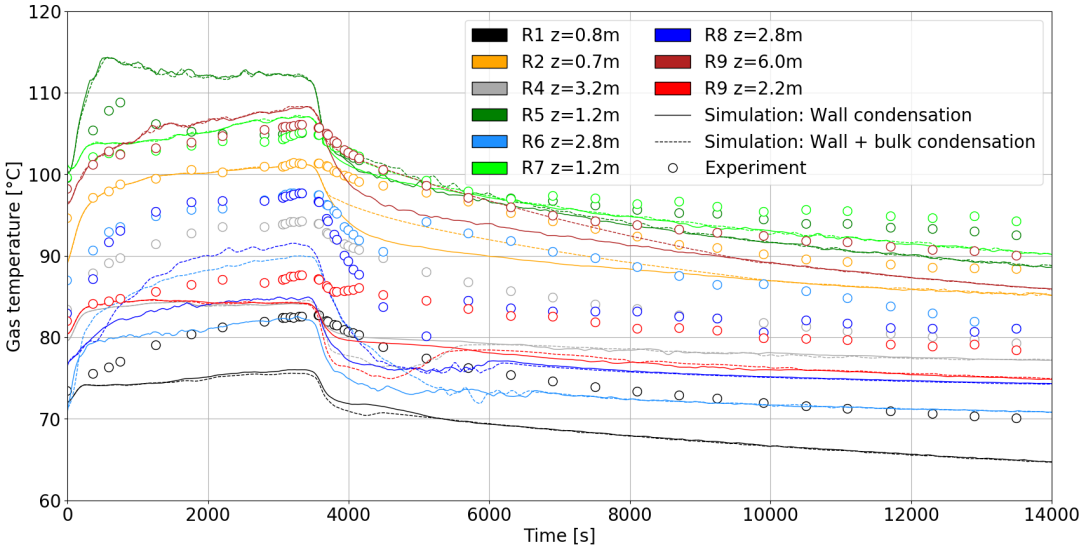

Figure 5.5.: VANAM: Comparison of gas temperature transients between the experiment and simulation with and without bulk condensation model.

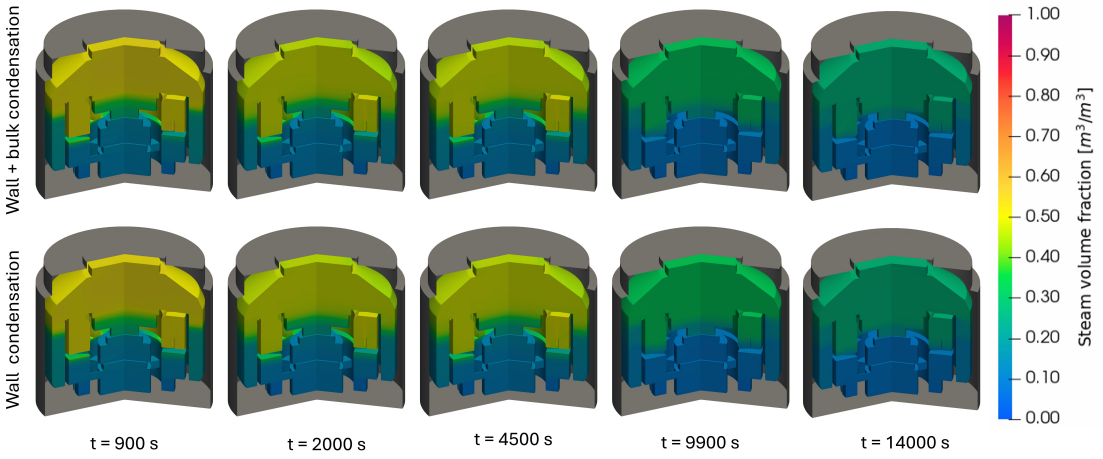

Figure 5.6.: VANAM: Comparison of transient steam volume fraction distribution between simulations with wall condensation and with wall and bulk condensation.

The comparison of the simulation gas temperatures with experimental values (Figure 5.5) during the transient revealed that the bulk condensation simulations are able to predict the temperature evolution in the containment compartments like R2 and the upper region of R9 more consistent with the measurement. The wall condensation model under-predicted the temperatures in these rooms during the mid-stage (t = 3500-8000 s), while the bulk condensation model improved the temperature predictions. This is due to the latent heat release and associated temperature rise caused by bulk condensation. Additionally, the bulk condensation model demonstrated better accuracy in temperature predictions for rooms R6 and R8 during the initial stages of the simulation. However, the temperatures in the compartment regions like R1 and the lower region of R9 showed further deviation from the experimental temperatures with bulk condensation.

The temperatures in these regions during their mid-stages (t = 1000-5000 s) are lower than the only wall condensation simulations. This phenomenon can be explained by the evaporation of fog droplets, which absorb the latent heat from the surroundings, decreasing the local temperatures. This process occurs due to the presence of fog droplets, which have been previously generated in the regions above them by bulk condensation. It was observed that some bulk condensation and fog formation happened in these regions (Figure 5.3) during the initial stages of the simulation (t = 900 s), even before the injected steam reached those locations. This unexpected early fog formation was interpreted as a result of uncertainties in domain initialization resulting from sparse instrumentation. Consequently, the under-prediction of temperatures in these regions by the bulk condensation model can be attributed to these initialization differences.

Nonetheless, the comparison of the vessel pressure evolution of both simulations with the experiment reveals that the pressurization during the injection phase (t = 0-3000 s) was consistent with the experiment (Figure 5.7). However, at later stages (t = 3000-14000 s), the peak value and depressurization phase pressures are overpredicted by the simulations. This is due to the discrepancies in the integral air mass between the experiment and simulations (Figure 5.8), arising from the uncertainty in the specified leakage rate. The integral air mass in the simulations indicated over-prediction in the depressurization phase. The additional mass of air in the containment resulted in the over-prediction of pressure during that phase. The influence of the bulk condensation on the containment pressure is marginal, which can be attributed to lower rates of bulk condensation compared to wall condensation.

The simulations with and without bulk condensation are stable for most of the transient (200-1400 s), except during the initial stages (0-200 s). To address the initial instability, smaller time-step sizes ranging from 10^{-5} to 10^{-4} seconds were employed, and once stability is achieved, the time-

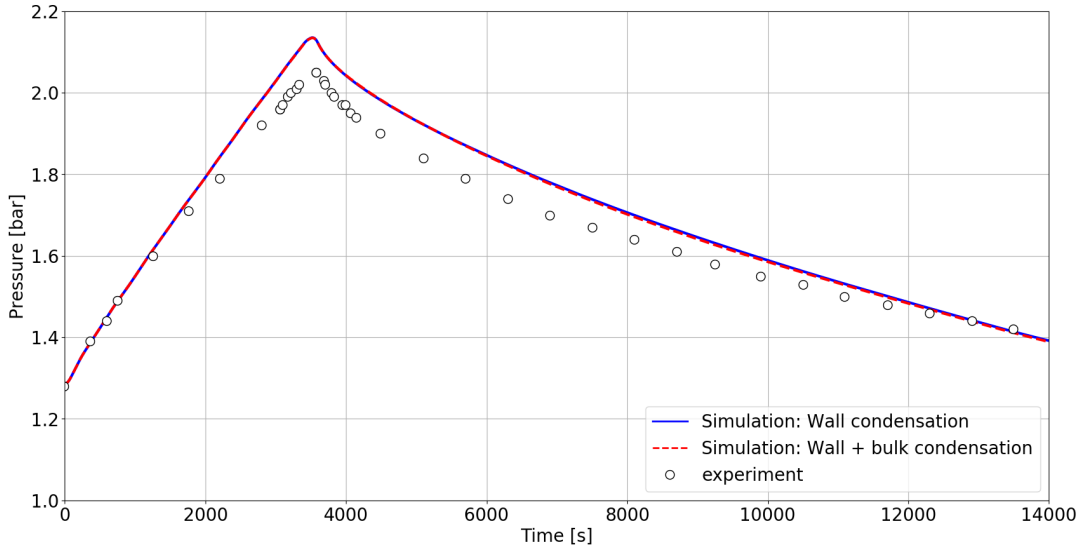

Figure 5.7.: VANAM: Transient evolution of the containment pressure.

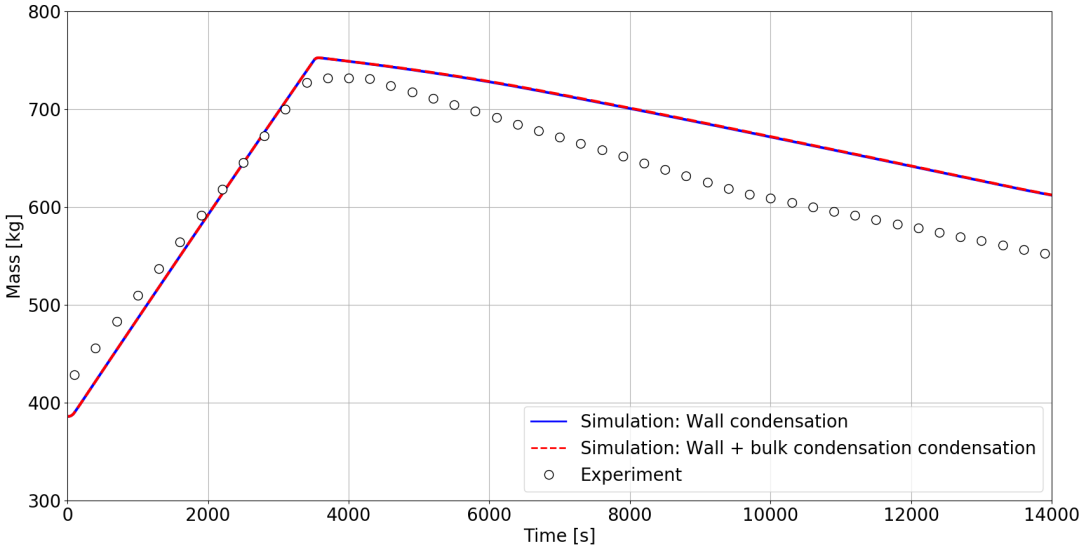

Figure 5.8.: VANAM: Transient evolution of the containment air mass.

step size is increased to 10^{-3} seconds. A comparison of overall processing times indicated that simulations involving bulk condensation required approximately 30 % more runtime than those that considered only wall condensation, which is reasonable for large-scale applications.

5.4. Discussion

The technical-scale assessment of the single-phase bulk condensation CFD models developed during this research work was conducted on the BMC using the VANAM M3 experiment. The objective of demonstrating the capability of the CFD solver to perform feasible simulations on an experiment replicating the severe accident conditions in a nuclear reactor was achieved. The interaction of the bulk condensation model with the other containment phenomena like turbulence, buoyancy-driven flows, multi-component gas diffusion, and wall condensation was examined. The bulk condensation model successfully simulated the fog formation, droplet growth and coalescence, and also its transport by convection and drift. While the inclusion of the bulk condensation model did not significantly affect the containment pressure predictions, there was a notable improvement

in the prediction of transient temperatures in the upper compartments of containment, to which the steam rises by buoyancy effects. The incorporation of the bulk condensation model, along with the associated latent heat release, resulted in increased local temperatures in these compartments, aligning more closely with experimental values. The simulations were stable for the majority of the transient, and the simulations with bulk condensation were only 30 % more expensive than without bulk condensation.

6. Summary and Conclusions

During a severe accident in nuclear power plants (NPP), the events inside the containment can lead to hydrogen combustion, which could damage the containment's structural integrity and allow harmful radioactive materials to be released into the surrounding environment. The reliable estimation of the gas mixture composition, the local temperatures, and pressure built-up in containment systems is fundamental for designing and evaluating an effective accident management strategy. There are several interacting thermo-fluid dynamic phenomena inside the containment, like multi-component gas diffusion, turbulence, buoyancy, wall and bulk condensation, fog transport and re-evaporation, wall film flows, condensate accumulation, radiation heat transfer, and conjugate heat transfer. The interplay of these various phenomena ultimately establishes both the local and overall conditions within the containment. The condensation of steam in the bulk and walls leads to the formation of fog droplets and films; their transport and re-evaporation affect the containment atmosphere. The latent heat released during the bulk condensation causes higher local temperatures, and the reverse process of fog droplet evaporation absorbs the latent heat from the surrounding gases and leads to lower local temperatures. These temperature gradients can significantly affect the local buoyancy forces, influence gas flow velocities, and thus the gas mixing in the containment. The fog droplet transport under the effects of convection, gravity, and inertia is also influenced by the droplet diameters, which evolve by condensational growth, evaporation shrink, and also coalescence. Consequently, a computational model is developed in this research work to examine the impact of bulk condensation, fog transport, and evolution on the containment behavior and its interaction with other phenomena. The model is implemented into the existing *containmentFOAM* solver [Kelm et al., 2021] which is equipped with models for turbulence, buoyancy, multi-component gas diffusion, wall condensation, conjugate heat transfer, and radiation heat transfer, using the single-phase approach. The present work also includes the extension of the solver to a two-phase approach to address the shortcomings of the single-phase approach and facilitate the investigation of condensate transport and accumulation under the containment conditions.

The objectives of this research work are two-fold: first, develop and implement a bulk condensation model to determine the fog formation rate, and transport, evolution and re-evaporation of the fog droplets using a computationally efficient passive scalar method incorporated with Population Balance Model (PBM), all within a single-phase framework; second, develop a two-phase approach combining the mixture, VOF and film approaches to reform the single-phase *containmentFOAM* solver to a two-phase solver to model the influence of condensate mass in the computational domain, and also simulate the formation of wall films, the deposition of droplets on these films and accumulation of condensation in the sump region forming gas-liquid interfaces. The computational models are developed systematically in the order of complexity, which begins with the single-phase passive scalar approach and ends with the two-phase mixture-film-VOF approach. Finally, the comparison of the modeling strategies is conducted to identify the required level of modeling detail and ensure an efficient representation of bulk condensation and for transport on large-scale dry containments.

For the single-phase passive scalar approach, the bulk condensation rate is modeled using a "*return to saturation at constant time scale*" method, which is simple to implement and also computes the bulk evaporation rate. A fog droplet transport equation is developed that considers the droplet's motion by the gas flow field, drift velocity, Brownian and turbulent diffusion, and also incorporates the source term from the bulk condensation model. This is implemented using a passive scalar approach in a Eulerian framework. The drift velocity of the droplets considers the effects of gravity, inertia, and drag, and two formulations, Manninen and Stokes, are used to compute the drift velocity. This fog transport volume transport equation is initially developed for mono-dispersed droplets and then extended for poly-dispersed droplets using a population balance model (PBM) employing the method of classes. The PBM model incorporates droplet evolution processes like nucleation, condensational growth, evaporational shrinkage, and coalescence.

For the two-phase mixture-film-VOF approach, a combination of the best features of the mixture, volume of fluid (VOF), and surface film approaches are utilized. The development of a hybrid mixture-VOF model is initially performed by deriving and formulating the governing equations for two-phase field variables. An indicator function is defined to determine the locations where the liquid phase is in dispersed form and in continuous form. The models and terms corresponding to the mixture approach and VOF approach are then added to the governing equations based on this indicator function value in a mesh element. For instance, the drift velocity model is relevant only for the mixture approach and hence, this term is added only to the elements where liquid is in dispersed form. Similarly, the interface compression velocity is only relevant for VOF approach and is added only to elements where a gas-liquid interface is present. The surface thin film approach is used to model the generation and flow of thin films over the walls, which reduces the film-governing equations to a two-dimensional form. The film approach is more accurate and computationally cheaper than VOF model to predict thin film flow over walls on coarse near-wall meshes. A film-liquid phase mass transfer model is implemented to facilitate mass, energy, and momentum exchange between the film and the liquid phase in VOF. This model enables the use of the surface film approach when the film thickness is less than the near-wall cell thickness of VOF, and when the film is thick enough to form an interface in the VOF region, then VOF approach is used. The bulk condensation rate is calculated using the same model as in single-phase, but some fraction of the latent heat released is absorbed by the fog droplets, which was not considered in the single-phase approach. The wall condensation model is in two-phase uses a mass sink method against the face-flux method used in the single-phase approach. The model is also extended to facilitate interface condensation in the VOF region. The PBM approach employed already for the single-phase model is extended to the two-phase approach by using the indicator function to compute the dispersed phase volume fraction and solve the PBM equations.

The systematic verification and validation of the CFD models are conducted using theoretical studies, separate-effect small-scale experiments, and integral-effect technical-scale experiments. The bulk condensation model is verified using Mollier diagram theory by simulating the mixing of cold and hot air-steam mixtures in a nozzle. The model predictions of final temperature, vapor content, and fog content exhibited good agreement with the theoretical data for both condensation and evaporation scenarios. The discrepancies between the single-phase and two-phase approaches are found to be marginal. The validation of the inertial part of the drift velocity model is performed by comparing the fog droplet deposition efficiency in a bent pipe simulation using Manninen and Stokes methods against experimental data. The Stokes method displayed slightly better accuracy than the Manninen method in both single-phase and two-phase approaches. However, the Stokes model was revealed to be three times computationally more expensive than the Manninen model, which cannot justify the minor additional improvement it offered. Hence, the Manninen model is recommended for most containment simulations. The gravitational part of the drift velocity model is validated by comparing the vertical particle concentration distribution in a ventilation chamber experiment. The Manninen and Stokes methods, employing the single-phase and the two-phase approaches, produced nearly identical results and also showed reasonable agreement

with the experimental data, substantiating the selection of Manninen model for future work. The Population Balance Model (PBM) is verified analytically using theoretical coalescence and growth models, which indicated that the numerical implementation is effective in predicting fog droplet size evolution. The surface film model is validated by simulating the flow of a thin water film flow down an inclined plate with and without counter-current flow. The mean film thickness predicted by the model matches the experiments, and the relative thickening of the film by the counter-current airflow is also well comparable with the experiment. The verification of the film-liquid phase mass transfer model done by simulating a hypothetical vessel in which the film is injected along the vertical walls of the vessel and the accumulation of the water in the sump region is examined. The model successfully simulated the vessel filling process while ensuring total liquid mass remains conserved.

The global performance of the wall condensation model is validated using the SETCOM experiment, at a scale and level of complexity closer to the technical-scale application. The single-phase approach is able to predict the total wall heat fluxes reasonably well for coarse and fine near-wall meshes, whereas the two-phase approach under-predicted the wall heat fluxes slightly on fine meshes and moderately on coarser meshes. This is attributed mainly to the differences in the model implementation in the phase approaches, in which a face-flux method is employed by the single-phase approach, while the two-phase approach uses a mass sink method. The influence of bulk condensation is observed to be marginal; nevertheless, the model is able to include its effect. The formation and transport of the wall condensate film are also observed with the two-phase approach incorporating the surface film model. The capability of the integral computational model in predicting the containment atmosphere conditions is initially examined using the THAI TH2 experiment. The comparison between the simulations with and without the bulk condensation model revealed that the bulk condensation leads to higher temperatures in the upper vessel zone due to the latent heat release. When these predictions were compared against actual sensor temperature readings, the results were overall more consistent with measurements. At certain locations, the model demonstrated improved accuracy, aligning more closely with experimental data. However, at a few other points within the containment, the predictions deviated more significantly from the measured values, which could not be explained based on the sparse experimental dataset. The model is able to simulate the fog transport, droplet evolution, and differential settling of the droplets depending on their diameter. The influence of bulk condensation on the pressure is marginal, as the overall condensation rate and equilibrium state remained the same with and without bulk condensation. The two-phase simulations turned out to be computationally intensive, resulting in higher processing times without yielding significant improvements in accuracy. Despite these limitations, the simulations successfully captured key physical phenomena. Notably, the model effectively represented the formation of a condensate film on containment walls and depicted the accumulation of condensate in the sump area, which might be a relevant insight for SMR containments. The validation study employing the THAI HM2 experiment revealed the substantial impact of bulk condensation on the local vessel temperature distribution and gas mixing. The latent heat release during bulk condensation led to higher temperatures and consequently higher buoyancy forces in the inner cylinder region, which is not captured in the simulation with only wall condensation. Additionally, the model accurately predicted the timing of the hydrogen cloud dissolution, a critical safety parameter in severe accident scenarios. Overall, the incorporation of the bulk condensation model significantly enhanced the accuracy of temperature and hydrogen concentration predictions throughout the vessel, underscoring the importance of including bulk condensation phenomena in containment simulations.

The difference in levels of influence of bulk condensation on containment conditions between the TH2 and HM2 can be attributed to the location of steam injection. In TH2, the steam injection is in the upper section close to the dome, providing insufficient distance for the buoyancy effects to have a significant impact. However, in HM2, the steam injection happens in the lower section, allowing buoyancy flows to exert a noticeable influence. Hence, the location of steam release can be a

crucial parameter that determines the scale of influence of bulk condensation within a containment. The practical application and scalability of the developed CFD model are finally demonstrated on the large-scale Batelle Model Containment (BMC) using the International Standard Problem (ISP-37) VANAM M3 experiment. While the bulk condensation model did not improve containment pressure predictions significantly, the accuracy of transient temperature predictions in the upper containment compartments increased notably, with the simulated local temperatures aligning more closely with experimental values.

In conclusion, this research successfully developed and implemented a bulk condensation model and fog droplet transport with PBM using both single-phase and two-phase approaches. The validity, applicability, and necessity of these models were successfully demonstrated through systematic testing and application runs. The single-phase approach is computationally efficient and feasible for large dry containment applications, while the two-phase approach requires substantial enhancements in the direction of stability and speed and might become necessary in SMR containment analysis. The significant impact of bulk condensation on local temperatures, gas compositions, and buoyancy forces underscores the need for inclusion of bulk condensation effects in CFD codes for containment flows. The bulk condensation model is a significant addition to *containmentFOAM* CFD toolbox, offering enhanced capabilities for analyzing containment atmosphere mixing, other effects related to fog transport such as aerosol behavior or gas radiation transport, and mitigating H_2/CO risks in nuclear reactor safety assessments.

7. Outlook

The current work presented the development, implementation, validation, and application of a bulk condensation model and the transport of generated fog using the PBM method to include the droplet evolution and drift velocity effects. The bulk condensation used a simple saturation temperature-based model, which was easy to implement and also very stable in technical-scale simulations. However, it was observed that in some cases, the bulk condensation rate was overpredicted because the local fluid was driven to saturation state faster than in a real scenario. Hence, improvements could be brought into the bulk condensation model to account for the delay in reaching the saturation state, thereby more accurately reflecting the physical process. An alternative bulk condensation model [Zhang & Laurien, 2014], which considers the droplet surface area and diffusion of steam to the droplet surface, was explored for implementation. However, this model exhibited stability issues, necessitating extremely small time-step sizes for reliable calculations. Further research is required to investigate ways to make this model stable in *containmentFOAM*. The PBM implementation was able to model the droplet evolution, but it was not possible to validate it directly against experiments due to a lack of droplet size measurements in experiment containment facilities. Therefore, experiments focused on fog formation and droplet size evolution could be performed, and droplet size distributions should be measured. This will provide valuable data for validation of the bulk condensation and PBM models in a containment scenario. The current work only considered coalescence by turbulent aggregation, while other mechanisms like ballistic and Brownian collisions could also be explored.

The single-phase approach addressed in the present work was found to be computationally efficient and feasible, whereas the two-phase approach demonstrated significant computational challenges. The two-phase simulation required smaller time step sizes to be stable for technical-scale containment simulations with phase change processes, particularly when thermal non-equilibrium existed between the phases; ultimately, the thermal equilibrium approach was successfully used. Hence, further research is required to find possible solutions to improve the stability and speed of the two-phase non-equilibrium solver. The assumption of thermal equilibrium between the phases in the two-phase approach will become unrealistic, especially in cases involving large droplets with high drift velocities like sprays. In such scenarios, these droplets would not instantly achieve thermal equilibrium with the surrounding gas phase.

Future improvements can explore the two-phase approach to account for thermal non-equilibrium effects by using separate energy equations for each phase instead of the mixture energy equation. Although the two-phase approach presented in this work did not indicate any improvements in predicting the vessel conditions in the validation experiments, it was able to demonstrate phenomena like wall condensate films and accumulation of water in the sump region. The approach requires further validation and testing using experiments with higher condensation rates, which could cause condensate accumulations large enough to influence the containment pressures.

Finally, this two-phase CFD approach holds significant potential for performing safety analyses in small modular reactors (SMRs), which feature large quantities of liquid water occupying considerable containment volumes and condensation on gas-liquid interfaces. The development of

containmentFOAM towards SMR safety analysis represents a crucial future direction for this research. The present work serves as an important initial step towards this ambitious objective, laying the groundwork for SMR-specific modeling capabilities.

Bibliography

[Abrahamson, 1975] Abrahamson, J. (1975). Collision rates of small particles in a vigorously turbulent fluid. *Chemical Engineering Science*, 30, 1371–1379.

[Allelein et al., 2008a] Allelein, H.-J., Arndt, S., Klein-Hessling, W., Schwarz, S., Spengler, C., & Weber, G. (2008a). COCOSYS: Status of development and validation of the german containment code system. nuclear engineering and design. *Nuclear Engineering and Design*, 238(4), 872–889.

[Allelein et al., 2008b] Allelein, H. J., Schwarz, S., Fischer, K., Vendel, J., Malet, J., Bentaib, A., Studer, E., Paillere, H., & Houkema, M. (Sep 2008b). *International standard problem ISP-47 on containment thermal hydraulics - Final report (NEA-CSNI-R–2007-10)*. Technical report, Nuclear Energy Agency of the OECD (NEA).

[Ambrosini et al., 2014] Ambrosini, W., Forgione, N., Merli, F., Oriolo, F., Paci, S., Kljenak, I., Kostka, P., Vyskocil, L., Travis, J., Lehmkuhl, J., Kelm, S., Chin, Y.-S., & Bucci, M. (2014). Lesson learned from the SARNET wall condensation benchmarks. *Annals of Nuclear Energy*, 74, 153–164.

[Andreani et al., 2010] Andreani, M., Paladino, D., & George, T. (2010). Simulation of basic gas mixing tests with condensation in the panda facility using the GOTHIC code. *Nuclear Engineering and Design*, 240(6), 1528–1547.

[ANSYS, Inc., 2013] ANSYS, Inc. (2013). *ANSYS FLUENT Population Balance Module Manual*. Canonsburg, PA: ANSYS Release 15.0.

[Antoine, 1888] Antoine, C. (1888). Tensions des vapeurs; nouvelle relation entre les tensions et les températures. *Comptes Rendus des Séances de l'Académie des Sciences (in French)*, 107, 681–684.

[Arnould et al., 2001] Arnould, F., Bachellerie, E., Auglaire, M., Boeck, B. d., Braillard, O., Eckardt, B., Ferroni, F., Moffett, R., & Van Goethem, G. (2001). State of the art on hydrogen passive auto-catalytic recombiner (European Union Parsoar project). In *9th International conference on nuclear engineering, France*.

[ASME, 2008] ASME (2008). Procedure for Estimation and Reporting of Uncertainty due to Discretization in CFD Applications. *Journal of Fluids Engineering*, 130(7), 078001.

[Bazin & Castelli, 1999] Bazin, P. & Castelli, P. (1999). COPAIN rapport d'essais, CEA/-DRN/DTP internal report. *SETEX/LETS/99-85*.

[Becker et al., 2011] Becker, P. J., Puel, F., Henry, R., & Sheibat-Othman, N. (2011). Investigation of discrete population balance models and breakage kernels for dilute emulsification systems. *Industrial & Engineering Chemistry Research*, 50(19), 11358–11374.

[Bentaib et al., 2015] Bentaib, A., Meynet, N., & Bleyer, A. (2015). Overview on hydrogen risk research and development activities: Methodology and open issues. *Nuclear Engineering and Technology*, 47(1), 26–32.

[Bertolotti et al., 2020] Bertolotti, L., Jefferson-Loveday, R., Ambrose, S., & Korsukova, E. (2020). A comparison of VOF and Euler-Euler approaches in CFD modelling of two-phase flows with a sharp interface. volume Volume 2C: Turbomachinery of *Turbo Expo: Power for Land, Sea, and Air* (pp. V02CT35A018).

[Bonneau et al., 2019] Bonneau, C., Josset, C., Melot, V., & Auvity, B. (2019). Comprehensive review of pure vapour condensation outside of horizontal smooth tubes. *Nuclear Engineering and Design*, 349, 92–108.

[Bosland et al., 2012] Bosland, L., Weber, G., Klein-Hessling, W., Girault, N., & Clement, B. (2012). Modeling and interpretation of iodine behavior in PHEBUS FPT-1 containment with ASTEC and COCOSYS codes. *Nuclear Technology*, 177(1), 36–62.

[Brackbill et al., 1992] Brackbill, J., Kothe, D., & Zemach, C. (1992). A continuum method for modeling surface tension. *Journal of Computational Physics*, 100(2), 335–354.

[Broxtermann & Allelein, 2013] Broxtermann, P. & Allelein, H.-J. (2013). Simulation of AP1000's passive containment cooling with the german containment code system COCOSYS. *Nuclear Engineering and Design*, 261, 326–332.

[Bucci et al., 2013] Bucci, M., Ambrosini, W., & Forgione, N. (2013). Experimental and computational analysis of steam condensation in the presence of air and helium. *Nuclear Technology*, 181(1), 115–132.

[Chen et al., 2006] Chen, F., Yu, S. C., & Lai, A. C. (2006). Modeling particle distribution and deposition in indoor environments with a new drift–flux model. *Atmospheric Environment*, 40(2), 357–367.

[Cheng & Wang, 1981] Cheng, Y. S. & Wang, C. S. (1981). Motion of particles in bends of circular pipes. *Atmospheric Environment*, 15(3), 301 – 306.

[Chung & Devaud, 2008] Chung, W. & Devaud, C. B. (2008). Buoyancy-corrected k–ε models and large eddy simulation applied to a large axisymmetric helium plume. *International Journal for Numerical Methods in Fluids*, 58(1), 57–89.

[de la Rosa et al., 2009] de la Rosa, J., Escrivá, A., Herranz, L., Cicero, T., & Muñoz-Cobo, J. (2009). Review on condensation on the containment structures. *Progress in Nuclear Energy*, 51(1), 32–66.

[Dehbi et al., 2013] Dehbi, A., Janasz, F., & Bell, B. (2013). Prediction of steam condensation in the presence of noncondensable gases using a CFD-based approach. *Nuclear Engineering and Design*, 258, 199–210.

[El Baamrani et al., 2021] El Baamrani, H., Bammou, L., Aharoune, A., & Boukhris, A. (2021). Volume of fluid (VOF) modeling of liquid film evaporation in mixed convection flow through a vertical channel. *Mathematical Problems in Engineering*, 2021(1), 9934593.

[Elghobashi, 1994] Elghobashi, S. (1994). On predicting particle-laden turbulent flows. applied scientific research. *Applied Scientific Research*, 52, 309–329.

[Firnhaber et al., 1996] Firnhaber, M., Kanzleiter, T., Schwarz, S., & Weber, G. (1996). *International standard problem ISP37: VANAM M3 - A Multi compartment aerosol depletion test with hygroscopic aerosol material: comparison report (NEA-CSNI-R–1996-26)*. Technical report, Nuclear Energy Agency of the OECD (NEA).

[Frederix et al., 2017] Frederix, E., Kuczajd, A. K., Nordlundd, M., Veldmanc, A. E. P., & Geurts, B. J. (2017). Eulerian modeling of inertial and diffusional aerosol deposition in bentpipes. *Computers and Fluids*, 159, 217 – 231.

[Fuller et al., 1966] Fuller, E. N., Schettler, P. D., & Giddings, J. C. (1966). New method for prediction of binary gas-phase diffusion coefficients. *Industrial & Engineering Chemistry*, 58(5), 18–27.

[Gennari et al., 2022] Gennari, G., Jefferson-Loveday, R., & Pickering, S. J. (2022). A phase-change model for diffusion-driven mass transfer problems in incompressible two-phase flows. *Chemical Engineering Science*, 259.

[Gubarevich et al., 2020] Gubarevich, T. A., Klementiev, A. A., Minko, K. B., & Yankov, G. G. (2020). Cross verification of a simplified model of pure steam condensation in a tube bundle using experimental and CFD-simulation data. *Journal of Physics: Conference Series*, 1683(2), 022092.

[Guelfi et al., 2007] Guelfi, A., Bestion, D., Boucker, M., Boudier, P., Fillion, P., Grandotto, M., Hérard, J.-M., Hervieu, E., & Péturaud, P. (2007). NEPTUNE: A new software platform for advanced nuclear thermal hydraulics. *Nuclear Science and Engineering*, 156(3), 281–324.

[Gärtner et al., 2020] Gärtner, J. W., Kronenburg, A., Rees, A., Sender, J., Oschwald, M., & Lamanna, G. (2020). Numerical and experimental analysis of flashing cryogenic nitrogen. *International Journal of Multiphase Flow*, 130, 103360.

[Hartley & Murgatroyd, 1964] Hartley, D. & Murgatroyd, W. (1964). Criteria for the break-up of thin liquid layers flowing isothermally over solid surfaces. *International Journal of Heat and Mass Transfer*, 7(9), 1003–1015.

[Harvill et al., 2022] Harvill, R. C., Lane, J. W., & George, T. L. (2022). Hybrid system level and coarse grid CFD tool for three-dimensional natural circulation, mixing, and stratification modeling. *Nuclear Technology*, 208(1), 1–26.

[Hinds, 1999] Hinds, W. C. (1999). *Aerosol Technology. 2nd Edition*. New York: John Wiley & Sons.

[Hirt & Nichols, 1981] Hirt, C. & Nichols, B. (1981). Volume of Fluid (VOF) method for the dynamics of free boundaries. *Journal of Computational Physics*, 39(1), 201–225.

[Hughes et al., 2000] Hughes, E., Niederauer, G., Wilkening, H., Travis, J., Spore, J., Royl, P., & Baumann, W. (2000). GASFLOW: A computational fluid dynamics code for gases, aerosols, and combustion, volume 3: Assessment manual.

[Hulburt & Katz, 1964] Hulburt, H. & Katz, S. (1964). Some problems in particle technology: A statistical mechanical formulation. *Chemical Engineering Science*, 19(8), 555–574.

[Höhne et al., 2017] Höhne, T., Gasiunas, S., & Šeporaitis, M. (2017). Numerical modelling of a direct contact condensation experiment using the AIAD framework. *International Journal of Heat and Mass Transfer*, 111, 211–222.

[IAEA, 2011] IAEA (2011). *Mitigation of Hydrogen Hazards in Severe Accidents in Nuclear Power Plants*. Number 1661 in TECDOC Series. Vienna: International Atomic Energy Agency.

[IAEA, 2022] IAEA (2022). *IAEA Nuclear Safety and Security Glossary*. Non-serial Publications. Vienna: International Atomic Energy Agency.

[Irizarry, 2012] Irizarry, R. (2012). Fast compartmental Monte Carlo simulation of population balance models: Application to nanoparticle formation in nonhomogeneous conditions. *Industrial & Engineering Chemistry Research*, 51(47), 15484–15496.

[Kakimpa et al., 2016] Kakimpa, B., Morvan, H. P., & Hibberd, S. (2016). The Numerical Simulation of Multi-Scale Oil Films Using Coupled VOF and Eulerian Thin-Film Models. Aircraft Engine; Fans and Blowers; Marine Turbo Expo: Power for Land, Sea, and Air (pp. V001T01A020).

[Kampili, 2024] Kampili, M. (2024). *Euler-Lagrangian Modeling of Aerosol Transport , Deposition and Impact of Nuclear Decay Heat*. PhD thesis, RWTH Aachen.

[Kampili et al., 2021] Kampili, M., Vijaya Kumar, G., Kelm, S., Arul Prakash, K., & Allelein, H.-J. (2021). Cfd simulations of stratified layer erosion in minipanda facility using the tailored cfd solver containmentfoam. *International Journal of Heat and Mass Transfer*, 178, 121568.

[Kanzleiter, 1993] Kanzleiter, T. (1993). *VANAM multi-compartment aerosol depletion test M3 with soluble aerosol material (BIeV–R67098-304)*. Technical report, Germany.

[Kanzleiter, 2002] Kanzleiter, T. (2002). *Experimental facility and program for the investigation of open questions on fission product behaviour in the containment (ThAI = Thermal Hydraulics, Aerosols, Iodine)*. Technical report, ThAI-Experiment TH2, Test Report to Reactor Safety Research Project No. 150 1218.

[Kanzleiter et al., 2008] Kanzleiter, T., Fischer, K., & Langer, G. (2008). *Helium/Hydrogen Material Scaling Test HM-2*. Technical report, Report No. 150 1326 – HM-2 TR, Becker Technologies GmbH, Eschborn.

[Kelm et al., 2021] Kelm, S., Kampili, M., Liu, X., George, A., Schumacher, D., Druska, C., Struth, S., Kuhr, A., Ramacher, L., Allelein, H.-J., Prakash, K. A., Kumar, G. V., Cammiade, L. M. F., & Ji, R. (2021). The tailored CFD package 'containmentFOAM' for analysis of containment atmosphere mixing, H2/CO mitigation and aerosol transport. *Fluids*, 6(3).

[Kelm et al., 2016] Kelm, S., Lehmkuhl, J., Jahn, W., & Allelein, H.-J. (2016). A comparative assessment of different experiments on buoyancy driven mixing processes by means of CFD. *Annals of Nuclear Energy*, 93, 50–57.

[Kelm et al., 2019] Kelm, S., Muller, H., Hundhausen, A., Druska, C., Kuhr, A., & Allelein, H.-J. (2019). Development of a multi-dimensional wall-function approach for wall condensation. *Nuclear Engineering and Design*, 353, 110239.

[Kelm et al., 2022] Kelm, S., Vijaya Kumar, G.and Kampili, M., Liu, X., Ji, R., Cammiade, L., George, A., Arul Prakash, K., & Allelein, H.-J. (2022). Technical scale CFD analysis of the pressurization and transport processes in the Battelle Model Containment during the ISP-37 VANAM M3 test. In *NUTHOS-13, Hsinchu, Taiwan, September 5-10, 2022*.

[Kim et al., 2011] Kim, D. E., Yang, K., Hwang, K., Ha, Y., & Kim, M. H. (2011). Pure steam condensation model with laminar film in a vertical tube. *International Journal of Multiphase Flow*, 37, 941–946.

[Kleiner et al., 2019] Kleiner, T., Rehfeldt, S., & Klein, H. (2019). CFD model and simulation of pure substance condensation on horizontal tubes using the volume of fluid method. *International Journal of Heat and Mass Transfer*, 138, 420–431.

[Kudriakov et al., 2008] Kudriakov, S., Dabbene, F., Studer, E., Beccantini, A., Magnaud, J., Paillère, H., Bentaib, A., Bleyer, A., Malet, J., Porcheron, E., & Caroli, C. (2008). The TONUS CFD code for hydrogen risk analysis: Physical models, numerical schemes and validation matrix. *Nuclear Engineering and Design*, 238(3), 551–565.

[Kumar & Ramkrishna, 1996a] Kumar, S. & Ramkrishna, D. (1996a). On the solution of population balance equations by discretization—I. a fixed pivot technique. *Chemical Engineering Science*, 51(8), 1311–1332.

[Kumar & Ramkrishna, 1996b] Kumar, S. & Ramkrishna, D. (1996b). On the solution of population balance equations by discretization—II. a moving pivot technique. *Chemical Engineering Science*, 51(8), 1333–1342.

[Lehnigk et al., 2022] Lehnigk, R., Bainbridge, W., Liao, Y., Lucas, D., Niemi, T., Peltola, J., & Schlegel, F. (2022). An open-source population balance modeling framework for the simulation of polydisperse multiphase flows. *AIChE Journal*, 68(3), e17539.

[Manninen et al., 1996] Manninen, M., Taivassalo, V., , & Kallio, S. (1996). *On the mixture model for multiphase*. Technical Research Center of Finland: VTT Publications 288.

[Marchisio & Fox, 2005] Marchisio, D. L. & Fox, R. O. (2005). Solution of population balance equations using the direct quadrature method of moments. *Journal of Aerosol Science*, 36(1), 43–73.

[McGraw, 1997] McGraw, R. (1997). Description of aerosol dynamics by the quadrature method of moments. *Aerosol Science and Technology*, 27(2), 255–265.

[Menter & Esch, 2001] Menter, F. & Esch, T. (2001). Elements of industrial heat transfer predictions. In *Proceedings of the 16th Brazilian Congress of Mechanical Engineering (COBEM-2001)*.

[Meredith et al., 2011a] Meredith, K., de Vries, J., & Xin, Y. (2011a). A numerical model for partially-wetted flow of thin liquid films. volume 6 (pp. 239–250).

[Meredith et al., 2011b] Meredith, K., Xin, Y., & de Vries, J. (2011b). A numerical model for simulation of thin-film water transport over solid fuel surfaces. *Fire Safety Science*, 10, 415––428.

[Mimouni et al., 2011] Mimouni, S., Foissac, A., & Lavieville, J. (2011). CFD modelling of wall steam condensation by a two-phase flow approach. *Nuclear Engineering and Design*, 241(11), 4445–4455.

[Mollier, 1929] Mollier, R. (1929). Ein neues Diagramm für Dampfluft Gemische. *Z. VDI*, 73, 1009 – 1013.

[NEA, 2007] NEA (2007). *International Standard Problem: ISP-47 on Containment Thermal Hydraulics – Final Report*. Technical report, Nuclear Energy Agency of the OECD (NEA).

[NEA, 2009] NEA (2009). *State-of-the-Art Report (SOAR) on Nuclear Aerosols*. Technical report, Nuclear Energy Agency of the OECD (NEA).

[Nusselt, 1916] Nusselt, W. (1916). Die Oberflachenkondesation des Wasserdamffes. *Zeitrschr. Ver. Deutch. Ing*, 60, 541–546.

[Okagaki et al., 2021] Okagaki, Y., Yonomoto, T., Ishigaki, M., & Hirose, Y. (2021). Numerical study on an interface compression method for the Volume of Fluid approach. *Fluids*, 6, 80.

[Onishi et al., 2022] Onishi, H., Goto, T., Haruki, M., & Tada, Y. (2022). Volume of Fluid-based numerical analysis of a pump-driven phase change heat transport device. *International Journal of Heat and Mass Transfer*, 186, 122429.

[OpenFOAM, 2023] OpenFOAM (2023). OpenFOAM Foundation version 11.

[Paladino & Dreier, 2012] Paladino, D. & Dreier, J. (2012). PANDA: A multipurpose integral test facility for LWR safety investigations. *Science and Technology of Nuclear Installations*, 2012(1), 239319.

[Paladino et al., 2012] Paladino, D., Guentay, S., Andreani, M., Tkatschenko, I., Brinster, J., Dabbene, F., Kelm, S., Allelein, H.-J., Visser, D., Benz, S., Jordan, T., Liang, Z., Porcheron, E., Malet, J., Bentaib, A., Kisselev, A., Yudina, T., Filippov, A., Khizbullin, A., & Loukianov, A. (2012). The euratom-rosatom ercosam-samara projects on containment thermal-hydraulics of current and future LWRs for severe accident management. *International Congress on Advances in Nuclear Power Plants 2012, ICAPP 2012*, 2, 1359–1368.

[Paladino et al., 2010] Paladino, D., Zboray, R., & Auban, O. (2010). The PANDA tests 9 and 9bis investigating gas mixing and stratification triggered by low momentum plumes. *Nuclear Engineering and Design*, 240(5), 1262–1270.

[Park & Rogak, 2004] Park, S. & Rogak, S. (2004). A novel fixed-sectional model for the formation and growth of aerosol agglomerates. *Journal of Aerosol Science*, 35(11), 1385–1404.

[Perry et al., 2018] Perry, R., Green, D., & Southard, M. (2018). *Perry's Chemical Engineers' Handbook. 9th Edition*. New York: McGraw-Hill Education.

[Pilou et al., 2011] Pilou, M., Tsangaris, S., Neofytou, P., Housiadas, C., & Drossinos, Y. (2011). Aerosol science and technology inertial particle deposition in a 90^{o} laminar flow bend: An eulerian fluid particle approach. *Aerosol Science and Technology*, 45(11), 1376 – 1387.

[Pui et al., 1987] Pui, D. Y. H., Romay-Novas, F., & Liu, B. Y. H. (1987). Experimental study of particle deposition in bends of circular cross section. *Aerosol Science and Technology*, 7(3), 301 – 315.

[Rattner & Garimella, 2014] Rattner, A. S. & Garimella, S. (2014). Simple Mechanistically Consistent Formulation for Volume-of-Fluid Based Computations of Condensing Flows. *Journal of Heat Transfer*, 136(7), 071501.

[Roy & Jain, 1959] Roy, R. & Jain, S. (1959). A study of thin water film flow down an inclined plate without and with countercurrent air flow. *Experiments in Fluids*, 7, 318–328.

[Saffman & Turner, 1956] Saffman, P. & Turner, J. (1956). On the collision of droplets in turbulent clouds. *Journal of Fluid Mechanics*, 1, 16–30.

[Scott, 1968] Scott, W. T. (1968). Analytic studies of cloud droplet coalescence I. *Journal of Atmospheric Sciences*, 25(1), 54 – 65.

[Sidin et al., 2009] Sidin, R. S. R., IJzermans, R. H. A., & Reeks, M. W. (2009). A Lagrangian approach to droplet condensation in atmospheric clouds. *Physics of Fluids*, 21(10), 106603.

[Siemens, 2007] Siemens (2007). *Psychrometric Chart - Structure and Application*. Siemens Switzerland Ltd.

[Singh et al., 2022] Singh, M., Ranade, V., Shardt, O., & Matsoukas, T. (2022). Challenges and opportunities concerning numerical solutions for population balances: a critical review. *Journal of Physics A: Mathematical and Theoretical*, 55, 383002.

[Sosnowski et al., 2013] Sosnowski, P., Petronio, A., & Armenio, V. (2013). Numerical model for thin liquid film with evaporation and condensation on solid surfaces in systems with conjugated heat transfer. *International Journal of Heat and Mass Transfer*, 66, 382–395.

[Trela, 1994] Trela, M. (1994). A semi-theoretical model of stability of vertical falling liquid films. *Chemical Engineering Science*, 49(7), 1007–1013.

[Vijaya Kumar, 2022] Vijaya Kumar, G. (2022). *CFD simulation of the interaction of buoyant flows with nuclear aerosols*. PhD thesis, RWTH Aachen.

[Vijaya Kumar et al., 2021] Vijaya Kumar, G., Cammiade, L. M., Kelm, S., Arul Prakash, K., Groß, E. M., Allelein, H.-J., Kneer, R., & Rohlfs, W. (2021). Implementation of a CFD model for wall condensation in the presence of non-condensable gas mixtures. *Applied Thermal Engineering*, (pp. 116546).

[Vijaya Kumar et al., 2020] Vijaya Kumar, G., Kampili, M., Kelm, S., Arul Prakash, K., & Allelein, H.-J. (2020). CFD modelling of buoyancy driven flows in enclosures with relevance to nuclear reactor safety. *Nuclear Engineering and Design*, 365, 110682.

[Vyskocil et al., 2014] Vyskocil, L., Schmid, J., & Macek, J. (2014). CFD simulation of air–steam flow with condensation. *Nuclear Engineering and Design*, 279, 147 – 157.

[W. Ambrosini & Oriolo, 2002] W. Ambrosini, N. Forgione, D. M. & Oriolo, F. (2002). Computational study of evaporative film cooling in a vertical rectangular channel. *Heat Transfer Engineering*, 23(5), 25–35.

[Welch & Wilson, 2000] Welch, S. W. & Wilson, J. (2000). A volume of fluid based method for fluid flows with phase change. *Journal of Computational Physics*, 160(2), 662–682.

[Weller, 2006] Weller, H. (2006). *A New Approach to VOF-Based Interface Capturing Methods for Incompressible, Compressible and Cavitating Flow*. Technical report, OpenCFD Technical Report TR/HGW/07; OpenCFD: Salfords, UK,.

[Wilke, 1950] Wilke, C. R. (1950). A viscosity equation for gas mixtures. *The Journal of Chemical Physics*, 18(4), 517—519.

[Xiao et al., 2016] Xiao, J., Travis, J. R., Royl, P., Necker, G., Svishchev, A., & Jordan, T. (2016). Three-dimensional all-speed CFD code for safety analysis of nuclear reactor containment: Status of GASFLOW parallelization, model development, validation and application. *Nuclear Engineering and Design*, 301, 290–310.

[Zambaux & Laborde, 2023] Zambaux, J. & Laborde, L. (2023). Interfacial heat transfer with non-condensable gas in ASTEC V2.2: Application to severe accidents study during PWR cold shutdown states. *Nuclear Engineering and Design*, 411, 112434.

[Zhang & Laurien, 2014] Zhang, J. & Laurien, E. (2014). 3D numerical simulation of flow with volume condensation in presence of non-condensable gases inside a PWR containment. In *W. E. Nagel, D. H. Kröner, M. M. Resch (eds.)High Performance Computing in Science and Engineering '14: Transactions of the high performance computing center, stuttgart (HLRS) 2014* (pp. 479 – 497).: Springer.

[Zschaeck et al., 2014] Zschaeck, G., Frank, T., & Burns, A. (2014). CFD modelling and validation of wall condensation in the presence of non-condensable gases. *Nuclear Engineering and Design*, 279, 137–146.

Own publications

Journal articles

George, A., Kelm, S., Cheng, X., Allelein, H.-J., (2023). Efficient CFD modelling of bulk condensation, fog transport and re-evaporation for application to containment scale. *Nuclear Engineering and Design*, 401, 112067. https://doi.org/10.1016/j.nucengdes.2022.112067

Kelm, S., Kampili, M., Liu, X., George, A., Schumacher, D., Druska, C.,Struth, S., Kuhr, A., Ramacher, L., Allelein, H.-J., Prakash, K. A., Kumar, G. V., Cammiade, L. M. F., & Ji, R. (2021). The Tailored CFD package 'containmentFOAM' for Analysis of Containment Atmosphere Mixing, H2/CO Mitigation and Aerosol transport. *Fluids*, 6(3). https://doi.org/10.3390/fluids6030100

Conference Proceedings

George, A., Kelm, S., Cheng, X., (2023). Two-phase modeling of wall and bulk condensation by hybrid VOF-mixture approach for containment applications, in: *20th International Topical Meeting on Nuclear Reactor Thermal Hydraulics (NURETH-20), August 20 -25 2023, Washington DC, USA*

George, A., Kelm, S., Allelein, H.-J., (2022). Efficient CFD modelling of bulk condensation, fog transport and re-evaporation for application to containment scale, in: *19th International Topical Meeting on Nuclear Reactor Thermal Hydraulics (NURETH-19), March 6 - 11 2022, Brussels, Belgium.*

Kelm, S., Vijaya Kumar, G., Kampili, M., Liu, X., Ji, R., Cammiade, L., George, A., Arul Prakash, K., Allelein, H.-J. (2022). Technical Scale CFD Analysis of the Pressurization and Transport Processes in the Battelle Model Containment during the ISP 37 VANAM M3 Test. *NUTHOS-13, Hsinchu, Taiwan, September 5-10, 2022*.

Appendix

A. Liquid phase volume fraction transport equation derivation

Starting with Eqn. 3.58 and expanding it,

$$\alpha_l \frac{\partial \rho_l}{\partial t} + \rho_l \frac{\partial \alpha_l}{\partial t} + \rho_l \nabla \cdot \left(\alpha_l \vec{U}_m\right) + \alpha_l \vec{U}_m \cdot \nabla \rho_l + \rho_l \nabla \cdot \left(\alpha_l \vec{U}_{ml}\right) + \alpha_l \vec{U}_{ml} \cdot \nabla \rho_l$$
$$- \rho_l \nabla \cdot (\Gamma_l \nabla \alpha_l) - (\Gamma_l \nabla \alpha_l) \cdot \nabla \rho_l = S_{ml} + S_{mf,transfer} \quad \text{(A.1)}$$

$$\implies \rho_l \left(\frac{\partial \alpha_l}{\partial t} + \nabla \cdot \left(\alpha_l \vec{U}_m\right) + \nabla \cdot \left(\alpha_l \vec{U}_{ml}\right) - \nabla \cdot (\Gamma_l \nabla \alpha_l) \right)$$
$$+ \alpha_l \left(\frac{\partial \rho_l}{\partial t} + \vec{U}_m \cdot \nabla \rho_l + \vec{U}_{ml} \cdot \nabla \rho_l - \left(\frac{\Gamma_l \nabla \alpha_l}{\alpha_l} \right) \cdot \nabla \rho_l \right) = S_{ml} + S_{mf,transfer} \quad \text{(A.2)}$$

Dividing A.2 by ρ_1 and reordering the terms,

$$\frac{\partial \alpha_l}{\partial t} + \nabla \cdot \left(\alpha_l \vec{U}_m\right) + \nabla \cdot \left(\alpha_l \vec{U}_{ml}\right) - \nabla \cdot (\Gamma_l \nabla \alpha_l) = -\frac{\alpha_l}{\rho_l} \frac{D\rho_l}{Dt} + \frac{S_{ml}}{\rho_l} + \frac{S_{mf,transfer}}{\rho_l} \quad \text{(A.3)}$$

where $\frac{D\rho_l}{Dt} = \frac{\partial \rho_l}{\partial t} + \vec{U}_m \cdot \nabla \rho_l + \vec{U}_{ml} \cdot \nabla \rho_l - \left(\frac{\Gamma_l \nabla \alpha_l}{\alpha_l} \right) \cdot \nabla \rho_l$

Similarly Eqn. 3.59 can be expanded to,

$$\frac{\partial \alpha_g}{\partial t} + \nabla \cdot \left(\alpha_g \vec{U}_m\right) + \nabla \cdot \left(\alpha_g \vec{U}_{mg}\right) - \nabla \cdot \left(\Gamma_g \nabla \alpha_g\right) = -\frac{\alpha_g}{\rho_g} \frac{D\rho_g}{Dt} + \frac{(S_{mg} + S_{mf})}{\rho_g} \quad \text{(A.4)}$$

where $\frac{D\rho_g}{Dt} = \frac{\partial \rho_g}{\partial t} + \vec{U}_m \cdot \nabla \rho_g + \vec{U}_{mg} \cdot \nabla \rho_g - \left(\frac{\Gamma_g \nabla \alpha_g}{\alpha_g} \right) \cdot \nabla \rho_g$

Adding Eqns. A.3 and A.4 gives,

$$\frac{\partial \left(\alpha_l + \alpha_g\right)}{\partial t} + \nabla \cdot \left(\alpha_l \vec{U}_m + \alpha_g \vec{U}_m\right) = -\nabla \cdot \left(\alpha_l \vec{U}_{ml} + \alpha_g \vec{U}_{mg}\right) + \nabla \cdot \left(\Gamma_l \nabla \alpha_l + \Gamma_g \nabla \alpha_g\right)$$
$$- \left(\frac{\alpha_l}{\rho_l} \frac{D\rho_l}{Dt} + \frac{\alpha_g}{\rho_g} \frac{D\rho_g}{Dt} \right) + \frac{S_{ml}}{\rho_l} + \frac{(S_{mg} + S_{mf})}{\rho_g} + \frac{S_{mf,transfer}}{\rho_l} \quad \text{(A.5)}$$

$$\implies \nabla \cdot \vec{U}_m = -\nabla \cdot \left(\alpha_l \vec{U}_{ml} + \alpha_g \vec{U}_{mg}\right) + \nabla \cdot \left(\Gamma_l \nabla \alpha_l + \Gamma_g \nabla \alpha_g\right) - \left(\frac{\alpha_l}{\rho_l}\frac{D\rho_l}{Dt} + \frac{\alpha_g}{\rho_g}\frac{D\rho_g}{Dt}\right) + S_{ml}\left(\frac{1}{\rho_l} - \frac{1}{\rho_g}\right) + \frac{S_{mf}}{\rho_g} + \frac{S_{mf,transfer}}{\rho_l} \quad \text{(A.6)}$$

$$\implies \nabla \cdot \vec{U}_m = \nabla \cdot \left[\alpha_l \left(\frac{\rho_l}{\rho_g} - 1\right)\vec{U}_{ml} - \Gamma_l \left(\frac{\rho_l}{\rho_g} - 1\right)\nabla \alpha_l\right] - \left(\frac{\alpha_l}{\rho_l}\frac{D\rho_l}{Dt} + \frac{\alpha_g}{\rho_g}\frac{D\rho_g}{Dt}\right) + S_{ml}\left(\frac{1}{\rho_l} - \frac{1}{\rho_g}\right) + \frac{S_{mf}}{\rho_g} + \frac{S_{mf,transfer}}{\rho_l} \quad \text{(A.7)}$$

Adding and subtracting $\alpha_l \nabla \cdot \vec{U}_m$ on the RHS of Eqn. A.3,

$$\frac{\partial \alpha_l}{\partial t} + \nabla \cdot \left(\alpha_l \vec{U}_m\right) + \nabla \cdot \left(\alpha_l \vec{U}_{ml}\right) - \nabla \cdot \left(\Gamma_l \nabla \alpha_l\right) = \alpha_l \nabla \cdot \vec{U}_m - \alpha_l \nabla \cdot \vec{U}_m - \frac{\alpha_l}{\rho_l}\frac{D\rho_l}{Dt} + \frac{S_{ml}}{\rho_l} + \frac{S_{mf,transfer}}{\rho_l} \quad \text{(A.8)}$$

Substituting for $\nabla \cdot \vec{U}_m$ from Eqn. A.7 only for the second term on the RHS of Eqn. A.8

$$\begin{aligned}\frac{\partial \alpha_l}{\partial t} + \nabla \cdot \left(\alpha_l \vec{U}_m\right) + \nabla \cdot \left(\alpha_l \vec{U}_{ml}\right) - \nabla \cdot \left(\Gamma_l \nabla \alpha_l\right) &= \alpha_l \nabla \cdot \vec{U}_m \\ &- \alpha_l \left[\nabla \cdot \left(\alpha_l \left(\frac{\rho_l}{\rho_g} - 1\right)\vec{U}_{ml} - \Gamma_l \left(\frac{\rho_l}{\rho_g} - 1\right)\nabla \alpha_l\right) - \left(\frac{\alpha_l}{\rho_l}\frac{D\rho_l}{Dt} + \frac{\alpha_g}{\rho_g}\frac{D\rho_g}{Dt}\right)\right] \\ &- \alpha_l \left[S_{ml}\left(\frac{1}{\rho_l} - \frac{1}{\rho_g}\right) + \frac{S_{mf}}{\rho_g} + \frac{S_{mf,transfer}}{\rho_l}\right] - \frac{\alpha_l}{\rho_l}\frac{D\rho_l}{Dt} + \frac{S_{ml}}{\rho_l} + \frac{S_{mf,transfer}}{\rho_l} \quad \text{(A.9)}\end{aligned}$$

Simplifying above equation and reordering the terms give the final transport equation of liquid phase volume fraction for hybrid mixture-VOF approach:

$$\begin{aligned}\frac{\partial \alpha_l}{\partial t} + \nabla \cdot \left(\alpha_l \vec{U}_m\right) + \nabla \cdot \left(\alpha_l \vec{U}_{ml}\right) - \nabla \cdot \left(\Gamma_l \nabla \alpha_l\right) &= \alpha_l \nabla \cdot \vec{U}_m - \alpha_l \left[\nabla \cdot \left(\alpha_l \left(\frac{\rho_l}{\rho_g} - 1\right)\vec{U}_{ml} - \Gamma_l \left(\frac{\rho_l}{\rho_g} - 1\right)\nabla \alpha_l\right)\right] + \alpha_l \alpha_g \left[\frac{1}{\rho_g}\frac{D\rho_g}{Dt} - \frac{1}{\rho_l}\frac{D\rho_l}{Dt}\right] \\ &+ S_{ml}\left[\frac{1}{\rho_l} - \alpha_l \left(\frac{1}{\rho_l} - \frac{1}{\rho_g}\right)\right] - \alpha_l \frac{S_{mf}}{\rho_g} + S_{mf,transfer}\left[\frac{1}{\rho_l} - \alpha_l \frac{1}{\rho_l}\right] \quad \text{(A.10)}\end{aligned}$$